DYNAMICAL STUDY OF MULTIFRAGMENTATION AND RELATED PHENOMENA IN HEAVY-ION COLLISIONS

A THESIS

submitted to the

FACULTY OF SCIENCE

PANJAB UNIVERSITY, CHANDIGARH

for the degree of

DOCTOR OF PHILOSOPHY

2010

YOGESH KUMAR VERMANI

DEPARTMENT OF PHYSICS

PANJAB UNIVERSITY, CHANDIGARH

INDIA

ACKNOWLEDGEMENT

A person finishes many things in life to fulfill his dream. It is often then good to look back in time and say a word of thanks and gratitude to all those who have supported him or her to achieve the goal.

First of all, I would like and must thank to my advisor **Dr. Rajeev K. Puri**, for invaluable supervision over my research. Without his blessings, it wouldn't have been possible to complete the Ph.D research and write dissertation. During the course of five years of my research work, his approach and advice at each time step has always been appropriate and encouraging. It was his enthusiasm and faith in me that helped me to feel the depth of problems and write papers and dissertation.

When I began research in nuclear theory, my senior colleagues Dr. Amandeep Sood and Dr. Jatinder K. Dhawan also took time to share their knowledge on heavy-ion physics with me. I would like to thank them for sincere help and co-operation. I am grateful to my colleagues Rajiv Chugh, Ishwar Dutt, Ms. Supriya Goyal, and Ms. Sakshi Gautam for constructive discussions and joyful company. During this period, I had many interesting and fruitful discussions with Drs. W. Trautmann at GSI, Germany; C. Samanta at SINP, Kolkata; M. Bruno and M. D'Agostino at INFN, Italy. I acknowledge their timely response towards my queries, whenever i asked.

Next, I would also like to thank Chairperson, Dept. of Physics, and Director, Computer Center for providing necessary computation facility in the lab. Most of calculations in my research work wouldn't have been easier without timely help from Sh. Ajay Guleria, System Manager at Dept. of Computer Science & Applications. I must express special thanks to him for providing necessary software support for our calculations.

A personal thanks to my friends Er. Hardeep Singh at Panjab University, Chandigarh & Er. Balwinder Raj at IIT Roorkee for joyful company. They were always ready to provide all necessary help and co-operation. Hardeep inspired me to learn elementary UNIX/Linux administration.

The financial assistance in the form of research fellowships from CSIR and UGC is gratefully acknowledged.

Last but not the least, I express sincere gratitude to my family: father Sh. Om Parkash Vermani, mother Smt. Usha Vermani, brothers and sisters. It was their constant faith in me that helped me face all the challenges with self-confidence.

(**Yogesh Kumar Vermani**)

Chandigarh

Contents

ABSTRACT

We present a systematic study of multifragmentation and associated phenomena such as finite size effects, role of momentum dependent potentials in heavy-ion (HI) collisions, thermalization and entropy production at intermediate energies. These aspects are studied within the framework of *quantum molecular dynamics* (QMD) model as primary transport theory.

In the first part of thesis, we study the beam energy and system size dependence of fragment production in central symmetric reactions. The fragment production at central geometries is still an unclear phenomenon which is significantly affected by the radial flow and squeeze out of nuclear matter. The collective transverse expansion tends to enhance the process of clusterization. Recently, the production of intermediate mass fragments (IMFs) was studied as a function of beam energy in the center-of-mass frame ($E_{c.m.}$) on MSU 4π-Array set-up. The peak $E_{c.m.}$ (at which maximal IMF emission occurs) reveals a clear system mass dependence. We shall show that our model calculations for the unfiltered events reproduce the linear dependence of peak $E_{c.m.}$ on system mass as is observed experimentally. We shall further show that multiplicities of various fragment species also reflect similar mass scaling behavior at peak $E_{c.m.}$ indicating the role of surface to volume ratio in clusterization process.

In the next part, we shall address the problem of spectator fragmentation at relativistic bombarding energies using advanced clusterization algorithm namely *simulated annealing clusterization algorithm* (*SACA*). For the first time, our calculations based on the *SACA* method explain successfully the *universality behavior* in the production of intermediate mass fragments over entire energy range between 400-1000 AMeV, as observed on AL-ADiN set-up. We shall also propose an improved version of *SACA* method where constant binding energy check of -4 MeV/nucleon will be replaced by realistic binding energy check leading to most bound fragment structure.

The application of *SACA* method will be made in describing the spectator fragmentation in ultra low-energy HI reactions. We shall simulate the peripheral collisions of Au+Au at 35 AMeV using *SACA* and conventional *minimum spanning tree* (MST) clusterization subroutines. The *SACA* method allows early recognition of fragment pattern. We shall demonstrate that our model calculations for charge yields and charge of the heaviest frag-

ment using *SACA* approach are in closer agreement with experimental data reported by Multics-Miniball Collaboration. Conventional MST procedure, however, completely fails to predict the dynamics of spectator fragmentation at such low incident energies.

The phenomenon of multi-fragment emission in low-density regime is least exploited to probe the nature of nuclear matter equation of state. The heavy-ion reactions at low incident energies are particularly suitable to extract the information on the nuclear EoS, as the role of different nucleon-nucleon scattering cross sections is minimal at these energies. To achieve this goal, we shall simulate the reaction of $^{197}Au + ^{197}Au$ at an incident energy of 35 AMeV and at different peripheral geometries. We shall show that fragment charge distributions obtained from spectator matter decay are highly sensitive towards the stiffness of nuclear EoS. The comparison of fragment charge multiplicities calculated at different peripheral geometries indicates preference for *soft* compressibility modulus of the nuclear matter.

We shall further extend our analysis by studying the consequences of implementing momentum dependent interactions on the stability of nuclei, stopping and fragment emission characteristics. The evolution of cold QMD nuclei using momentum dependent interactions depict no artificial emission of heavier clusters and nuclei remain stable for the characteristic reaction times. The IMF multiplicity calculated using soft momentum dependent EoS for the Au+Au reactions as a function of impact parameter will be shown to reproduce the experimental trends very nicely.

As the last piece of research work discussed here, we aim to understand the thermal properties of hot & dense nuclear matter formed in HI reactions. For central symmetric reactions at relativistic energies, the fireball formed at midrapidity is expected to be equilibrated. This aspect is implemented to extract the baryonic entropy from the yield ratio of *deuteron-like* to *proton-like* clusters using Siemens and Kapusta's formalism. For this analysis, we shall simulate central symmetric reactions of $^{40}Ca+^{40}Ca$, $^{93}Nb+^{93}Nb$ and $^{197}Au + ^{197}Au$ at different incident energies. Our model calculations predict 'universality characteristics' for baryonic entropy produced *i.e.* it depends upon the participant proton multiplicity irrespective of the system mass chosen. Nearly no effect of beam energy is visible on the magnitude of baryonic entropy.

Chapter 1

Heavy-Ion Physics: Introduction and Present Status

Atomic nucleus is a fascinating bit of matter unlike any other familiar thing in daily life. Although nuclei have been studied for over a century for different aspects of nuclear matter such as properties of nuclides away from the valley of stability, formation and decay of super heavy elements (SHE) *etc* [1–3]. Of particular interest is the response of nuclear matter towards changes in temperature, density and pressure. Quest for bulk dynamics of nuclear matter *i.e.* nuclear matter equation of state (EoS) and possible co-existence of liquid-gas phases of nuclear matter, is of relevance not only for nuclear physics community but also in astrophysicists [4, 5] where origin of early universe, formation and structure of compact heavenly bodies such as neutron stars [4–6], and supernova explosions [7] are still open questions.

In last few decades, due to advances in accelerator technologies [8–10], it has become possible to bombard projectile nucleus onto the target at higher incident energies. This has led to emergence of a new branch in nuclear physics namely *intermediate energy heavy-ion physics*. Heavy-ion (HI) collisions at intermediate energies result into the formation of highly dense and hot piece of nuclear matter in laboratory. The nuclear matter density reaches several times the normal nuclear matter density $\rho_\circ (= 0.17\ fm^{-3})$ and heats the nucleus to typical temperatures in excess of $10^{12} K$. The nuclear matter under such extreme conditions of density and temperature is similar to that existed in the interior of neutron star or sun. It becomes, therefore, an important goal of HI experiments to explore the equation of state of nuclear matter.

In low-energy regime, the reaction mechanism is marked by the events of fusion-fission, deep-inelastic scattering and incomplete fusion [11–17]. Nucleons being in the

Fermi energy domain, there exists a significant Pauli Blocking of n-n collisions. The non-equilibrium effects, however, are negligible. On the other hand, in intermediate and high energy collisions, it becomes possible to excite the nucleons above Fermi-energy. As a result, mean field picture becomes less pronounced and non-equilibrium effects emerge. The clusterization (*i.e.* the breaking of nucleus into many pieces) and related phenomena such as collective flow, composite particles formation and entropy production, become important decay channels.

At intermediate energies, several observables have been found sensitive towards the stiffness of nuclear matter. In one of the earlier attempts, Scheid *et al* [18] and Amsden *et al* [19] tried to link nuclear shock waves with phenomenon of collective expansion of nuclear matter. One of the very first attempts on the emission of clusters *viz.* deuterons, ^3He, ^4He, as a signal of collective behavior was made by the Plastic Ball group [20, 21]. Further, sideward flow in HI reactions at intermediate energies, is closely linked with phenomena of stopping and thermal equilibrium in nuclear matter. The collective flow, as an outcome to the pressure and field gradient has nowadays become an important tool to infer the nature of medium dependent nucleon-nucleon (n-n) interactions and nature of EoS [22–24]. For incident energies $\geq$ 400 AMeV, the participant-spectator picture emerges [2, 7, 25], where spectators move at projectile and target rapidities in the center-of-mass frame. The participant matter *i.e.* fireball is, however, equilibrated in midrapidity region. This fireball formed is of immense interest since its formation is governed by the density achieved in the violent phase, colliding geometry as well as incident energy.

As far as spectator matter physics is concerned, the ALADiN Collaboration have explored many aspects related with the decay of heavy Au projectiles after collisions with different targets of C, Al, Cu, Pb and Au-nuclei [26–28]. Prominent features in these experiments were the '*rise and fall*' trend in the production of intermediate mass fragments (IMFs) with colliding geometry and *universal* behavior with respect to target mass and bombarding energy chosen. Apart from this, a calorific curve was also extracted that has been linked with the phenomenon of liquid-gas phase co-existence [29–31]. Many studies have reported the signals for phase co-existence [29, 32, 33] in nuclear matter. Recent experiments have also generated evidences in support of phase transition occurring in HI reactions and critical exponents determined [26, 29, 34]. This kind of phase co-existence is commonly observed in matter around us in everyday experience. In case of nuclei, however, the concept is quite new and challenging. Firstly, nuclides being finite

entities can not provide information on the bulk properties of nuclear matter directly. Secondly, there are non-equilibrium aspects associated with the heavy-ion collisions and strong nature of n-n interactions. Even calorific curve has been extracted for the heavy-ion collisions using isotope temperature T_{He-Li}. The occurrence of plateau region in the calorific curve as a signal of liquid-gas phase transition is still under intense debate [35–37]. A recent experiment by EOS Collaboration, however, showed that temperature T increases continuously with excitation energy E^* over the entire plateau region [38].

The symmetry energy in nuclear matter is another important observable that has gained much attention in present day heavy-ion research [5, 39]. The disassembly of hot fragmenting system can be looked as an important tool to characterize the symmetry energy of nuclear matter [40, 41]. Its role is equally important in astrophysical processes such as neutron star (NS) cooling, density and radii. The uncertainty in the equation of state of NS can lead to 50 % variation in the predictions of neutron star radii. With new laboratories coming up world wide such as proposed Facility for Rare Isotope Beams (FRIB) in USA [42, 43], Radioactive Ion Beam Factory (RIBF) at RIKEN in Japan [44], and the more versatile and multi-million Euros project 'FAIR' at GSI, Germany [45], it would become possible to compress the matter to several times its saturation density. Various exotic nuclei, and radio-isotopes along the drip line can be generated to study their peculiar nuclear structure and improve our knowledge on nuclear EoS of asymmetric nuclear matter. These terrestrial experiments would be helpful for theoretical models to put important constraints on nuclear equation of state at high densities [46–48] and predict structure of neutron stars. The radius of NS is mainly sensitive to neutron skin and symmetry energy. At present, heaviest neutron star has mass of 1.671 $\pm$ 0.008 $M_\odot$ [49], but possibility of neutron stars with mass $\geq 2M_\odot$ is still there [50].

At present, the Facility for Antiproton and Ion Research (FAIR) is upcoming heavy-ion laboratory at GSI, Germany. This will be deciding the future research in nuclear structure, nuclear reactions with radioactive beams, and astrophysics. The proposed facility consists of super-conducting synchrotron SIS 100/300 with a complex system of storage rings that will generate high intensity ion beams at 35 AGeV with mass of heavy-ions upto uranium-238. The FAIR project is quite diversified one that would be capable of providing high quality beams of all ion species from hydrogen to uranium along with antiprotons and kaons. It has strength for mass measurement of wider range of nuclei to predict the mass models with uncertainty less than 100 KeV/c^2. Apart from radio-isotope facility, FAIR

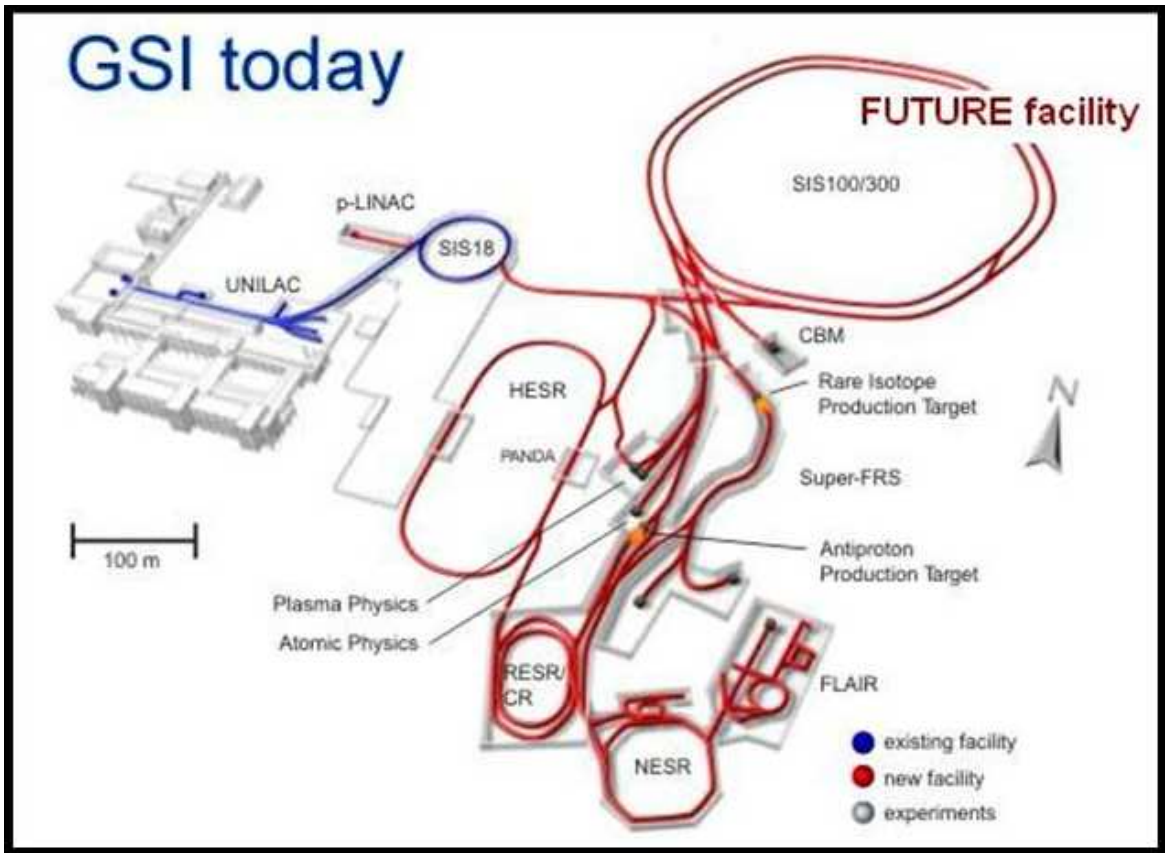

Figure 1.1: The schematic layout of existing GSI facility (in blue color) and upcoming FAIR facility (in red color).

will serve for future research in the field of atomic and molecular physics, radiobiological applications, and high-density plasma physics. The FAIR project is remarkable in view of its versatile design keeping in mind the future needs of scientific community and society. The FAIR project has huge budget estimate around 1,187 million Euros (M€). The full operation of all experimental programs is expected to start in 2015. The FAIR would be serving a user community of about 2500 researchers with 25 % working in rare-isotope beam capability.

Figure 1.1 gives a schematic layout of present and future of FAIR facility at GSI. The existing facility (in blue) at Gesellschaft für Schwerionenforschung (GSI) consists of linear accelerator UNILAC, heavy-ion synchrotron SIS 18, the fragment separator FRS and experimental storage ring ESR. The present UNILAC/SIS 18 complex (indicated in blue color) would serve as an injector for the upcoming double-ring SIS 100/300 synchrotron

facility. The projectile fragment separator FRS is the powerful in-flight facility for investigating relativistic exotic nuclei. The selected fragment beam is separated spatially during the flight that gives access to very short lived nuclei. The experiments at FRS has indicated the isomeric decays in the waiting point nucleus ^{130}Cd [51]. The FAIR facility (in red) gives site-map of accelerators such as high-energy storage ring (HESR), collector ring (CR), new experimental storage ring (NESR), super-conducting fragment separator (Super-FRS), and double ring synchrotron SIS 100/300. Masses of more than 1110 different nuclei have been measured in several FRS-ESR experiments [45, 52]. FRS would open-up new eras for the nuclear structure, astrophysics, and production of fragments at relativistic energies 400-1500 AMeV.

The Rare-Isotope Beam (RIB) factory is another high power heavy-ion beam facility at RIKEN, Japan. The RIB factory would provide (a) heavy-ions upto uranium-238, (b) a fragment separator, and (c) multifunction beam line spectrometer. Expected energies are 440 AMeV for light ions and 350 AMeV for ^{238}U. The in-beam spectroscopy of radio-isotopes would search for halo nuclei and magic number nuclei. The main focus of RIB factory would be the investigation of nuclear structure and astrophysical phenomena with user number of 500 researchers. A similar project known as Facility for Rare-Isotopes Beams (FRIB) is also proposed at Michigan State University, USA. This facility, formerly known as Rare Isotope Accelerator (RIA), would aim at low cost, next generation competitive radioactive beam facility. FRIB would strive for excellence in the studies of nuclear structure with extreme N/Z ratios and under the extreme conditions of density and temperature that have existed only in nature's spectacular explosions, the supernovae. FRIB would also provide rare-isotopes for application in human health, environmental issues, food technology and biotechnology. FRIB facility is expected to start experiments in 2017. For productive and competitive atmosphere, existing detectors at Argonne National Laboratory (ANL) and National Superconducting Cyclotron Laboratory (NSCL) would also be clubbed with FRIB. The FRIB project would also test the limiting values of N and Z in different nuclei, and properties of different neutron skins several times thicker than is possible to do currently.

For the proper understanding of properties of hot and dense nuclear matter which is accessible now due to advanced HI accelerators, one needs to employ theoretical tools for simulation. In the ultra-relativistic energy regime, reaction dynamics is quite different where elementary particles emerge with properties quite different from those in entrance

channel. Physicists have been mainly trying to understand multiple-particle production similar to that in cosmic ray cascades via simulation of ultra-relativistic collisions of hadrons and nuclei. In these Monte-Carlo simulations, one is always interested to extract information on the nuclear EoS and other observables such as temperature, entropy or chemical potential. Dynamical evolution of central collisions of Au+Au and Pb+Pb systems within the ultra-relativistic quantum molecular dynamics (UrQMD) model [53, 54] has shown that *global* equilibrium is unlikely even at SPS and AGS energies. The energy spectra of pions obtained in Au+Au collisions at 10.7 AGeV and Pb+Pb collisions at 40 and 160 AGeV within UrQMD calculations significantly deviated from the assumption of statistical equilibrium [53]. The question of nuclear EoS is also of principal interest for compressed baryon matter (CBM) experiments at GSI-FAIR [55]. Microscopic calculations based upon UrQMD [54] and quark-gluon string model (QGSM) [56] have show that equation of state has simple linear dependence: $P = {c_s}^2\varepsilon$, where ${c_s}^2$ is the squared sound velocity. It varies from 0.12 ± 0.01 at 11.6 AGeV to 0.1145 ± 0.005 at 160 AGeV [55, 57]. This has been conjectured as transition at bombarding energies around $\sim$ 40 GeV from the baryon -dominant matter to meson dominated one.

For the present thesis, we shall be investigating multi-fragment disintegration and related aspects in HI reactions at intermediate energies. For this study we shall employ the dynamical N-body theory namely quantum molecular dynamics (QMD) model [58, 59]. The brief overview of transport models used to probe nucleus-nucleus collisions at intermediate energies has been given in the next chapter. Details of the QMD model will be given in chapter 3.

As discussed above, the disintegration of of Au-projectiles as studied on ALADiN set-up is characterized by *rise and fall* behavior in the IMF multiplicity with impact parameter. This feature is remarkable in the sense that it remains unchanged for the relativistic bombarding energies $E \geq 400$ AMeV and independent of the target mass. This phenomenon has also been linked with the bi-modality character *i.e.* coexistence of multifragmentation events and residue formation [60]. One is always curious to see whether theoretical models having different reaction scenarios can explain this universality characteristic or not. Statistical reaction models assume that fragment production is determined in phase space when nuclear matter is in low-density phase and equilibrium is established [32, 61]. On the contrary, dynamical models rely on the initial-final states correlations which are not destroyed completely during the HI reactions. Probing dynam-

ical evolution of reaction at every time step would be of interest as it can also tell when and in which region of phase space fragments are formed.

Statistical approaches such as GEMINI [62], however, under-estimated the fragment yield for decay of excited Xe and Au nuclei. For larger charged particle multiplicity (*i.e.* central geometry) the calculated IMF multiplicity is much smaller than observed experimentally. Even a statistical code was also implemented, but none of these calculations could predict higher multiplicities of IMFs in central collisions [63]. Even the results obtained from statistical approaches like GEMINI a sequential decay, and COPENHAGEN a simultaneous break-up differ from each other [64]. In this direction, two-lattice percolation (TLP) model has been satisfactory in reproducing various features of nuclear multifragmentation as observed by MSU [63] and GSI [26, 27] groups. In the TLP model, target (projectile) nucleus is assumed to occupy sites in a simple cubic (SC) lattice. This picture is valid only for fragmentation process at relativistic bombarding energies when participant and spectator regions are clearly demarcated. Further this percolation theory assumes no critical behavior. The IMF correlations and elemental charge distribution are satisfactorily explained if percolation probability are associated with geometry of the collision [65]. The application of TLP model is, however, limited to nucleus-nucleus collisions at high incident energies only so that participant-spectator picture remains a good approximation.

These limitations of different statistical models suggest that multi-fragment emission is quite sensitive to how the phase-space is populated [64]. We have studied the spectator matter fragmentation in $^{197}Au + ^{197}Au$ collisions using microscopic cluster recognition method namely '*simulated annealing clusterization algorithm*' (SACA) [66–68]. Apart from coordinate space correlations [58], this novel algorithm also uses momentum space information of nucleons to construct the fragments. Here one obtains most bound fragment structure *i.e.* having maximum binding energy using simulated annealing technique [68]. This algorithm has been adapted from the early cluster recognition algorithm (ECRA) proposed by Dorso & Radrup [69]. We have shown that this novel algorithm remarkably explains the IMF yield particularly at large impact parameters and also the universality behavior in $^{197}Au + ^{197}Au$ reactions at 400, 600 and 1000 AMeV. A comparison with MST calculations showed the ability of SACA method to reproduce fragment multiplicities and mean charge of the heaviest fragment $\langle Z^{max} \rangle$ as early as 60 fm/c when the spectator matter is still interacting with hot participant zone. We have also proposed an improve-

ment over present SACA version where fragments are identified based upon their true binding energies. In this improvisation labeled as *SACA (2.1)*, we calculate fragments' total binding energy using the modified Bethe-Weizsäcker (BWM) mass formula [70–72].

For low energy HI collisions jus above the Coulomb barrier, fragment production for the projectile-like and target-like spectator components becomes dominant. It is worthwhile to explore the applicability of SACA method in describing the spectator matter fragmentation at these energies. We have studied spectator matter decay in peripheral $^{197}Au + ^{197}Au$ collisions at 35 AMeV *i.e. SACA (2.1)* and standard MST procedures. The comparison with experimental data taken with Multics-Miniball combined array [73] demonstrated the capability of *SACA (2.1)* method to reproduce the experimental b-dependence of mean charge of heaviest fragment at 35 AMeV accurately. This study validates the applicability of sophisticated algorithm such as SACA to study early dynamics of HI reactions at low energies. As mentioned above, evolution of spectator matter is governed by response to participant blast, and hence is highly sensitive towards nuclear EoS [74]. At higher incident energies, many theoretical and experimental studies exist that shed light on the nature of nuclear equation of state. Collective behavior being closely related to nuclear incompressibility is also widely discussed in literature to obtain information on energy-density relations in nuclear matter (that is , the EoS) [75–77]. For instance, systematic study of sideward flow from experiments and theoretical models could pin down the stiffness of nuclear matter to a very precise level [77, 78], but uncertainties are still very large [36, 78–80]. However as already discussed, simulation of nuclear reactions at supranormal densities reaching at higher incident energies is strongly influenced by momentum dependence of mean field and reduced in-medium scattering cross sections [76, 77]. Recently, it has been shown that non-equilibrium effects result in softening of nuclear EoS, that too complicates the process of extracting information on nuclear EoS [82]. This however, isn't much of the problem at low incident energies, when most of n-n collisions are Pauli blocked and choice of different nucleon-nucleon cross sections has only marginal effect on fragment emission.

The field of multifragmentation in low-energy regime is, however, least exploited to probe nuclear EoS. For the fission path of heavy nucleus, at low energy regime, the fission barrier is also found to depend sensitively on the choice of nuclear EoS [83]. For a *stiff* EoS, a lower fission barrier was obtained at T = 0 and 2 MeV. The information on incompressibility of nuclear matter and thus, nuclear EoS is also crucial for understanding

the structural properties of celestial objects like neutron stars [6]. From this review of literature, it is clear that future work on nuclear equation of state via simulation of HI reactions should be attributed to more refined comparison of theoretical predictions with the experimental data. The quest for nuclear incompressibility and thus nuclear EoS is, therefore, still pending problem of heavy-ion physics. We aim to probe nature of nuclear EoS via spectator fragmentation in Au+Au reactions at 35 AMeV. Fragment emission from the decay of *quasi-projectile* depends upon compression achieved by participant zone, and therefore, on nuclear incompressibility. We measured the fragment charge distribution obtained from the decay of spectator matter in peripheral Au (35 AMeV)+Au collisions using a 'soft' and a 'hard' EoS. The comparison of model calculations for charged particle multiplicity with experimental data taken with Multics-Miniball combined array [84] predicted a *soft* equation of state.

For proper understanding of equation of state in intermediate energy HI collisions, one also needs to take into account the momentum dependence of nuclear mean field [85, 86]. Extraction of nuclear compressibility from the experimental data, therefore, requires a knowledge of energy of deformation of nuclear matter in momentum space. Momentum dependence of mean field is one of the important factor behind the effective mass m^* of nucleon. We define m^* of a nucleon as:

$$\frac{m^*(e)}{m} = 1 - \frac{dV(e)}{de}, \tag{1.1}$$

where V(e) denotes the mean potential energy of a nucleon with energy 'e'. In an effective *n-n* potential, there is a fall in m^* since with deformation, potential energy is expected to decrease. Detailed calculations within microscopic DBHF approach and comparison with experimental data have shown that collective flow especially elliptical flow is quite sensitive to medium dependence of *n-n* cross section and nuclear equation of state [87]. This fact is also supported by relativistic Boltzmann-Uehling-Uhlenbeck (RBUU) model calculations for elliptical flow [88, 89] which shows that soft EoS along with momentum dependence of nuclear force is essential to account for non-equilibrium effects observed in heavy-ion reactions. At intermediate energies, momentum dependence of nucleon-nucleon potential plays major role in describing the fragmentation and associated phenomena such as collective flow, pion production *etc* [4, 85, 86, 90]. The BUU calculations for elliptical flow in Bi+Bi collisions have shown that momentum dependence of nuclear mean field characterized by $m^*/m \sim 0.7$ can describe the measured data very well [77]. In the present

work, we made systematic study on the importance of including momentum dependent interactions in cluster production and finite size effects. Main interest in the simulation of HI collisions at intermediate energies is whether nuclear system can acquire thermal equilibrium before break up or not. The question of equilibrium is closely related with nuclear matter stopping [24, 85, 91, 92]. The dynamical scenario of multifragmentation allows fast break-up of nuclear system leaving no scope for establishment of equilibrium. The FOPI experiments have also shown using rapidity spectra of protons and deuterons that complete stopping isn't possible in heavy-ion reactions [92]. We have emphasized on the question of nuclear matter stopping in the presence of momentum dependent interactions (MDI) and compare with static soft EoS. A systematic study over wide range of system masses suggested that maximum stopping occurs in heavier systems such as Au+Au system. With inclusion of MDI, peak obtained at midrapidity get broadened indicating *transparency* effect. This phenomenon is closely linked with expansion of nuclear matter in transverse direction that favors clusterization also. This behavior points towards importance of MDI in fragment production. Further, we have shown that there is a clear need of momentum dependent forces to explain spectator matter fragmentation at relativistic bombarding energies.

The formation of composite particles in the fireball also bears relevance as it can give clues on degree of stopping, equilibrium, temperature reached and entropy production [21, 93–95]. Entropy is one of the thermodynamical variables that is believed to remain unchanged through final stage of interaction [96]. Siemens and Kapusta made one of earliest attempts to estimate baryonic entropy S_N from deuteron-to-proton ratios R_{dp} for Ne+NaF and Ar+KCl reaction at 100 and 200 AMeV c.m. kinetic energies [93]. We have addressed these issues in detail in the last part of thesis. Our model predictions showed that nuclear matter may not achieve full equilibrium even for central geometry. Our calculations for baryonic entropy using the formula: $S_N = 3.945 - \ell n\tilde{R}_{dp}$ compare well with entropy derived from the measured yield ratios in Plastic Ball experiments [21].

Bibliography

[1] A. A. Stefanini *et al.*, Z. Phys. A **351**, 167 (1995).

[2] M. Leino and F. P. Heßberger, Annu. Rev. Nucl. Part. Sci. **54**, 175 (2004).

[3] D. F. Geesaman, C. K. Gelbke, R. V. F. Janssens and B. M. Sherrill, Annu. Rev. Nucl. Part. Sci. **56**, 53 (2006).

[4] L. W. Chen, C. M. Ko, B. A. Li and G. C. Yong, Front. Phys. China **2**, 327 (2007).

[5] B.-A Li, L. W. Chen and C. M. Ko, Phys. Rep. **464**, 113 (2008).

[6] J. M. Lattimer and M. Prakash, Phys. Rep. **333**, 121 (2000); J. Carriere, C. J. Horowitz and J. Piekarewicz, Astrophys. J. **593**, 463 (2003).

[7] E. A. Baron, J. Cooperstein and S. Kahana, Phys. Rev. Lett. **55**, 126 (1985); H. A. Bethe, Rev. Mod. Phys. **62**, 801 (1990).

[8] Amit Roy, Current Science **76**, 149 (1999); Pramana J. Phys. **57**, 659 (2001).

[9] W. F. Henning in *Proceedings of the Particle Accelerator Conference, Potland, Oregon*, **Vol 1**, 16 (2003).

[10] P. Spiller *et al.* in *Proceedings of* 10^{th} *European Particle Accelerator Conference, Edinburg, UK, 2006*, p. 24.

[11] W. J. Swiatecki, Nucl. Phys. A **376**, 275 (1982).

[12] A. Ono, H. Horiuchi and Toshiki Maruyama, Phys. Rev. C **48**, 2946 (1993).

[13] C. Bhattacharya, S. Bhattacharya and K. Krishan, Phys. Rev. C **49**, 3147 (1994); C. Bhattacharya, S. Bhattacharya and K. Krishan, Phys. Rev. C **54**, 3099 (1996).

[14] N. Wang, Z. Li and X. Wu, Phys. Rev. C **65**, 064608 (2002).

[15] Aparajita Dey, C. Bhattacharya, S. Bhattacharya, T. K. Rana, S. Kundu, K. Banerjee, S. Mukhopadhyay, S. R. Banerjee, D. Gupta and R. Saha, Phys. Rev. C **75**, 064606 (2007).

[16] S. Kundu, A. Dey, K. Banerjee, T. K. Rana, S. Muhkopadhayay, D. Gupta, R. Saha, S. Bhattacharya and C. Bhattacharya, Phys. Rev. C **78**, 044601 (2008).

[17] C. Beck *et al.*, Phys. Rev. C **80**, 034604 (2009).

[18] W. Scheid, H. Müller and W. Greiner, Phys. Rev. Lett. **32**, 741 (1974).

[19] A. A. Amsden, G. F. Bertsch, F. H. Harlow and J. R. Nix, Phys. Rev. Lett. **35**, 905 (1975).

[20] G. D. Westfall *et al.*, Phys. Lett. B **116**, 118 (1982).

[21] K. G. R. Doss *et al.*, Phys. Rev. C **32**, 116 (1985); K. G. R. Doss *et al.*, Phys. Rev. C **37**, 163 (1988).

[22] J. Jiang *et al.*, Phys. Rev. Lett. **68**, 2739 (1992).

[23] P. Danielewicz and Q. Pan, Phys. Rev. C **46**, 2002 (1992).

[24] M. Berenguer, Ch. Hartnack, G. Peilert, H. Stöcker, W. Greiner, J. Aichelin and A. Rosenhauer, J. Phys. G: Nucl. Part. Phys. **18**, 655 (1992).

[25] G. D. Westfall, J. Gosset, P. J. Johansen, A. M. Poskanzer, W. G. Meyer, H. H. Gutbrod, A. Sandoval and R. Stock, Phys. Rev. Lett. **37**, 1202 (1976).

[26] A. Schüttauf *et al.*, Nucl .Phys. A **607**, 457 (1996).

[27] J. Hubele *et al.*, Z. Phys. A **340**, 263 (1991).

[28] J. Hubele *et al.*, Phys. Rev. C **46**, R1577 (1992).

[29] J. Pochodzalla *et al.*, Phys. Rev. Lett. **75**, 1040 (1995).

[30] S. K. Samaddar and J. N. De, Phys. Rev. C **76**, 044607 (2007).

[31] G. Chaudhuri and S. Das Gupta, Phys. Rev. C **80**, 044609 (2009).

[32] J. P. Bondorf, A. S. Botvina, A. S. Iljinov, I. N. Mishustin and K. Sneppen, Phys. Rep. **257**, 133 (1995).

[33] M. F. Rivet *et al.*, Nucl. Phys. A **749**, 73 (2005).

[34] J. B. Elliott *et al.*, Phys. Rev. C **67**, 024609 (2003).

[35] S. Das Gupta, A. Z. Mekjian and M. B. Tsang, Adv. Nucl. Phys. **26**, 89 (2001).

[36] A. Barrañón, J. Escamilla Roa and J. A. López, Phys. Rev. C **69**, 014601 (2004).

[37] Y. G. Ma *et al.*, Phys. Lett. B **390**, 41 (1997); Y. G. Ma *et al.*, Phys. Rev. C **71**, 054606 (2005).

[38] J. A. Hauger *et al.*, Phys. Rev. C **57**, 764 (1998).

[39] M. Baldo and C. Maieron, J. Phys. G: Nucl. Part. Phys. **34**, R243 (2007).

[40] S. K. Samaddar, J. N. De, X. Viñas and M. Centelles, Phys. Rev. C **78**, 034607 (2008).

[41] S. K. Samaddar, J. N. De, X. Viñas and M. Centelles, Phys. Rev. C **80**, 035803 (2009).

[42] See *e.g.*, http://dnp.aps.org/

[43] See *e.g.*, http://frib.msu.edu/

[44] Y. Yano, Nucl. Instr. and Meth. B **261**, 1009 (2007).

[45] H. Geissel and Yu. A. Litvinov, Nucl. Instr. and Meth. **266**, 4176 (2008).

[46] L. V. Bravina *et al.*, Phys. Rev. C **78**, 014907 (2008).

[47] P. Senger *et al.*, J. Phys. G: Nucl. Part. Phys. **36**, 064037 (2009).

[48] P. P. Bhaduri and S. Chattopadhyay, Phys. Rev. C **81**, 034906 (2010).

[49] D. J. Champion *et al.*, Science **230**, 1390 (2008).

[50] P. C. Freire *et al.*, arXiv:astro-ph/0902.2891.

[51] A. Jungclaus *et al.*, Phys. Rev. Lett. **99**, 132501 (2007).

[52] A. Litvinov *et al.*, Hyperfine Interact. **173**, 55 (2006).

[53] L. V. Bravina *et al.*, Phys. Rev. C **60**, 024904 (1999).

[54] M. Bleicher *et al.*, J. Phys. G: Nucl. Part. Phys. **25**, 1859 (1999).

[55] E. E. Zabrodin *et al.*, J. Phys. G: Nucl. Part. Phys. **36**, 064065 (2009).

[56] L. V. Bravina *et al.*, Heavy Ion Phys. **5**, 455 (1997).

[57] L. V. Bravina *et al.*, Phys. Rev. C **78**, 014907 (2008).

[58] J. Aichelin, Phys. Rep. **202**, 233 (1991).

[59] Ch. Hartnack, R. K. Puri, J. Aichelin, J. Konopka, S. A. Bass, H. Stöcker and W. Greiner, Eur. Phys. J A **1**, 151 (1998).

[60] M. Pichon *et al.* (INDRA Collaboration), Nucl. Phys. A **749**, 93 (2004).

[61] D. H. E. Gross, Rep. Prog. Phys. **53**, 605 (1990).

[62] R. J. Charity *et al.*, Nucl. Phys. A **483**, 371 (1988).

[63] D. R. Bowman *et al.*, Phys. Rev. Lett. **67**, 1527 (1991).

[64] P. Kreutz *et al.*, Nucl. Phys. A **556**, 672 (1993).

[65] A. J. Santiago *et al.*, Phys. Scr. **55**, 152 (1997).

[66] P. B. Gossiaux, R. K. Puri, Ch. Hartnack and J. Aichelin, Nucl. Phys. A **619**, 379 (1997).

[67] J. Singh and R. K. Puri, J. Phys. G: Nucl. Part. Phys. **27**, 2091 (2001).

[68] R. K. Puri and J. Aichelin, J. Comp. Phys. **162**, 245 (2000).

[69] C. O. Dorso and J. Randrup, Phys. Lett. B **301**, 328 (1993).

[70] C. Samanta and S. Adhikari, Phys. Rev. C **65**, 037301 (2002); C. Samanta and S. Adhikari, Phys. Rev. C **69**, 049804 (2004).

[71] C. Samanta and D. N. Basu, Mod. Phys. Lett. A **20**, 1605 (2005).

[72] D. N. Basu, P. Roy Chowdhury and C. Samanta, AIP Conf. Proc. **802**, 142 (2005).

[73] M. D'Agostino and M. Bruno, private communication.

[74] L. Shi, P. Danielewicz and R. Lacey, Phys. Rev. C **64**, 034601 (2001).

[75] P. Danielewicz, Nucl. Phys. A **314**, 465 (1979).

[76] D. J. Magestro, W. Bauer and G. D. Westfall, Phys. Rev. C **62**, 041603(R) (2000), and references therein.

[77] P. Danielewicz, Acta Phys. Pol. B **33**, 45 (2002).

[78] P. Danielewicz, R. Lacey and W. G. Lynch, Science **298**, 1592 (2002).

[79] Q. Pan and P. Danielewicz, Phys. Rev. Lett. **70**, 2062 (1993).

[80] M. D. Partlan *et al.*, Phys. Rev. Lett. **75**, 2100 (1995).

[81] A. B. Larionov, W. Cassing, C. Greiner and U. Mosel, Phys. Rev. C **62**, 064611 (2000).

[82] C. Fuchs, P. Essler, T. Gaitanos and H. H. Wolter, Nucl. Phys. A **626**, 987 (1997).

[83] M. M. Majumdar, J. N. De, C. Samanta and S. K. Samaddar, Phys. Rev. C **48**, 2093 (1993).

[84] M. D'Agostino *et al.*, Nucl. Phys. A **650,** 329 (1999).

[85] J. Aichelin, A. Rosenhauer, G. Peilert, H. Stöcker and W. Greiner, Phys. Rev. Lett. **58**, 1926 (1987).

[86] C. Gale, G. Bertsch and S. Das Gupta, Phys. Rev. C **35**, 1666 (1987).

[87] A. Andronic *et al.*, Phys. Lett. B **612**, 173 (2005).

[88] T. Gaitanos, C. Fuchs and H. H. Wolter, Nucl. Phys. A **741**, 287 (2004).

[89] C. Fuchs and T. Gaitanos, Nucl. Phys. A **714**, 643 (2003).

[90] H. Stöcker and W. Greiner, Phys. Rep. **137**, 277 (1986).

[91] F. Rami *et al.*, Phys. Rev. Lett. **84**, 1120 (2000).

[92] W. Reisdorf, Acta. Phys. Pol. B **33**, 107 (2001).

[93] P. J. Siemens and J. I. Kapusta, Phys. Rev. Lett. **43**, 1486 (1979); P. J. Siemens and J. O. Rasmussen, Phys. Rev. Lett. **42**, 880 (1979).

[94] J. L. Klay *et al.*, Phys. Rev. C **68**, 054905 (2003).

[95] A. Andronic, P. Braun-Munzinger and J. Stachel, Nucl. Phys. A **772**, 167 (2006).

[96] I. M. Mishustin, F. Myhrer and P. J. Siemens, Phys. Lett. B **95**, 361 (1980); H. H. Gutbrod, A. M. Poskanzer and H. G. Ritter, Rep. Prog. Phys. **52**, 1267 (1989).

Chapter 2

Brief Survey of Various Transport Models used for Heavy-Ion Collisions

2.1 Introduction

The nuclear collisions in medium energy regime are associated with various phenomena like collective flow [1–3], multi-fragment emission [4, 5], and subthreshold particle production [6]. One needs proper transport theories to simulate the HI reactions and understand the reaction dynamics. In the current scenario, theoretical interest lies in the investigation of nuclear equation of state [7, 8], dynamics of fragmentation [9, 10], and bimodal-distribution of fragments [11, 12] *etc.* Theoretical description of heavy-ion collisions is also important to explain phenomena beyond nuclear physics. For instance, the stability and radius of neutron stars, as well as formation of stars and supernovae explosions strongly depend upon the character of nuclear equation of state.

The main purpose of this chapter is to highlight various important features of commonly used transport models in different incident energy regimes. No single transport model is capable of describing the reaction dynamics for the whole incident energy range. One has to employ a specific theory depending upon the incident energy regime. To interpret the experimental observables, different theoretical efforts have been made in past, which describe the evolution of such non-equilibrium processes. One of the primary microscopic theory to describe the heavy-ion collisions was inter nuclear cascade (INC) model. This type of model has been extensively employed in relativistic HI collisions [13–15], where one assumes that nucleons interact via binary collisions only. With coalescence, it could create fragments upto alpha particles (^4He) only. This limits the scope of INC model to study the fragment formation and related observables at intermediate energies.

Molitoris *et al* [16] showed that INC approach lacks dynamical flow due to very little intrinsic pressure built up in the cascade model. It reflects the absence of compression energy in the nuclear system.

In the present day scenario, two different semi-classical theoretical approaches, namely Boltzmann-Uehling-Uhlenbeck (BUU) model [17, 18] and molecular dynamics approach, the so-called 'quantum' molecular dynamics (QMD) model [19–21] are in use. These models include important quantum features *viz.* Fermi motion of nucleons, stochastic nucleon-nucleon (n-n) scattering and Pauli blocking. At low energies (below 50 AMeV), Pauli principle dominates the physics suppressing the 2-body collisions. In the latter case, mean field approaches like TDHF [22] or its semi classical version (Vlasov equation) [23–25] are suitable candidates. Some attempts have also been made to incorporate residual n-n collisions in extended approach (ETDHF) [26]. In the following sections, we shall be having an overview of these transport models.

2.2 On the derivation of time dependent Hartree-Fock (TDHF) theory

The TDHF theory belongs to the class of microscopic models to describe heavy-ion collisions. In Schrödinger picture, time development of the system is given as:

$$|\psi(t)\rangle = e^{-iHt/\hbar}|\psi(0)\rangle, \tag{2.1}$$

where H is the many-body Hamiltonian. The one-body density matrix is then given by

$$\rho_{ji}(t) = \langle\psi|c_j^+ c_i|\psi\rangle. \tag{2.2}$$

Differentialting w.r.t time t, we get

$$i\hbar\dot{\rho_{ji}} \;=\; \langle\psi|\left[c_j^+ c_i, H\right]|\psi\rangle. \tag{2.3}$$

The Hamiltonian H is defined as:

$$H = T + V = \sum_{\alpha\beta} T_{\alpha\beta} c_\alpha^+ c_\beta + \frac{1}{4}\sum_{\alpha\beta\gamma\delta} V_{\alpha\beta\gamma\delta} c_\alpha^+ c_\beta^+ c_\delta c_\gamma, \tag{2.4}$$

with T as the single particle kinetic energy operator and V as the two-body interactions. c_α^+ and c_β represent the creation and destruction operators, respectively.

Defining Hartree-Fock (HF) potential as:

$$\langle j|U|\gamma\rangle = \sum_{\alpha\delta} \left[\langle j\alpha|V|\gamma\delta\rangle - \langle \alpha j|V|\gamma\delta\rangle\right] \rho_{\alpha\delta} \tag{2.5}$$

and using in Eq. (2.3), we obtain Liouville's equation for the density matrix in the interaction representations:

$$\dot{\rho_{ji}} = \frac{1}{i\hbar}\left[T + U, \rho\right]_{ji}. \tag{2.6}$$

This is familiar TDHF equation with time dependent potential.

The TDHF equations has also been used with Skyrme energy density functional [27, 28]. The main feature of this theory is to ensure antisymmetrized independent particle states so as to simulate the Pauli principle. It has been extensively employed to heavy-ion fusion reactions for last three decades [27–30]. Recently TDHF method predicted that nucleus-nucleus potential becomes energy dependent when center-of-mass energy approaches corresponding Coulomb barrier [30]. Such energy dependence is expected to affect the sub-barrier fusion process.

2.3 The intranuclear cascade (INC) model

In contrast to the TDHF theory, the intranuclear cascade model treats the n-n collisions in an explicit way. In this model, no Fermi momenta are assigned to nuclei. Each nucleon is treated as a collection of point nucleons distributed within a sphere. Initial coordinates of nucleons within a sphere are assigned by Monte Carlo procedure. When two nucleons collide, a Monte Carlo sampling decides whether scattering is elastic or inelastic. Cascade is a rapid process that takes place in about $10^{-22}s$. The intranuclear cascade models rely on the assumption that incoming particles interact with individual nucleons of the target and not the nucleus as a whole. This assumption is easily justified at higher incident energies since the *de Broglie* wavelength is much smaller than the average distance between the nucleons in a nucleus. It has been proposed that a sufficient condition for this justification is [31]:

$$\lambda_B \ll r_o \ll v t_{coll} \ll d,$$

where λ_B is the *de Broglie* wavelength, r_o is the range of the interaction, v is the relative speed, t_{coll} is the collision time and d is the average distance between nucleons in a nucleus. For beam energy of 150 AMeV or more, only inelastic channel of importance

is the pion channel. This is commonly included as the $\triangle-$formation: $nn \rightarrow n\triangle$, and $\triangle-$absorption: $n\triangle \rightarrow nn$. For these inelastic and elastic channels ($nn \rightarrow nn$, $n\triangle \rightarrow n\triangle$ and $\triangle\triangle \rightarrow \triangle\triangle$), the Cugnon parametrization of scattering cross section is employed [32]. At the end of multiple collision process, $\triangle$ particles are allowed to decay isotropically into a pion and a nucleon. In fact, intra-nuclear cascade codes treat the interaction of incident nucleons with a piece of matter providing them with a random mean free path. An excited remnant, the residue, is formed in initial stage which decays through sequential evaporation of nucleons and heavier fragments. It may be worth noticing that INC model neglects the interaction between cascading particles.

Cascade model left a great deal of things to be dealt with. For instance, Fermi momentum should be assigned to nucleons in the initial state. Fermi motion also demands inclusion of potential wells to model the reaction correctly. Some versions of this model have also tried inclusion of Fermi momenta for both target and projectiles [33]. However, potential well is not included in these Monte-Carlo calculations. The absence of potential well rules out its applicability in describing the production of composite particles as well as projectile fragmentation. Further possibility of using INC model to study heavy-ion collisions is limited to high-energy regimes, particularly. This is due to the absence of interactions among cascading particles.

The INC calculations can explain the high energy tail of the emitted protons and neutrons energy spectra, but failed to explain the low energy tail and energy spectra of composite particles *i.e.* deuterons, tritons and heavier particles. The cascade model is, therefore, well suited for studying the equation of state (EoS) of an ideal gas only. Now, we shall discuss various transport theories that employ mean field along with n-n collisions. These theories include one-body approach namely Boltzmann-Uehling-Uhlenbeck (BUU) model [17, 18] and many-body approaches such as quantum molecular dynamics (QMD) model [20], antisymmetrized molecular dynamics (AMD) [34–36], and fermionic molecular dynamics (FMD) [37]. Also these models include various quantum effects such as Pauli-blocking, Fermi momentum *etc.*

2.4 The Boltzmann-Uehling-Uhlenbeck (BUU) equation

The BUU model can be regarded as an improvisation of the cascade model with inclusion of mean field. Under TDHF scheme, two-body correlations are retained at various levels. BUU equation describes the time evolution of one-body distribution function in six-dimensional phase space. Consider the coordinate space density matrix

$$\rho_{\mathbf{r}\acute{\mathbf{r}}} = \sum_i \psi_i(\mathbf{r})\psi_i^*(\acute{\mathbf{r}}), \tag{2.7}$$

Instead of considering $\rho_{\mathbf{r}\acute{\mathbf{r}}}$, we find the equation of motion of its Fourier transform $f(\mathbf{r},\mathbf{p})$:

$$f(\mathbf{r},\mathbf{p}) = \frac{1}{(2\pi\hbar)^3}\int e^{-\frac{i\mathbf{p}\cdot\mathbf{s}}{\hbar}}\rho_{\mathbf{r}+\frac{\mathbf{s}}{2},\mathbf{r}-\frac{\mathbf{s}}{2}}d^3s. \tag{2.8}$$

An equivalent definition in momentum representation will be

$$f(\mathbf{r},\mathbf{p}) = \frac{1}{(2\pi\hbar)^3}\int e^{-\frac{i\mathbf{q}\cdot\mathbf{r}}{\hbar}}g_{\mathbf{p}+\frac{\mathbf{q}}{2},\mathbf{p}-\frac{\mathbf{q}}{2}}d^3q. \tag{2.9}$$

The quantity $f(\mathbf{r},\mathbf{p})$ is the closest analogue to classical phase space density that satisfies following relations:

$$\int f(\mathbf{r},\mathbf{p})d^3p = \rho(\mathbf{r}), \tag{2.10}$$

$$\int f(\mathbf{r},\mathbf{p})d^3r = g(\mathbf{p}), \tag{2.11}$$

$$\int g(\mathbf{p})\frac{\mathbf{p}^2}{2m}d^3p = \langle\psi|T|\psi\rangle. \tag{2.12}$$

From TDHF equation, we have

$$\dot{\rho_{ji}} = \frac{1}{i\hbar}\sum_\gamma\left[\langle j|T+U|\gamma\rangle\rho_{\gamma i} - \rho_{j\gamma}\langle\gamma|T+U|i\rangle\right]. \tag{2.13}$$

Using Eq. (2.13),(2.9) and (2.8), we calculate $\frac{df}{dt}$ as

$$\frac{df(\mathbf{r},\mathbf{p})}{dt} = A + B, \tag{2.14}$$

where

$$\begin{aligned} A &= \frac{1}{(2\pi\hbar)^3}\frac{1}{i\hbar}\int e^{-i\mathbf{q}\cdot\mathbf{r}/\hbar}[\langle\mathbf{p}+\mathbf{q}/2|T|\acute{\mathbf{p}}\rangle g_{\acute{\mathbf{p}},\mathbf{p}-\mathbf{q}/2} \\ &\quad -g_{\mathbf{p}+\mathbf{q}/2,\acute{\mathbf{p}}}\langle\acute{\mathbf{p}}|T|\mathbf{p}-\mathbf{q}/2\rangle]d^3\acute{p}d^3q, \qquad (2.15) \\ B &= \frac{1}{(2\pi\hbar)^3}\frac{1}{i\hbar}\int e^{-i\mathbf{p}\cdot\mathbf{s}/\hbar}\left[\langle\mathbf{r}+\mathbf{s}/2|U|\acute{\mathbf{r}}\rangle\rho_{\acute{\mathbf{r}},\mathbf{r}-\mathbf{s}/2}\right. \\ &\quad \left.-\rho_{\mathbf{r}+\mathbf{s}/2,\acute{\mathbf{r}}}\langle\acute{\mathbf{r}}|U|\mathbf{r}-\mathbf{s}/2\rangle\right]d^3\acute{r}d^3s. \qquad (2.16) \end{aligned}$$

Here '$\mathbf{q}$' is the relative pair momentum ($= \mathbf{q}_1 - \mathbf{q}_2$) between two particles. Similarly '$\mathbf{s}$' denotes relative distance in coordinate space. Equation (2.14) then reduces to

$$\frac{\partial f(\mathbf{r},\mathbf{p},t)}{\partial t} + \mathbf{v}\cdot\nabla_{\mathbf{r}} f(\mathbf{r},\mathbf{p},t) - \nabla_{\mathbf{r}} U(\mathbf{r},\mathbf{p},t)\cdot\nabla_{\mathbf{p}} f(\mathbf{r},\mathbf{p},t) = \left.\frac{\partial f}{\partial t}\right|_{coll}. \tag{2.17}$$

Here $U(\mathbf{r},\mathbf{p},t)$ is a self-consistent mean field associated with one-body distribution function $f(\mathbf{r},\mathbf{p},t)$. The term on r.h.s. of Eq. (2.17) is a collision term which shows that $f(\mathbf{r},\mathbf{p},t)$ will change when there is an interaction among particles. Assuming that only binary collisions dominate and ignoring the possibility that three or more particles collide simultaneously, we have from Eq. (2.17):

$$\left(\frac{\partial}{\partial t} + \mathbf{v_1}\cdot\nabla_{\mathbf{r1}} - \nabla_{\mathbf{r1}} U\cdot\nabla_{\mathbf{v}1}\right) f_1 = \int d\Omega\; d^3v_2\; \sigma(\omega)|\mathbf{v}_1 - \mathbf{v}_2|\left(\acute{f}_1\acute{f}_2 - f_1 f_2\right). \tag{2.18}$$

$\sigma(\omega)$ is the differential cross-section for the collision $(\mathbf{v}_1,\mathbf{v}_2) \rightarrow (\mathbf{\acute{v}_1},\mathbf{\acute{v}_2})$. Here, following abbreviations have been used [38]:

$$\begin{aligned} f_1 &\equiv f(\mathbf{r},\mathbf{v}_1,t), \\ f_2 &\equiv f(\mathbf{r},\mathbf{v}_2,t), \\ \acute{f}_1 &\equiv f(\mathbf{r},\acute{\mathbf{v}}_1,t), \\ \acute{f}_2 &\equiv f(\mathbf{r},\acute{\mathbf{v}}_2,t). \end{aligned}$$

This is integro-differential equation for $f(\mathbf{r},\mathbf{p},t)$. Bertsch and Das Gupta have solved this equation for A-particles [17], where for the general case Eq. (2.18) is replaced by a set of A-coupled equations.

In the BUU model, particles are point like entities in configuration and momentum space. BUU equation (2.17) describes the time evolution of one body distribution function in six-dimensional phase space using Hamiltonian formulation:

$$\begin{aligned} \dot{\mathbf{r}}_i &= \{\mathbf{p}_i, H\} = \{\mathbf{p}_i, T+U\}, \\ \dot{\mathbf{p}}_i &= -\{\mathbf{r}_i, H\} = -\{\mathbf{r}_i, T+U\}, \end{aligned} \tag{2.19}$$

where T and U represent the total kinetic and potential energies of all nucleons and 'i' is index of the nucleons. For the mean field, one takes a Skyrme type potential $U(\rho)$ as has been used in TDHF calculations:

$$U(\rho) = \alpha(\frac{\rho}{\rho_o}) + \beta(\frac{\rho}{\rho_o})^{\gamma}. \tag{2.20}$$

The density in BUU approach is determined by means of a cubic grid of size 'a' in the coordinate space. At each time step, one-particle distribution function $f^{(1)}$ has to be generated from the pseudo A-particles. Then, one can choose again randomly the test particles according to distribution function $f^{(1)}$. Therefore, this treatment retains some correlations but destroys all n-n correlations at each time step. For realistic calculations, one prefers to retain these correlations which would be suitable in many dynamical scenarios like instabilities, fission, multifragmentation and chaos *etc.* As far as single particles are concerned, BUU theory has been established as one-body approach to HI reactions. The recent advances in the BUU simulation incorporate momentum dependent [39] and isospin dependent potentials as well as isospin dependent n-n scattering cross section [40]. A good agreement has been found for longitudinal and transfer momenta, particle multiplicities and double differential cross section from the predictions of BUU model. The BUU equation is found suitable for describing the flow angle, which has a relevance to the nuclear EoS. Recently, BUU transport model was applied to calculate the anisotropy ratio $\langle E^{\perp}/E^{||}\rangle$ for $^{197}Au + ^{197}Au$ collisions as a function of impact parameter at incident energies of 100, 250 and 400 AMeV [41]. A better agreement with FOPI data was reached employing a stiff EoS. These predictions on stopping of nuclear matter indicate preferential expansion of nuclear matter into transverse direction rather than longitudinal direction for the head-on $^{197}Au + ^{197}Au$ collisions. However, predictive power for the 'best fit' equation of state is limited one, since FOPI data can not be used to directly decide on incompressibility due to acceptance cuts. Detector inefficiency naturally, tends to reduce the sensitivity of this ratio towards incompressibility. Therefore, one needs systematic study and reliable information from various transport models rather than immediately running into best choice for EoS.

A covariant description of BUU equation has also been advanced to study the hadron-nucleus and heavy-ion collisions [42]. This relativistic kinetic equation also termed as relativistic Boltzmann-Uehling-Uhlenbeck (RBUU) equation is defined as:

$$[k^{*\mu}\partial^{x}_{\mu} + (k^{*}_{\nu}F^{\mu\nu} + M^{*}(\partial^{\mu}_{x}M^{*}))\partial^{k^{*}}_{\mu}]f(x.k^{*}) =$$
$$\frac{1}{2(2\pi)^{9}}\int \frac{d^{3}k_{2}}{E^{*}_{k_{2}}}\frac{d^{3}k_{3}}{E^{*}_{k_{3}}}\frac{d^{3}k_{4}}{E^{*}_{k_{4}}}W(kk_{2}|k_{3}k_{4})[f_{3}f_{4}\tilde{f}\tilde{f}_{2} - ff_{2}\tilde{f}_{3}\tilde{f}_{4}]. \qquad (2.21)$$

This approach is reported to explain the cross section for kaon momentum distribution at SIS energies quite well as measured by the KaoS Collaboration at GSI [43]. Equation (2.21) gives the evolution of single particle distribution $f_i \equiv f(x, k^{*}_{i})$ under the influence

of a mean field that enters via effective mass M^* and the field tensor $F^{\mu\nu}$. The r.h.s. term is the collision integral in which $f_i \equiv f(x, k_i^*)$ for the particle and $\tilde{f}_i \equiv (1 - f(x, k_i^*))$ for the hole distributions with four-momentum $k^{*\mu} = (E_k^*, \mathbf{k})$. In fact, the collision integral includes all inelastic channels such as resonances production and absorption along with meson production. This theory recently explained the K^+ mesons energy spectrum in C+C @ 2 AGeV collisions which was measured by HypHI Collaboration at GSI [44, 45]. This theory is well suited for energetic collisions between light nuclei. Choice of heavier nuclei hinders identification of hyper nuclei via weak decay of hyperons into pions.

2.5 Molecular dynamics approaches

Inherent problems of these models is to extract more complicated 2-body observables. It has always remained a problem of how to deal with composite particles formation. At present, dynamical models based upon molecular dynamics picture are well suited to handle phenomena such as multi-fragment emission. Molecular dynamics approaches ensure retention of multi-particle correlations and are able to address the phenomena like cluster formation. This has led to preference for molecular dynamics model to remove the grey area of mean field models which treat the single particle phase space density $f(\mathbf{r}, \mathbf{p})$ and are most suitable for the calculation of quantities which are expressed as expectation values of one-body observables. Basic character of QMD is similar to classical molecular dynamics model [10] *i.e.* it solves classical equations of motion for the position and momenta of A-particles:

$$\dot{\mathbf{r}_i} = \nabla_{\mathbf{p}_i} \langle H \rangle; \ \dot{\mathbf{p}_i} = -\nabla_{\mathbf{r}_i} \langle H \rangle, \ i = 1, ..., A. \tag{2.22}$$

The QMD model differs from its classical versions in two aspects. One is the inclusion of Fermi character in ground state of nuclei and second is appearance of *both* a collision and a potential term generated by same bare interaction. Our findings in present work have been compiled in the framework of *quantum molecular dynamics* (QMD) model which will be discussed in detail in chapter 3.

For the study of heavy-ion collisions at relativistic energies, ultra-relativistic quantum molecular dynamics (UrQMD) model has also been designed [47, 48]. This theory is well suited to describe nucleus-nucleus collisions at AGS and SPS energies where quark and gluon degrees of freedom become relevant. This relativistic version contains 55 baryons

and 32 meson states together with their antiparticles and isospin projected states. For masses greater than 2.0 GeV/c^2, a string picture is used by incorporating color string formation and resonance decay. Nucleons interact via two- and three-body Skyrme potential supplemented with Yukawa and Coulomb potentials as in non-relativistic version of the QMD model. The total nucleon-nucleon cross section σ_{nn} depends upon isospin of the colliding nucleons, their flavor and center-of-mass energy. A collision between two hadrons would occur if relative distance $d < \sqrt{\frac{\sigma_{nn}(\sqrt{s})}{\pi}}$, where 'd' and '$\sigma_{nn}$' are the impact parameter and total scattering cross section of two hadrons. The neutron-neutron cross section is assumed to be equal to proton-proton cross section [49]. The total and elastic proton-antiproton cross section at higher incident energies are calculated according to CERN-HERA parameterization:

$$\sigma_{pp}^{el} = A + Bp^n + C\ell n^2(p) + D\ell n(p), \tag{2.23}$$

with laboratory momentum 'p' in GeV/c and cross section σ in mb. Parameters of this fit are listed in Ref. [48]. Recently nuclear matter stopping was studied over wide range of beam energy from SIS, and AGS upto SPS within UrQMD model. There, medium modification of *n-n* cross section and stiffness of equation of state are found to strongly affect the nuclear stopping at SIS energies [50]. With increase in energy from AGS to SPS, the so-called gaussian shape rapidity distribution gets changed to two-bump structure. This reflected dominance of *transparency* behavior in the high SPS energy region.

2.6 Molecular dynamics for fermions (FMD/AMD)

Recently, molecular dynamics approach has been advanced to describe the fermionic nature of nuclear matter using antisymmetrized wave packets. The fermionic molecular dynamics (FMD) model was proposed by Feldmeier *et al* [37, 51, 52]. In this approach, the total wave function of the system is represented by a Slater determinant of gaussian wave packets. The width of gaussian wave packet is treated as a variable in time which is an important non-classical degree of freedom [52, 53]. This helps to allow for evaporation of nucleons. This model is well suited for the study of low-energy fusion fission events and nuclear structure [54, 55]. The FMD approach has been recently employed to study the ground state band in ^{12}C nucleus [56]. The FMD calculations are found to give good description of negative parity states [55], whereas α-cluster model predicted too

small excitation energy for the 2^+ state. On the similar lines, antisymmetrized molecular dynamics (AMD) model has been extended in which A-nucleon system is represented by a Slater determinant of single particle gaussian wave packets [34, 35, 57, 58]. The AMD model assumes width of gaussian wave packet as a constant parameter unlike FMD model. This simplification nevertheless reduces computational time and ensures that there is no spurious coupling of internal motion and c.m. motion of a cluster or a nucleus. The set of single particle wave function is given as:

$$\phi_i(t) = \{\mathbf{Z}_i(t),\ \chi_i,\ \xi_i\}, \tag{2.24}$$

where the centroid of wave function $\mathbf{Z}_i(t)$ is a complex variable defined as:

$$\mathbf{Z}_i = \sqrt{L}\ \mathbf{r}_i + \frac{i}{2\hbar\sqrt{L}}\ \mathbf{p}_i, \tag{2.25}$$

with L as width parameter taken to be equal to 0.16 fm^{-2} and is time independent. The variables $(\chi_i,\ \xi_i)$ represent the spin-isospin states of a nucleon in p↑, p↓, n↑, and n↓ states. $(\mathbf{r}_i, \mathbf{p}_i)$ corresponds to position and momentum coordinates of each nucleon. The time evolution of centroids $\mathbf{Z}_i$ in Eq.(2.25) is treated in a classical manner. The important point on which these approaches differ from the QMD model is that physical momentum in AMD model is taken to be centroid of the gaussian wave packet in momentum distribution. In QMD model, usually, it represents the definite momentum of a nucleon. The AMD simulations of Ca+Ca reactions have recently shown that rms radii, fragment kinetic energies, and yield of light charged particles (Z=1, and 2) were larger than those of equilibrium ensemble prepared by confining the many body system in a container at all reaction times [59]. These calculations depict the significance of flow effects and transverse kinetic energy of fragments.

2.7 Summary

In this chapter, we have recaptured the basic details of transport models used in low and intermediate energy heavy-ion reactions. The mean field approaches like TDHF are suitable candidates for low energy heavy-ion reactions. At intermediate energies, phenomena such as multi-fragment emission, particle production and collective flow require more advanced transport models that can handle mean field and nucleon-nucleon collisions at the same level. We address the importance of one-body approach namely Boltzmann-Uehling-Uehlenbeck (BUU) equation and many-body approaches such as QMD, FMD

and AMD models. The quantum molecular dynamics (QMD) approach is an important tool to describe the multi-fragment emission and related phenomena such as transverse expansion, entropy production, system size effects *etc*. For the present thesis work we shall use the QMD model that is described in detail in the next chapter. The QMD calculations are suitably compared with experimental observables, wherever it is needed. An attempt shall also be made to probe nuclear incompressibility via spectator matter fragmentation at ultra-low excitation energies.

Bibliography

[1] A. Andronic *et al.*, Phys. Lett. B **612**, 173 (2005).

[2] Y. Zhang and Z. Li, Phys. Rev. C **74**, 014602 (2006).

[3] S. Kumar, S. Kumar and R. K. Puri, Phys. Rev. C **81**, 014611 (2010).

[4] X. Campi, H. Krivine, N. Sator and E. Plagnol, Eur. Phys. J. D **11**, 233 (2000).

[5] B. Borderie and M. F. Rivet, Prog. Part. Nucl. Phys. **61**, 551 (2008).

[6] B. A. Li, B. Zhang, A. T. Sustich and C. M. Ko, Phys. Rev. C **60**, 034902 (1999); S. Pal, C. M. Ko, Z. Lin and B. Zhang, Phys. Rev. C **62**, 061903 (2000).

[7] E. Santini, T. Gaitanos, M. Colonna and M. Di Toro, Nucl. Phys. A **756**, 468 (2005).

[8] O. Lopez and M. F. Rivet, Eur. Phys. J. A **30**, 263 (2006).

[9] J. B. Garcia and C. Cerruti, Nucl. Phys. A **578**, 597 (1994); M. Papa, T. Maruyama and A. Bonasera, Phys. Rev. C **64**, 024612 (2001).

[10] Y. K. Vermani and R. K. Puri, Europhys. Lett. **85**, 62001 (2009).

[11] G. Chaudhuri, S. Das Gupta and F. Gulminelli, Nucl. Phys. A **815**, 89 (2009).

[12] B. Borderie *et al.*, Nucl. Phys. A **834**, 535c (2010).

[13] Y. Yariv and Z. Fraenkel, Phys. Rev. C **20**, 2227 (1979).

[14] J. Cugnon, T. Mizutani and J. Vandermeulen, Nucl. Phys. A **352**, 505 (1981).

[15] Y. Kitazoe, M. Sano, Y. Yamamura, H. Furutani and K. Yamamoto, Phys. Rev. C **29**, 828 (1984).

[16] J. J. Molitoris, H. Stöcker, H. A. Gustafsson, J. Cugnon and D. L'Hôte, Phys. Rev. C **33**, 867 (1986).

[17] G. F. Bertsch and S. Das Gupta, Phys. Rep. **160**, 189 (1988); P. Ring and P. Schuk, The nuclear many-body problem, Springer-Verlag (1980).

[18] G. F. Bertsch, H. Kruse and S. Das Gupta, Phys. Rev. C **29**, 673 (1984); C. Grégoire, B. Remaud, F. Sébille, L. Vincet and Y. Raffay, Nucl. Phys. A **465**, 317 (1987); W. Bauer, Prog. Part. Nucl. Phys. **30**, 45 (1993); T. Reposeur, V. de la Mota, F. Sébille and C. O. Dorso, Z. Phys A **357**, 79 (1997); J. Aichelin, Ch. Hartnack, A. Bohnet, L. Zhuxia, G. Peilert, H. Stöcker and W. Greiner, Phys. Lett. B **224**, 34 (1989).

[19] J. Aichelin and H. Stöcker, Phys. Lett. B **176**, 14 (1986).

[20] J. Aichelin, Phys. Rep. **202**, 233 (1991).

[21] J. Aichelin, Ch. Hartnack, A. Bohnet, Li Zhuxia, G. Peilert, H. Stöcker and W . Greiner, Phys. Lett. B **224**, 34 (1989).

[22] H. Stöcker and W. Greiner, Phys. Rep. **137**, 277 (1986); F. Sakata, T. Kubo, T. Marumori, K. Iwasawa and Y. Hashimoto, Phys. Rev. C **50**, 138 (1994); D. Lacroix and Ph. Chomaz, Phys. Rev. C **58**, 1604 (1998).

[23] R. Y. Cusson, J. A. Maruhn and H. W. Meldner, Phys. Rev. C **18**, 2589 (1978).

[24] K. T. R. Davies and S. E. Koonin, Phys. Rev. C **23**, 2042 (1981).

[25] K. Goeke and P.-G. Reinhard (Eds.), *TDHF and beyond*, Lecture Notes in Physics, Vol. **171**, Springer-Verlag, New York/Berlin, 1982.

[26] S. Ayik, D. Lacroix and P. Chomaz, Phys. Rev. C **61**, 014608 (1999).

[27] C. Simenel and B. Avez, Int. J. Mod. Phys. E **17**, 31 (2008).

[28] C. Golabek and C. Simenel, Phys. Rev. Lett. **103**, 042701 (2009).

[29] C. Simenel, Ph. Chomaz and G. de France, Phys. Rev. C **76**, 024609 (2007).

[30] K. Washiyama and D. Lacroix, Phys. Rev. C **78**, 024610 (2008).

[31] J. Cugnon and P. Henrotte, Eur. Phys. J. A **16**, 393 (2003).

[32] J. Cugnon, T. Mizutani and J. Vandermeulen, Nucl. Phys. A **352**, 505 (1981).

[33] J. Cugnon, Phys. Rev. C **22**, 1885 (1980).

[34] A. Ono, S. Hudan, A. Chbihi and J. D. Frankland, Phys. Rev. C **66**, 014603 (2002).

[35] R. Wada *et al.*, Phys. Rev. C **69**, 044610 (2004).

[36] J. Rizzo, M. Colonna and A. Ono, Phys. Rev. C **76**, 024611 (2007).

[37] H. Feldmeier and J. Schnack, Prog. Part. Nucl. Phys. **39**, 393 (1997).

[38] F. Reif, *Fundamental of Statistical and Thermal Physics* (McGraw-Hill, 1965), Chapter 13.

[39] Q. Pan and P. Danielewicz, Phys. Rev. Lett. **70**, 2062 (1993); J. Zhang, S. Das Gupta and C. Gale, Phys. Rev. C **50**, 1617 (1994); V. Greco, A. Guarnera, M. Colonna and M. Di Toro, Phys. Rev. C **59**, 810 (1999).

[40] B. A. Li and S. J. Yennello, Phys. Rev. C **52**, R1746 (1995); B. A. Li, Z. Ren, C. M. Ko and S. J. Yennello, Phys. Rev. Lett. **76**, 4492 (1996).

[41] P. Danielewicz, Phys. Rev. C **51**, 716 (1995).

[42] C. M. Ko and G. Q. Li, J. Phys. G: Nucl. Part. Phys. **22**, 1673 (1996).

[43] T. Gaitanos, H. H. Wolter and C. Fuchs, Phys. Lett. B **478**, 79 (2000).

[44] T. Gaitanos, H. Lenske and U. Mosel, Phys. Lett. B **675**, 297 (2009).

[45] T. Gaitanos, A. B. Larionov, H. Lenske and U. Mosel, Phys. Rev. C **81**, 054316 (2010).

[46] R. J. Lenk and V. R. Pandharipande, Phys. Rev. C **34**, 177 (1986); T. J. Schlagel and V. R. Pandharipande, Phys. Rev. C **36**, 162 (1987).

[47] L. V. Bravina *et al.*, Phys. Rev. C **60**, 024904 (1999).

[48] M. Bleicher *et al.*, J. Phys. G: Nucl. Part. Phys. **25**, 1859 (1999).

[49] R. M. Barnett *et al.*, Phys. Rev. D **54**, 1 (1996).

[50] Y. Yuan, Q. Li, Z. Li and F.-H. Liu, Phys. Rev. C **81**, 034913 (2010).

[51] H. Feldmeier, Nucl. Phys. A **515**, 147 (1990).

[52] H. Feldmeier and J. Schnack, Rev. Mod. Phys. **72**, 655 (2000).

[53] K. H. O. Hasnaouia, Ph. Chomaz and F. Gulminelli, Nucl. Phys. A **834**, 571c (2010).

[54] Y. Funaki, A. Tohsaki, H. Horiuchi, P. Schuck and G. Röpke, Phys. Rev. C **67**, 051306(R) (2003).

[55] T. Neff and H. Feldmeier, J. Phys.: Conf. Ser. **111**, 012007 (2008).

[56] M. Chernykh, H. Feldmeier, T. Neff, P. von Neumann-Cosel and A. Richter, Phys. Rev. Lett. **98**, 032501 (2007).

[57] A. Ono, Phys. Rev. C **59**, 853 (1999).

[58] T. Watanabe *et al.*, J. Phys. G: Nucl. Part. Phys. **36**, 015001 (2009).

[59] T. Furuta and A. Ono, Phys. Rev. C **79**, 014608 (2009).

Chapter 3

Our Principal Theoretical Approach

3.1 Introduction

The inherent limitations of one-body theories led to the development of molecular dynamics models. This class of models parameterize the many-body fermionic state of the nucleus in terms of gaussian wave packets for single particles. The *quantum molecular dynamics* (QMD) model is one of the widely used dynamical approaches in heavy-ion physics to study many-body phenomena such as fragment formation [2–9]. The primary QMD model was suggested by Aichelin and Stöcker [8]. The initial states of nuclei in terms of mean coordinates and momenta are assigned randomly so as to produce the experimental ground state density profile and binding energy of a nucleus. This version was designed to be isospin independent where all nucleons carry an effective charge.

We have chosen the original QMD code (version 1.02) developed and rewritten by Bohnet *et al* [6]. This version was dubbed as BQMD since it was designed to describe the proper binding energy of a nucleus. We have employed this version in the present work to explore still unrevealed aspects of multifragmentation such as universality behavior of the spectator fragmentation, system size effects in fragment production, and determination of the appropriate nuclear equation of state. This study naturally requires an efficient transport model like *quantum molecular dynamics* (QMD) model which takes into account the quantum aspects of heavy-ion collisions as well. The QMD model goes beyond the conventional molecular dynamics approach by incorporating the Pauli blocked collision term so as to mimic the manner in which Fermi motion takes place in the nuclear system. Further, a gaussian smearing is performed to obtain the spatial density of the nucleons at any point in time to emulate the effect of individual wave packets. For typical time scale

of heavy-ion collisions around 200 fm/c, one expects non-interacting nuclei to be stable, otherwise one can not extract reliable physics out of the model calculations. The stability of nuclei in the ground state is, thus, an important requirement before one studies the evolution of $A_T + A_P$ system in time. The fine details of this transport code are discussed under the following sub-sections.

3.1.1 General assumptions

We start with nuclear wave function as a product of A-gaussian wave packets *i.e.*

$$\begin{aligned} \Phi &= \prod_{i=1}^{A} \psi_i(\mathbf{r}, \mathbf{r}_i, \mathbf{p}_i, t), \\ &= \prod_{i=1}^{A} \frac{1}{(2\pi L)^{3/4}} e^{-(\mathbf{r}-\mathbf{r}_i(t))^2/4L} \cdot e^{\frac{\iota}{\hbar}\mathbf{p}_i(t)\cdot\mathbf{r}}. \end{aligned} \tag{3.1}$$

Smearing in momentum space is ignored as in classical version (CMD) [10]. Nucleons possess kinetic energy taken to be $\mathbf{p}_i^2(t)/2m$ with 'm' as nucleon mass. Note that we don't use a Slater determinant and thus antisymmetrization is neglected here. The A-body Wigner distribution function $f^{(n)}$ is the direct product of A-coherent states [3, 8]:

$$f^{(n)}(\mathbf{r}_1, ..., \mathbf{r}_A, \mathbf{p}_1, ..., \mathbf{r}_A, t) = \prod_{i=1}^{A} \frac{1}{(\pi\hbar)^3} e^{-(\mathbf{r}-\mathbf{r}_i(t))^2/2L} \cdot e^{-(\mathbf{p}-\mathbf{p}_i(t))^2 2L/\hbar^2}, \tag{3.2}$$

where, the squared width 'L' of gaussian is assumed to be independent of time. We don't allow spread of wave function in space which is also physically undesirable. Choice of gaussian width 'L' has to be made carefully, since too large value of L shall not produce effective surfaces and distort the outcome of reaction later on. A very small value of 'L' is also not desirable, due to the uncertainty principle. Standard value of 'L' is chosen to be $1.08 fm^2$, which corresponds to *rms* radius of the nucleon of 1.08 fm. Next, we have to assign the co-ordinates $(\mathbf{r}_i, \mathbf{p}_i)$ to the centers of gaussian wave packets. In co-ordinate space $(\mathcal{R}_3)$, centers are randomly distributed in a sphere of radius $R = R_o A^{1/3}$. Similarly, in momentum space $(\mathcal{P}_3)$, momenta are assigned between zero value and local Fermi momentum $P_F(\mathbf{r}_i)(= \sqrt{-2mU(\mathbf{r}_i)})$. Finally, the randomly distributed ensemble of $A_T + A_P$ nucleons should satisfy the relation: $(\mathbf{r}_i - \mathbf{r}_j)^2(\mathbf{p}_i - \mathbf{p}_j)^2 \geq d_{min}$ in phase space; A_T and A_P being the number of nucleons in target and projectile nuclei, respectively.

3.1.2 The nucleonic potential

Since we wish to solve an A-body problem, so we need to employ n-n potential instead of the average mean field. There are numerous effective n-n potentials that yield a given equation of state (EoS). The potential part used in the QMD model is taken from the original Skyrme interaction that can be written as [11]:

$$V^{Sk} = \frac{1}{2!}\sum_{j;i\neq j} V_{ij}^{(2)} + \frac{1}{3!}\sum_{j,k;i\neq j\neq k} V_{ijk}^{(3)}. \tag{3.3}$$

This potential consists of 2-body part V_{ij} and 3-body part V_{ijk} with

$$V_{ij}^{(2)}(\mathbf{r}_i - \mathbf{r}_j) = t_\circ(1 + \chi_\circ \mathbf{P}_\sigma)\delta + \frac{t_1}{2}(\acute{\mathbf{k}}^2\delta + \delta\mathbf{k}^2) + t_2\acute{\mathbf{k}}\cdot\delta\mathbf{k} + \iota W_\circ \acute{\mathbf{k}}\ \delta\hat{\sigma}\cdot\mathbf{k}. \tag{3.4}$$

Here, $\delta = \delta(\mathbf{r}_i - \mathbf{r}_j)$ and $\mathbf{k} = \frac{1}{2\iota}(\nabla_i - \nabla_j)$ is the relative momentum operator acting on the wave function. $\acute{\mathbf{k}}$ is the disjoint of $\mathbf{k}$. $\mathbf{P}_\sigma$ is the spin exchange operator. The three body term in Eq.(3.3) for spin-isospin saturated even-even nuclei can be expressed as:

$$V_{ijk}^{(3)}(\mathbf{r}_i, \mathbf{r}_j, \mathbf{r}_k) = t_3\delta(\mathbf{r}_i - \mathbf{r}_j)\delta(\mathbf{r}_j - \mathbf{r}_k) \tag{3.5}$$

The total ground state energy can be expressed as:

$$E = \langle\psi|\mathbf{T} + \mathbf{V}|\psi\rangle = \int \mathcal{H}(\mathbf{r})d\mathbf{r}. \tag{3.6}$$

For infinite nuclear matter, $\nabla\rho$=0, then expression for energy density $\mathcal{H}(\mathbf{r})$ becomes

$$\mathcal{H}(\mathbf{r}) = \frac{3}{5}T_F\rho + \frac{3}{8}t_\circ\rho^2 + \frac{1}{16}t_3\rho^3 + \frac{3}{80}(3t_1 + 5t_2)\rho^2 k_F^2, \tag{3.7}$$

where $T_F = \frac{\hbar^2 k_F^2}{2m}$ is the kinetic energy of a particle at Fermi surface. The density-dependent Skyrme potential $U^{Sk}(\rho)(= \frac{\partial\mathcal{H}}{\partial\rho})$ then reduces to:

$$U^{Sk}(\rho) = \alpha\rho + \beta\rho^\gamma. \tag{3.8}$$

Here we have generalized the quadratic three-body term ($= \frac{3}{16}t_3\rho^2$) so as to allow variation of nuclear compressibility. Now, the expectation value of total Hamiltonian H for the system of A-particles is given as:

$$\begin{aligned}\langle H\rangle &= \sum_{i=1}^{A}\frac{\mathbf{p}_i^2}{2m_i} + V^{Sk} \\ &= \sum_{i=1}^{A}\frac{\mathbf{p}_i^2}{2m_i} + \frac{1}{2!}\sum_{j;i\neq j}^{A} V_{ij}^{(2)} + \frac{1}{3!}\sum_{j,k;i\neq j\neq k}^{A} V_{ijk}^{(3)}.\end{aligned} \tag{3.9}$$

Now 2-body interaction part is:

$$\begin{aligned}
\sum_{j;i\neq j} V_{ij}^{(2)} &= \sum_{j;i\neq j} \int f_i(\mathbf{r}_i,\mathbf{p}_i,t) f_j(\mathbf{r}_j,\mathbf{p}_j,t) V(\mathbf{r}_i,\mathbf{r}_j) \\
&\quad \times d^3r_i d^3r_j d^3p_i d^3p_j, \\
&= \sum_{j;i\neq j} \int f_i(\mathbf{r}_i,\mathbf{p}_i,t) f_j(\mathbf{r}_j,\mathbf{p}_j,t) t_1 \\
&\quad \times \delta(\mathbf{r}_i-\mathbf{r}_j) d^3r_i d^3r_j d^3p_i d^3p_j, \\
&= \sum_{j;i\neq j} t_1 \int f_i(\mathbf{r}_i,\mathbf{p}_i,t) f_j(\mathbf{r}_j,\mathbf{p}_j,t) \\
&\quad \times d^3r_i d^3p_i d^3p_j, \\
&= \sum_{j;i\neq j} t_1 \int \frac{1}{(\pi\hbar)^3} e^{-(\mathbf{r}-\mathbf{r}_i(t))^2/2L} e^{-(\mathbf{p}-\mathbf{p}_i(t))^2 2L/\hbar^2} \\
&\quad \times \frac{1}{(\pi\hbar)^3} e^{-(\mathbf{r}-\mathbf{r}_j(t))^2/2L} e^{-(\mathbf{p}-\mathbf{p}_j(t))^2 2L/\hbar^2} d^3r_i d^3p_i d^3p_j, \\
&= \sum_j t_1 \frac{1}{(4\pi L)^{3/2}} e^{-(\mathbf{r}_i-\mathbf{r}_j)^2/4L}, \\
&= t_1 \sum_{j;i\neq j} \rho_{ij}, \qquad (3.10)
\end{aligned}$$

Similarly 3-body part is calculated as:

$$\begin{aligned}
\sum_{j,k;i\neq j\neq k} V_{ijk}^{(3)} &= \sum_{j,k;i\neq j\neq k} \int f_i(\mathbf{r}_i,\mathbf{p}_i,t) f_j(\mathbf{r}_j,\mathbf{p}_j,t) f_k(\mathbf{r}_k,\mathbf{p}_k,t) V(\mathbf{r}_i,\mathbf{r}_j,\mathbf{r}_k) \\
&\quad \times d^3r_i d^3r_j d^3r_k d^3p_i d^3p_j d^3p_k, \\
&= \sum_{j,k;i\neq j\neq k} \int f_i(\mathbf{r}_i,\mathbf{p}_i,t) f_j(\mathbf{r}_j,\mathbf{p}_j,t) f_k(\mathbf{r}_k,\mathbf{p}_k,t) t_2 \\
&\quad \times \delta(\mathbf{r}_i-\mathbf{r_j}) \delta(\mathbf{r}_i-\mathbf{r}_k) d^3r_i d^3r_j d^3r_k d^3p_i d^3p_j d^3p_k, \\
&= \frac{t_2}{(2\pi L)^3 \cdot 3^{3/2}} \sum_{j,k;i\neq j\neq k} e^{-\left[(\mathbf{r}_i-\mathbf{r}_j)^2+(\mathbf{r}_i-\mathbf{r}_k)^2+(\mathbf{r}_k-\mathbf{r}_j)^2\right]/6L}, \\
&= \frac{t_2}{(2\pi L)^3 3^{3/2}} \sum_{j,k;i\neq j\neq k} e^{-\left[(\mathbf{r}_i-\mathbf{r}_j)^2+(\mathbf{r}_i-\mathbf{r}_k)^2\right]/6L\times\frac{3}{2}}, \\
&= \frac{t_2 (4\pi L)^{3/2\times 2}}{(2\pi L)^3 \cdot 3^{3/2}} \left(\sum_{j\neq i} \frac{1}{(4\pi L)^{3/2}} e^{-(\mathbf{r}_i-\mathbf{r}_j)^2/4L} \right)^2, \\
&= \frac{t_2 2^3}{3^{3/2}} \left(\sum_{j\neq i} \rho_{ij} \right)^2. \qquad (3.11)
\end{aligned}$$

where interaction density ρ_{ij} is given as:

$$\rho_{ij} = \int d^3r \rho_i(\mathbf{r}) \rho_j(\mathbf{r}) = \frac{1}{(4\pi L)^{3/2}} e^{-(\mathbf{r}_i-\mathbf{r}_j)^2/4L}. \qquad (3.12)$$

Clearly 2-body contribution to the potential part is directly proportional to ρ/ρ_o while 3-body interaction term is proportional to $(\rho/\rho_o)^2$, where ρ_o is the normal nuclear matter density. In the nuclear matter limit, we can generalize the Skyrme-like potential as

$$\begin{aligned} V^{Sk} &= \frac{\alpha}{2\rho_o}\sum_{i,j}\frac{e^{-(\mathbf{r}_i-\mathbf{r}_j)^2/4L}}{(4\pi L)^{3/2}} \\ &\quad +\sum_i \frac{\beta}{\gamma+1}\cdot\frac{1}{{\rho_o}^\gamma}\left(\sum_{j,j\neq i}\frac{1}{(4\pi L)^{3/2}}e^{-(\mathbf{r}_i-\mathbf{r}_j)^2/4L}\right)^\gamma, \end{aligned} \tag{3.13}$$

where parameters α, β and γ are adjusted to reproduce the correct ground state properties of infinite nuclear matter *i.e.* binding energy per nucleon and pressure as:

$$\left.\frac{E}{A}\right|_{\rho=\rho_o} = -15.75\ MeV, \tag{3.14}$$

$$P = \rho^2\left.\frac{\partial(E/A)}{\partial\rho}\right|_{\rho=\rho_o} = 0\ MeVfm^3. \tag{3.15}$$

Parameter γ controls the incompressibility $\mathcal{K}(=9\rho^2\frac{\partial^2}{\partial\rho^2}(\frac{E}{A}))$ of the nuclear matter. Now this local Skyrme-type interaction in co-ordinate space is supplemented by Yukawa and Coulomb interactions, Hence total Hamiltonian reads:

$$\begin{aligned} \langle H\rangle &= \sum_{i=1}^{A}\frac{\mathbf{p}_i^2}{2m_i}+\frac{\alpha}{2\rho_\circ}\sum_{i,j\neq i}^{A}\frac{e^{-(\mathbf{r}_i-\mathbf{r}_j)^2/4L}}{(4\pi L)^{3/2}} \\ &\quad +\sum_{i=1}^{A}\frac{\beta}{\gamma+1}\cdot\frac{1}{\rho_\circ^\gamma}\left[\sum_{j,j\neq i}^{A}\frac{1}{(4\pi L)^{3/2}}e^{-(\mathbf{r}_i-\mathbf{r}_j)^2/4L}\right]^\gamma \\ &\quad +\frac{1}{2}(Z/A)^2\sum_{i,j\neq i}\frac{e^2}{|\mathbf{r}_i-\mathbf{r}_j|}erf\left(\frac{|\mathbf{r}_i-\mathbf{r}_j|}{\sqrt{4L}}\right) \\ &\quad +\frac{1}{2}\sum_{i,j\neq i}\frac{V_{Yuk}^o}{2|\mathbf{r}_i-\mathbf{r}_j|}e^{L/\mu^2}\{e^{-|\mathbf{r}_i-\mathbf{r}_j|/\mu}[1-erf(\frac{2L/\mu-|\mathbf{r}_i-\mathbf{r}_j|}{\sqrt{4L}})]- \\ &\quad e^{-|\mathbf{r}_i-\mathbf{r}_j|/\mu}[1-erf(\frac{2L/\mu+|\mathbf{r}_i-\mathbf{r}_j|}{\sqrt{4L}})]\} \end{aligned} \tag{3.16}$$

The first term in Eq. (3.16) denotes the kinetic energy of centroids of nucleons, second term describes the Skyrme interaction, characterized by parameters α, β, and γ. The third term signifies the Coulomb interaction while the last term denotes the Yukawa interaction. Parameters corresponding to soft (S) and hard (H) equations of state are given in table 3.1. The two Yukawa parameters V_{Yuk}^o and μ are adjusted to obtain reasonable simulation of finite nuclei. Yukawa parameters are also responsible for the nature of

Table 3.1: Parameters employed in QMD model for the Skyrme parametrization of EoS and the incompressibility values.

EoS	$\mathcal{K}$(MeV)	α (MeV)	β (MeV)	γ	V^o_{Yuk} (MeV)	μ (fm)
S	200	-356	303	7/6	-10	1.5
H	380	-124	70.5	2	-10	1.5

equation of state which must be taken into account when adjusting the parameters. The short range interaction is taken into account in the same way as in INC and VUU models via stochastic term.

3.1.3 The nucleon-nucleon scattering

Initially, the cold QMD nuclei are assumed to move along the classical Coulomb trajectories until the distance between their surfaces is 3 fm *i.e.* $r = R_P + R_T + 3\ fm$. This positions is treated as starting point for the nucleus-nucleus collision. The time evolution of the centroids of gaussian wave packets is described by two processes: the propagation according to classical equations of motion and stochastic n-n scattering. We solve the Hamilton's equations of motion for the centroids of individual gaussian wave packets as:

$$\begin{aligned} \dot{\mathbf{r}}_i &= \nabla_{\mathbf{p}_i}\langle H\rangle,\ i = 1, ..., A; \\ \dot{\mathbf{p}}_i &= -\nabla_{\mathbf{r}i}\langle H\rangle,\ i = 1, ..., A. \end{aligned} \tag{3.17}$$

Here H is the total Hamiltonian of A-nucleons in the reaction system and 'i' denotes index of the nucleon. These differential equations of motion are solved using an Eulerian integration routine with a fixed time step Δt:

$$\begin{aligned} \mathbf{p}_i(n+1) &= \mathbf{p}_i(n) - \nabla_{\mathbf{r}_i} U_i(n+\frac{1}{2})\Delta t, \\ \mathbf{r}_i(n+\frac{1}{2}) &= \mathbf{r}_i(n-\frac{1}{2}) + \frac{\mathbf{p}_i(n)}{\sqrt{\mathbf{p}_i^2(n)+m_i^2}} + \nabla_{\mathbf{p}_i} U_i(n-\frac{1}{2})\Delta t. \end{aligned} \tag{3.18}$$

To mimic the fermionic motion, we introduce the Pauli blocking of n-n scattering in the final states. The influence of Pauli blocking of intermediate states in a highly non-thermal environment at the beginning of a heavy-ion collision has never been investigated in detail.

Effective n-n cross section becomes smaller due to the Pauli blocking of final state. Unlike INC model, in QMD approach, the dynamical motion of nucleons breaks the nucleus into smaller pieces *i.e.* pre-fragments already in the initial stage. These pre-fragments can decay by emitting nucleons and light charged particles (LCPs).

We assume that two nucleons coming closer become candidate for scattering if their inter-nucleon distance $r_{ij} < \sqrt{\frac{\sigma_{nn}(\sqrt{s})}{\pi}}$ in their center-of-mass frame. Here $\sigma_{nn}(\sqrt{s})$ represents the total nucleon-nucleon cross section and '$\sqrt{s}$' is the center-of-mass energy. This condition was extensively checked by Hartnack [13], who found that other possible prescriptions don't influence the final observables. The scattering angles of colliding nucleons are chosen in such a way that scattering angle distribution of all nucleon-nucleon collisions agree with calculated angular distribution for elastic and in-elastic channels. Inelastic collisions lead to formation of Δ^{123} resonance particles which can be reabsorbed by inverse reaction.

In the past, several refinements has been made in the original QMD code with specialized features. The isospin of protons and neutrons is explicitly treated in the so called 'isospin-dependent quantum molecular dynamics' (IQMD) model [5]. The IQMD version includes explicit Coulomb forces between Z_P and Z_T protons apart from isospin dependent mean field. In this flavor of QMD model, an additional potential component namely the symmetry potential is included:

$$V_{ij}^{sym} = \frac{t_6}{\rho} T_{3i} T_{3j} \delta(\mathbf{r}_i - \mathbf{r}_j);\ t_6 = 100\ MeV. \tag{3.19}$$

Here T_{3i} and T_{3j} being the T_3-components of respective nucleons. The pion production is treated via Δ resonances. The IQMD model has been extensively used to study FOPI data on pion production in heavy-ion reactions at SIS/GSI energies [13, 14]. The covariant description of the QMD model has also been attempted so as to extend its application to relativistic collisions [7, 8]. This extension of QMD model is commonly known as relativistic quantum molecular dynamics (RQMD) model. This code includes relativistic covariant propagation scheme [7, 8]. Here Lehmann and Puri have used potential part as a function of Lorentz squared transverse distance [8].

$$q_{Tij}^2 = q_{ij}^2 - \frac{(q_{ij}^\mu p_{ij\mu})^2}{p_{ij}^2}, \tag{3.20}$$

with $q_{ij}^\mu = q_i^\mu - q_j^\mu$ being the simple four dimensional distance and $p_{ij}^\mu = p_i^\mu + p_j^\mu$ the sum of the momenta of the two interacting particles i and j. This version along with

ultra-relativistic version (UrQMD) are well suited to study reaction dynamics with RHIC energies upto $\sim$ 100 AGeV. Recently, these models have been employed to gain understanding of momentum-space correlations for nucleons and particle-type dependence of elliptical flow v_2 [15]. In another study on elliptical flow in Au+Au collisions at $\sqrt{s_{NN}}$=200 GeV, the two hadronic models RQMD and UrQMD suggested particle-type dependence [16]. Particles with large v_2 decouple earlier than those with smaller v_2. This kind of mass dependence is also observed in STAR measurements [17].

There are other versions of QMD such as PQMD [4] and Japanese QMD (JQMD) [18] that explicitly include the Pauli potential so as to mimic the fermionic nature of nuclear matter. This version is mainly useful in low-energy reactions where Pauli blocking of final states become effective. Another version labeled as EQMD model treats width of gaussian wave packet as dynamical variable in time [19]. Recently, an improved version of QMD model labeled as ImQMD model has also been reported [20]. It considers an extra surface energy term in the effective interaction potential. This version has been quite successful to describe low energy fusion reactions. It not only reproduces the ground state properties of nuclei, but also provides reasonable Coulomb barrier for fusion process. Even the hybrid model has also been used [21] in a recent study, where the ImQMD model clubbed with extended Thomas-Fermi approximation [22] successfully explained the experimental data on fusion barriers for the reactions of ^{40}Ca + ^{40}Ca, ^{48}Ca + ^{208}Pb, ^{126}Sn + ^{130}Te.

3.2 Summary

In summary, we have discussed the fine details of *quantum molecular dynamics* (QMD) model and its various flavors in this chapter. The many-body nature of distribution function allows us to maintain the n-n correlations during the propagation of heavy-ion system. The QMD theory is, therefore, suitable candidate to investigate the many-body phenomena such as multifragmentation. In the subsequent chapters, we shall give detailed applications of the QMD model in describing the spectator matter fragmentation, system size effects, fragment-emission in central collisions, stopping phenomenon, entropy production and determination of nuclear incompressibility *etc.*

Bibliography

[1] J. Aichelin and H. Stöcker, Phys. Lett. B **176**, 14 (1986).

[2] G. Peilert, H. Stöcker, W. Greiner, A. Rosenhauer, A. Bohnet and J. Aichelin, Phys. Rev. C **39**, 1402 (1989).

[3] J. Aichelin, Phys. Rep. **202**, 233 (1991).

[4] G. Peilert, J. Konopka, H. Stöcker, W. Greiner, M. Blann and M. G. Mustafa, Phys. Rev. C **46**, 1457 (1992).

[5] C. Hartnack, R. K. Puri, J. Aichelin, J. Konopka, S. A. Bass, H. Stöcker and W. Greiner, Eur. Phys. J A **1**, 151 (1998).

[6] A. Bohnet, J. Aichelin, J. Pochodzalla, W. Trautmann, G. Peilert, H. Stöcker and W. Greiner, Phys. Rev. C **44**, 2111 (1991).

[7] H. Sorge, H. Stöcker and W. Greiner, Ann. Phys. (N.Y.) **192**, 266 (1989); H. Sorge, Phys. Rev. C **52**, 3291 (1995).

[8] E. Lehmann, R. K. Puri, A. Faessler, G. Batko, and S. W. Huang, Phys. Rev. C **51**, 2113 (1995).

[9] Ch. Hartnack, L. Zhuxia, L. Neise, G. Peilert, A. Rosenhauer, H. Sorge, J. Aichelin, H. Stöcker and W. Greiner, Nucl. Phys. A **495**, 303 (1989).

[10] T. J. Schlagel and V. R. Pandharipande, Phys. Rev. C **36**, 162 (1987); R. J. Lenk and V. R. Pandharipande, Phys. Rev. C **34**, 177 (1986).

[11] T. H. R. Skyrme, Nucl. Phys. **9**, 615 (1959).

[12] Ch. Hartnack, Ph.D Thesis, University of Frankfurt, Frankfurt, 1993.

[13] V. S. Uma Maheshwari, C. Fuchs, Amand Faessler, Z. S. Wang and D. S. Kosov, Phys. Rev. C **57**, 922 (1998).

[14] Z. G. Xiao, B. A. Li, L. W. Chen, G. C. Yong and M. Zhang, Phys. Rev. Lett. **102**, 062502 (2009).

[15] W. F. Juan, S. L. Qiang, F. Q. Chun and H. Lei, Chin. Phys. C **34**, 62 (2010).

[16] F. Liu and Y. Lu, J. Phys. G: Nucl. Part. Phys. **34**, S1073 (2007).

[17] J. Adams *et al.*, Phys. Rev. Lett. **92**, 052302 (2004).

[18] T. Maruyama, K. Niita, K. Oyamatsu, T. Maruyama, S. Chiba and A. Iwamoto, Phys. Rev. C **57**, 655 (1992); G. Watanabe, K. Sato, K. Yasuoka and T. Ebisuzaki, Phys. Rev. C **69**, 055805 (2004).

[19] T. Maruyama, K. Niita and A. Iwamoto, Phys. Rev. C **53**, 297 (1996).

[20] N. Wang, Z. Li and X. Wu, Phys. Rev. C **65**, 064608 (2002); N. Wang, Z. Li, X. Wu, J. Tian, Y. X. Zhang and M. Liu, Phys. Rev. C **69**, 034608 (2004).

[21] K. Zhao, X. Wu and Z. Li, Phys. Rev. C **80**, 054607 (2009).

[22] Y. Jiang, N. Wang, Z. Li and W. Scheid, Phys. Rev. C **81**, 044602 (2010).

Chapter 4

Onset of Multifragmentation in Low Energy Heavy-Ion Collisions: System Size Effects and Comparison with MSU-NSCL Data

4.1 Introduction

The dynamical calculations have shown that fragment-emission is the result of compressional energy stored in early phase of the reaction in central collisions [1–3]. The fragment emission from hot and compressed nuclear system is believed to occur due to fluctuations in the mean field and instability generated by the Coulomb forces. Longer the system stays in the instability region, more probable it is bound to break into smaller pieces. If system is light, break-up is expected to occur at incident energies as low as $\sim$ 40-60 AMeV. For heavier systems naturally, the demand for compression energy and hence beam energy is more to cause the effective break-up. QMD calculations by Puri *et al* [4] have shown that maximal fragment production in central $^{40}Ca + ^{40}Ca$ collisions takes place around 60 AMeV. An earlier attempt by Bauer *et al* [5] showed that for the collisions of two heavy-ions, maximum multiplicity of intermediate mass fragments is observed around 100 AMeV in central collisions . This existence of peak IMF emission was in accord with similar study by Peilert *et al* [6] using Au-nuclei. The multi-fragment emission in central collisions at low incident energies, therefore, reveals a complex picture with energy deposition and system mass as the controlling factors.

However, very few attempts have been reported in literature that are concerned with beam energy dependence and system size effects [7–11]. In the past, percolation ap-

proaches have been successfully applied to study fragment emission pattern, kinetic energy of emitted fragments, IMF yields from the decay of heavy projectiles and beam energy dependence [8–10, 12]. Li *et al* [8] based upon percolation model calculated the fit parameter λ in the power law: $\sigma(Z) \propto Z^{-\lambda}$ for different lattice sizes. Interestingly the critical parameter λ was observed to scale with size of the fragmenting system. Similarly, the 'LATINO' model simulations were performed for central collisions of ^{58}Ni + ^{58}Ni at different incident energies to extract the entropy produced [13]. The maximum entropy generated is observed to decrease with size of the asymptotic source. This analysis showed that lighter sources tend to produce more entropy.

Another important phenomenon such as flow effects also witness similar system size effects. The elliptical flow is found to shift from the positive value (in-plane emission) to negative value (out-of-plane emission) at certain beam energy called as *transition energy*. Recently transition energies in the reaction systems with masses between ^{58}Ni+ ^{58}Ni and ^{197}Au+ ^{197}Au were calculated within improved quantum molecular dynamics (ImQMD) model [14]. The transition energy was observed to follow the power law: $E_{trans} \propto (A_{tot})^{-\tau}$ with exponent $\tau \approx 0.22$. Similar mass dependence is reported for transition energy of light charged particles studied within isospin dependent quantum molecular dynamics (IQMD) model [15].

As far as fragment production is concerned, the recent experiments performed on MSU 4π-Array set up indicated a *rise and fall* pattern in the multiplicity of intermediate mass fragments (IMFs) as a function of beam energy in the center-of-mass frame [9]. The calculations based on percolation theory, however, could not accurately predict the system size dependence of peak $E_{c.m.}$ (at which maximal IMF production occurs). Even maximal multiplicity of IMFs was also overestimated. This led Sisan *et al* [9] to the conclusion that perhaps phase space model could correctly interpret this dependence. We plan to address this situation by employing the QMD model, in which reaction dynamics can be followed from the start to the end where matter is cold and fragmented. We have used a *soft* EoS along with Cugnon parametrization of *n-n* cross section [16]. The choice of soft EoS has been advocated in many theoretical studies. Recently, Magestro *et al* [17] tried to pin down the nuclear incompressibility using balance energy. Their detailed study pointed towards a *softer* equation of state. Another study concerning the linear momentum transfer occurring in central HI collisions also showed that a soft compressibility modulus is needed to explain the experimental data [18]. The cluster yield

is obtained through standard *minimum spanning tree* (MST) procedure with additional binding energy check. In the following section, we shall give details of MST clusterization algorithm along with its extensions.

4.2 Minimum Spanning Tree (MST) method

The variational approach employed in QMD model reduced the complication of following time evolution of an A-body wave function by resolving to 6A coupled differential equations for the centroids of the coherent wave functions in configuration and momentum space. This approach allows us to define clusters in a very convenient manner. At the end of the reaction, phase space occupancy is quite low, so nucleons forming a cluster will be one closer in coordinate space. This simplest approach of identifying clusters is well known as *minimum spanning tree* (MST) method [6, 19–26]. In this method, two nucleons share the same cluster if their centroids in coordinate space are closer than a given clusterization radius R_{clus}, that is

$$|\mathbf{r}_i - \mathbf{r}_j| \leq R_{clus}, \tag{4.1}$$

where $\mathbf{r}_i$, $\mathbf{r}_j$ are the spatial coordinates of the two nucleons. The clusterization radius R_{clus} is used as a free parameter which may lie between 2-4 fm. The variation in the clusterization radius is found to have negligible influence on the final state fragment pattern at the end of reaction ($\sim$ 300 fm/c), since nucleons belonging to different clusters are well separated in spatial coordinates [6, 27].

An improvisation over MST approach has also been tried which look for bound two-nucleon structure in the same cluster. This algorithm labeled as MSTE [28, 29] recognizes two nucleons *i and j* bound in a cluster if

$$e_{ij} \leq 0, \tag{4.2}$$

with $e_{ij} = V_{ij} + \frac{(p_i - p_j)^2}{4\mu}$; μ being the reduced mass.

4.2.1 Minimum Spanning Tree with Momentum cut (MSTM) method

In addition to spatial cut of Eq. (4.1), we introduce a cut on relative momentum of two nucleons. That is, we demand [25, 30]:

$$\begin{aligned} |\mathbf{r}_i - \mathbf{r}_j| &\leq R_{clus}, \\ |\mathbf{p}_i - \mathbf{p}_j| &\leq P_F. \end{aligned} \tag{4.3}$$

Here, P_F is the average Fermi momentum of nucleons bound in a nucleus (≈150 MeV/c) in its ground state. This improvisation checks the formation of artificial and unbound fragments by excluding those nucleons having relative momenta larger than P_F. Eventually, MST and MSTM methods give different results at the start of a reaction. The MST method gives one largest cluster of size ($=A_P + A_T$), while MSTM method gives two distinct clusters of masses A_P and A_T having very large relative momenta. This algorithm identifies the largest fragment A^{max} as early as 50-60 fm/c [23]. As a result, fragment emission starts earlier with MSTM, when MST method just detects a single biggest cluster.

4.2.2 Minimum Spanning Tree with Binding energy check (MSTB) method

In this modified version, pre-clusters obtained with conventional MST approach are subjected to the binding energy check:

$$\zeta = \frac{1}{N_f} \sum_{i=1}^{N_f} \left[\frac{\left(\mathbf{p_i} - \mathbf{P_{N_f}^{c.m.}}\right)^2}{2m_i} + \frac{1}{2} \sum_{j \neq i}^{N_f} V_{ij}\left(\mathbf{r_i}, \mathbf{r_j}\right) \right] < -E_{bind}. \tag{4.4}$$

We take $E_{bind} = 4.0$ MeV, if $N_f \geq 3$ else, $E_{bind} = 0$. N_f is the number of nucleons in a fragment and $\mathbf{P}_{N_f}^{cm}$ is the center-of-mass momentum of a fragment. This criterion forbids the formation of loosely bound clusters. The role of MSTB method is quite important in central symmetric reactions [23, 26]. The MSTB method doesn't recognize the largest fragment A^{max} during early violent phase. Therefore, it shows the nucleus as unbound group of nucleons. A properly bound A^{max} is identified only around 120 fm/c [24, 31]. In addition, binding energy check helps to obtain the stable fragment configuration quite early and reduces the computation time for multifragmentation.

4.3 The time evolution of fragments using MST and MSTB approaches

Our calculations within QMD model are done employing *minimum spanning tree* procedure with additional binding energy check. Additional condition of minimum fragment binding energy rules out formation of improper and unbound clusters and speeds up the fragment recognition procedure [23, 24, 31]. One has to also keep in the mind that semi-classical models like QMD can not keep nuclei stable for long time. A typical stability of nuclei can be seen till 200 fm/c. If one analyzes the fragment formation with MST alone, then one may not achieve true fragment structure at 200 fm/c. To support this fact, we display in Fig. 4.1, the multiplicities of various fragment species, size of heaviest fragment A^{max} as well as binding energy of light charged particles (LCPs) and intermediate mass fragments (IMFs) as a function of time. In the beginning, MST could detect only a bigger A^{max} and small yield of free nucleons. On other hand, MSTB approach detects all nucleons to be free entities in the violent phase of reaction. Free nucleons begin to clusterize into lighter fragments and heavier residues as the time goes on and saturate around $t \sim 150$ fm/c. It is only after 150 fm/c that MSTB is capable of identifying the properly bound A^{max}. The evolution of fragments' binding energy suggests that fragment structure with MSTB approach is earlier decided. A time scale of 200 fm/c is enough to pin down the IMF yield since all fragments would be having binding energy $\leq$ -4.0 AMeV.

It may mentioned that for asymptotic times, both MST and MSTB approaches yield same fragment multiplicities [23, 24]. The binding energy check *i.e.* Eq.(4.4) helps to a greater extent in identifying the fragments quite earlier. The normal MST method would, however, takes a long time to identify stable fragmentation pattern.

4.4 Beam energy dependence of fragmentation in central collisions

Here, we simulate the central heavy-ion collisions of $^{20}Ne + ^{20}Ne$ (E_{lab}=10-55 AMeV), $^{40}Ar + ^{45}Sc$ (E_{lab}=35-115 AMeV), $^{58}Ni + ^{58}Ni$ (E_{lab}=35-95 AMeV), $^{86}Kr + ^{93}Nb$ (E_{lab}=35-95 AMeV), $^{129}Xe + ^{124}Sn$ (E_{lab}=45-130 AMeV) and $^{197}Au + ^{197}Au$ (E_{lab}=70-130 AMeV). The systematic study over a wide range of beam energies and system masses allows one to confront the theoretical predictions with experimental findings and search for the

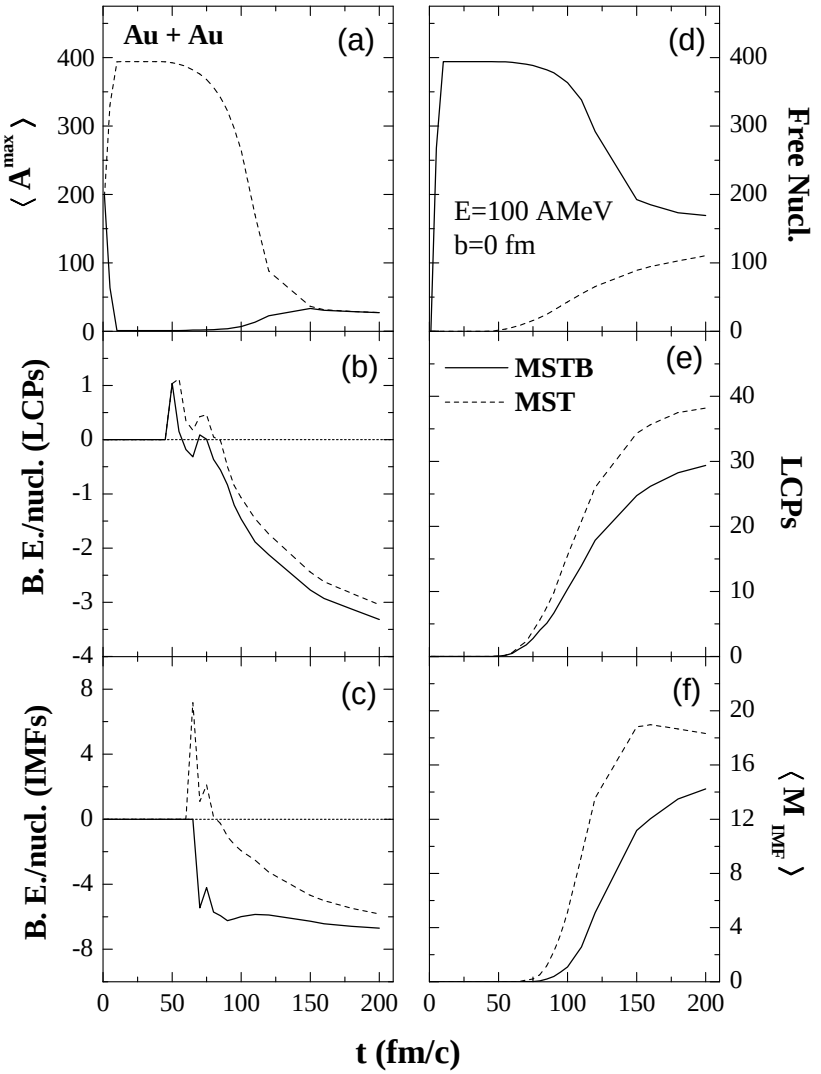

Figure 4.1: Central Au+Au collision at incident energy of 100 AMeV. Results shown here are for (a) size of heaviest fragment A^{max}, (b)-(c) binding energy per nucleon (in MeV) for light charged particles and intermediate mass fragments, (d)-(f) multiplicity of free nucleons, light charged particles [$2 \leq A \leq 4$] and intermediate mass fragments [$5 \leq A \leq 44$] as a function of time. Calculations done for MST and MSTB approaches are shown as dashed and solid curves, respectively.

mass dependence. Note that only symmetric reactions are taken for present analysis. The choice of symmetric systems allows us to neglect asymmetry affects in the fragment production. Our calculations were performed at fixed impact parameter of b= 0 fm and employing a soft equation of state. We simulated the reactions at fixed incident energies and then calculated corresponding center-of-mass energies. For each such set, 500 events were simulated that minimizes the fluctuations to greater extent. The choice of central

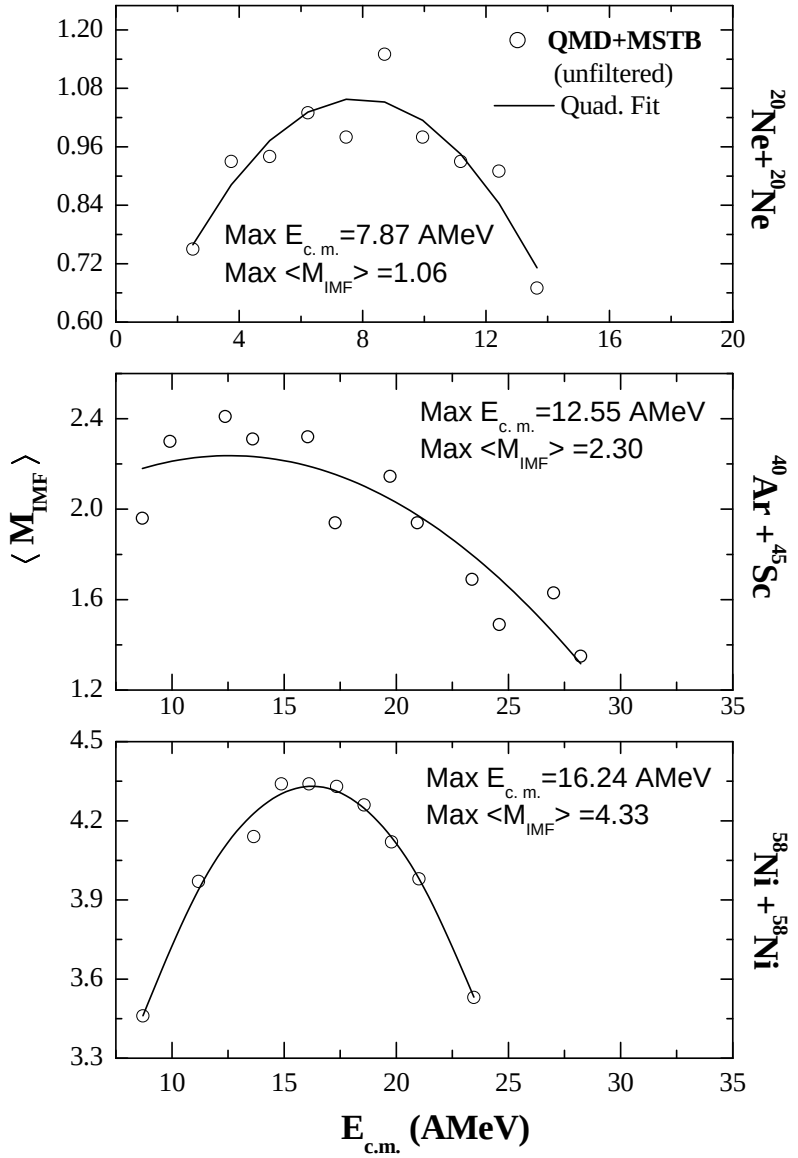

Figure 4.2: The mean IMF multiplicity $\langle M_{IMF} \rangle$ versus beam energy $E_{c.m.}$ for the reactions of $^{20}Ne +^{20} Ne$, $^{40}Ar +^{45} Sc$, and $^{58}Ni +^{58} Ni$. Open circles depict the calculations employing QMD + MSTB approach for unfiltered events. The quadratic fits (solid curves) to the model calculations are drawn to estimate the peak energy at which the maximal IMF emission occurs.

collisions for the present study guarantees the formation of highly excited systems that may break into a large number of pieces. Further, the emission from such events is almost isotropic, which may represent a '*single source*' emission. In Fig. 4.2, we display the average multiplicity of intermediate mass fragments $\langle M_{IMF} \rangle$ calculated as a function of beam energy $E_{c.m.}$ available in the center-of-mass frame for $^{20}Ne +^{20} Ne$, $^{40}Ar +^{45} Sc$, and $^{58}Ni +^{58} Ni$ reactions. Similarly, calculated IMF multiplicities for $^{86}Kr +^{93} Nb$,

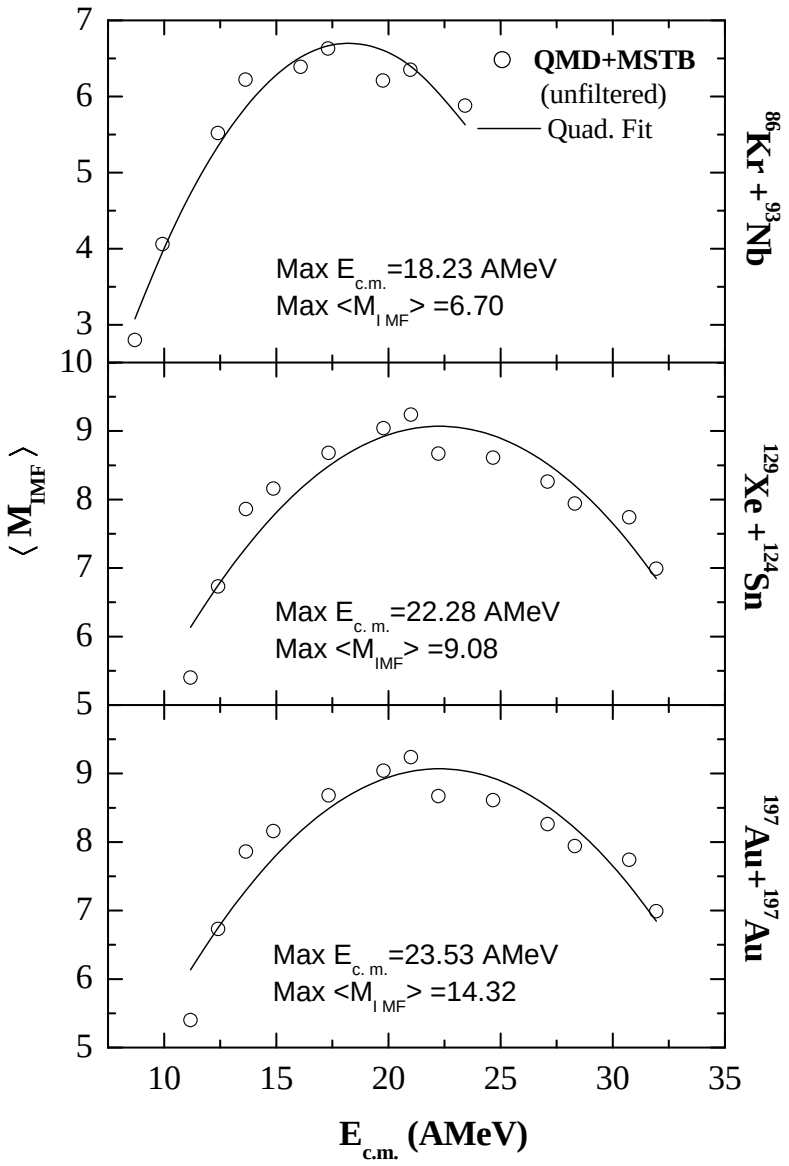

Figure 4.3: Same as in Fig. 4.2, but for the reactions of $^{86}Kr +^{93} Nb$, $^{129}Xe +^{124} Sn$ and $^{197}Au +^{197} Au$.

$^{129}Xe +^{124} Sn$ and $^{197}Au +^{197} Au$ reactions are displayed in Fig. 4.3. The mean IMF multiplicity first increases with beam energy, reaches a peak value and then decreases. This trend is visible in all the entrance channels as shown in Figs. 4.2 and 4.3. This trend is less clearly visible for lighter $^{40}Ar +^{45} Sc$ system, whereas it is more clearly visible for the heavier systems. It is quite interesting to see that similar dependence of $\langle M_{IMF} \rangle$ on center-of-mass energy is also observed in experimental data taken with the MSU 4π-Array [9]. This behavior can be understood in terms of compression energy of the system. With the rise in beam energy, compression energy breaks the IMFs into smaller fragments

leading to smaller number of IMFs. The maximal $E_{c.m.}$ and corresponding peak $\langle M_{IMF} \rangle$ was obtained through a quadratic fit to the model calculations. One should also note that the shape of the beam energy dependence of IMF production is quite close to one reported in the experimental data [9]. As reported by Sisan *et al* [9], the peak $E_{c.m.}$ extracted for different entrance channels scales with the size of the system. Such scaling is also visible in our present calculations (see Figs. 4.2 & 4.3). In the next section, we report the fragmentation characteristics observed at peak $E_{c.m.}$.

4.5 Fragmentation dynamics at the peak IMF emission and system size effects

We now study the fragment emission pattern at peak $E_{c.m.}$ *i.e.* energy of maximal IMF emission. Figure 4.4 displays the time evolution of average nucleon density ρ^{avg}, multiplicity of free nucleons emitted, light charged particles LCPs [$2 \leq A \leq 4$], and intermediate mass fragments IMFs [$5 \leq A \leq 44$] at the peak $E_{c.m.}$. As expected, the average nucleonic density ρ^{avg} has a mass dependence, being maximal for the ^{197}Au+^{197}Au system and minimal for the ^{20}Ne +^{20} Ne system. This also indicates a linear density dependence on the system size. As discussed earlier, we observed an artificial emission of free nucleons in the beginning with MSTB approach which diminishes and saturates beyond 150 fm/c. One can see that final state multiplicities (at 200 fm/c) of different fragment species depict linear increase with size of the system. One can also notice that fragment emission almost saturates around 200 fm/c.

The maximal fragment production is for ^{197}Au +^{197} Au system whereas ^{20}Ne +^{20} Ne system results in minimum value. It may be mentioned that IMF multiplicities obtained in ^{20}Ne +^{20} Ne and ^{40}Ar +^{45} Sc collisions exclude the largest and second largest fragment respectively to infer the system size dependence accurately.

In Fig. 4.5, we further extend the above study for various fragments consisting of free nucleons, fragments with mass A=2, light charged particles LCPs [$2 \leq A \leq 4$], medium mass fragments MMFs [$5 \leq A \leq 9$] as well as heavy mass fragments HMFs [$10 \leq A \leq 44$]. Interestingly, in all the above cases, a clear system size dependence can be seen in a manner similar to that for $\langle M_{IMF} \rangle$. We observe a power law of the form cA_{tot}^{τ}; where A_{tot} is the mass of composite system. In all the cases, exponent τ is very close to unity. As noted in Ref. [9], the percolation model failed badly to reproduce the power law dependence.

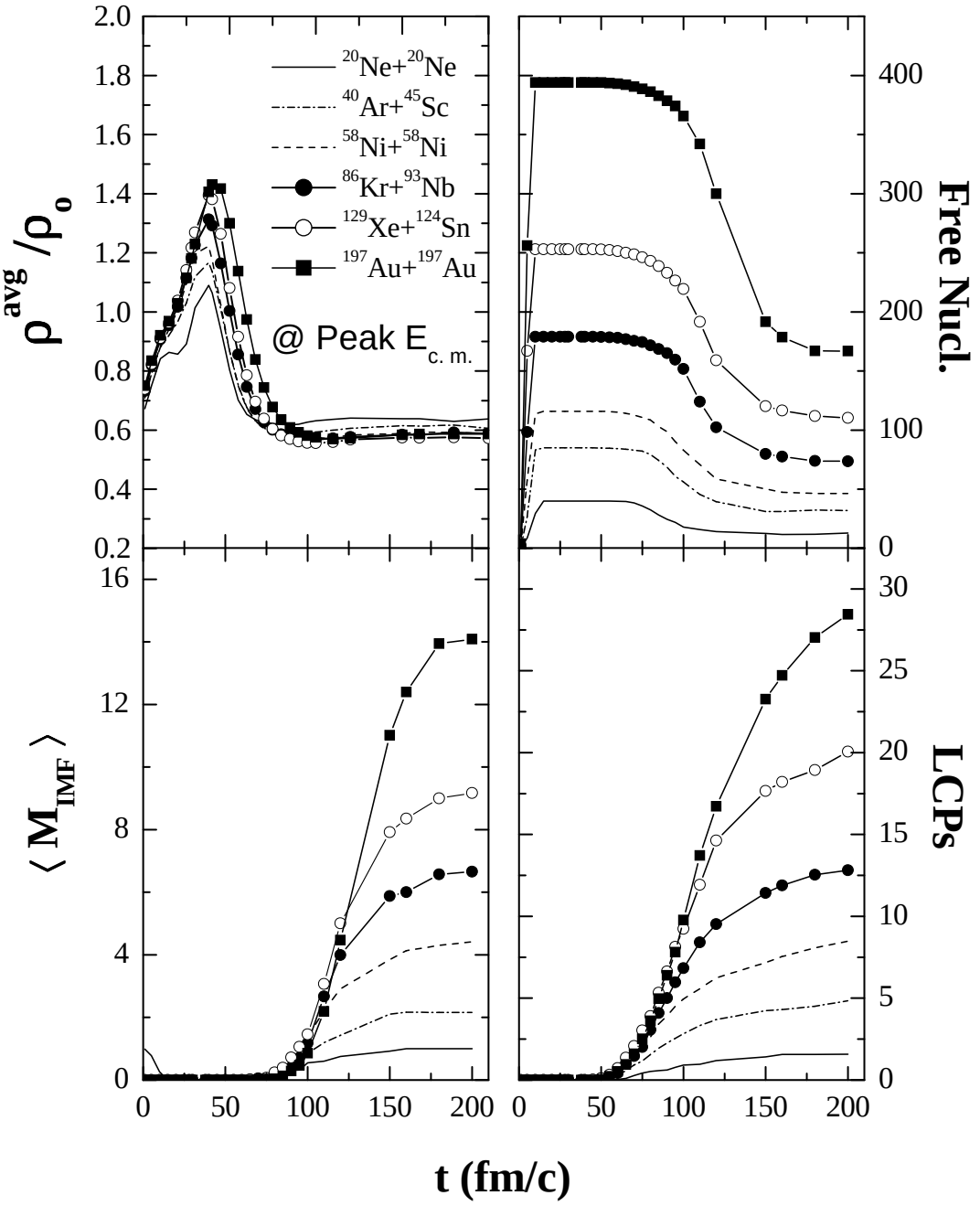

Figure 4.4: The time evolution of average nucleon density ρ^{avg}, multiplicity of free nucleons, light charged particles LCPs [$2 \leq A \leq 4$], intermediate mass fragments IMFs [$5 \leq A \leq 44$] for the systems indicated. Calculations shown here are done at the energy for peak IMF production.

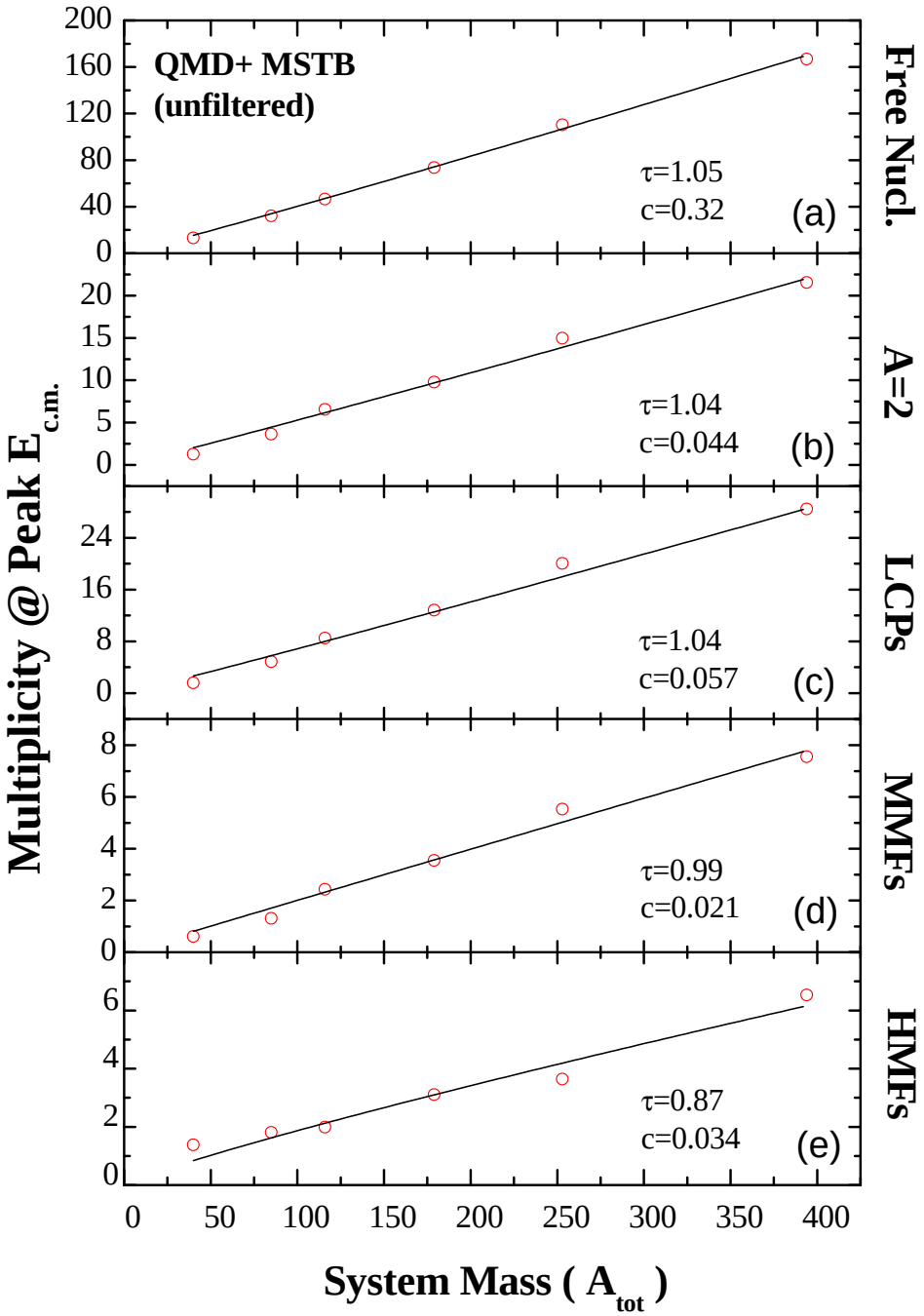

Figure 4.5: The final state multiplicities of (a) free nucleons, (b) fragments with mass A=2, (c) light charged particles LCPs, (d) medium mass fragments MMFs, and (e) heavy mass fragments HMFs as a function of total mass of the system $A_{tot}(=A_T + A_P$; A_T and A_P being mass of the target and projectile, respectively). Model calculations done at peak $E_{c.m.}$ (open circles) are fitted with power law of the form cA_{tot}^{τ}.

A linear mass dependence observed with value of $\tau \sim 1$ depicts the picture of vanishing surface-Coulomb effects. Experiments are called for to verify this new prediction.

4.6 Confrontation with MSU 4π-Array data

Finally we confront our model calculations for the mass dependence of peak $E_{c.m.}$ as well as peak $\langle M_{IMF} \rangle$ with experimental data [9]. The measurements of mean IMF multiplicity in different symmetric reactions were carried out at the National Superconducting Cyclotron Laboratory (NSCL) at Michigan State University. Central events were selected to be 10 % of all events with largest transverse energy. MSU 4π-Array detector is comprised of the main ball and the High Rate Array (HRA) with geometrical coverage of nearly 4π solid angle. We have, therefore, compared our unfiltered calculations with the data. From Fig. 4.6, one can see that our model calculations employing MSTB approach (open circles) are in good agreement with the experimental data (solid squares) of MSU 4π-Array for peak $E_{c.m.}$. For peak $\langle M_{IMF} \rangle$, some deviation can be seen for heavier masses. This could also be due to fact that our calculations are not filtered for experimental acceptance. One can also see that the predictions of percolation model fail to explain the sharp dependence of peak $E_{c.m.}$ on system mass. Our present analysis shows a linear mass dependence of the form $mA_{tot} + c$ for the peak $E_{c.m.}$. These observations suggest that peak $E_{c.m.}$, thus, acts as a measure of *finite size* effect. It is worth mentioning that the critical excitation energy was estimated from the cluster size distribution fitted to power law: $\sigma(A) \propto A^{-\lambda}$ at different beam energies for which the exponent λ reaches a minimum. Based on the percolation calculations, the critical excitation energy is also found to increase with initial lattice size [8]. Interestingly, the mass scaling of peak $\langle M_{IMF} \rangle$ can be reproduced using a power law: cA_{tot}^{τ} with exponent τ close to unity.

4.7 Summary

We present in this chapter, the quantum molecular dynamics description of beam energy dependence of fragment production. Reactions were simulated selecting a wide range of symmetric systems at zero impact parameter. To obtain the final state fragment multiplicity, we employ minimum spanning tree method with additional binding energy check to recognize the final fragment pattern. This approach ensures that fragments obtained at the end of reaction are properly bound and stable. Our calculations remarkably

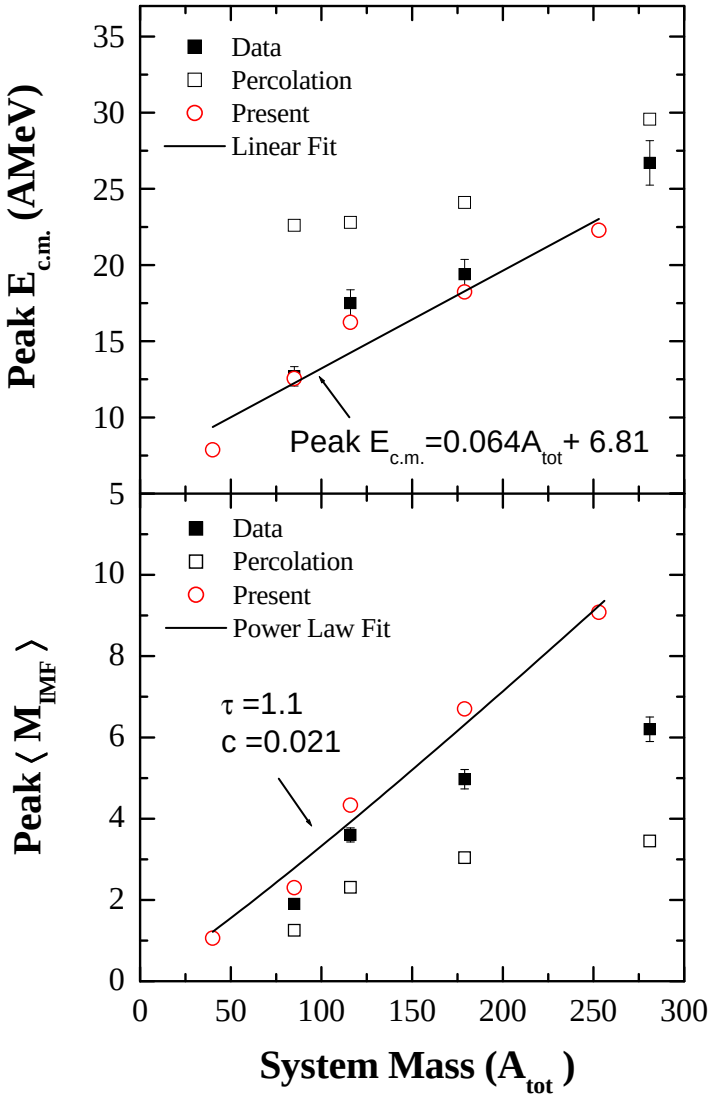

Figure 4.6: The system size dependence of the peak $E_{c.m.}$ and peak $\langle M_{IMF} \rangle$. Our model calculations (open circles) for unfiltered events are compared with experimental data (solid squares). Also shown in figure are the percolation calculations (open squares) [9].

reproduce the trend of *rise and fall* in IMF multiplicity with beam energy $E_{c.m.}$ in the center-of-mass frame as observed experimentally. Peak energy $E_{c.m.}$ is found to scale linearly with system size. Average nucleon density as expected also showed systematic mass dependence. Mean multiplicities of IMFs as well as other fragment species are found to follow the power law cA_{tot}^{τ} ; A_{tot} being the total mass of the system. Interestingly, exponent τ is close to unity in all cases, indicating vanishing of surface-Coulomb effects. Experiments are called to verify this new prediction.

Bibliography

[1] C. A. Ogilvie *et al.*, Phys. Rev. Lett. **67**, 1214 (1991).

[2] B. Jakobsson *et al.*, Nucl. Phys. A **509**, 195 (1990).

[3] S. R. Souza, L. De Paula, S. Leray, J. Nemeth, C. Ngô and H. Ngô, Nucl. Phys. A **571**, 159 (1994).

[4] R. K. Puri and S. Kumar, Phys. Rev. C **57**, 2744 (1998).

[5] W. Bauer *et al.*, Nucl. Phys. A **553**, 749 (1993).

[6] G. Peilert, H. Stöcker, W. Greiner, A. Rosenhauer, A. Bohnet and J. Aichelin, Phys. Rev. C **39**, 1402 (1989).

[7] T. Li *et al.*, Phys. Rev. Lett. **70**, 1924 (1993).

[8] T. Li *et al.*, Phys. Rev. C **49**, 1630 (1994).

[9] D. Sisan *et al.*, Phys. Rev. C **63**, 027602 (2001).

[10] A. J. Santiago, K. C. Chung and C. S. Wang, Phys. Scr. **55**, 152 (1997).

[11] W. Reisdorf *et al.*, Phys. Lett. B **595**, 118 (2004).

[12] X. Campi, H. Krivine, N. Sator and E. Plagnol, Eur. Phys. J. D **11**, 233 (2000).

[13] A. Barrañón, J. Escamilla and J. A. López, Phys. Rev. C **69**, 014601 (2004).

[14] Y. Zhang and Z. Li, Phys. Rev. C **74**, 014602 (2006).

[15] S. Kumar, S. Kumar and R. K. Puri, Phys. Rev. C **81**, 014611 (2010).

[16] J. Aichelin *et al.*, Phys. Lett. B **176**, 14 (1986).

[17] D. J. Magestro, W. Bauer and G. D. Westfall, Phys. Rev. C **62**, 041603(R) (2000).

[18] F. Haddad *et al.*, Phys. Rev. C **53**, 1437 (1996).

[19] J. Aichelin, Phys. Rep. **202**, 233 (1991).

[20] J. Aichelin, Prog. Part. Nucl. Phys. **30**, 191 (1993).

[21] Ch. Hartnack, J. Jaenicke, L. Sehn, H. Stöcker and J. Aichelin, Nucl. Phys. A **580**, 643 (1994).

[22] P. B. Gossiaux and J. Aichelin, Phys. Rev. C **56**, 2109 (1997).

[23] S. Kumar and R. K. Puri, Phys. Rev. C **58**, 320 (1998).

[24] J. Singh and R. K. Puri, J. Phys. G: Nucl. Part. Phys. **27**, 2091 (2001); J. K. Dhawan and R. K. Puri, Eur. Phys. J. A **33**, 57 (2007).

[25] J. K. Dhawan and R. K. Puri, Phys. Rev C **75**, 057901 (2007).

[26] Y. K. Vermani and R. K. Puri, J. Phys. G: Nucl. Part. Phys. **36**, 105103 (2009)

[27] J. Singh, S. Kumar and R. K. Puri, Phys. Rev. C **62**, 044617 (2000); J. Singh and R. K. Puri, Phys. Rev. C **62**, 054602 (2000).

[28] S. Pratt, C. Montoya and F. Ronning, Phys. Lett. B **349**, 261 (1995); J. Pan and S. Das Gupta, Phys. Rev. C **51**, 1384 (1995).

[29] A. Strachan and C. O. Dorso, Phys. Rev. C **56**, 995 (1997).

[30] A. Bonasera, M. Colonna, M. Di Toro, F. Gulminelli and H. H. Wolter, Phys. Lett. B **244**, 169 (1990).

[31] S. Kumar and R. K. Puri, Phys. Rev. C **58**, 2858 (1998).

Chapter 5

Spectator Matter Fragmentation at Relativistic Energies

5.1 Introduction

A highly excited system formed in energetic heavy-ion (HI) collisions is expected to break into several pieces consisting of free nucleons, light charged particles LCPs, intermediate mass fragments IMFs as well as heavier residues. This phenomenon as discussed in previous chapters, is known as multifragmentation. Excitation energy deposited in the system plays important role in the fragmentation of spectator matter in peripheral HI collisions. It is well established that in peripheral collisions at relativistic energies, the main contribution towards IMFs comes from the spectator decay [1–6]. At intermediate energies, IMFs emission becomes the dominant exit channel. The most complete experiments of ALADiN Collaboration have shown that mean IMF multiplicity $\langle N_{IMF} \rangle$ and charge of heaviest fragment $\langle Z^{max} \rangle$, are independent of target and incident energies [5].

On the theoretical front however, not much success has been reported to explain the spectator matter fragmentation at intermediate energies [3, 4, 7]. The molecular dynamics approaches like the QMD model [8] and quasi-particle dynamics (QPD) [9] models though were able to explain some of the features of experimental data [4], the fragment yields at higher impact parameters were largely underpredicted with these models. This questions the validity of *dynamical* scenario of multifragmentation. The statistical model calculations [10–12], on the other side, showed quite good reproduction of ALADiN data on IMF yields, charge correlations and fragments' kinetic energy. There are also some attempts to employ hybrid models to explain spectator fragmentation, where statistical calculations are clubbed with dynamical or percolation approaches [12–14]. The incomplete-fusion-

fragmentation model [15], has its model parameters adjusted for excitation energy so as to produce the correlations of mean IMF multiplicity, charge of heaviest fragment Z^{max}, and asymmetry of largest-to-second largest fragment $\langle a_{12} \rangle$ as a function of Z_{bound} (*i.e.* sum of charges bound in fragments with Z$\geq$2). These model predictions led to the common standpoint of thermal origin of fragments, in which reaction system has attained statistical equilibrium and final fragment formation is obtained when nuclear density is well below saturation nuclear density.

The problem with dynamical approaches seems to be their inability to transfer excitation energy to the spectator zones. This fallacy was largely attributed to the lack of advanced secondary clustering models [6, 16–18]. Theoretical approaches which follow the evolution of target and projectile to complete disassembly needs secondary algorithm to clusterize the phase space. Puri *et al* have devised a sophisticated clusterization algorithm based on the energy minimization criterion namely *Simulated Annealing Clusterization Algorithm* (SACA) [19]. As a first attempt, results with this algorithm were quite promising one for $^{197}Au + ^{197}Au$ reactions at 600 AMeV [6]. Earlier SACA method was reported to successfully explain charge yields in mass asymmetric reactions of O+Ag/Br at incident energies between 25 and 200 AMeV [20]. In another study, SACA method was tested against INDRA experimental data at 50 AMeV [21]. In this study, Xe+Sn reaction was subjected to multifragmentation and various variables such as charge yields, proton-like fragments and IMFs yields, angular distribution, average kinetic energies *etc* were analyzed. SACA method explained all these observables quite nicely, whereas conventional method based on spatial correlations failed badly [21]. It may be mentioned that in the same spirit, some other sophisticated algorithms are also reported in literature that can address the fragment formation on the reaction time scale [22–24].

Based on the ALADiN results, it remains to be seen whether QMD model can reproduce the universality behavior observed in the fragmentation of Au-projectiles or not. In the present chapter, we plan to analyze systematically the fragmentation process in peripheral $^{197}Au + ^{197}Au$ collisions at relativistic bombarding energies of 400, 600 and 1000 AMeV. We shall label model calculations using original SACA version as SACA (1.1). Our results obtained using MST and SACA (1.1) approaches are finally confronted with ALADiN multifragmentation data [5] for the mean multiplicity of IMFs. In the following section, we shall give details of ALADiN experimental set-up.

5.2 Overview of ALADiN experimental set-up

The ALADiN experimental facility at GSI, Darmstadt has been primarily focussing on the spectator decays of heavy projectiles at relativistic energies [3–5, 25]. A series of experiments performed on ALADiN set-up have indicated that isotopic effects, even though small can be observed on the projectile fragmentation [26, 27]. The fluctuation of the largest fragment charge Z^{max}, and the asymmetry between largest and second largest fragments $a_{12} = (Z^{max} - Z^{max-1})/(Z^{max} + Z^{max-1})$ are found to show bimodal distribution [26]. At lower energy tail, the fission of ^{238}U after Coulomb and nuclear excitations has also been investigated on ALADiN set-up [28]. The ALADiN spectrometer was designed for the forward focussing of product emission in laboratory frame. At relativistic energies and with inverse kinematics, the product emission in forward hemisphere is even better realized. This reduces the number of detectors required and associated electronics also. A cross sectional layout of ALADiN set-up is displayed in Fig. 5.1.

The beam entering from left is recorded for its positions and arrival time with two thin plastic scintillation counters. The beam spot had a size of about 2 mm in horizontal and 3 mm in vertical directions. The charge and multiplicity of fragments were detected by multiple-sampling-ionization-chamber (TP-MUSIC III) along with extended time-of-flight (TOF) wall located at the end of the ALADiN spectrometer. The TOF wall consisted of two vertically mounted layers of scintillations of 2.5 cm width and 1.0 cm thickness. A Si-CsI (Tl) hodoscope was positioned 60 cm beyond the target position with total solid angle covered is about 85 % of 4π. A lower limit for rapidity: $y > 0.75 y_{beam}$ was chosen so as to select the spectator source emission from the disassembly of projectile nucleus. This condition was applied on fragments detected in the TOF wall. For light charged particles with $Z = 3$, the probability of acceptance in TOF wall is around 95 % [1].

The detection efficiency for ALADiN setup is quite good and close to 100 %. For instance, all projectile fragments with charge $Z \geq 2$ at E=1000 AMeV are detected. We have, therefore, compared our unfiltered calculations for the multiplicity of IMFs in the forward hemisphere with ALADiN data at incident energies of 400, 600 and 1000 AMeV, respectively.

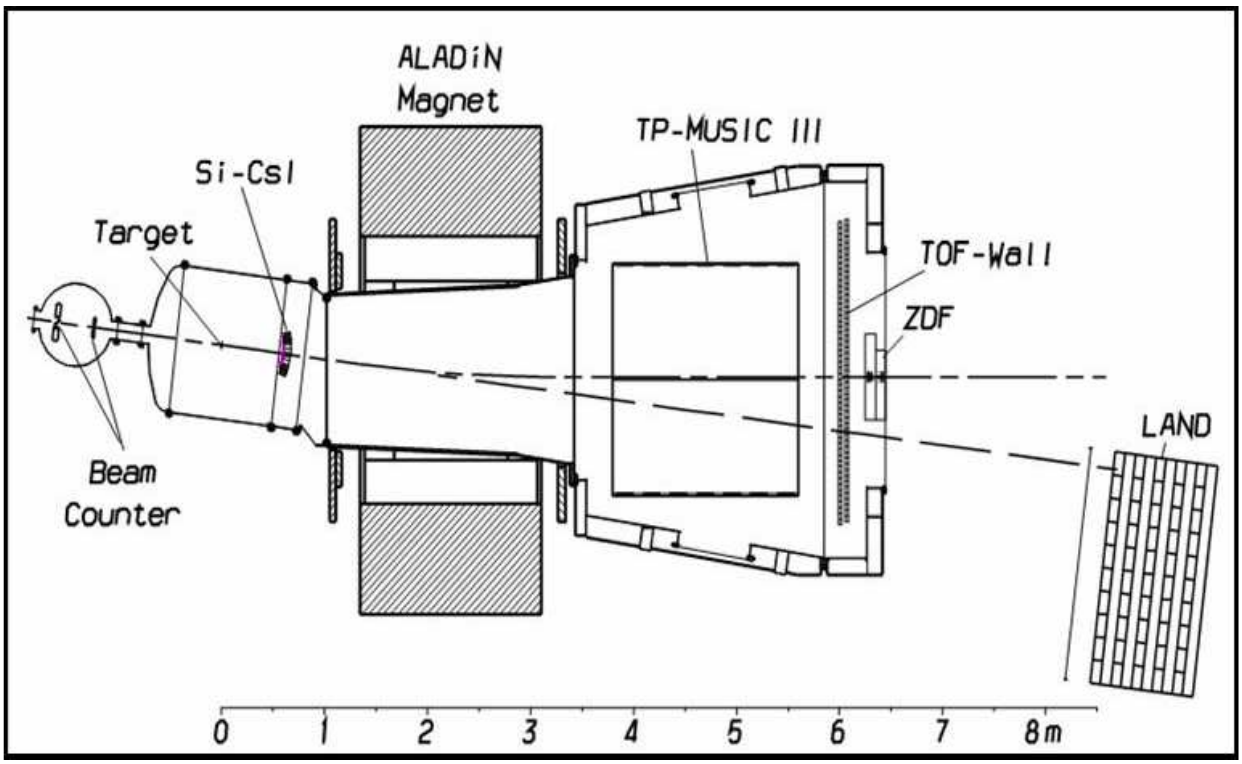

Figure 5.1: The cross sectional view of ALADiN set-up at GSI Darmstadt.

5.3 Simulated Annealing Clusterization Algorithm (SACA (1.1))

This algorithm was devised by Puri *et al* [19–21] based upon the idea that fragment configuration can be realized in nature at an earlier time, when nucleons are still compact in hot and dense environment. Need of this algorithm also arose due to the failure of QMD model to explain higher IMF multiplicity obtained in spectator matter fragmentation at relativistic bombarding energies [3–5]. The IMF emission at incident energies greater than 100 AMeV is characterized by well-known *rise and fall* behavior with a variation in impact parameter. In this energy regime, the onset of multifragmentation and then vaporization sets in leading to very few intermediate mass fragments (IMFs) in central collisions. It shall be worthwhile to see whether limitation of the QMD model can be resolved if one shifts from conventional MST algorithm based upon spatial correlation principle to more sophisticated algorithm using simulated annealing technique.

The first attempt in this direction was made by Dorso *et al* [18], where a Metropolis algorithm [29] was invoked to obtain optimal fragment configuration which maximizes the

binding energy of the system. The limitation of that procedure was the prohibitively too slow algorithm and poses a serious problem for studying the heavier systems where number of possible configurations tremendously increases. These difficulties were overcome in this novel algorithm namely *simulated annealing clusterization algorithm* (SACA). In addition to this, SACA method avoids getting stuck into any local minima and gives global minimum at the end of the procedure.

In this approach, following assumption are made:

1. The nucleons from target and projectile are grouped into fragments (of any size) and into free nucleons.

2. Though the nucleons inside a fragment can interact with each other, they do not interact with the nucleons from other fragments or free nucleons.

3. That pattern of nucleons and fragments is realized in nature which gives the highest binding energy.

We employ a binding energy check to avoid unnecessary formation of too many fragments:

$$\zeta_a = \frac{1}{N_f} \sum_{i=1}^{N_f} \left[\sqrt{\left(\mathbf{p}_i - \mathbf{P}_{N_f}^{cm}\right)^2 + m_i^2} - m_i + \frac{1}{2} \sum_{j \neq i}^{N_f} V_{ij}\left(\mathbf{r}_i, \mathbf{r}_j\right) \right] < -E_{bind}, \tag{5.1}$$

with $E_{bind} = 4.0$ MeV if $N_f \geq 3$, else $E_{bind} = 0$. In this equation E_{bind} is the fragment's binding energy per nucleon, N_f is the number of nucleons in a fragment, and $P_{N_f}^{cm}$ is the center-of-mass momentum of the fragment. Such binding energy check is very useful to identify the most bound fragment configuration out of huge number of possible configurations.

An iterative procedure is followed, where a transition to the fragment configuration with higher binding energy is always accepted. The transitions leading to lower binding energies are also accepted, but with a certain probability. Since this procedure is called as simulated annealing [30], hence this clusterization method is dubbed as *Simulated Annealing Clusterization Algorithm* (SACA). This name has been derived from the 'annealing' process used in solidification of liquid metals. It is a sequence of Metropolis algorithm with gradually decreasing control parameter 'ϑ' which can be interpreted as a *tempera-*

ture. For each metropolicity at a given temperature, one has to perform a sequence of steps until the binding energy does not change anymore. Each step is executed as follows:

1. Given some initial fragment configuration 'a' with energy ζ_a, a new configuration 'b' with energy ζ_b is generated in the neighborhood of 'a' using a Monte-Carlo procedure.

2. Let the energy difference between a and b is $\Delta\zeta = \zeta_b$ -ζ_a.

3. If $\Delta\zeta$ is negative, the new configuration is always accepted. If $\Delta\zeta$ is positive, it is accepted with a probability $e^{-\Delta\zeta/\vartheta}$.

At the start, the temperature 'ϑ' is taken to be large enough so that almost all attempted transitions are accepted. This is to overcome any kind of the local minima. After the binding energy remains constant, a gradual decrease in the control temperature 'ϑ' is made and the Metropolis algorithm is repeated. The clustering algorithm is executed in two-steps. First steps involves exchange of nucleons only among the fragments. Second step involves exchange of sub-clusters *i.e.* group of nucleons among the fragments.

I. **Nucleon exchange procedure**

To start with, a random configuration a (which consists of fragments and free nucleons) is chosen. The total energy associated with configuration a is given by:

$$\begin{aligned}
\zeta_a = &\sum_{i=1}^{N_f^l} \left\{ \sqrt{(\mathbf{p}_i - \mathbf{P}_{N_f^l}^{cm})^2 + m_i^2} - m_i + \frac{1}{2}\sum_{j\neq i}^{N_f^l} V_{ij}(\mathbf{r}_i, \mathbf{r}_j) \right\}_1 \\
&+ \cdots \sum_{i=1}^{N_f^\nu} \left\{ \sqrt{(\mathbf{p}_i - \mathbf{P}_{N_f^\nu}^{cm})^2 + m_i^2} - m_i + \frac{1}{2}\sum_{j\neq i}^{N_f^\nu} V_{ij}(\mathbf{r}_i, \mathbf{r}_j) \right\}_\nu \\
&+ \sum_{i=1}^{N_f^\mu} \left\{ \sqrt{(\mathbf{p}_i - \mathbf{P}_{N_f^\mu}^{cm})^2 + m_i^2} - m_i + \frac{1}{2}\sum_{j\neq i}^{N_f^\mu} V_{ij}(\mathbf{r}_i, \mathbf{r}_j) \right\}_\mu \\
&+ \cdots \sum_{i=1}^{N_f^n} \left\{ \sqrt{(\mathbf{p}_i - \mathbf{P}_{N_f^n}^{cm})^2 + m_i^2} - m_i + \frac{1}{2}\sum_{j\neq i}^{N_f^n} V_{ij}(\mathbf{r}_i, \mathbf{r}_j) \right\}_n .
\end{aligned}$$

Here N_f^μ is the number of nucleons in a fragment μ, $\mathbf{P}^{cm}_{N_f^\mu}$ is the center-of-mass momentum of the fragment μ and $V_{ij}(\mathbf{r}_i, \mathbf{r}_j)$ is the interaction energy between nucleons i and j in a given fragment μ. Note that the total energy is the sum of the energies of individual fragments in their respective center-of-mass system. Therefore, ζ_a differs from the (conserved) total energy of the system because (i) the kinetic energies of fragments calculated in their center-of-masses and (ii) the interactions between fragments/free nucleons are neglected.

A new configuration is generated using Monte-Carlo procedure by either (a) transferring a nucleon from some randomly chosen fragment to another fragment or by (b) setting a nucleon of a fragment free or (c) absorbing a free nucleon into a fragment. Let the new configuration b be generated by transferring a nucleon from fragment ν to fragment μ. Then the energy of new configuration b is given by:

$$
\begin{aligned}
\zeta_b = &\sum_{i=1}^{N_f^l} \left\{ \sqrt{(\mathbf{p}_i - \mathbf{P}^{cm}_{N_f^l})^2 + m_i^2} - m_i + \frac{1}{2} \sum_{j \neq i}^{N_f^l} V_{ij}(\mathbf{r}_i, \mathbf{r}_j) \right\}_1 \\
+ \cdots &\sum_{i=1}^{N_f^\nu - 1} \left\{ \sqrt{(\mathbf{p}_i - \mathbf{P}^{cm}_{N_f^\nu - 1})^2 + m_i^2} - m_i + \frac{1}{2} \sum_{j \neq i}^{N_f^\nu - 1} V_{ij}(\mathbf{r}_i, \mathbf{r}_j) \right\}_\nu \\
+ &\sum_{i=1}^{N_f^\mu + 1} \left\{ \sqrt{(\mathbf{p}_i - \mathbf{P}^{cm}_{N_f^\mu + 1})^2 + m_i^2} - m_i + \frac{1}{2} \sum_{j \neq i}^{N_f^\mu + 1} V_{ij}(\mathbf{r}_i, \mathbf{r}_j) \right\}_\mu \\
+ \cdots &\sum_{i=1}^{N_f^n} \left\{ \sqrt{(\mathbf{p}_i - \mathbf{P}^{cm}_{N_f^n})^2 + m_i^2} - m_i + \frac{1}{2} \sum_{j \neq i}^{N_f^n} V_{ij}(\mathbf{r}_i, \mathbf{r}_j) \right\}_n
\end{aligned}
$$

Note that in this procedure, the individual energies of all fragments except for the donor fragment (ν) and the receptor fragment (μ) remain the same. The change in the energy when going from configuration a to new configuration b is:

$$\Delta\zeta = \zeta_b - \zeta_a. \tag{5.2}$$

Between the Metropolis algorithms, the system is cooled by decreasing the control parameter ϑ. A decrease in the temperature means that we narrow the energy difference which is accepted in a metropolis step. After many Metropolis steps, one would arrive at a minimum *i.e.* the most bound configuration.

II. **Fragment exchange procedure**

The problem with the above nucleon-exchange procedure is that one usually arrives at a local minimum only. Between the two local minima, we find a huge maxima. Let us give an example: assume we have two fragments, but the most bound configuration would be one single fragment which combines both. Now each exchange of a single nucleon raises the binding energy and only the exchange of all nucleons at the same time lowers the total binding energy. This effect is well-known in chemistry, where it is called activation energy. In order to avoid this, one adds, therefore, a second simulated annealing algorithm in which the nucleons aren't anymore considered as the entities to be exchanged in each Metropolis step (like in the first simulated annealing), but also fragments or nucleons obtained after the first step. This second stage of minimization is called fragment exchange procedure. Note that even in this stage, the free nucleons can be exchanged as before. The total energy associated with any configuration c during the second stage of iterations is given by:

$$\begin{aligned}
\zeta_c = &\left\{ \sum_{i=1}^{N_{S_1}} \left[\sqrt{(\mathbf{p}_i - \mathbf{P}^{cm}_{N_{S_1}})^2 + m_i^2} - m_i + \frac{1}{2} \sum_{j \neq i}^{N_{S_1}} V_{ij}(\mathbf{r}_i, \mathbf{r}_j) \right] \right\}_1 \\
&+ \cdots \left\{ \sum_{i=1}^{N_{S_\nu}} \left[\sqrt{(\mathbf{p}_i - \mathbf{P}^{cm}_{N_{S_\nu}})^2 + m_i^2} - m_i + \frac{1}{2} \sum_{j \neq i}^{N_{S_\nu}} V_{ij}(\mathbf{r}_i, \mathbf{r}_j) \right] \right\}_\nu \\
&+ \left\{ \sum_{i=1}^{N_{S_\mu}} \left[\sqrt{(\mathbf{p}_i - \mathbf{P}^{cm}_{N_{S_\mu}})^2 + m_i^2} - m_i + \frac{1}{2} \sum_{j \neq i}^{N_{S_\mu}} V_{ij}(\mathbf{r_i}, \mathbf{r}_j) \right] \right\}_\mu \\
&+ \cdots \left\{ \sum_{i=1}^{N_{S_n}} \left[\sqrt{(\mathbf{p}_i - \mathbf{P}^{cm}_{N_{S_n}})^2 + m_i^2} - m_i + \frac{1}{2} \sum_{j \neq i}^{N_{S_n}} V_{ij}(\mathbf{r}_i, \mathbf{r}_j) \right] \right\}_n .
\end{aligned}$$

Here N_{S_μ} is the number of nucleons in a super-fragment $S_\mu = \sum_{k=1}^{N^f_{S_\mu}} N^k_{S_\mu}$, where $N^k_{S_\mu}$ is the number of nucleons in the k^{th} fragment contained in the super-fragment, S_μ and $N^f_{S_\mu}$ is the number of pre-fragments contained in the super-fragment S_μ. The $\mathbf{P}^{cm}_{N_{S_\mu}}$ is the center-of-mass momentum of the super fragment S_μ and $V_{ij}(\mathbf{r}_i, \mathbf{r}_j)$ is the interaction energy between nucleons i and j in a given super-fragment. Note that now the particle i interacts with its fellow nucleons in the same pre-fragment and also with the nucleons of other pre-fragments which are contained in a given super fragment S_μ. The new configuration is generated using Monte-Carlo procedure by either (a) transferring a pre-fragment from

some randomly chosen super-fragment to another super-fragment or by (b) setting a pre-fragment free or (c) absorbing a single isolated pre-fragment into a super-fragment. Let us suppose that a new configuration d is generated by transferring a pre-fragment 'k' (with mass $N^k_{S_\nu}$) from super-fragment ν to super-fragment μ. The associated energy of new configuration d reads as:

$$\zeta_d = \left\{ \sum_{i=1}^{N_{S_1}} \left[\sqrt{(\mathbf{p}_i - \mathbf{P}^{cm}_{N_{S_1}})^2 + m_i^2} - m_i + \frac{1}{2} \sum_{j \neq i}^{N_{S_1}} V_{ij}(\mathbf{r}_i, \mathbf{r}_j) \right] \right\}_1$$
$$+ \cdots \left\{ \sum_{i=1}^{N_{S_\nu} - N^k_{S_\nu}} \left[\sqrt{(\mathbf{p}_i - \mathbf{P}^{cm}_{N_{S_\nu} - N^k_{S_\nu}})^2 + m_i^2} - m_i + \frac{1}{2} \sum_{j \neq i}^{N_{S_\nu} - N^k_{S_\nu}} V_{ij}(\mathbf{r}_i, \mathbf{r}_j) \right] \right\}_\nu$$
$$+ \left\{ \sum_{i=1}^{N_{S_\mu} + N^k_{S_\nu}} \left[\sqrt{(\mathbf{p}_i - \mathbf{P}^{cm}_{N_{S_\mu} + N^k_{S_\nu}})^2 + m_i^2} - m_i + \frac{1}{2} \sum_{j \neq i}^{N_{S_\mu} + N^k_{S_\nu}} V_{ij}(\mathbf{r}_i, \mathbf{r}_j) \right] \right\}_\mu$$
$$+ \cdots \left\{ \sum_{i=1}^{N_{S_n}} \left[\sqrt{(\mathbf{p}_i - \mathbf{P}^{cm}_{N_{S_n}})^2 + m_i^2} - m_i + \frac{1}{2} \sum_{j \neq i}^{N_{S_n}} V_{ij}(\mathbf{r}_i, \mathbf{r}_j) \right] \right\}_n .$$

The only difference between the nucleon and the fragment exchange procedures occurs for the bound nucleons. Now the bound nucleons cannot change their identity neither by being absorbed by other pre-fragments nor by becoming free. They will remain bound in a pre-fragment. The pre-fragment itself can change its identity by either getting transferred to a new super-fragment, or be set free. As in the first stage, one calculates the energy difference between the new and the old configurations $\Delta\zeta$ and the metropolis procedure is continued till the most bound configuration is obtained.

To apply simulated annealing (SA) algorithms to a specific problem, one needs to generate neighborhood solutions, and reduce the control temperature 'ϑ' etc. One has to also design a *cooling schedule* to properly execute the SA algorithm. In other words, performance of simulated annealing process depends on following cooling parameters [30]:

a. The initial temperature ϑ_i.

b. Cooling function to decrease the temperature ϑ gradually.

c. The length of Markov chain M_{ch}. The SA algorithm will repeat the process M_{ch} times at a given temperature.

d. Final temperature ϑ_f to terminate the SA algorithm.

In fact, simulated annealing algorithm has basic capability to converge to best solution, no matter, it may require large computation time. Many of its components can be adjusted to optimize the algorithm for better performance and future research.

5.4 Cluster distribution in phase space

First of all, we analyze the phase space distribution of nucleons obtained in a single event of $^{197}Au +^{197} Au$ collision at 1000 AMeV and at an impact parameter of 10 fm. Figure 5.2 displays the cluster distribution (in color) obtained using MST (at 200 fm/c) and SACA (1.1) (at 60 fm/c) methods for heaviest fragment A^{max}, IMFs and LCPs in coordinate ($\mathcal{R}_3$) and momentum ($\mathcal{P}_3$) spaces, respectively. One can see that SACA method could recognize the largest fragment quite earlier when nuclear matter is still compact in $\mathcal{R}_3$ space.

The MST method, on other hand, overestimated the size of largest fragment. Further, there is not even a single IMF produced with MST approach. With SACA method, however, significant yield of IMFs is obtained. This reflects the importance of considering momentum space information of nucleons to identify the fragment structure in SACA formalism.

5.5 Time evolution of fragments using MST and SACA (1.1) formalisms

We first calculate the evolution of mean nucleon density ρ^{avg}/ρ_o, size of largest fragment A^{max} and mean multiplicity of intermediate mass fragments $\langle N_{IMF} \rangle$ at incident energies of 400, 600 and 1000 AMeV and impact parameter of 8 fm. The average nucleon density reaches its maximal around 25 fm/c (See Fig. 5.3). This time domain also witnesses the maximum collision rate and nuclear interactions which are going on between target and projectile nucleons. This maximal density shifts towards later times as we go down the incident energies. The fine point is that there is an insignificant change in the density profile while enhancing the incident energy by the factor of 2.5 times *i.e.* going from 400 to 1000 AMeV. At the final stage of the reaction, we don't see any significant change

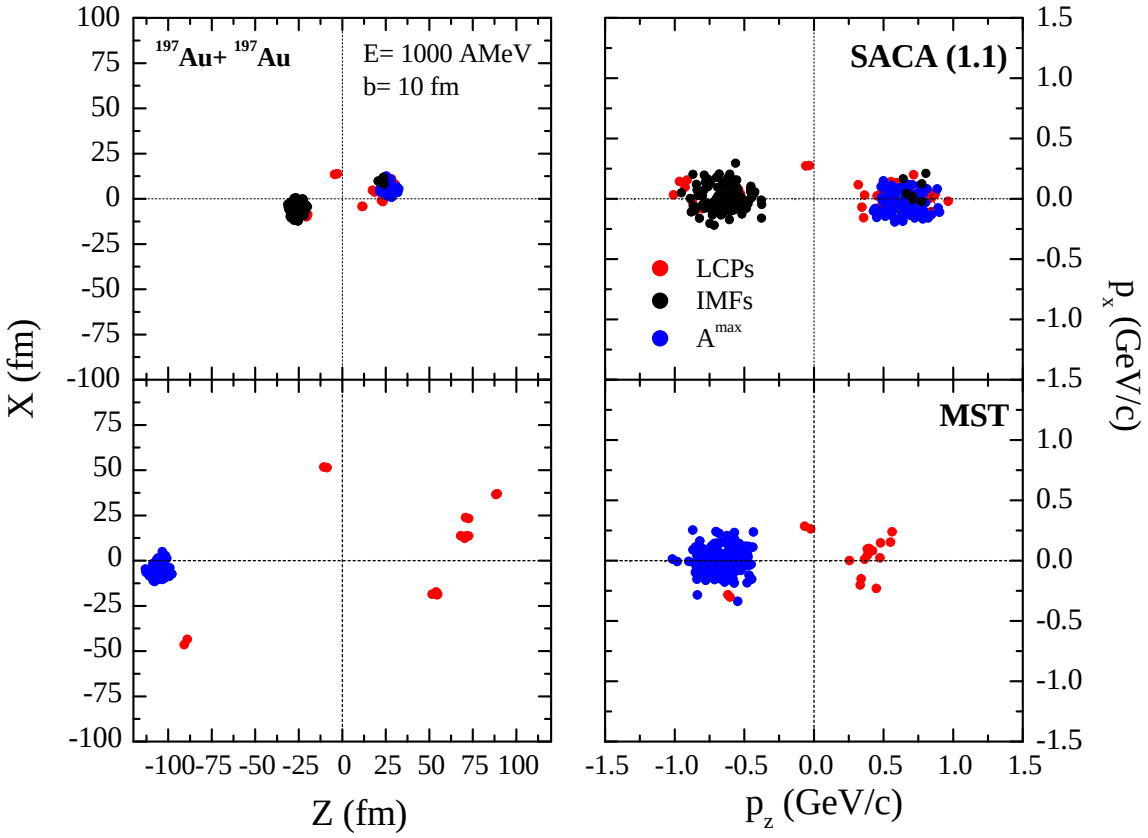

Figure 5.2: The 2-D snapshots for the distribution of nucleons in various fragments in a single event of Au(1 AGeV) +Au collision at b=10 fm in Z-X (left) and $p_z - p_x$ (right) planes. Results are shown for the distribution of clusters recognized with SACA (1.1) and MST approaches.

with the incident energy. The middle panel of Fig. 5.3 shows the time evolution of the heaviest fragment A^{max} using MST and SACA techniques. The MST method gives one big cluster at the time of maximum density, whereas one sees striking ability of SACA method in identifying the heaviest fragment quite early when violent phase of the reaction still continues. This suggests that evolution of multifragmentation is an intricate process. In other words, fragmentation starts at quite early stage when nucleons are still interacting among themselves vigorously. The early recognition of heaviest fragment $\langle A^{max} \rangle$ rules out its formation out of the neck region *i.e.* geometrical overlap between projectile and target. This suggests the emission of $\langle A^{max} \rangle$ from the spectator region. Similar trends of transition from the participant to spectator fragmentation has also been observed and

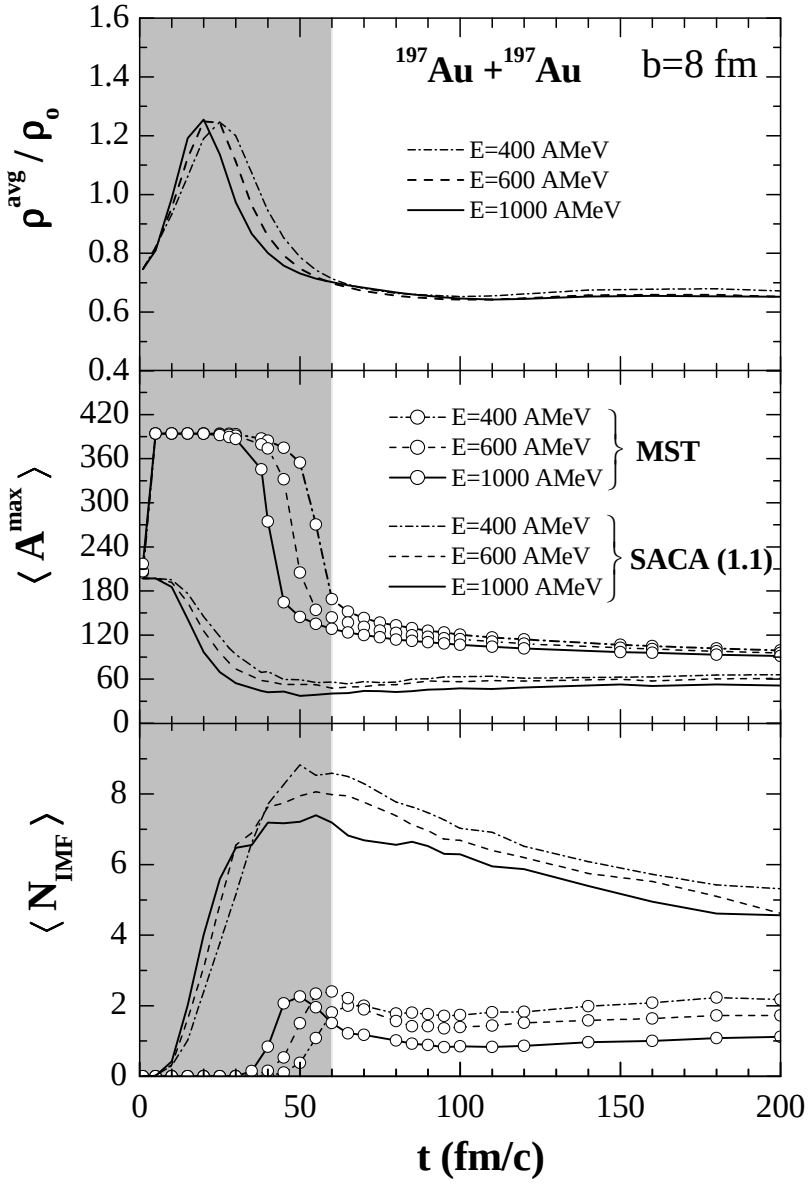

Figure 5.3: The time evolution of mean nucleon density (top), size of heaviest fragment (middle), and multiplicity of IMFs (bottom) obtained in $^{197}Au +^{197} Au$ collisions at incident energies of 400, 600 and 1000 MeV and at b=8 fm.

reported by ALADiN Collaboration [5, 31, 32]. The ability of SACA (1.1) method is also clear from evolution of mean IMF multiplicities $\langle N_{IMF} \rangle$ at all the three incident energies. As shown in Fig. 5.3 (bottom panel), the IMF yields saturate much earlier than with conventional MST approach. Clearly, the IMF yield obtained using SACA (1.1) method at 60 fm/c (shown as shaded boundary), is underestimated in MST approach even at asymptotic times. These findings also confronts the common standpoint of thermal origin

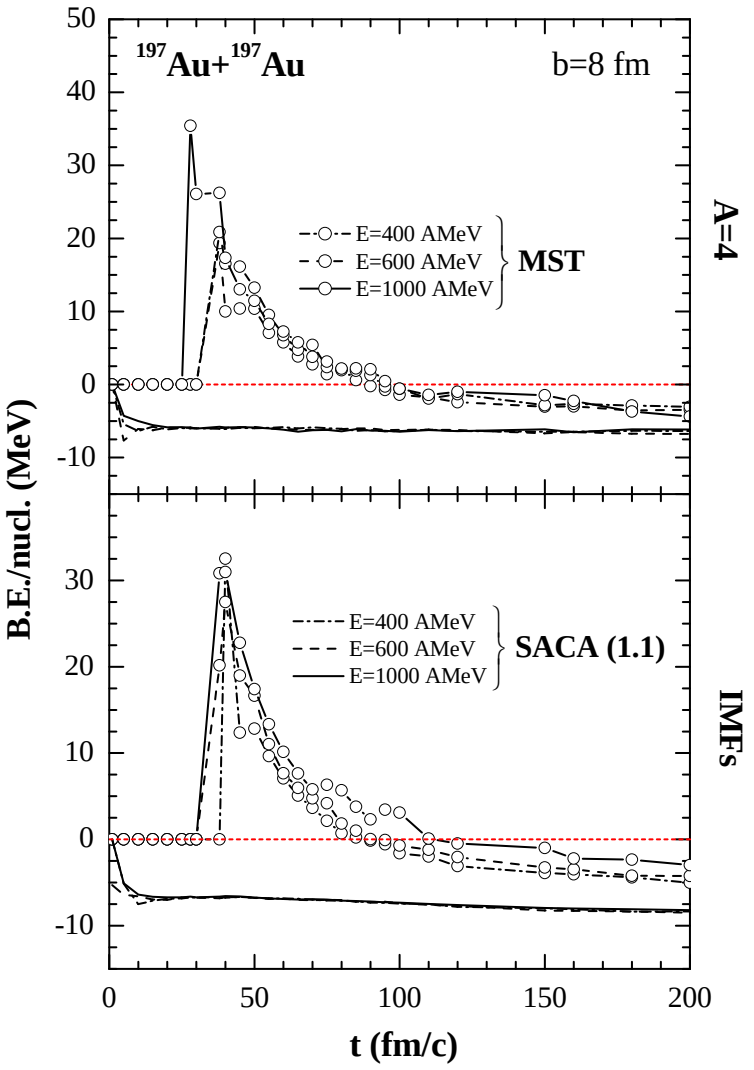

Figure 5.4: Average binding energy per nucleon calculated as a function of time in $^{197}Au+^{197}Au$ collisions at incident energies of 400, 600 and 1000 AMeV and at an impact parameter of 8 fm.

of fragments *i.e.* fragments are created after the thermalization sets in. The further rise in $\langle A^{max} \rangle$ after 60 fm/c in SACA (1.1) is due to the reabsorption of surrounding light fragments by the heavier fragments [33]. We see that heavier $\langle A^{max} \rangle$ survives at smaller incident energies than at higher incident energies. Further early fragment recognition is also supported by stability of the fragments predicted at earlier times. Figure 5.4 shows the binding energy per nucleon for fragments with mass A=4 and intermediate mass fragments IMFs [$5 \leq A \leq 65$] as a function of time. In MST calculations, the binding energy turns negative around 100 fm/c. However, with SACA method one obtains stable fragment configuration at much earlier times. As is clear from the figure that bound

fragments can be identified as early as 60 fm/c just after violent phase is over. All the fragments at this time posses binding energy greater than 4 AMeV. Strikingly, earlier detection of fragments at all incident energies upto 1000 AMeV gives us possibility to look into the n-n interactions when nuclear matter is still hot and dense. Further, one is also free from the problem of stability of fragments. The failure of MST method to detect the final fragment pattern also questions its validity at incident energies as high as 1000 AMeV.

5.6 The persistence coefficient and gain factor

The time development of fragments and stability at microscopic level can also be checked via persistence coefficient and gain factor terms. Let's first understand the definition of these terms in brief. Let N_C be the number of nucleons in a cluster C at time t. The number of nucleon pairs in cluster C at that time t is defined as $b_C(t) = 0.5N_C(N_C - 1)$. After certain time interval Δt, some nucleons have left the cluster C and are part of other cluster or are singles. Let N_{C_A} be the number of nucleons which have been part of cluster C at time t and are at $t+\Delta t$ in the cluster A. We define $a_C(t+\Delta t) = \sum_A 0.5N_{C_A}(N_{C_A}-1)$ where sum goes over all clusters A present at time $(t + \Delta t)$. The persistence coefficient for the cluster C is then defined as [19, 20]:

$$P_C(t + \frac{\Delta t}{2}) = a_C(t + \frac{\Delta t}{2})/b_C(t). \tag{5.3}$$

The average persistence coefficient P for an ensemble of clusters is then defined as:

$$P(t + \frac{\Delta t}{2}) = \langle \frac{1}{N_t} \sum_{C=1}^{N_t} P_C(t + \frac{\Delta t}{2}) \rangle, \tag{5.4}$$

where N_t is the number of fragments present at time t in single simulation. The quantity is then averaged over large number of QMD simulations.

The gain factor is another important quantity that estimates the inter-fragment interactions at given time step. It represents the percent gain of nucleons for a given cluster between two times steps. Let N_C be the number of nucleons in cluster C at the time t. Let N_{C_A} be number of clusters which have been part of cluster C at time t and are at $t + \Delta t$ in cluster A. Gain factor at later time $(t + \Delta t)$ is, therefore, defined as:

$$Gain(t + \frac{\Delta t}{2}) = \eta \times \frac{\sum_A (N_A - N_{C_A})}{N_C}. \tag{5.5}$$

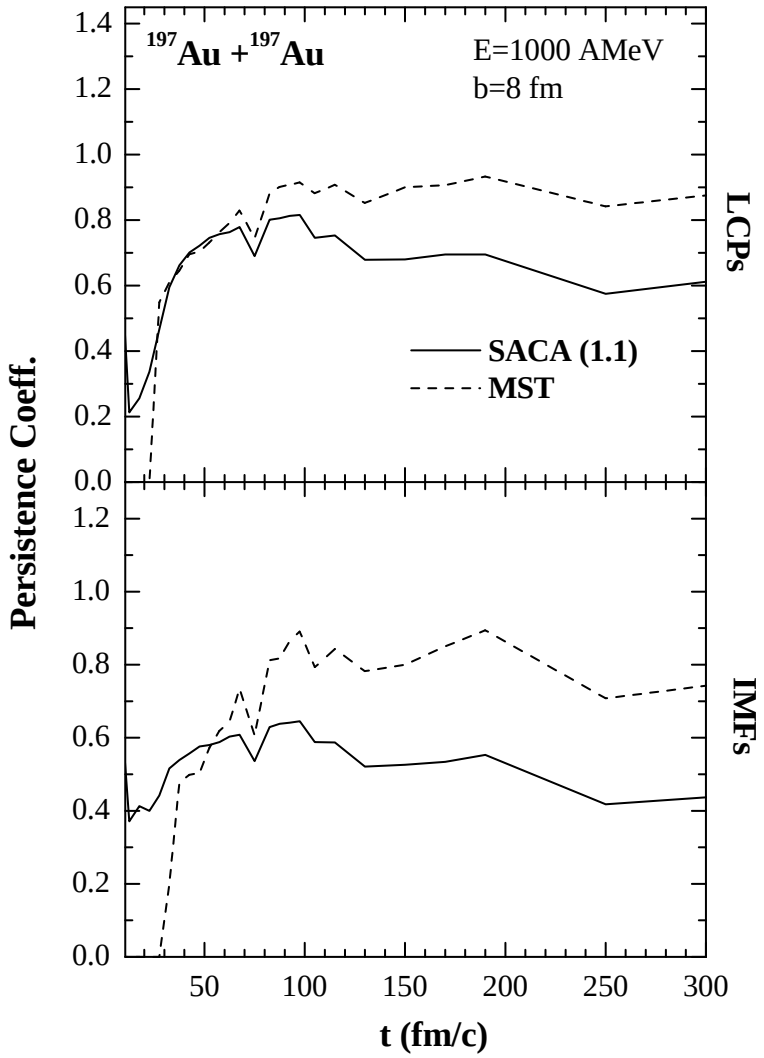

Figure 5.5: The persistence coefficient of LCPs (top panel) and IMFs (bottom panel) displayed as a function of time for $^{197}Au +^{197} Au$ reaction at incident energy of 1AGeV and impact parameter of 8 fm.

We take $\eta = 0$, 0.5 and 1 if $N_{C_A} < 0.5N_A$, $N_{C_A} = 0.5N_A$, if $N_{C_A} > 0.5N_A$ respectively. True gain for the fragment C is there if its nucleons constitutes at least half of the mass of new fragment A. In Fig. 5.5, we display the persistence coefficient for LCPs (top panel) and IMFs (bottom panel) observed at incident energy of 1000 AMeV and at an impact parameter of 8 fm. We see that persistence coefficient saturates earlier in SACA (1.1) method than in the MST method. This indicates significant production of LCPs using SACA (1.1) method. The MST approach, however, does not yield too much LCPs. In other words, *n*-*n* correlations in MST method are preserved, giving rise to fewer LCPs and

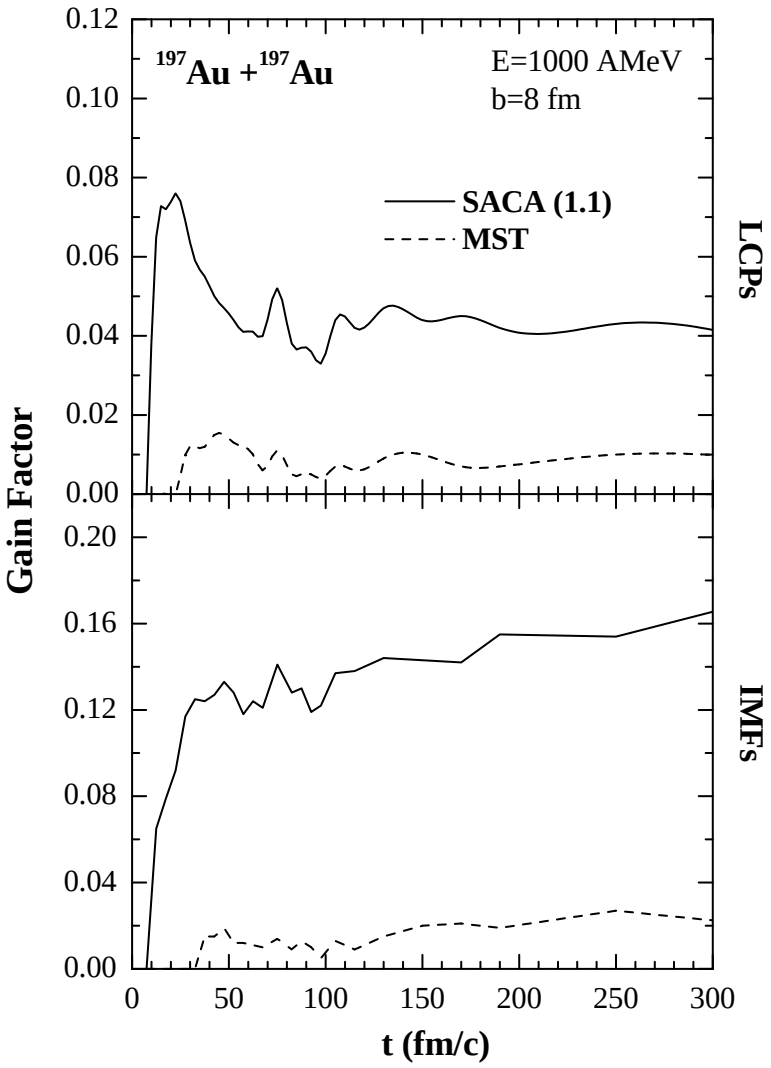

Figure 5.6: Same as in Fig. 5.5, but for the gain factor of LCPs (top panel) and IMFs (bottom panel).

IMFs, but heavier A^{max}. These trends are visible at all the three incident energies (See Fig. 5.3). In Fig. 5.6, is displayed the gain term for the same reaction. Top and bottom panels show the calculated gain term for LCPs and IMFs, respectively. It again shows significant yields of LCPs and IMFs obtained using SACA (1.1) method. It implies that MST method does detect a single heavier $\langle A^{max} \rangle$ which gets detached from the rest of the system earlier leading to smaller yield of IMFs in peripheral collisions. Contrary to this, higher gain factor for IMFs using SACA (1.1) method implies swallowing of surrounding lighter clusters.

5.7 Impact parameter dependence of various fragment species

It would be of interest to compare fragment multiplicities obtained using MST (at 200 fm/c) and SACA (1.1) (at 60 fm/c) approaches. For this, we simulate Au+Au collisions at E=600 AMeV as a function of impact parameter b. Figure 5.7 displays the average size of largest fragment A^{max}, multiplicity of free nucleons, fragments with mass A=2, light charged particles LCPs [$2 \leq A \leq 4$] and intermediate mass fragments IMFs [$5 \leq A \leq 65$] as a function of impact parameter b. For the central geometry, one can see that SACA (1.1) approach compares well with MST method for the multiplicities of different fragment species as well as for $\langle A^{max} \rangle$. It shows the capability of SACA method to recognize the final fragment pattern at the time as early as 60 fm/c. MST approach, however, is able to detect fragmentation pattern only at asymptotic times. Multiplicity of free nucleons, fragments with mass A=2, and LCPs depict a falling pattern with increase in impact parameter indicating their origin from participant region mainly. The *rise and fall* pattern in IMF yield is underestimated by MST approach, which is a positive feature with SACA (1.1) method. One can clearly see that IMF yield at higher impact parameters change drastically if SACA (1.1) method is employed. This shows the importance of binding energy correlations among fragments at microscopic level to recognize the final fragmentation pattern. This is not, however, possible with MST approach where fragments are detected based upon simple coordinate-space correlations. MST approach sees intermediate mass fragments just as the constituents of A^{max}, being very close in coordinate space.

5.8 Confrontation with ALADiN experimental data

Finally, we aimed to confront our model calculations using SACA (1.1) and MST methods with $^{197}Au + ^{197}Au$ fragmentation data taken on ALADiN set-up. Figure 5.8 displays the mean IMF multiplicity $\langle N_{IMF} \rangle$ as a function of impact parameter b in Au+Au reactions at bombarding energies of 400, 600 and 1000 AMeV. Our model calculations for $^{197}Au + ^{197}Au$ reactions with SACA (1.1) method are in nice agreement with ALADiN data [5] at all incident energies. As is clear from the figure, we also achieved a reasonable reproduction of the shape of impact parameter dependence of $\langle N_{IMF} \rangle$. Due to the

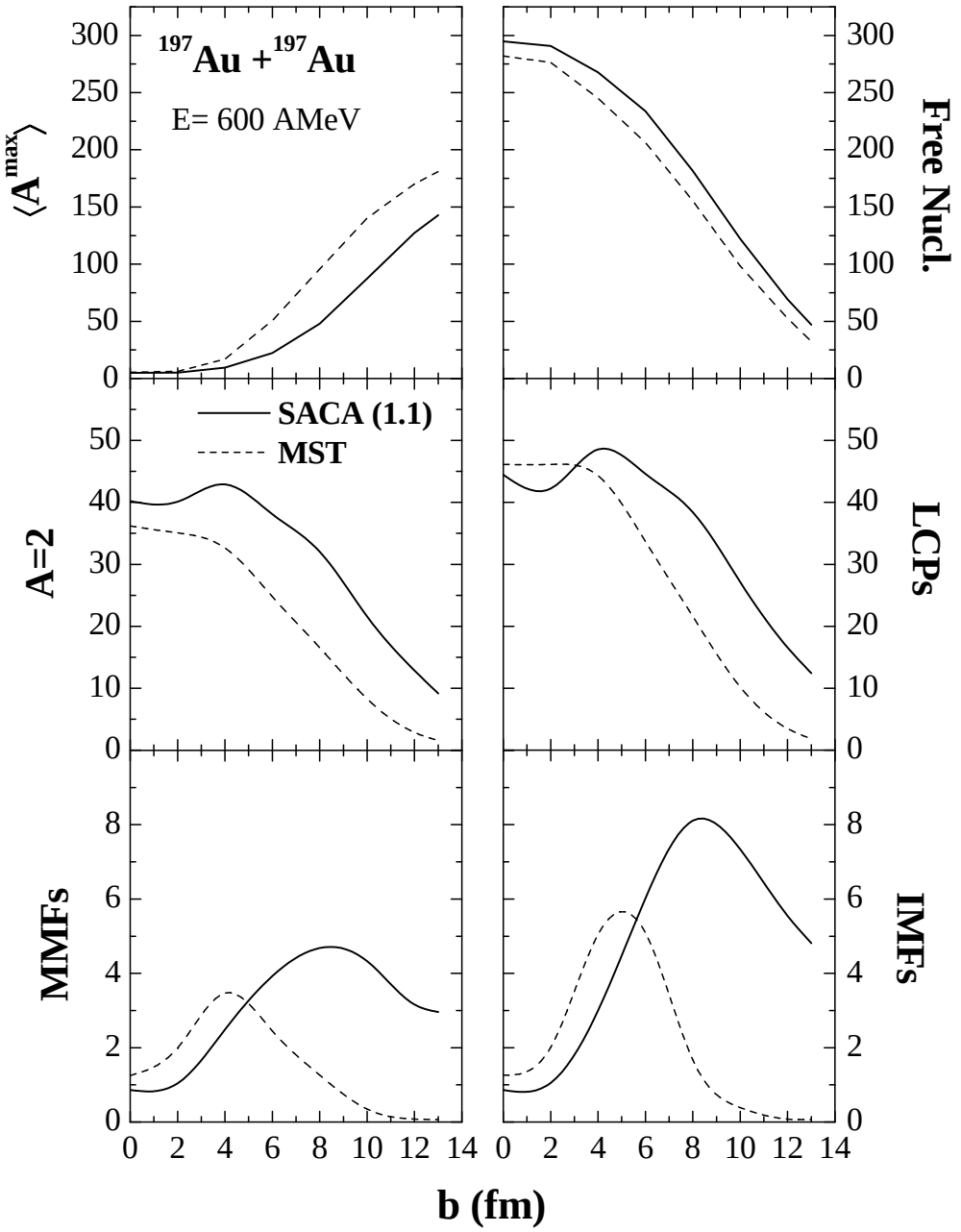

Figure 5.7: The mean size of heaviest fragment A^{max}, multiplicities of free nucleons, fragments with mass A=2, light charged particles LCPs [$2 \leq A \leq 4$], medium mass fragments MMFs [$5 \leq A \leq 9$], and intermediate mass fragments IMFs [$5 \leq A \leq 65$] as a function of impact parameter b. Results are shown here for MST and SACA (1.1) analysis for $^{197}Au + ^{197}Au$ reactions at an incident energy of 600 AMeV.

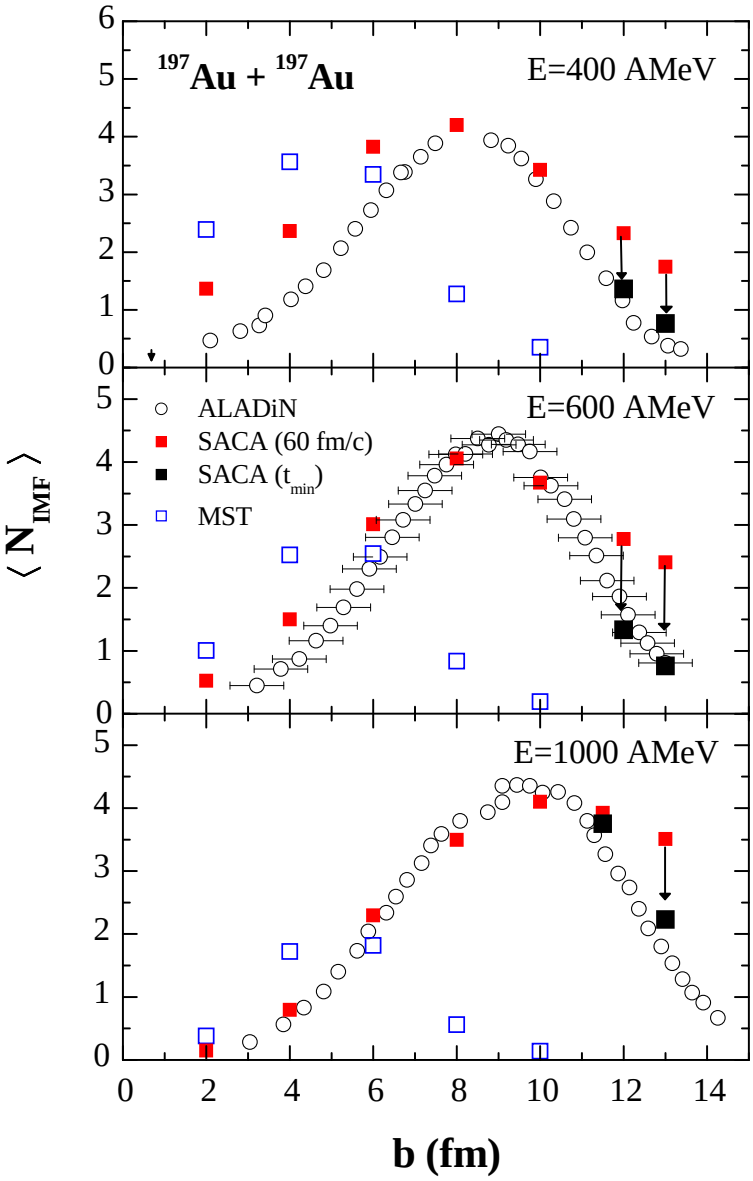

Figure 5.8: The mean multiplicity of intermediate mass fragments $\langle N_{IMF} \rangle$ vs impact parameter b for the reaction of $^{197}Au+^{197}Au$. The model calculations with SACA (1.1) (red, solid squares) and MST (blue, open squares) methods are compared with experimental data (open circles) reported by ALADiN group [5].

shallow minima in the size of A^{max} sometimes, we also display the mean IMF multiplicity observed at second local minimum (earlier than 60 fm/c) for peripheral geometries. The calculated values at these minima using SACA (1.1) method are marked as black filled squares. These values are further closer to the data reflecting the philosophy behind SACA technique to detect the fragment yield faster. Further, the peak value of $\langle N_{IMF} \rangle$ and the corresponding impact parameter b is also well estimated with QMD + SACA method. The prominent feature of the spectator decay is the invariant nature of the IMF distribution with respect to the bombarding energy. The SACA method successfully reproduced the universal nature of spectator fragmentation at all the three bombarding energies. It is worth interesting to note that these universal features observed in multifragmentation of gold nuclei persist upto much higher bombarding energies than explored in this work [34]. Contrary to this, the normal spatial correlation method fails badly to estimate yields of IMFs at all peripheral geometries. This analysis questions the validity of MST method in describing the fragmentation pattern in HI collisions.

In recent literature, the fragment emission from the decay of *quasi-projectiles* has been linked to bimodality behavior in nuclear system [35–37]. The bimodality distribution is regarded as co-existence of two event classes: one with residue-evaporation channel and other with multifragmentation channel. With an increase in the excitation energy, the probability of residue formation and evaporation decreases while that of 'gas' like multifragmentation events increases. This non-equilibrium feature of co-existence of 'liquid' and 'gas' like phases has been regarded as signature of critical behavior in nuclear matter [36, 38–41]. Various models have employed charge asymmetry variables such as $a_{12} = (Z^{max} - Z^{max-1})/(Z^{max} + Z^{max-1})$ to study bi-modal behavior in fragmentation [5, 10, 12]. Such asymmetry can be related to density partition between 'liquid' type (residue matter) and 'gas' type (fragmented matter) phases. Recently, Aichelin and Collaborators investigated asymmetry parameter a_{12} within the QMD model [37, 40]. Their calculations, however, pointed towards bimodality as fast process which is a quite general trend in heavy-ion reactions. Next, we calculate the charge asymmetry variable $\langle a_{12} \rangle$ for Au+Au collisions at incident energies 400, 600 and 1000 AMeV to see whether invariance with respect to incident energy also holds true for charge correlations or not. We display in Fig. 5.9, the time evolution of charge asymmetry of two heaviest fragments *i.e.* $\langle a_{12} \rangle$ using MST and SACA (1.1) approaches for the unfiltered events. One can see that at the start of the reaction, a_{12} is equal to unity. With the passage of time, heaviest fragment

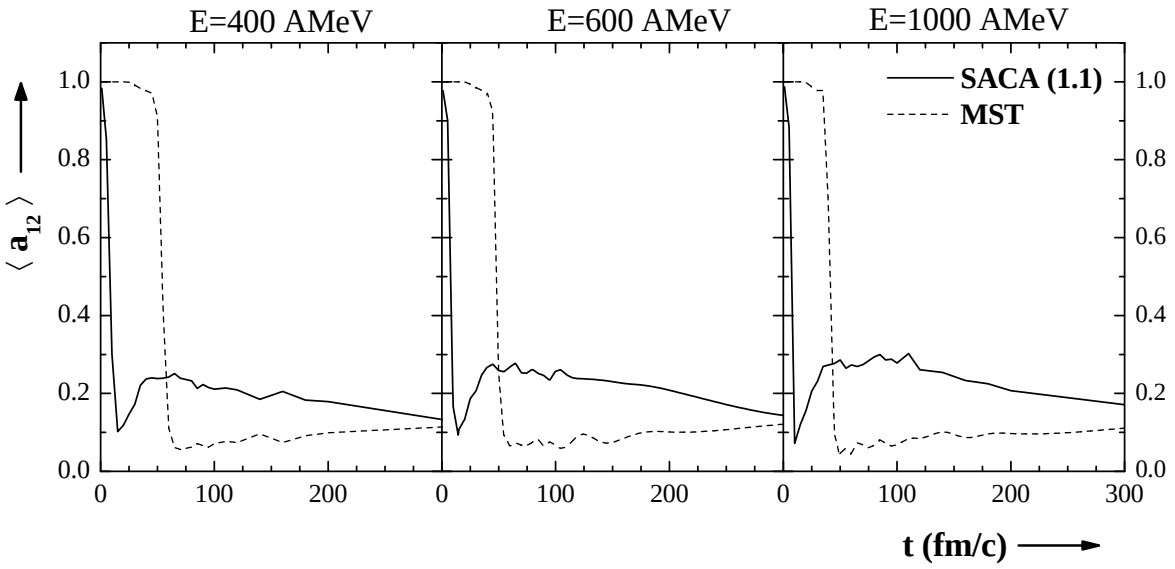

Figure 5.9: The asymmetry of heaviest to second heaviest fragment $\langle a_{12} \rangle$ as a function of time for $^{197}Au + ^{197}Au$ reactions at 400 (left), 600 (middle), and 1000 (right) AMeV and with b=8 fm.

decays into second heaviest and other light fragments. This leads to decrement in the values of a_{12}. With SACA (1.1) method, final a_{12} can be realized quite early just after the high density phase is over. The asymmetry parameters for both approaches, however, converge to same value at asymptotic times as expected. Interestingly, our calculations also highlight the invariant nature of calculated $\langle a_{12} \rangle$ with respect to projectile beam energy.

5.9 Summary

In this chapter, we have studied spectator fragmentation at relativistic bombarding energies at microscopic level using advanced clustering techniques namely *Simulated Annealing Clusterization Algorithm* (SACA (1.1)). For this analysis, we performed QMD simulation of $^{197}Au + ^{197}Au$ collisions at incident energies of 400, 600 and 1000 AMeV and over full geometrical overlap. Fragments obtained using MST and advanced SACA techniques were compared for phase space characteristics, their time evolution as well as impact parameter dependence. Our calculations for the mean multiplicity of intermedi-

ate mass fragments employing SACA (1.1) method indicated strikingly nice agreement with ALADiN data. Further, SACA (1.1) method allows us to study time scale of multifragmentation phenomenon in nuclear collisions. One can, therefore, predict the time when fragment configuration can be realized in phase space. The universality behavior in fragmentation *i.e.* independence from the incident energy chosen is also well reproduced. This universality characteristic has also been there for other charge correlations such as charge asymmetry between the two heaviest fragments. This study puts SACA approach on reliable footing to probe the dynamics of fragmentation process in intermediate energy heavy-ion collisions.

Bibliography

[1] J. Hubele *et al.*, Z. Phys. A **340**, 263 (1991).

[2] G. J. Kunde *et al.*, Phys. Rev. Lett. **74**, 38 (1995).

[3] M. Begemann-Blaich *et al.*, Phys. Rev. C **48**, 610 (1993).

[4] M. B. Tsang *et al.*, Phys. Rev. Lett. **71**, 1502 (1993).

[5] A. Schüttauf *et al.*, Nucl. Phys. A **607**, 457 (1996).

[6] P. B. Gossiaux, R. K. Puri, Ch. Hartnack and J. Aichelin, Nucl. Phys. A **619**, 379 (1997).

[7] C. B. Das, A. Das, M. Satpathy and L. Satpathy, Phys. Rev. C **56**, 1444 (1997).

[8] J. Aichelin, Phys. Rep. **202,** 233 (1991); J. Aichelin and H. Stöcker, Phys. Lett. B **176**, 14 (1986).

[9] D. H. Boal and J. N. Glosli, Phys. Rev. C **38**, 1870 (1988).

[10] P. Kreutz *et al.*, Nucl. Phys. A **556**, 672 (1993).

[11] A. S. Botvina *et al.*, Nucl. Phys. A **584**, 737 (1995).

[12] Y. M. Zheng, F. Wang, B. H. Sa and X. Z. Zhang, Phys. Rev. C **53**, 1868 (1996).

[13] A. S. Botvina and I. N. Mishustin, Phys. Lett. B **294**, 23 (1992); H. W. Barz *et al.*, Nucl. Phys. A **561**, 466 (1993).

[14] Y. M. Zheng, J. Richert and P. Wagner, Chin. J. Nucl. Phys. **17**, 215 (1995).

[15] W. X. Li *et al.*, Phys. Rev C **48**, 628 (1993).

[16] A. Chernomoretz and C. O. Dorso, Eur. Phys. J. D **24**, 197 (2003).

[17] A. Barrañón, J. Escamilla Roa and J. A. López, Phys. Rev. C **69**, 014601 (2004).

[18] C. Dorso and J. Randrup, Phys. Lett. B **301**, 328 (1993).

[19] R. K. Puri and J. Aichelin, J. Comput. Phys. **162**, 245 (2000).

[20] R. K. Puri, J. Singh and S. Kumar, Pramana J. Phys. **59**, 19 (2002).

[21] R. Nebauer, A. Guertin, R. Puri, Ch. Hartnack, P. B. Gossiaux and J. Aichelin, in *Proceedings of the International Workshop XXVII, Hirschegg, Austria, 1999*, edited by H. Feldmeier, J. Knoll, W. Noerenberg and J. Wambach (GSI, Darmstadt, 1999), p.43.

[22] J.B. Garcia and C. Cerruti, Nucl. Phys. A **578**, 597 (1994).

[23] J. P. Bondorf, A. S. Botvina, A. S. Iljinov, I. N. Mishustin and K. Sneppen, Phys. Rep. **257**, 133 (1995).

[24] A. Puente, Phys. Lett. A **260**, 234 (1999).

[25] J. Pochodzalla, Prog. Part. Nucl. Phys. **39**, 443 (1997).

[26] C. Sfienti *et al.*, Nucl. Phys. A **787**, 627 (2007); W. Trautmann *et al.*, Phys. Rev. C **76**, 064606 (2007).

[27] R. Ogul *et al.*, arXiv:nucl-ex/1006.3723.

[28] Th. Rubehn *et al.*, Phys. Rev. C **53**, 3143 (1996).

[29] N. Metropolis, A. W. Rosenbluth, M. N. Rosenbluth, A. H. Teller and E. Teller, J. Chem. Phys. **21**, 1087 (1953).

[30] P. J. M. Laarhoven and E. H. L. Aarts, *Simulated Annealing: Theory and Applications* (Reidel, Dordrecht, 1987).

[31] J. Łukasik *et al.*, Phys. Lett. B **566**, 76 (2003).

[32] K. Zbiri *et al.*, Phys. Rev. C **75**, 034612 (2007).

[33] Y. K. Vermani and R. K. Puri, Euorphys. Lett. **85**, 62001 (2009).

[34] M. I. Adamovich *et al.*, Z. Phys. A **359**, 277 (1997).

[35] O. Lopez and M. F. Rivet, Eur. Phys. J. A **30**, 263 (2006).

[36] A. Le Fèvre *et al.*, Phys. Rev. C **80**, 044615 (2009).

[37] E. Bonnet *et al.*, Phys. Rev. Lett. **103**, 072701 (2009).

[38] B. Borderie, J. Phys. G: Nucl. Part. Phys. **28**, R217 (2002).

[39] G. Tăbăcaru *et al.*, Nucl. Phys. A **764**, 371 (2006).

[40] A. Le Fèvre and J. Aichelin, Phys. Rev. Lett. **100**, 042701 (2008).

[41] M. Bruno, F. Gulminelli, F. Cannata, M. D'Agostino, F. Gramegna and G. Vannini, Nucl. Phys. A **807**, 48 (2008).

Chapter 6

Simulated Annealing Clusterization Algorithm with Realistic Binding Energy Check: Application to ultra low energy collisions

6.1 Introduction

The production of intermediate mass fragments (IMFs) in spectator zone has been recognized as a response towards compression and expansion of participant nuclear matter [1–3]. It is well established that spectator components contribute significantly towards IMF emission at relativistic energies. An extensive experimental study over ALADiN set-up has shown universality pattern in spectator fragmentation and which remains insensitive towards target-projectile combination and beam energy [4]. This observation implies that gold residuals from $^{197}Au+^{197}Au$ reaction would be having nearly the same excitation energies at different bombarding energies. However, as discussed earlier in chapter 5, the molecular dynamics approaches such as the QMD model and microscopic models based on purely statistical mechanics such as statistical simultaneous multifragmentation (SSM) model [5] underestimated the fragment yield from the decay of spectator matter [6–9]. Further, peak IMF multiplicity was also observed at smaller impact parameters than in experiments. Donangelo *et al* [1] has related this discrepancy towards the lesser heat capacity. Due to this, much lesser excitation energy is deposited in the spectator matter which does not produce sizeable number of IMFs. As reported in previous chapters, a novel clusterization algorithm based upon simulated annealing technique [10] was quite successful in explaining the universality characteristics over incident energies 400-1000

AMeV as reported by ALADiN Collaboration [4]. The basic principle behind this algorithm is energy minimization via *simulated annealing technique* which yields maximum binding energy of the system. In this algorithm, each cluster is subjected to a constant binding energy check of -4 MeV/nucleon.

In the present chapter, we aim to propose an extension over the original SACA method via optimization of cluster binding energy check. As we know, the binding energy depends on the mass of the fragment/nucleus, one is always wondering whether criterion of average binding energy is justified or not. We wish to address the above question by subjecting each fragment to its true binding energy that has now been measured to a very precise level with reference to unstable and stable isobars, proton-rich and neutron-rich nuclei. We shall show that this improvement for binding energy check does not yield different results even at relativistic incident energies, justifying the validity of extended version of SACA subroutine. In the following section, we shall describe the extended SACA formalism. This approach shall then be investigated for its ability to reproduce experimental trends in spectator decay at ultra low excitation energies.

6.2 Extended SACA formalism

In SACA method, due heed is given to momentum correlations among nucleons to recognize final bound fragment structure. This aspect is totally neglected in conventional MST method. As explained in chapter 5, the SACA (1.1) method imposes a constant binding energy check of -4 AMeV on fragment's binding energy per nucleon. This assumption of constant binding energy for each cluster in *SACA (1.1)* is crude one. However, we know that binding energy depends on mass and/or neutron-to-proton and thus can't be the same for all nuclei in the periodic table. In this chapter we are interested to optimize the binding energy criterion and study its influence on fragment multiplicities in detail. The choice of proper binding energy can be based on either experimental information or theoretical one. Since experimental information is range bound, we shall use theoretical formulation.

6.2.1 Different nuclear mass formulae

In nuclear physics, one strives for improvised mass formulas that would not only predict masses of β-stable nuclei but also nuclei lying along neutron and proton drip lines with

quite different features and shell effects. In last few decades, several global as well as local mass formulas have been advanced which are quite useful in determining gross properties of nuclei especially those which are far from β-stability line. On experimental front, main interest has been focussed on discovery of super heavy elements (SHE), or isotopes close to proton/neutron drip lines. These observations demand careful checking of theoretical formulas for the prediction of nuclear masses and revision of parameters. For instance, the finite range droplet model (FRDM) combines macroscopic terms with microscopic pairing and shell effects [13]. This mass formula has now become a standard reference chart to calculate the nuclear masses and other properties such as deformations, quadrupole moments, compressibility, and fission barrier heights.

One of the earlier attempts to reproduce the gross features of nuclear binding energies was made by Bethe and Weizsäcker [14]. This formula also known as Bethe-Weizsäcker (BW) mass formula was an empirical refinement of the liquid drop model (LDM) given as [15]:

$$E(N_f, N_f^z) = \ a_v N_f - a_s N_f^{2/3} - a_c \frac{N_f^z(N_f^z-1)}{N_f^{1/3}} - a_{sym}\frac{(N_f-2N_f^z)^2}{N_f} + \delta. \tag{6.1}$$

Here, N_f^z stands for the proton number of the nucleus. The various terms involved in BW mass formula are the volume, surface, Coulomb, asymmetry and pairing terms. The strength of different parameters is: a_v=15.777 MeV, a_s=18.34 MeV, a_c=0.71 MeV and a_{sym}=23.21 MeV, respectively [16]. The pairing term δ is given by:

$$\delta = +a_p N_f^{-1/2} \ for\ even\ N_f^z \ - \ even\ N_f^n,$$

$$\delta = -a_p N_f^{-1/2} \ for\ odd\ N_f^z \ - \ odd\ N_f^n,$$

$$\delta = 0 \ for\ odd\ N_f\ nuclei,$$

with a_p = 12 MeV and N_f^n being the neutron content of the nucleus.

This formula (6.1) was based upon the bulk properties of nuclear matter, thus can reproduce gross properties of medium and heavy mass nuclei. However, it faces serious problem for light nuclei along the drip line and with nuclei having rich neutron or proton content. The liquid drop model (LDM) incorporates macroscopic terms such as volume, surface and Coulomb terms to describe the bulk properties of very dense, charged liquid drop apart from microscopic interactions *i.e.* asymmetry and pairing interactions.

Another attempt to extract liquid drop parameters was made using relativistic mean field theory (RMFT) [17]. The macroscopic part of binding energy of the nucleus was obtained by subtracting the Strutinsky shell corrections from the RMFT energy as:

$$E_{macro}^{RMFT} = E_{RMFT} - E_{shell}^{n} - E_{shell}^{p}. \tag{6.2}$$

The RMFT calculations were performed for 150 even-even nuclei only between proton and neutron drip lines with almost zero quadrupole moment. The parameters obtained by fitting these even-even nuclei using liquid drop model of Myers and Świątecki [18] gave following expression:

$$E_{macro}^{RMFT}(A,Z) = -15.19(1-1.66I^2)A + 16.81(1-1.21I^2)A^{2/3} + 0.68\frac{Z^2}{A^{1/3}} - 1.3\frac{Z^2}{A} \tag{6.3}$$

with (A,Z) as mass and charge of a nucleus and asymmetry $I = \frac{N-Z}{A}$. The main demerit of this mass parametrization is large deviation for the binding energies of several isotopes and isotones that can reach as high as 30 MeV. Another model known as Duflo-Zucker (DZ) mass formula is considered as most predictive model that can consistently predict nuclear masses as given in recent Atomic Mass Evaluation 2003 (AME-03) [19]. The DZ model consists of pairing and Wigner terms apart from isospin dependence of nuclear radii [20]. This model gave more accurate information on nuclear masses as compared to FRDM model [21].

Recently, Souza *et al* [22] tried to include density dependence of symmetry energy for the highly asymmetric nuclear matter. The surface asymmetry and Coulomb terms are added to existing liquid drop model (LDM) parametrization (Eq. (6.1)). Resulting parametrization dubbed as improved liquid drop model (ILDM) reads as:

$$\begin{aligned} E_{bind}^{ILDM}(A,Z) &= a_v\{1-k\left[\frac{(A-2Z)}{A}\right]^2\}A - a_s\{1-k\left[\frac{(A-2Z)}{A}\right]^2\}A^{2/3} \\ &\quad -a_cZ^2/A^{1/3} + a_pA^{-1/2} + c_dZ^2/A. \end{aligned} \tag{6.4}$$

Here, the extra term c_dZ^2/A takes into account Coulomb corrections due to surface diffuseness. The parameters corresponding to ILDM fit (6.4) can be found in Ref. [22].

A recent work by Samanta *et al* [16, 23, 24] highlighted the discrepancy of LDM model (Eq.(6.1)), and its extended versions in explaining the binding energy versus neutron

number curve of several light nuclei near drip lines. They rectified earlier discrepancy by modifying the asymmetry and pairing energy terms in the liquid drop model. This new mass formula dubbed as modified Bethe-Weizsäcker (BWM) mass formula [16] is given as [16]:

$$E^{BWM}(N_f, N_f^z) = \ a_v N_f - a_s N_f^{2/3} - a_c \frac{N_f^z(N_f^z-1)}{N_f^{1/3}} - a_{sym} \frac{(N_f-2N_f^z)^2}{N_f(1+e^{-N_f/17})} + \delta_{new}. \quad (6.5)$$

The strength of various parameters now reads: a_v=15.777 MeV, a_s=18.34 MeV, a_c=0.71 MeV and a_{sym}=23.21 MeV, respectively. The pairing term δ_{new} is given by:

$$\delta_{new} = +a_p N_f^{-1/2} \ (1 - e^{-N_f/30}) \ for \ even \ N_f^z \ - \ even \ N_f^n,$$

$$\delta_{new} = -a_p N_f^{-1/2} (1 - e^{-N_f/30}) \ for \ odd \ N_f^z \ - \ odd \ N_f^n,$$

$$\delta_{new} = 0 \ for \ odd \ N_f \ nuclei,$$

with a_p = 12 MeV.

It may be stated that though BWM formula doesn't incorporate any shell effects, it is quite promising formula to predict nuclear masses along the β-stability line. This formula with modified asymmetry and pairing energy terms was able to predict binding energy versus neutron number curve of all elements from Li to Bi. It particularly explains the binding energies and one-nucleon separation energies of lighter nuclei near the drip line [23, 24].

We shall extend the SACA (1.1) method by incorporating this binding energy check (6.5) during the formation of clusters. Each fragment at the end of the Metropolis procedure is subjected to the new binding energy check (Eq.(6.5)). Any fragment that fails to fulfil this binding energy criterion is treated as a group of free nucleons. At the end, all fragments obtained will be bound and stable. This version is labeled as *SACA (2.1)* [25].

6.3 Spectator matter fragmentation using SACA (1.1) and SACA (2.1) versions

In this section we shall study the results obtained with original SACA version and improvised version *i.e. SACA (2.1)* and compare with ALADiN multifragmentation data [4] at relativistic energies.

6.3.1 Time evolution of various fragments

To investigate the influence of modified binding energy check (Eq. 6.5), we compare the time evolution of average size of largest fragment $\langle A^{max} \rangle$, multiplicity of various fragments obtained using original *SACA (1.1)* and extended *SACA (2.1)* versions. First we study the fragment observables for $^{197}Au + ^{197}Au$ at 600 AMeV and impact parameter of 12 fm. Figure 6.1 displays the mean size of the largest fragment $\langle A^{max} \rangle$, multiplicities of free nucleons, light charged particles LCPs [$2 \leq A \leq 4$], medium mass fragments MMFs [$5 \leq A \leq 20$], heavy mass fragments HMFs [$21 \leq A \leq 65$] and intermediate mass fragments IMFs [$5 \leq A \leq 65$] as a function of time. We have used here a *soft* equation of state along with standard energy dependent n-n cross section [26]. As expected, $\langle A^{max} \rangle$ is nearly independent of the binding energy criterion. As far as different fragment species are concerned, very insignificant different can be seen of this modification. Similar trends are also visible for same reaction but at an impact parameter b=3 fm (See Fig. 6.2.)

6.3.2 Persistence coefficient and gain factor

We have to also find out the time step at which fragment structure is clearly recognized and can be easily compared with experimental data. For this, persistence coefficient and gain factor are the two terms which can give us useful information. As discussed earlier in chapter 5, the persistence coefficient gives fraction of nucleons in i^{th} cluster at time $(t + \Delta t)$ which are also part of the cluster at earlier time t. From Fig. 6.3, we can see that persistence coefficient for MMFs [$5 \leq A \leq 20$] and IMFs [$5 \leq A \leq 65$] nearly saturates to the value 0.7 at 60 fm/c and for later times. One can see that similar profiles of persistence coefficient and gain factor are obtained for the two versions. There is a sharp decrease in the persistence coefficient of LCPs during early stage. It means that light fragment are swallowed by heavier fragments and A^{max}. After the compressed phase is over, it stays constant beyond 60 fm/c with value ~ 0.8. It indicates that heavier fragments have detached themselves and no longer interact with participant zone afterwards.

6.3.3 Impact parameter dependence of the various fragment multiplicities

To further explore the characteristics of fragment structure obtained with modified *SACA (2.1)* method, we analyzed the impact parameter dependence of mean size of $\langle A^{max} \rangle$ and

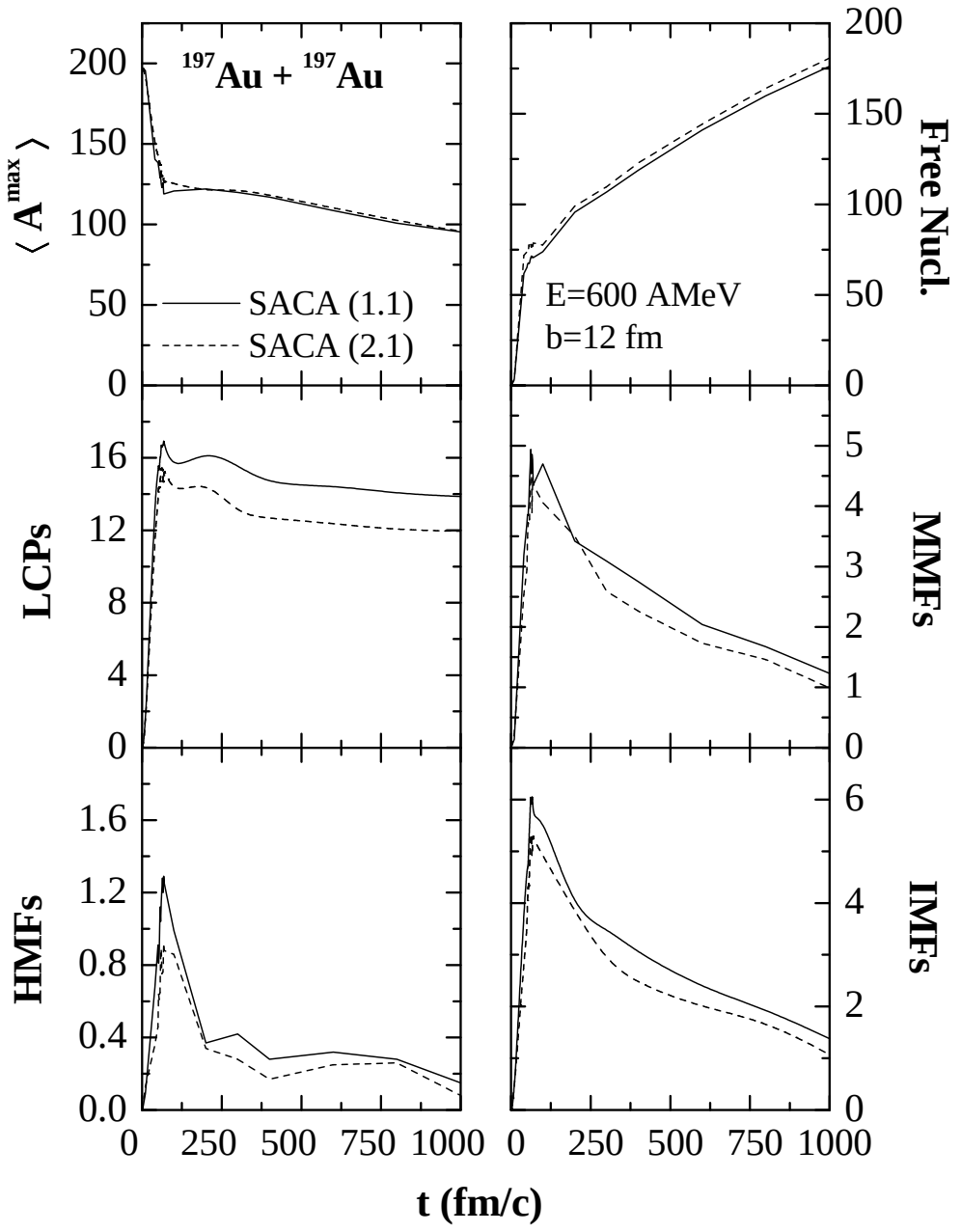

Figure 6.1: The size of heaviest fragment $\langle A^{max} \rangle$ and the multiplicities of various fragment species as a function of time for the reaction of $^{197}Au + ^{197}Au$ at 600 AMeV and at an impact parameter of 12 fm. The solid and dashed lines depict the results due to original SACA and its extension, respectively.

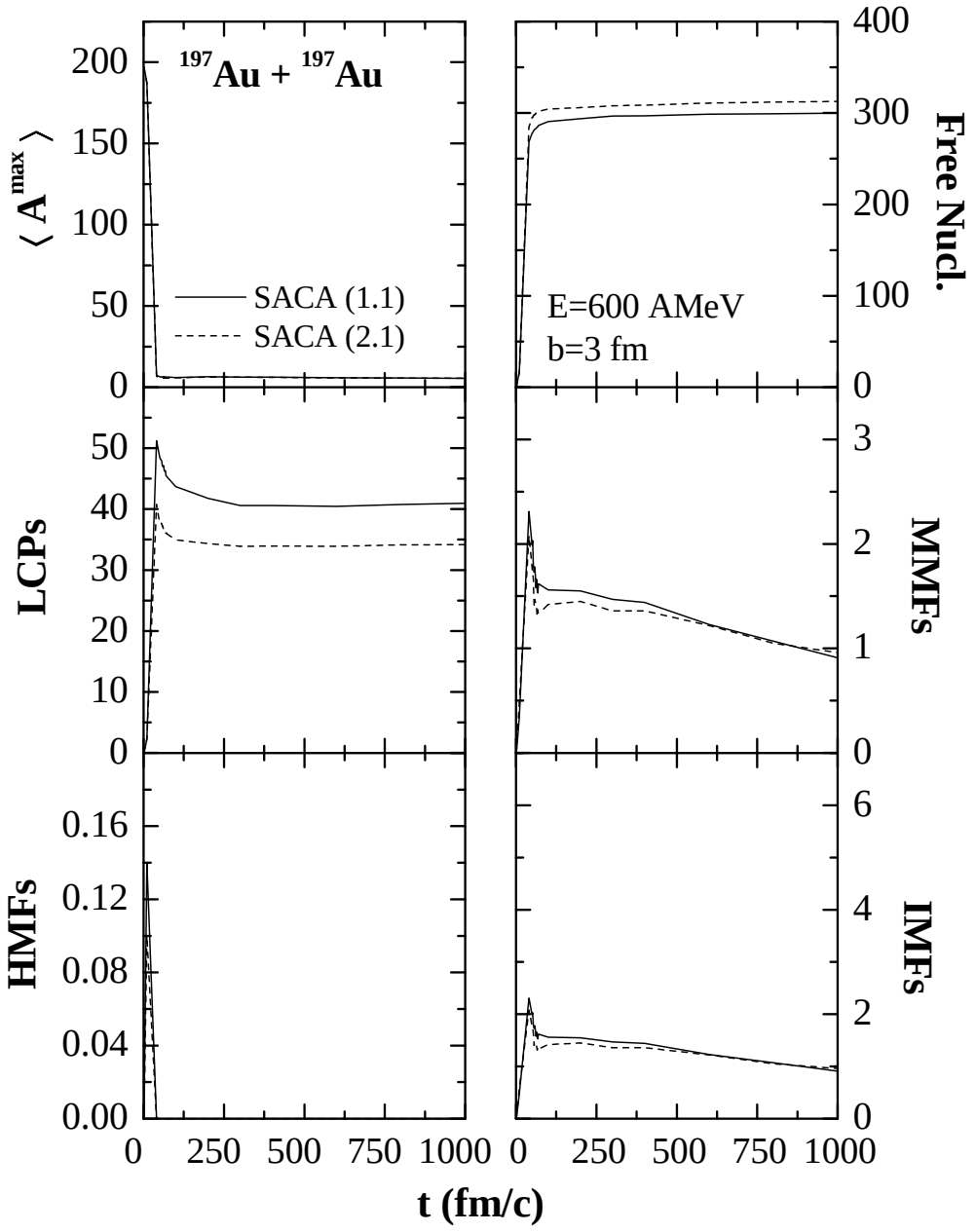

Figure 6.2: Same as in Fig. 6.1, but at impact parameter b= 3 fm.

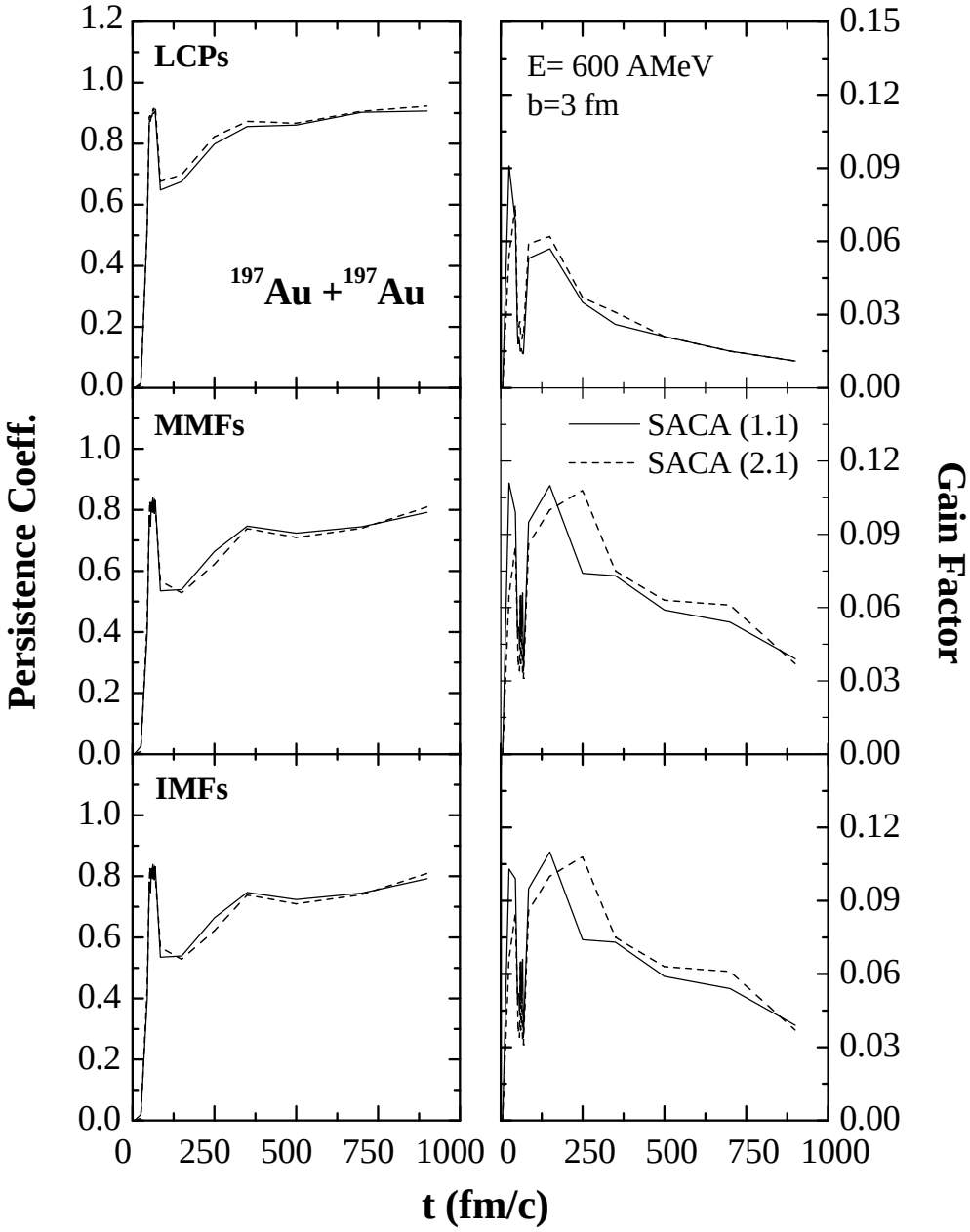

Figure 6.3: The persistence coefficient and gain factor for various fragment species as a function of time for the reaction of $^{197}Au + ^{197}Au$ at 600 AMeV and at impact parameter b=3 fm. The solid and dashed lines depict the results due to original SACA and its extension.

multiplicities of various fragment species This will also help to understand the energy deposition in spectator matter properly. The results obtained using *SACA (1.1)* and *SACA (2.1)* for $^{197}Au + ^{197}Au$ collisions at incident energies 400, 600, and 1000 AMeV are displayed in Figs. 6.4, 6.5 and 6.6, respectively. The time for realization of different fragments was chosen to be 60 fm/c. We can see that similar fragment emission profiles are observed at all the three incident energies. In central collisions, *SACA (2.1)* predicts smaller $\langle A^{max} \rangle$, whereas trend reverses in peripheral collisions. As a result, free nucleons also behave accordingly. The yields of IMFs and MMFs don't reduce considerably for central as well as peripheral geometries using extended version of SACA. This is due to the fact that fragments recognized by SACA method are properly bound, therefore, simple cut also yields same results.

6.3.4 Confrontation with ALADiN multifragmentation data

Finally, we are also interested to check the performance of improvised version of SACA in explaining the ALADiN data. For this purpose, we compare the model predictions using *SACA (2.1)* and original *SACA (1.1)* versions with ALADiN data on $^{197}Au + ^{197}Au$ collisions at 600 AMeV. Figure 6.7 displays our calculations for mean IMF multiplicity $\langle N_{IMF} \rangle$ (top panel) and mean charge of heaviest fragment $\langle Z^{max} \rangle$ (bottom panel) as a function of impact parameter b. One can see that *SACA (2.1)* compares well with *SACA (1.1)* in reproducing the overall b-dependence of IMF yield and charge of heaviest fragment. Agreement is quite satisfactory in peripheral collisions where results obtained *SACA (2.1)* version agree closely with experimental trends for IMF multiplicity and mean charge of heaviest fragment.

We extend our analysis to investigate IMF yields at two other incident energies of 400 and 1000 AMeV also. Figure 6.8 shows the calculated $\langle N_{IMF} \rangle$ as a function of impact parameter b at these energies using *SACA (1.1)* and *SACA (2.1)* versions. Also shown is the ALADiN data for IMF yield [4]. Overall we see that both versions are close to each other and *SACA (2.1)* method explains the experimental data quite nicely. We have also tested the spectrum for actual experimental binding energies [19]. Negligible difference has been seen for the case of very light nuclei only. This analysis shows that *SACA (2.1)* version is working satisfactorily and is well suited to describe the spectator fragmentation at relativistic energies.

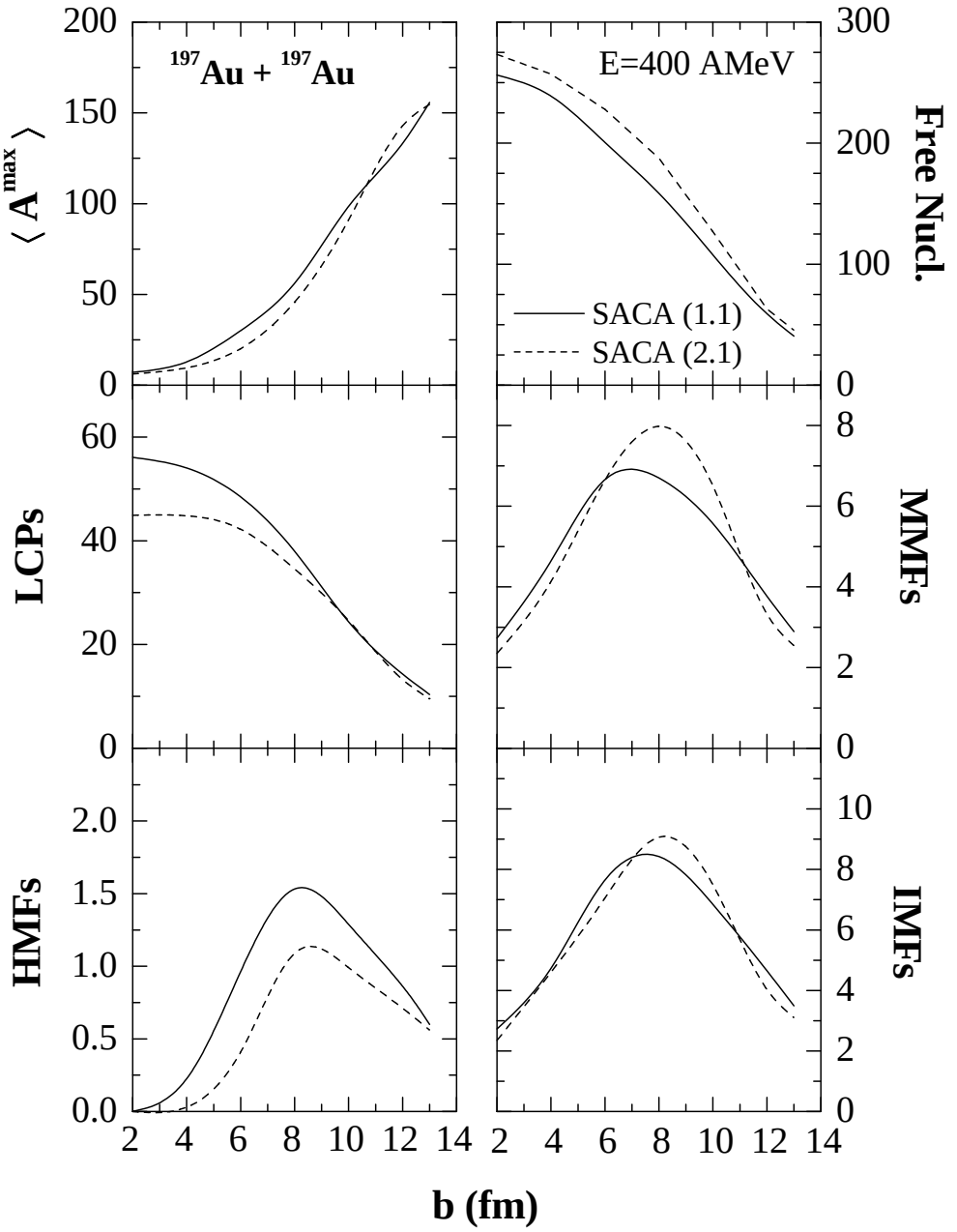

Figure 6.4: The impact parameter dependence of $\langle A^{max} \rangle$ and multiplicities of various fragment species for the reactions of $^{197}Au + ^{197}Au$ at incident energy 400 AMeV. The solid and dashed curves depict results of *SACA (1.1)* and *SACA (2.1)*, respectively.

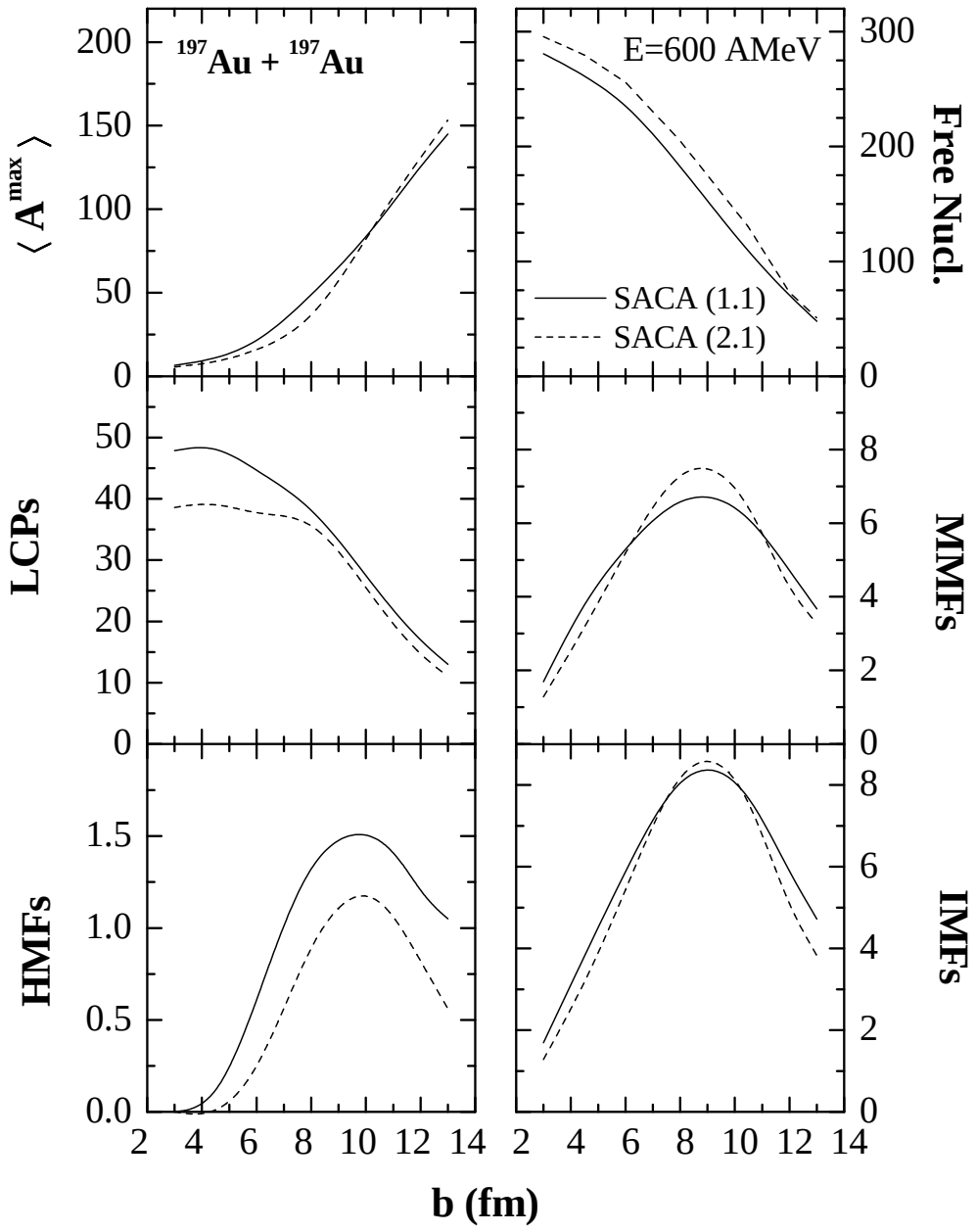

Figure 6.5: Same as in Fig. 6.4, but at incident energy 600 AMeV.

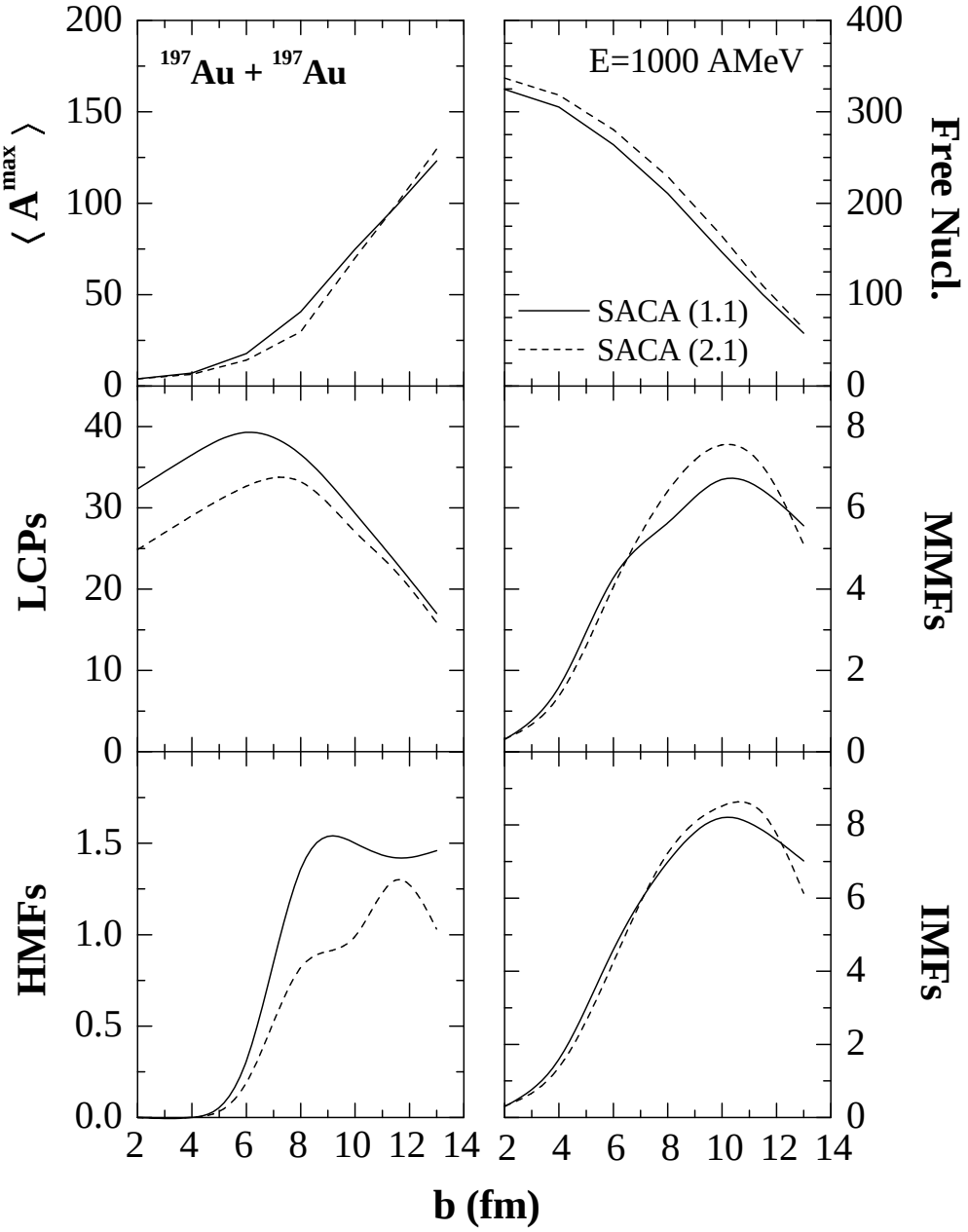

Figure 6.6: Same as in Fig. 6.4, but at incident energy 1000 AMeV.

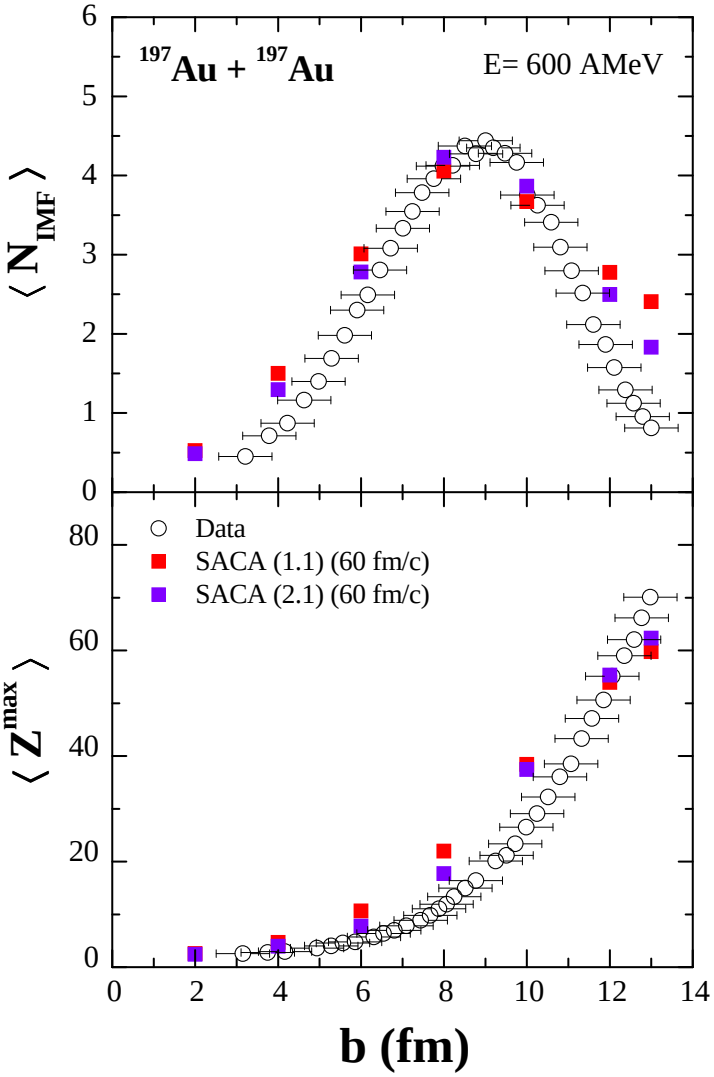

Figure 6.7: The IMF multiplicity $\langle N_{IMF} \rangle$ (top panel) and charge of the heaviest fragment $\langle Z^{max} \rangle$ (bottom panel) as a function of impact parameter for the $^{197}Au + ^{197}Au$ reaction at incident energy of 600 AMeV. Open circles depict the experimental data points [4].

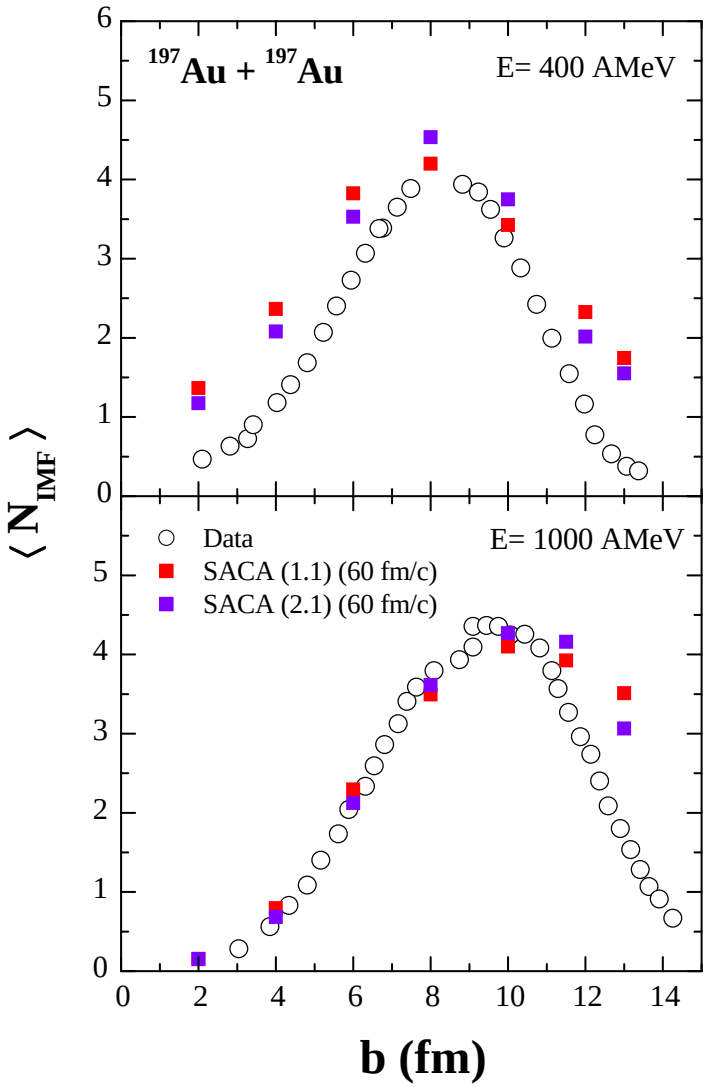

Figure 6.8: The mean IMF multiplicity $\langle N_{IMF} \rangle$ vs impact parameter b. The $^{197}Au+^{197}Au$ reaction has been studied at incident energies of 400 AMeV (top panel) and 1000 AMeV (bottom panel). Open circles depict the experimental data points [4].

6.4 Spectator matter fragmentation at low excitation energies

As far as peripheral collisions are concerned, pattern of '*rise and fall*' in the IMF multiplicity is observed as a function of impact parameter at higher incident energies ($\geq$ 400AMeV). In the collision of two Au nuclei, maximum multiplicity is observed around $\approx$ 100 AMeV. Above 100 AMeV, there is a fall in multiplicity of IMFs observed at central impact parameter. In low incident energy channels, dynamics involved is quite different, which is mainly dominated by the fusion-fission events, deep-inelastic scattering and dissipative *n-n* collisions. The final fragmentation pattern takes time long enough to realize. The question of thermal equilibrium also becomes important at such low incident anergies. Within conventional *minimum spanning tree* (MST) method, one may not obtain the fragment structure accurately as it would take a longer time for separation of fragments in configuration space and get identified. Recently, charge distributions for the $^{40}Ca+^{40}Ca$ collision at 35 AMeV were analyzed within QMD and CoMD approaches [27]. The results obtained with MST method [27–30] highlighted discrepancy in the QMD calculations in accurately reproducing experimental data [31]. We aim to apply advanced SACA approach to see whether it can explain spectator fragmentation in low excitation channels or not. Finally, we shall confront model calculations employing *SACA (2.1)* and MST approaches with experimental data taken with Multics-Miniball array [32].

6.4.1 Time evolution of fragments with MST and SACA (2.1)

First of all, we study the time evolution of Au(35 AMeV)+Au reaction at a 'reduced' impact parameter $b/b_{max} = 0.55$ using two clusterization approaches. We have chosen here a *soft* equation of state ($\mathcal{K} = 200\ MeV$) and standard energy dependent *n-n* cross section. The reactions are followed for a time span of 300 fm/c. Figure 6.9 shows that *SACA (2.1)* is able to predict the mean size of heaviest fragment $\langle A^{max} \rangle$ as early as 100 fm/c, just after violent stage of the reaction is over. The QMD+MST approach, on the other hand, detects a single heavier $\langle A^{max} \rangle$ even when average nucleonic density has reached saturation. Heavier A^{max} obtained using MST method implies that it actually consists of smaller heavy fragments *viz.* medium mass fragments (MMFs), light charged particles (LCPs) *etc*, and aren't recognized being very close in configuration space. The bottom panel displays the evolution of clusters with mass $A \geq 5$. One can see that *SACA*

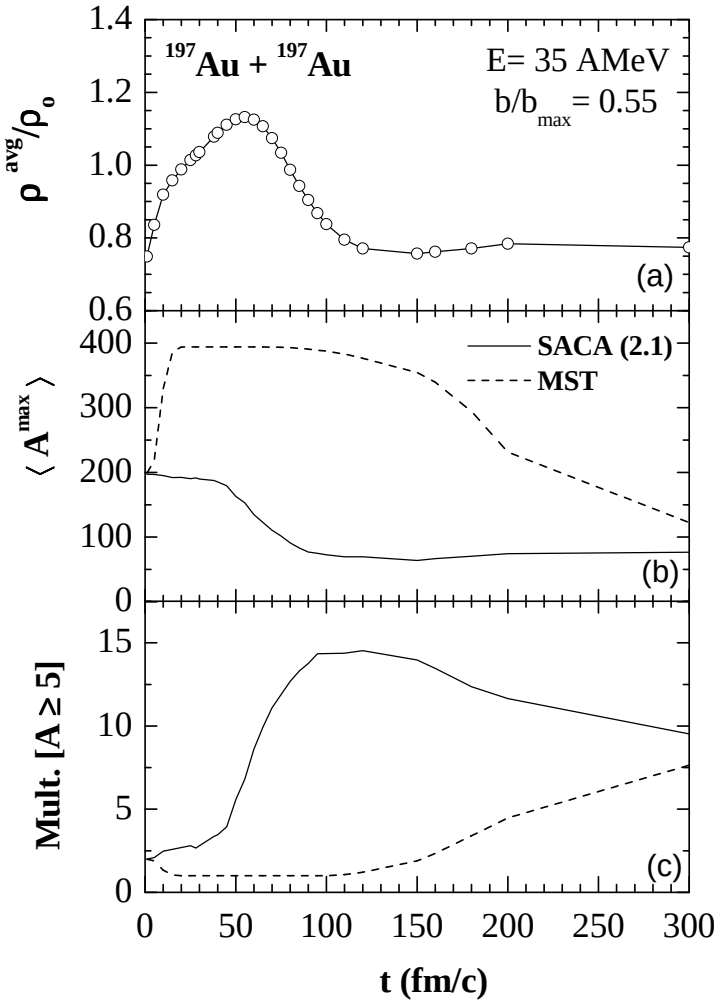

Figure 6.9: The time evolution of (a) mean nucleon density ρ^{avg}, (b) size of heaviest fragment A^{max}, and (c) multiplicity of heavier clusters with mass $A \geq 5$ in Au(35 AMeV)+Au collisions at reduced impact parameter $b/b_{max} = 0.55$ ($b_{max} = 1.142[A_T{}^{1/3} + A_P{}^{1/3}]$).

(2.1) approach significantly alters the dynamics of cluster recognition in phase space. For asymptotic times, however, both clusterization techniques converge to same cluster configuration, as expected.

6.4.2 Fragment charge distribution

Another interesting observation can be seen if we compare the charge dispersion obtained with these two clusterization approaches. Figure 6.10 depicts the charge distribution N(Z) obtained using MST and *SACA (2.1)* approaches for unfiltered events in Au (35 AMeV)+ Au collisions. Filled circles represent the experimental charge distribution obtained from

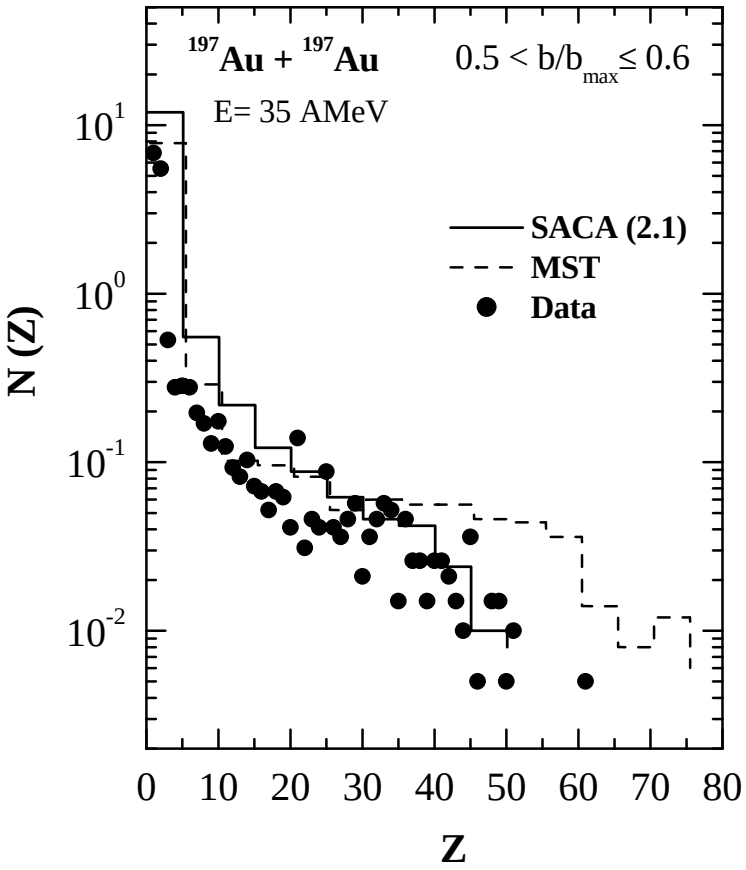

Figure 6.10: The charge dispersion of nuclear fragments in peripheral Au (35 AMeV)+ Au collisions in the impact parameter interval $0.5 < b/b_{max} \leq 0.6$. Models calculations using MST (dashed curve, 300 fm/c) and *SACA (2.1)* (solid curve, 100 fm/c) approaches are compared with experimental data (filled circles) [33].

decay of the *quasi-projectile* (QP) in the impact parameter interval $0.5 < b/b_{max} \leq 0.6$ [33]. One can clearly see that MST method predicts larger production probability of heavier charges. *SACA (2.1)* finds that heavier $\langle Z^{max} \rangle$ is further composed of smaller charged products which MST fails to recognize, being very close in configuration space. As a result, the tail of charge spectrum shifts towards high Z values with MST method. Moreover, it also neglects the momentum correlations among the nucleons of the fragment. Hence, MST method can't address the time scale of fragment formation as well. SACA method, therefore, seems to be well suited to study early dynamics of cluster production in low energy HI reactions.

6.4.3 Rapidity distribution

To derive quantitative information on the temperature and excitation energy deposited in the spectator matter, one needs to investigate the stopping behavior of particle emission. Next, we address the question of stopping of fragments in the reaction system which has an overall influence on thermalization achieved in the reaction. It may be mentioned that complete equilibration of nuclear matter isn't, however, possible except for central collisions when all nucleons are expected to be stopped at midrapidity. Fragment rapidity distribution dN/dy of different fragments is one of the dynamical observables to infer stopping of nuclear matter in heavy-ion collisions. Figure 6.11 depicts the longitudinal rapidity distribution dN/dy for light charged particles LCPs [$2 \leq A \leq 4$] and intermediate mass fragments IMFs[$5 \leq A \leq 65$] calculated in the reaction Au(35 AMeV)+Au at $b/b_{max} = 0.55$. We find that MST method is able to generate the fragments out of the participant zone only as indicated by peak at $(y/y_{beam})_{c.m.} = 0$. Here 'y_{beam}' is the rapidity of projectile beam in the center-of-mass frame. It fails to explain the fragment yield away from the midrapidity zone. Using the *SACA (2.1)* method one obtains, however, significant contribution from spectator-like remnants. The emission of LCPs and IMFs near projectile and target velocities reflects essentially the binary character of collisions, apart from midrapidity source emission. There are observed clearly the two maxima for IMFs that implies that entire system isn't fully equilibrated. It is indicative of non-thermal origin of fragments in peripheral geometries. Dynamical fragment production mechanism is there for participant zone with *quasi-projectile* and *quasi-target* zones also contributing as IMF emission source. Similar fragment production mechanism has been suggested in the experimental study of $^{58}Ni + ^{58}Ni$ collisions at 30 AMeV [34]. There also IMF production was observed due to two different mechanisms namely statistical and dynamical one.

6.4.4 Cluster distribution in 3D-coordinate space

Next, we turn to study the cluster distribution in three-dimensional (3-D) coordinate space obtained using MST and extended *SACA* pictures. Figure 6.12 depicts the 3-D snapshots of single event of Au(35 AMeV) + Au reaction at $b/b_{max} = 0.55$ obtained using these clusterization techniques. In MST picture, free nucleons and LCPs [$2 \leq A \leq 4$] are abundantly scattered in whole space (shown as red hollow spheres) indicating their

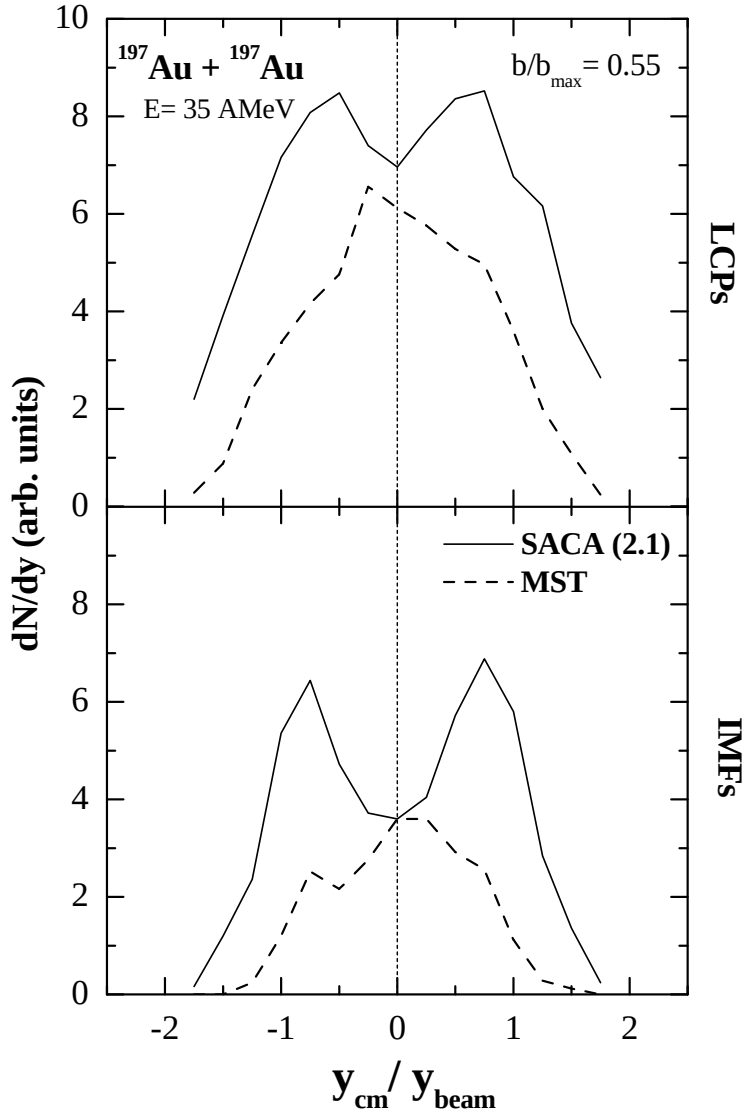

Figure 6.11: The longitudinal rapidity distribution dN/dy of LCPs (top panel) and IMFs (bottom panel) in Au (35 AMeV) + Au collision at a 'reduced' impact parameter of $b/b_{max} = 0.55$. Model calculations are done with MST (dashed curve) and *SACA (2.1)* (solid curve) approaches.

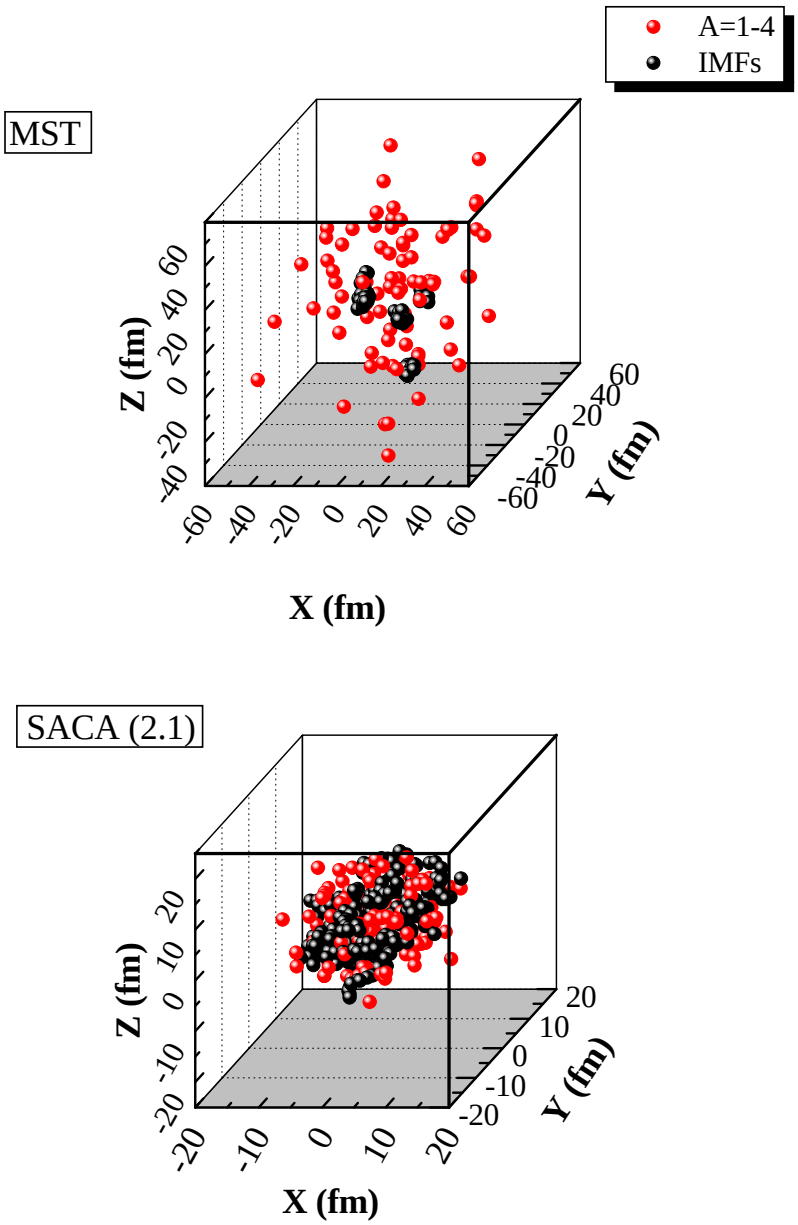

Figure 6.12: 3-D snapshots of single event of Au (35 AMeV) + Au at $b/b_{max} = 0.55$ obtained within MST (top) and *SACA (2.1)* (bottom) pictures. Black spheres represent the nucleon distribution in IMFs and red hollow spheres represent the nucleon distribution in clusters with mass $A = 1 - 4$.

isotropic emission from the participant zone. A very small fraction of nuclear matter is emitted as intermediate mass fragment IMFs [$5 \leq A \leq 65$]. The formation of IMFs is seen to be coming from the overlap region of two colliding nuclei only. On the other hand, significant enhancement in the production of IMFs is evident within *SACA (2.1)* picture. The contribution towards IMFs doesn't seem to come from any specific region or participant zone only, rather spectator zones also contribute significantly. In other words, QMD calculation with *SACA (2.1)* suggests that IMFs originate from 'extended neck' region as well as from the spectator components. The MST approach fails to efficiently break the spectator component and generate sizable number of IMFs. This shows that QMD contains the essential ingredients to describe the excitation energy transfer to spectator region, provided the momentum space information of nucleons is given due importance in cluster recognition algorithms.

6.4.5 Confrontation with Multics-Miniball experimental data

Taking the advantage of the fact that *SACA (2.1)* method is capable of realizing the fragment structure quite earlier on reaction time scale, we compare the model calculations of mean charge of heaviest fragment $\langle Z^{max} \rangle$ using extended SACA version (at 100 fm/c) and MST (at 300 fm/c) for unfiltered events with experimental data [32] taken with combined Multics-Miniball (MM) array. This is a combined array situated at K1200 cyclotron, Michigan State University (MSU) with detection efficiency greater than 87 % of 4π. For the data presented here, events were recorded in forward hemisphere from the decay of *quasi-projectile* [33]. Multics array can detect reactions products with charge $Z \leq 80$ in the angular range $\theta_{lab} = 3^{\circ} - 23^{\circ}$. The MSU Miniball detector, on other hand, is designed for detection of fragments with charge $Z \leq 20$ in the angular range $\theta_{lab} = 23^{\circ} - 160^{\circ}$.

Figure 6.13 shows the calculated $\langle Z^{max} \rangle$ as a function of reduced impact parameter b/b_{max} for the reaction Au(35 AMeV)+ Au. The QMD+MST approach shows inability to break-up spectator matter and overpredicts the mean charge of heaviest fragment $\langle Z^{max} \rangle$ even at 300 fm/c. *SACA (2.1)* method, on other hand, reproduces the experimental $\langle Z^{max} \rangle$ at different peripheral geometries quite satisfactorily. From the point of view of better agreement with experimental data, *SACA (2.1)* turns out to be reliable clusterization algorithm which can be clubbed with molecular dynamics approach such as QMD model. These findings suggest that *SACA (2.1)* method is well suited to investigate early

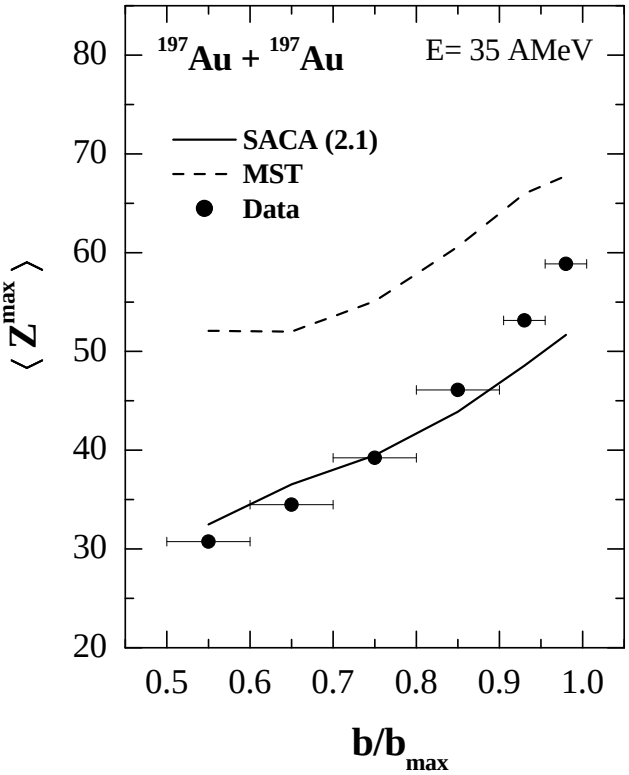

Figure 6.13: The mean charge of heaviest fragment $\langle Z^{max} \rangle$ as a function of reduced impact parameter b/b_{max}. The QMD calculations employing MST (dashed curve) and *SACA (2.1)* (solid curve) approaches are compared with experimental data (filled circles) [32].

dynamics of low energy HI reactions.

6.5 Summary

In this chapter, we have proposed an improvisation over original SACA method by incorporating the microscopic binding energy calculated from the modified Bethe-Weizsäcker (BWM) mass formula. Based on our calculations, we noticed that results obtained with *SACA (2.1)* version doesn't differ much from those obtained with original SACA version. Further, calculated IMFs yields using improved *SACA (2.1)* method reproduce the ALADiN multifragmentation data quite well at relativistic energies. Results obtained with *SACA (2.1)* method are particularly encouraging in describing the Au+Au fragmentation data at 35 AMeV, whereas standard *minimum spanning tree* method completely fails. The SACA approach along with its extension are, therefore, suitable can-

didates to address time scale of fragment formation and predict early dynamics of HI reactions at low and intermediate energies.

Bibliography

[1] R. Donangelo and S. R. Souza, Phys. Rev. C **58**, R2659 (1998).

[2] W. Reisdorf, Nucl. Phys. A **630**, 15 (1998).

[3] L. Shi, P. Danielewicz and R. Lacey, Phys. Rev. C **64**, 034601 (2001).

[4] A. Schüttauf *et al.*, Nucl .Phys. A **607**, 457 (1996).

[5] D. H. E. Gross, L. Satpathy, M. T.-Chung and M. Satpathy, Z. Phys. A **309**, 41 (1982); D. H. E. Gross, Phys. Rep. **53**, 605 (1990); J. P. Bondorf *et al.,* Phys. Rep. **257**, 133 (1996).

[6] J. Hubele *et al.*, Z. Phys. A **340**, 263 (1991).

[7] M. B. Tsang *et al.*, Phys. Rev. Lett. **71**, 1502 (1993).

[8] C. B. Das, A. Das, M. Satpathy and L. Satpathy, Phys. Rev. C **56**, 1444 (1997).

[9] A. Iwamoto, K. Niita, T. Maruyama and T. Maruyama, Rep. Prog. Phys. **98**, 87 (1997).

[10] Y. K. Vermani and R. K. Puri, Europhys. Lett. **85**, 62001 (2009).

[11] J. Singh and R. K. Puri, J. Phys. G: Nucl. Part. Phys. **27**, 2091 (2001).

[12] R. K. Puri, J. Singh and S. Kumar, Pramana J. Phys. **59**, 19 (2002).

[13] P. Möller, J.R. Nix, W.D. Myers and W. Swiatecki, At. Data Nucl. Data Tables **59**, 185 (1995).

[14] H. A. Bethe and R. F. Bacher, Rev. Mod. Phys. **8**, 82 (1936); C. F. von Weizsäcker, Z. Phys. A. **96**, 431 (1935).

[15] K. Heyde, *Basic Ideas and Concepts in Nuclear Physics* (IOP, Bristol, 1999).

[16] C. Samanta and S. Adhikari, Phys. Rev. C **65**, 037301 (2002); C. Samanta and S. Adhikari, Phys. Rev. C **69**, 049804 (2004).

[17] Bożena Nerlo-Pomorska and K. Mazurek, Phys. Rev. C **66**, 064305 (2002).

[18] W. D. Myers and W. J. Świątecki, Nucl. Phys. **81**, 1 (1966).

[19] G. Audi and A. H. Wapstra, Nucl. Phys. A **595**, 409 (1995).

[20] J. Duflo, Nucl. Phys. A **576**, 29 (1994); J. Duflo and A. P. Zuker, Phys. Rev. C **52**, R23 (1995).

[21] J. Barea, A. Frank, J. G. Hirsch, P. Van Isacker, S. Pittel and V. Velázquez, Phys. Rev. C **77**, 041304(R) (2008).

[22] S. R. Souza *et al.*, Phys. Rev. C **67**, 051602(R) (2003).

[23] C. Samanta and D. N. Basu, Mod. Phys. Lett. A **20**, 1605 (2005).

[24] D. N. Basu, P. Roy Chowdhury and C. Samanta, AIP Conf. Proc. **802**, 142 (2005).

[25] Y. K. Vermani, J. K. Dhawan, S. Goyal, R. K. Puri and J. Aichelin, J. Phys. G: Nucl. Part. Phys. **37**, 015105 (2010).

[26] J. Cugnon, T. Mizutani and J. Vandermeulen, Nucl. Phys. A **352**, 505 (1981).

[27] M. Papa, T. Maruyama and A. Bonasera, Phys. Rev. C **64**, 024612 (2001).

[28] M. Begemann-Blaich *et al.*, Phys. Rev. C **48**, 610 (1993).

[29] P. B. Gossiaux, R. K. Puri, Ch. Hartnack and J. Aichelin, Nucl. Phys. A **619**, 379 (1997).

[30] J. K. Dhawan and R. K. Puri, Eur. Phys. J. A **33**, 57 (2007).

[31] K. Hagel *et al.*, Phys. Rev. C **50**, 2017 (1994).

[32] M. D'Agostino and M. Bruno (2010)-private communication.

[33] M. D'Agostino *et al.*, Nucl. Phys. A **650**, 329 (1999).

[34] P. M. Milazzo *et al.*, Phys. Lett. B **509**, 204 (2001).

Chapter 7

On the Nuclear Incompressibility via Au+Au Fragmentation at 35 MeV/nucleon

7.1 Introduction

One of the important goal of heavy-ion (HI) physics is to gain information about the nuclear equation of state (EoS) by modeling interactions among nucleons and nucleon-nucleon scattering. An empirical property that is used to characterize the equation of state of nuclear matter is the nuclear incompressibility '$\mathcal{K}$' which is a measure of the stiffness of nuclear matter in ground state against change in the density ρ [1]. Response of nuclear matter towards external pressure (or, change in the density) can be studied via change in the compression energy stored in cold nuclear matter as shown in Fig. 1. This relationship is what commonly known as equation of state (EoS). For a given nuclear interaction employed, it should be able to reproduce the well-known ground state properties of nuclear matter in ground state *i.e.* binding energy of about -16 MeV/nucleon at $\rho_\circ$=0.17 fm^{-3} [2]. The labels $\boxed{1}$, $\boxed{2}$, & $\boxed{3}$ in the Fig. 7.1 depict the stages arrived during the compression of nuclear matter in heavy-ion collisions. Red arrows in Fig. 7.1 indicate how the total center-of-mass energy per baryon $E_{c.m.}$ is divided into compressional part E_c and thermal part E_{th}. It is worthwhile to see that the curvature of the binding energy is a measure of the stiffness of nuclear matter near the saturation point ($\rho_\circ$,T=0). A larger curvature implies that more energy is needed to compress the nucleus and makes the nuclear matter *stiffer*. The key question is how to measure the density, compression energy E_c and/or temperature reached in such highly excited nuclear matter.

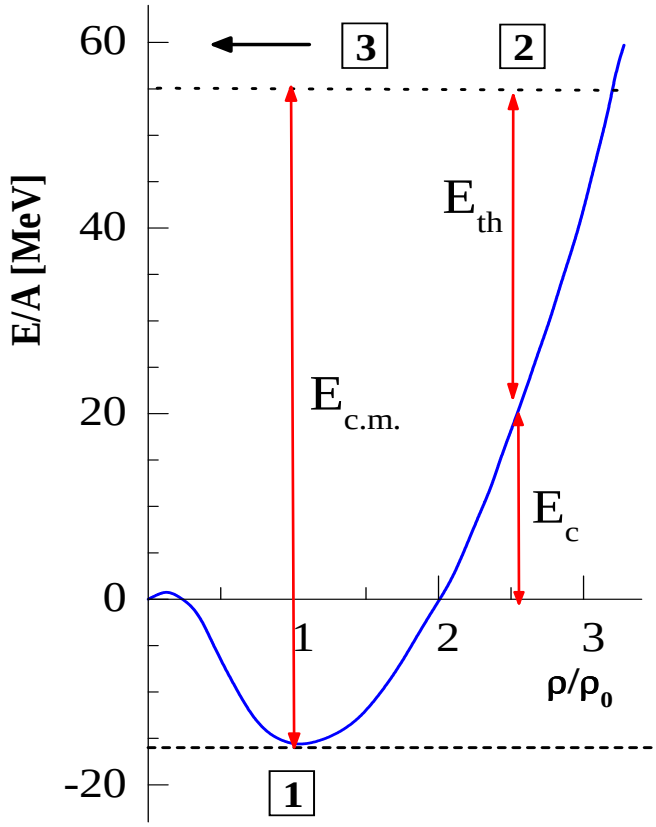

Figure 7.1: A sketch of the nuclear EoS relating the energy per baryon E/A (ρ,T=0) to the density of nuclear matter. The labels [1], [2], and [3] indicate various stages arrived in a reaction.

7.2 Nuclear equation of state and heavy-ion collisions

Earliest attempts to pin down the nuclear EoS (or, incompressibility) were based upon the study of giant monopole resonance (GMR) [3]. The scattering of α-particles off the nucleus induces volume oscillations with L=0, which can be used to determine the incompressibility '$\mathcal{K}$' of that nucleus. These results generally yield incompressibility in the range $\mathcal{K} \sim$ 250-270 MeV indicating the matter to be softer. A recent GMR study in the ^{208}Pb and ^{90}Zn nuclei showed that softening of nuclear matter is needed to explain the collective modes with different neutron-to-proton ratios [4]. Another study on the fusion reported linear momentum transfer to be sensitive to both the EoS and n-n cross

section [5]. Within the *quantum molecular dynamics* (QMD) model, an incompressibility of $\mathcal{K}$=200 MeV (*i.e.* soft EoS) was reported to explain the experimental data on energy transfer in a compound nucleus formation [5].

The study of heavy-ion collisions at intermediate energies can be of importance to probe the compressibility of nuclear matter and/or nuclear EoS. Various attempts have been made to find the observables which are sensitive to the nuclear EoS [6–14]. These microscopic transport models have the convenience to use EoS as input directly and study different quantitative aspects. The main problem in dealing with heavy-ion collisions is that the equilibrium can not be guaranteed always even at later stages of the reaction. The concept of equation of state is, however, valid for the system under equilibrium. This picture is very well realized in neutron stars (NS). In fact, internal structure and composition of neutron stars and supernovae depend strongly on the high density behavior of nuclear EoS.

To find an appropriate nuclear EoS, one should, in principle, develop a many-body theory whose parameters governing n-n interactions should describe the behavior of nucleons in vacuum as well as in bulk nuclear medium. Earlier attempts using realistic n-n interactions could not accurately reproduce the ground state characteristics *i.e.*, binding energy and saturation density $\rho_\circ$ of the nuclear matter [15]. Even higher order correlations were also taken into account to explain the ground state characteristics of normal nuclear matter [16]. The microscopic models like Hartree-Fock theory, VUU and QMD [17–20] use phenomenological parametrization of the nuclear EoS that originates from the Skyrme-type interaction [21]. For the cold and symmetric nuclear matter, the baryonic energy $e(\rho, T=0)$ is given as:

$$e(\rho, T=0) = T_F(\rho, T=0) + \frac{\alpha}{2}\rho + \frac{\beta}{\gamma+1}\rho^\gamma. \tag{7.1}$$

The first term in Eq.(7.1) is the kinetic energy of a non-relativistic cold Fermi gas. Remaining terms constitute the potential energy. In the vicinity of saturation density, the energy density per nucleon $e(\rho, T=0)$ can be expanded around $\rho_\circ$ as:

$$e(\rho, T=0) = e(\rho_\circ, T=0) + \frac{\mathcal{K}}{18}\left(\frac{\rho-\rho_\circ}{\rho_\circ}\right)^2 + - - . \tag{7.2}$$

Clearly from Eq.(7.2), compressibility $\mathcal{K}$ is defined as curvature of $e(\rho, 0)$ versus ρ curve near $\rho_\circ$ *i.e.*

$$\mathcal{K} = 9\rho^2 \left.\frac{\partial^2 e(\rho,0)}{\partial\rho^2}\right|_{\rho=\rho_\circ}. \tag{7.3}$$

For the case of asymmetric nuclear matter at supra-normal densities, different values of nuclear compressibility have been predicted by microscopic approaches such as Brueckner-Hartree-Fock (BHF) [22], Dirac-Brueckner-Hartree-Fock (DBHF) [23] and phenomenological models like NL_3 [24]. This has led to intense focus on constraining the symmetry energy component of nuclear EoS [25, 26] in high density region. The isospin dependence of nuclear EoS finds immense application in understanding the structure of neutron stars (NS) [26]. Unfortunately, due to different density dependence of symmetry energy, it has remained difficult till now to constrain the exact relationship between mass and radius of NS. For instance, BHF calculations give maximum mass of NS close to two solar masses ($=2M_{\odot}$), while DBHF and variational equations predicted slightly higher value $\simeq$ 2.2 - $2.3M_{\odot}$ [25]. Besides this, knowledge of symmetry energy component of the nuclear EoS is important for understanding structure of radioactive nuclei, nuclear reactions with radio-isotopes as well as liquid-gas phase transition in asymmetric nuclear matter [26–30]. For asymmetric nuclear matter with asymmetry $\delta = \frac{\rho_n - \rho_p}{\rho}$, the energy density upto second order expansion is given as:

$$e(\rho, \delta) = e(\rho_{\circ}, 0) + \delta^2 e_{sym}(\rho), \tag{7.4}$$

where $\rho = \rho_n + \rho_p$ is the baryon density with ρ_n and ρ_p denoting neutron and proton densities, respectively. The symmetry energy term e_{sym} is, therefore, defined as:

$$e_{sym}(\rho) = \frac{1}{2} \frac{\partial^2}{\partial \delta^2} (e(\rho, \delta)) \Big|_{\delta=0}. \tag{7.5}$$

To illustrate the effect of isospin content and thus, asymmetry of nuclear matter on equation of state, we display in Fig. 7.2, the energy per baryon for pure neutron matter (upper curve) and symmetric nuclear matter (lower curve). From Eq.(7.4), we can now define e_{sym} for the extreme cases of pure neutron matter and symmetric matter (as shown in Fig. 7.2) as:

$$e_{sym}(\rho) = e(\rho, 1) - e(\rho, 0) \tag{7.6}$$

Frankfurt-Heidelberg-Chandigarh Collaboration has made extensive efforts to investigate observables which are sensitive towards nuclear EoS. Hahn and Stöcker have proposed a thermal model which could reproduce the measured pion multiplicity over incident energy 30 AMeV upto 4 AGeV. In the comparison of thermal energies with experimental values, a surplus of about 60-70 % was found in the experimental data [32]. Their investigation have shown that in-medium effects strongly influence the observables related to

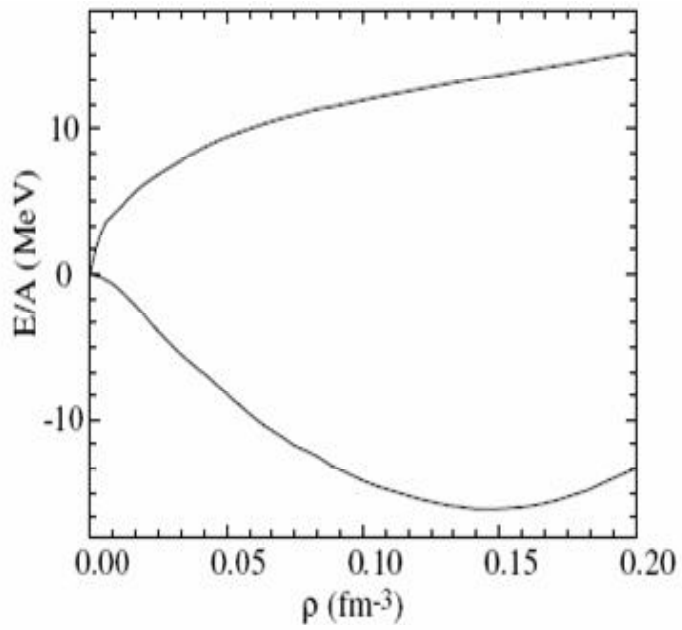

Figure 7.2: Energy per nucleon E/A is shown as a function of nucleon density ρ for pure neutron matter (upper line) and symmetric nuclear matter (lower line). The figure is taken from Ref. [31]).

particle production for instance, π, K, λ yields, and deuteron-to-proton yield ratios *etc* [7, 14, 20, 33]. The collective flow observed in HI collisions is another observable which is very sensitive towards the stiffness of nuclear EoS [7, 8, 10, 11]. The collective transverse in-plane flow and balance energy (the energy at which flow becomes zero) have been studied extensively over the past two decades so as to constrain the EoS, but still the uncertainties are very large. For example, a stiff EoS with $\mathcal{K}$=380 MeV reproduces the transverse flow data equally well as obtained with soft momentum dependent EoS with $\mathcal{K}$=210 MeV [6, 12, 20, 34]. Similarly, comparison of transport model calculations with data of EOS Collaboration for the energy dependence of collective flow favored neither the 'soft' nor the 'hard' equation of state [10]. Another study by Pan and Danielewicz estimated the value of $\mathcal{K}$ in range $\sim$ 160-220 MeV for the multiplicity dependence of sideward flow [34]. In recent comparison of elliptic flow data with microscopic transport model calculations of the Refs. [35, 36], no consistent agreement between data and calculations could be obtained [37] for two different models of Refs. [35] & [36].

It is clear from the above review that an appropriate choice of nuclear equation of state is still far from settlement. The task of deriving quantitative information about the EoS requires detailed comparison of theoretical calculations assuming different equations of

state with experimental data. At lower beam energies, mean-field effects and long range Coulomb force govern the reaction dynamics. The phenomena such as fusion-fission, cluster decay, and deep-inelastic scattering dominate the heavy-ion physics in low energy regime [38–41]. At incident energies above 20 AMeV, non-fusion events like production of intermediate mass fragments (IMFs), projectile-like and target-like fragments (PLFs and TLFs) dominate the exit channel. The phenomenon of multi-fragment emission in low energy domain is, however, least exploited to infer the nuclear EoS. Naturally, the study of fragment-emission in low energy domain may be of importance in probing the nuclear incompressibility, where the role of different n-n cross sections is minimal.

7.3 Au+Au collision as a probe to determine the incompressibility

To explore the possibility of extracting information on the nuclear incompressibility via low energy nuclear collisions, we proposed to study the peripheral reactions of ^{197}Au $+^{197}$Au at 35 AMeV and at different peripheral geometries where accurate data has been measured recently [42]. We shall perform the QMD simulation of Au+Au reactions using a 'soft'(S) and a 'hard'(H) equations of state. Parameters corresponding to the two equations of state employed in the QMD model can be found in chapter 3. If propagating nucleons come too close, these can scatter elastically or inelastically depending upon available center-of-mass energy. The influence of different n-n scattering cross sections (σ_{nn}) will be determined by employing a set of different cross sections varying from energy-dependent cross section [43] to constant and isotropic cross sections of 40 and 55 mb strengths.

For the present study Au+Au with mass A_{tot}=394 is the system of choice. This is because, Au nucleus is nearly the largest drop of nuclear matter that can be created on the earth. Further, it also approximates infinite nuclear matter in some traits; most encompassing of which is the nuclear equation of state. It has been shown previously that for Au+Au system, the balance energy E_{bal} (at which attractive and repulsive parts of nuclear interaction balance each other) has weaker dependence on the impact parameter as well as on the n-n cross section in mass-impact parameter plane [11]. For the lighter systems such as Ar+Sc, the balance energy is found to show little sensitivity towards nuclear incompressibility $\mathcal{K}$ [11]. Magestro *et al* have [11] studied the balance energy

for different values of compressibility: $\mathcal{K}$ =180, 200, 235, and 380 MeV. Their calculations based on the BUU approach showed that only $\mathcal{K}$=200 MeV can explain the data accurately. This value of incompressibility corresponds to *softer* nuclear matter.

7.4 Different nucleon-nucleon cross sections

The choice of different nucleon-nucleon cross sections σ_{nn} tends to influence the reaction observables such as fragment emission [7] and collective transverse expansion [44]. Peilert *et al* had earlier shown that the effective in-medium cross section led to appreciable transparency in the reaction system [7]. One may expect that cross sections have more or less same strength at low incident energies. However, it may not be the case always. A parametrization of the in-medium cross section was proposed based upon Bonn meson exchange potential and Dirac-Brueckner theory for nuclear matter [45]. This cross section is observed to deviate substantially from the energy dependent cross section parameterized by Cugnon [43]. In the following subsections, we shall elaborate various kinds of n-n cross section employed in the QMD approach.

7.4.1 In-medium cross section

It has been shown that medium-dependent cross section strongly affects the reaction observables such as density, temperature [6], fragment and flow variables [46–48]. Not only static properties of hadrons (*e.g.* rest mass) but also the dynamical ones (*e.g.* n-n scattering) differ from the corresponding counterparts in free space. In this direction, Tübingen Collaboration led by Prof. Faessler has extensively studied the in-medium scattering [49] based upon non-relativistic Brueckner theory and Reid soft-core optical potential [50]. Using this approach, mean field, and in-medium total cross section as well as differential n-n cross section are calculated self-consistently in the QMD approach. We call this as self-consistent quantum molecular dynamics model since we now have consistency between mean field and n-n cross section which together govern the dynamical evolution of nucleus-nucleus collisions. The essential ingredient to investigate the microscopic optical potential between two nucleons is the Bethe-Goldstone (BG) equation [49]:

$$G(\omega) = V + V\frac{Q_F}{\omega - H_\circ + \iota\epsilon}G(\omega), \tag{7.7}$$

where V is bare n-n interaction (Reid soft-core interaction, in our case), ω is the starting energy and Q_F is the Pauli operator. To solve the BG equation in momentum space, matrix inversion method proposed by Haftel and Tabakin [51] is employed. Here, we introduce the c.m. momentum $\mathbf{K} = \frac{1}{2}(\mathbf{k}_1 + \mathbf{k}_2)$ and relative momentum $\mathbf{k} = \frac{1}{2}(\mathbf{k}_1 - \mathbf{k}_2)$ of the two nucleons with momenta $\mathbf{k}_1$ and $\mathbf{k}_2$. The Hamiltonian operator $H_\circ$ acting on a two-nucleon state gives:

$$H_\circ|\mathbf{k}_1\mathbf{k}_2\rangle = (\varepsilon(\mathbf{k}_1) + \varepsilon(\mathbf{k}_2))|\mathbf{k}_1\mathbf{k}_2\rangle, \tag{7.8}$$

The single-particle potential $U(\mathbf{k})$ is calculated in a self-consistent manner as:

$$U(\mathbf{k}) = \frac{1}{4}\sum_{spin,isospin} \int_F \frac{d^3\acute{\mathbf{k}}}{(2\pi)^3} \langle \mathbf{k}, \acute{\mathbf{k}}|G(\omega = \epsilon(\mathbf{k}_1) + \epsilon(\mathbf{k}_2))|\mathbf{k}, \acute{\mathbf{k}}\rangle, \tag{7.9}$$

where integration is done over all occupied states in Fermi sea F occupied by two colliding Fermi spheres F_1 and F_2. The numerical calculations of G-matrix is done using standard averaging for Pauli operator and single particle potential in the energy denominator. We, thus obtain decoupled partial wave BG equations:

$$\begin{aligned}\langle \acute{k}|G_{ji}(\omega, \mathbf{K})|k\rangle &= \langle \acute{k}|V_{ji}|k\rangle + \frac{2}{\pi}\sum_l \int dk'' \; k''^2 \langle \acute{k}|V_{jl}|k''\rangle \\ &\times \frac{\bar{Q}_F(k'', \mathbf{K})}{\omega - \bar{E}(k'', \mathbf{K}) + i\epsilon}\langle k''|G_{li}(\omega, \mathbf{K})|k\rangle,\end{aligned} \tag{7.10}$$

where i, j, and l represent partial wave (LSJT) and $\overline{Q}_F$ and $\overline{E}$ are averaged quantities. The differential cross section $\frac{d\sigma}{d\Omega}$ for n-n scattering is calculated as a function of relative momentum $\mathbf{k}$ for two nucleons with $\mathbf{K}$=0. Solution of Eq.(7.10) *i.e.* $\langle k|G_{ji}(\omega = 2\,\varepsilon(\mathbf{k}), \mathbf{K} = 0)|k\rangle$ then corresponds to the partial wave scattering amplitude in the c.m. system. The differential cross section is given by:

$$\frac{d\sigma}{d\Omega} = \frac{1}{4}\sum_{m_s, \acute{m}_s} |T^{S=1}_{\acute{m}_s, m_s}(\theta)|^2 + |T^{S=0}(\theta)|^2, \tag{7.11}$$

with

$$\begin{aligned}T^S_{\acute{m}_s, m_s}(\theta) &= \sum_{L\acute{L}J} \sqrt{\frac{2L+1}{4\pi}} Y^{\acute{L}}_{m_s - \acute{m}_s}(\theta, 0)\langle L0Sm_s|Jm_s\rangle\langle \acute{L}m_s - \acute{m}_s S\acute{m}_s|Jm_s\rangle \\ &\times \langle k, \acute{L}SJ|G|k, LSJ\rangle.\end{aligned} \tag{7.12}$$

Equation (7.12) contains an appropriate combination of T=0 and T=1 parts depending on nn, pp, or pn scattering. As an example, we display the G-matrix cross section

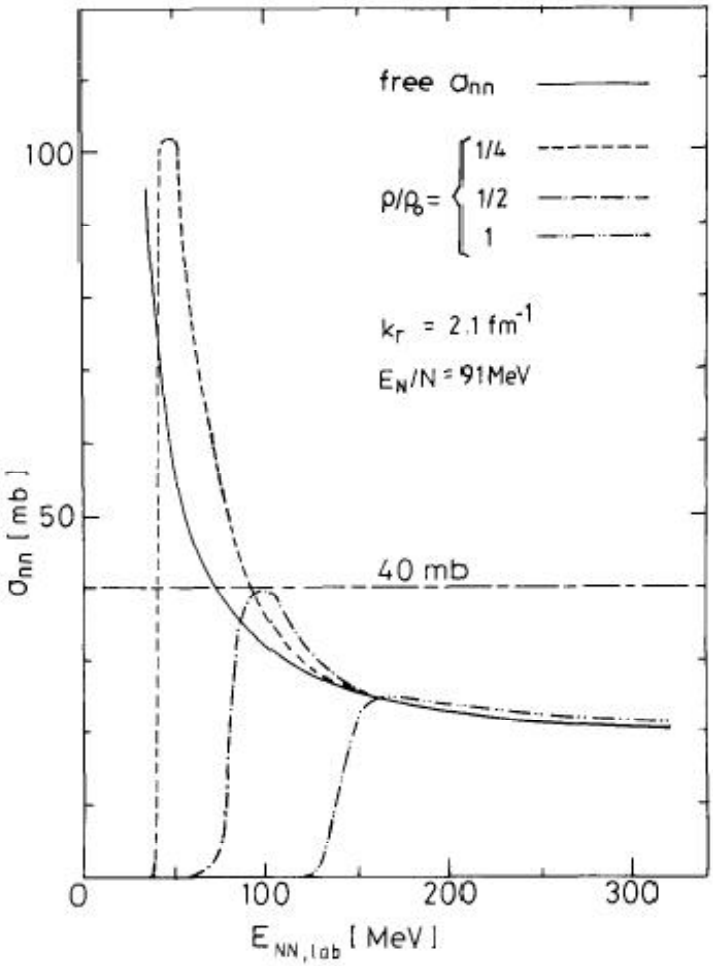

Figure 7.3: The in-medium total cross section σ_{nn} calculated using non-relativistic Brueckner theory as a function of incident energy per nucleon $E_{NN,lab}$ in the laboratory frame (Figure is taken from Ref. [52]).

$\sigma_{nn} = \int \frac{d\sigma}{d\Omega} d\Omega$ in Fig. 7.3 as a function of incident energy $E_{NN,\ lab}$ for the average relativistic momentum per nucleon K_r=2.1 fm^{-1}. Also shown in the figure is free nucleon-nucleon cross section for comparison. At low incident energies, G-matrix cross section drops to zero as expected due to Pauli blocking of final state. A horizontal dashed line represents constant cross section of 40 mb.

7.4.2 Energy-dependent cross section

For energy dependent cross section, parametrization proposed by Cugnon *et al* is employed in the QMD model. In this parametrization, $\triangle$ resonance is included in elastic and inelastic channels. For $\triangle$-excitation channel ($nn \rightarrow n\triangle$), the total inelastic cross-section is calculated as [43]:

$$\begin{cases} \sigma^{in}_{nn\rightarrow n\Delta}(\sqrt{s}) = 0 & ;\ \sqrt{s} \leq 2.015 \\ \qquad\qquad = \frac{20(\sqrt{s}-2.015)^2}{0.015+(\sqrt{s}-2.015)^2} & ;\ \sqrt{s} > 2.015 \\ angular\ distribution: \quad isotropic. \end{cases} \tag{7.13}$$

The cross section for $\triangle$-absorption channel ($n\triangle \rightarrow nn$) can be obtained from Eq. (7.13) with the use of detailed balance principle:

$$\begin{cases} \sigma_{n\Delta\rightarrow nn}(\sqrt{s}) = \frac{1}{8}(p_f^2/p_i^2)\sigma_{nn\rightarrow n\Delta}(\sqrt{s}), \\ angular\ distribution: \quad isotropic. \end{cases} \tag{7.14}$$

Here p_f is the momentum in final n-n state given as:

$$p_f = \frac{[s^2 - 2s(m_1^2+m_2^2) + (m_1^2-m_2^2)^2]^{1/2}}{\sqrt{s}}. \tag{7.15}$$

For elastic channels ($nn \rightarrow nn$, $n\triangle \rightarrow n\triangle$ and $\triangle\triangle \rightarrow \triangle\triangle$), we use the following total and differential cross-sections:

$$\begin{cases} \sigma^{el}_{nn}(\sqrt{s}) & = 55, & ;\ \sqrt{s} \leq 1.8993 \\ & = 20 + \frac{35}{1+100(\sqrt{s}-1.8993)} & ;\ \sqrt{s} > 1.8993 \\ \frac{d\sigma}{dt} = ae^{bt} & & ;\ t = -2p^2(1-cos\theta), \end{cases} \tag{7.16}$$

with $\sqrt{s}$ as n-n center-of-mass energy. $\sigma(\sqrt{s})$ and $\sqrt{s}$ are taken to be in mb and GeV respectively. Parameter b($\sqrt{s}$) is chosen to be:

$$b(\sqrt{s}) = \frac{6[3.65(\sqrt{s}-1.8666)]^6}{1+[3.65(\sqrt{s}-1.66)]^6}. \tag{7.17}$$

Angular distribution has been studied intensively by Puri and Collaborators and no influence of this has been seen on fragment formation and rapidity distribution [53].

7.4.3 Constant and isotropic cross section

The constant and isotropic σ_{nn} of magnitudes 40 and 55 mb have been widely used in the simulation of heavy-ion collisions [54]. The choice of constant cross section of such high values becomes essential in low energy collisions where most of the collisions are Pauli blocked and wavelength of incoming particle is comparable with nuclear size. It is worth interesting to state that a large reaction cross section was reported for the reaction of ^{22}C on a liquid hydrogen target at 40 AMeV. It was significantly larger than corresponding to neighboring ^{19,20}C isotopes [55]. A constant cross section of 40 mb has been motivated by the hard core radius of the nucleon-nucleon potential. Further, a constant cross section of 55 mb corresponds to the cut off value in the Cugnon parametrization for invariant energy $\sqrt{s}$ <1.8993 GeV. It is the only medium effect present in this parametrization based upon free nucleon-nucleon scattering data. As mentioned above, strengths of σ_{nn} obtained from different G-matrix calculations vary considerably. It is, therefore, more useful to employ constant cross sections of 40 and 55 mb strengths to probe the collision of Au+Au at such low energy.

7.5 Results and discussion

7.5.1 Effect of different σ_{nn} on reaction dynamics

As mentioned above, one may not expect different nucleon-nucleon cross sections to have same strength even at lower energy regime. It is, therefore, important to understand the inter-play of different n-n cross sections. We have studied characteristics of fragment emission in peripheral $^{197}Au + ^{197}Au$ collisions at 35 AMeV employing various strengths of n-n cross sections. A hard EoS with energy dependent cross section is labeled as H^{Cg}. Incorporation of isotropic and constant cross sections of 40 and 55 mb strengths have been labeled as H^{40} and H^{55}, respectively. Similarly, for the soft equation of state, we have S^{Cg}, S^{40} and S^{55}, respectively. The phase space, thus obtained was subjected to *SACA(2.1)* clusterization subroutine [56, 57]. In Fig. 7.4, we display the average values of nucleon density ρ^{avg}, nucleon-nucleon collision rate $\mathrm{dN}_{coll}/\mathrm{dt}$, and size of heaviest fragment A^{max} as a function of time. As expected, the choice of different cross sections σ_{nn} has negligible role to play at such a low incident energy. However, n-n collision rates differ appreciably due to medium-dependence of these cross sections. One notices several interesting points

from these results:

(i) Maximal density is obtained nearly at same time at both impact parameters, whereas saturated value is slightly more at more peripheral geometries.

(ii) The choice of different σ_{nn} has negligible effect on present results. This happens due to effective Pauli blocking at such a low incident energy that prohibits binary n-n collisions.

(iii) However, stronger dependence can be seen on the nuclear EoS. This difference is clearly visible in the evolution of heaviest fragment $\langle A^{max} \rangle$.

The mean size of the heaviest fragment $\langle A^{max} \rangle$ reaches minimum value around 100 fm/c, where stable fragment configuration can be realized and compared with experimental results. With stiff EoS, heavier $\langle A^{max} \rangle$ is registered as shown in Fig. 7.4. Significant differences are also visible for the multiplicity of free particles, light charged particles LCPs [$2 \leq A \leq 4$], and clusters with mass $A \geq 5$ obtained using soft and stiff equations of state (See Fig. 7.5). Using the hard EoS, dissipation of energy takes place mainly via emission of free-nucleons that cools down the nuclear system in case of hard EoS. Consequently, lesser yields of LCPs and fragments with mass $A \geq 5$ are obtained with a stiff EoS. On the other hand, soft EoS favors emission of LCPs and heavier fragments ($A \geq 5$) from the spectator zone, thereby decreasing the size of A^{max}. One can, thus, conclude that fragment observables are least affected with the choice of different σ_{nn}. This observation would be helpful to constrain the nuclear EoS. To investigate further the role of different nuclear EoS, we have used standard energy-dependent cross section.

7.5.2 Stopping phenomenon and nuclear EoS

The phenomenon of stopping and equilibration of various fragment species is closely related with n-n interactions used and thus nuclear EoS. We display in Figs. 7.6 and 7.7, the spectrum of scaled transverse (left panel) and longitudinal (right panel) rapidity distributions of free particles and intermediate mass fragments IMFs [$5 \leq A \leq 65$] at 'reduced' impact parameters of b/b_{max}=0.55 and 0.85 respectively.

We find that cluster emission is quite sensitive to nuclear incompressibility that brings significant changes in their stopping as well as transverse expansion. Using a 'stiff' EoS, the system seems to cool-off via abundant production of free nucleons from midrapidity

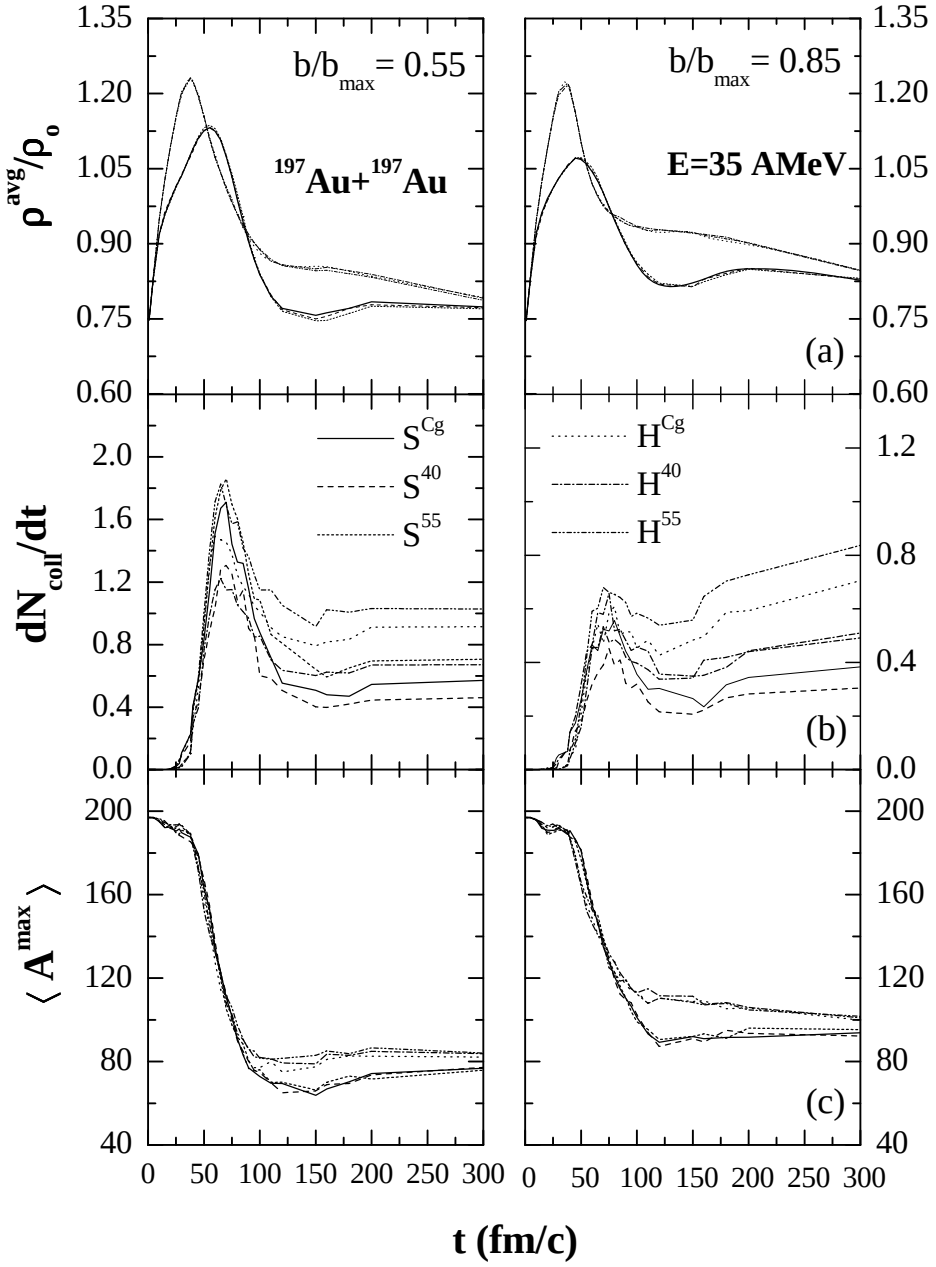

Figure 7.4: QMD simulation of Au (35 AMeV)+Au collisions at reduced impact parameter b/b_{max}=0.55 (left panel) and b/b_{max}=0.85 (right panel) as a function of time for (a) mean nucleon density ρ^{avg}/ρ_o; (b) n-n collision rate $\mathrm{dN}_{coll}/\mathrm{dt}$; (c) size of heaviest fragment A^{max}, respectively.

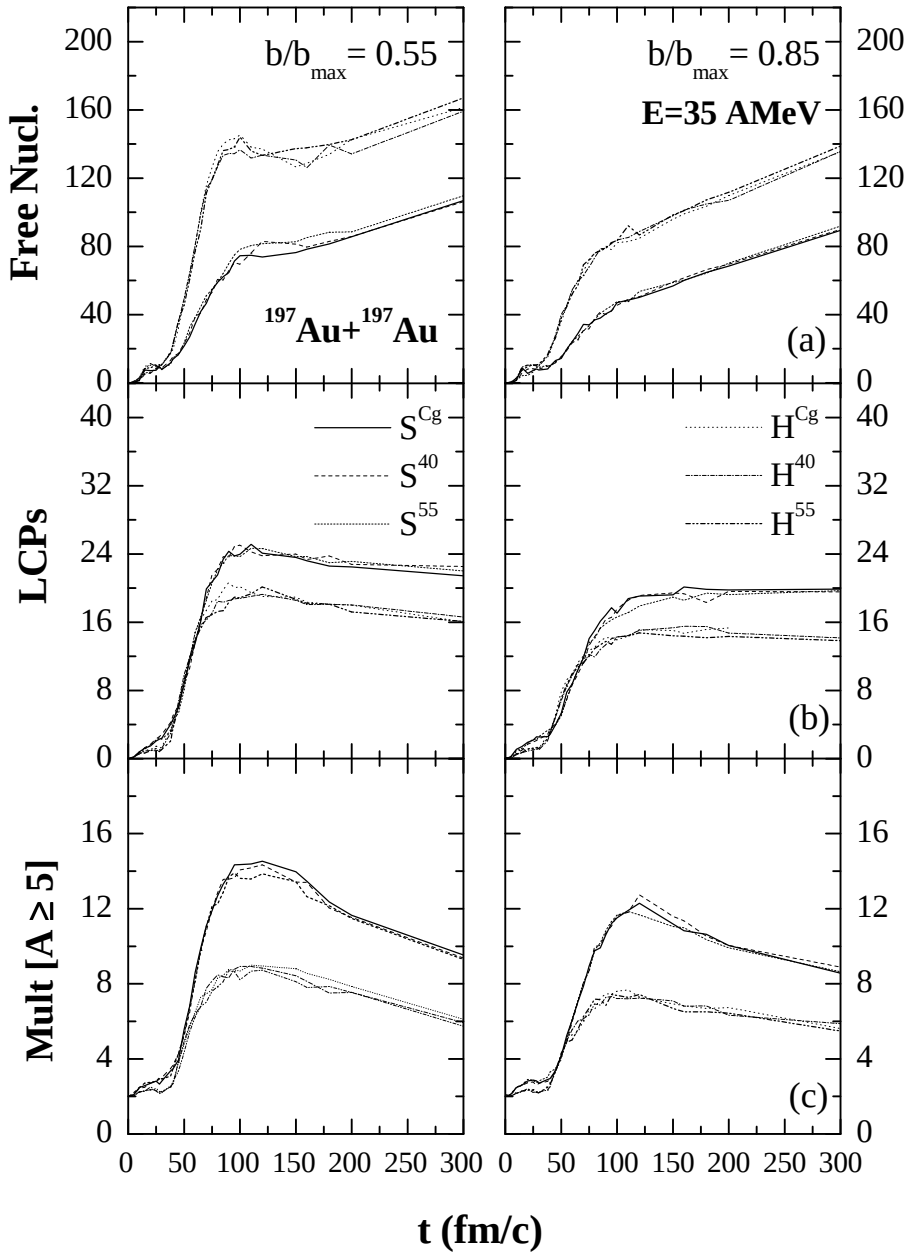

Figure 7.5: QMD simulation of Au (35 AMeV)+Au collisions at reduced impact parameter b/b_{max}=0.55 (left panel) and b/b_{max}=0.85 (right panel) as a function of time for the multiplicities of (a) free nucleons; (b) light charged particles LCPs; (c) fragments with mass $A \geq 5$, respectively.

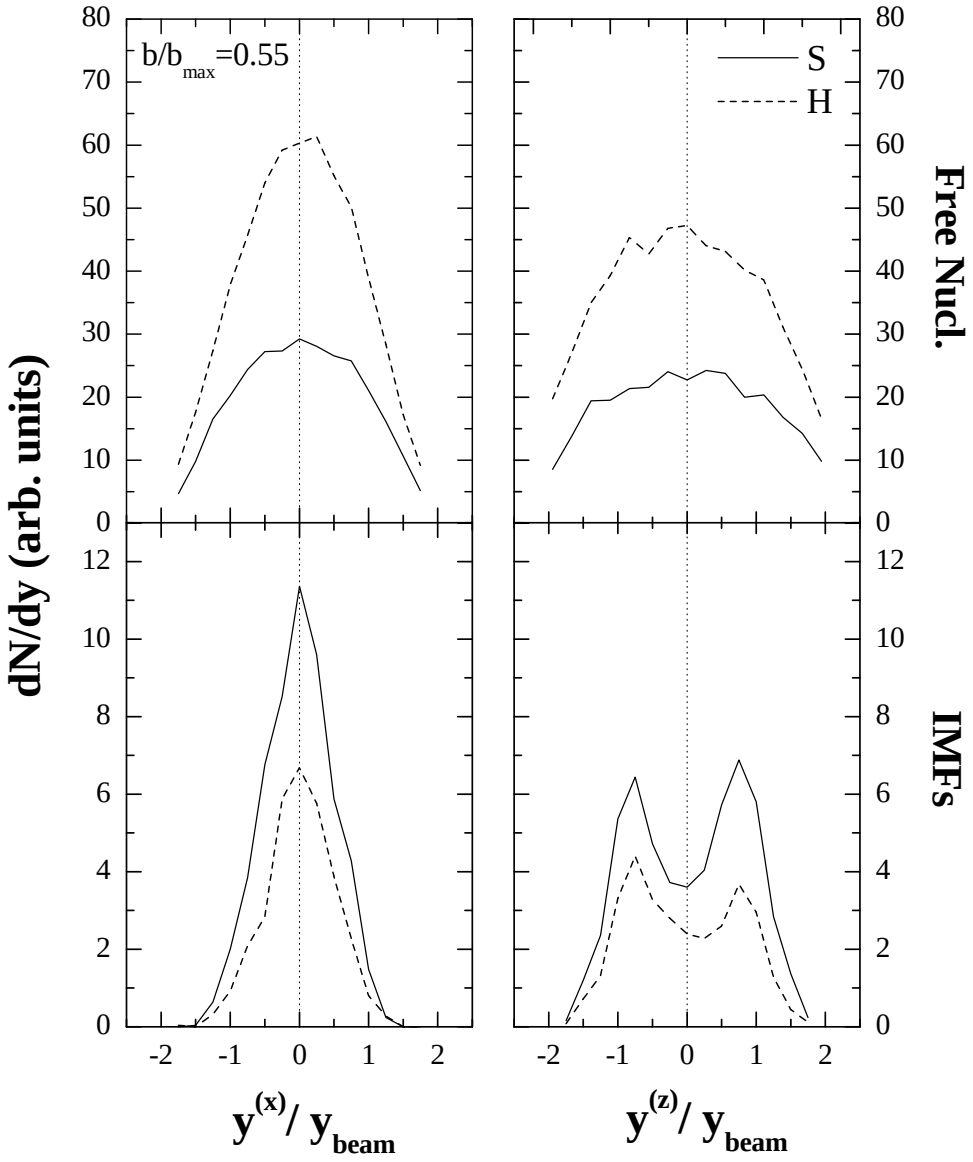

Figure 7.6: The rapidity distribution dN/dy as a function of scaled transverse, $y^{(x)}/y_{beam}$ (left) and longitudinal, $y^{(z)}/y_{beam}$ (right) rapidities for Au(35 AMeV) + Au reaction at reduced impact parameter b/b_{max}=0.55. Solid and dashed curves correspond to model calculations using a 'soft'(S) and a 'hard'(H) EoS, respectively.

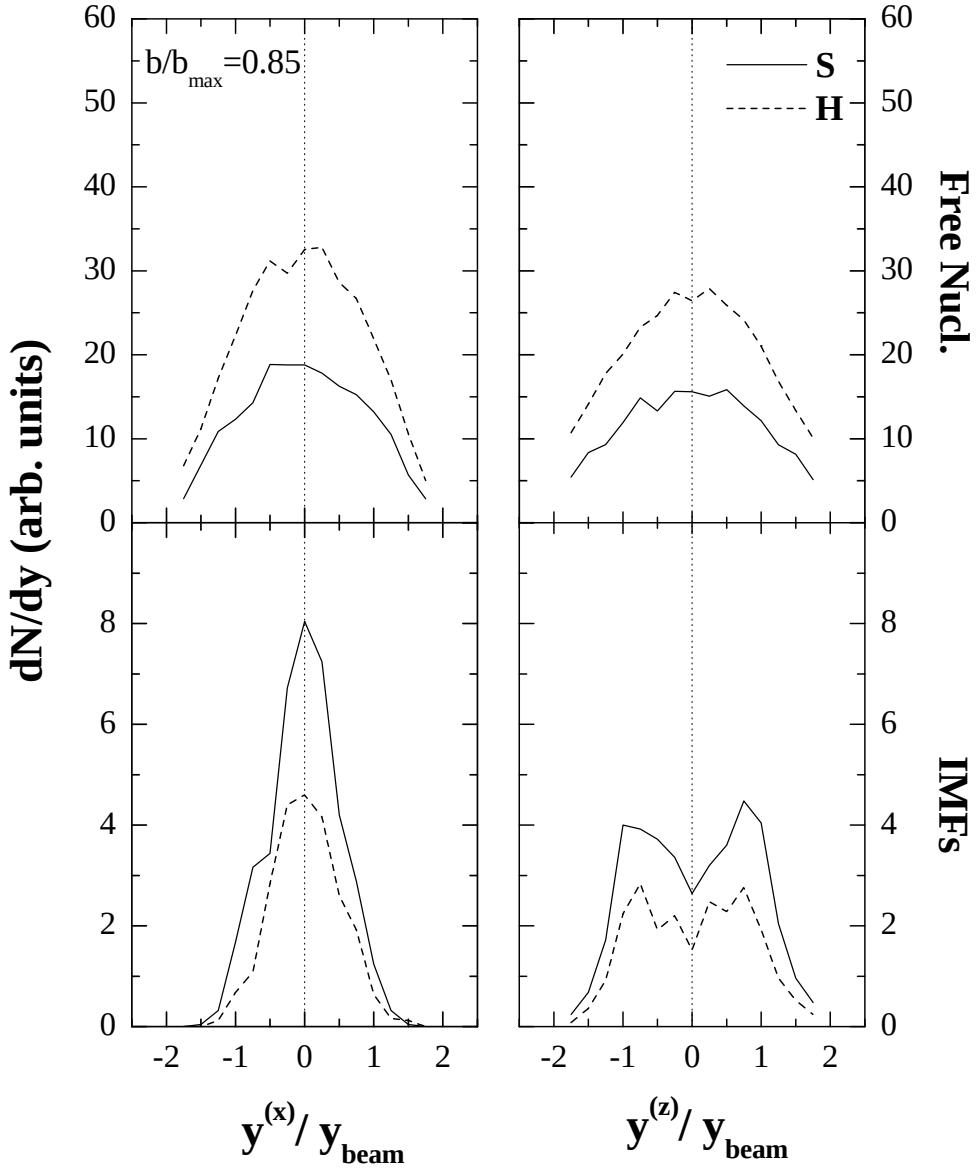

Figure 7.7: Same as Fig. 7.6, but at reduced impact parameter b/b_{max}=0.85.

as well as from spectator zones, whereas a 'soft' EoS contributes significantly towards the emission of IMFs at target and projectile rapidities. It means that system propagating under the soft interactions is less equilibrated. Similar trends are also visible in the transverse rapidity ($y^{(x)}$) distribution of free nucleons and IMFs. Using hard interactions, a larger fraction of free nucleons are emitted into transverse direction. IMFs are not, however, dispersed much into transverse directions and continue to move at target and projectile velocities. As a result, heavier fragments leave the participant zone quite early and suffer less binary collisions. These findings suggest that fragment emission from the decay of spectator component is quite sensitive to the mean field and compressibility of participant nuclear matter.

7.5.3 Fragment charge yields and comparison with experimental data

Next, we turn to estimate the fragment charge yield N(Z) from the spectator matter decay in peripheral Au (35 AMeV)+Au collisions. We shall also attempt to compare our model predictions using soft (S) and hard (H) equations of state with experimental data of Multics-Miniball Collaboration taken at K1200-NSCL cyclotron [42]. Beams of Au ion at E=35 AMeV were accelerated by K1200 cyclotron which were used to bombard Au foils of about 5 mg/cm^2 arial density. The light charged products with charge $Z \leq 20$ were detected in the angular range $23^\circ < \theta_{lab} < 160^\circ$ by the MSU Miniball detector [58]. Reaction products with charge $Z \leq 83$ were detected in the angular range $3^\circ < \theta_{lab} < 23^\circ$ by the Multics array [59]. To account for events from the decay of *quasi-projectile* in forward hemisphere, the charge dispersion at six different impact parameter intervals has been calculated using forward rapidity condition (y $>$ 0.5 y_{beam}) in the center-of-mass frame. Further, it also exclude events from midrapidity and *quasi-target* emission. We can see from Fig. 7.8 that QMD model can reproduce experimental trends in charge distribution quite well at all impact parameter intervals. In the last panel (for $b/b_{max} > 0.95$), two peaks can be seen in experimental charge distribution. As one moves towards semi-peripheral impact parameters, U-shape disappears and slopes of curves become steeper. This also indicates more input of excitation energy into the spectator zone. Further, systematic differences can be seen clearly in the charge distributions obtained with soft (solid line) and hard (dashed line) equations of state. To make the picture more clear and distinguish between the two equations of state, we calculated the integrated multiplicity

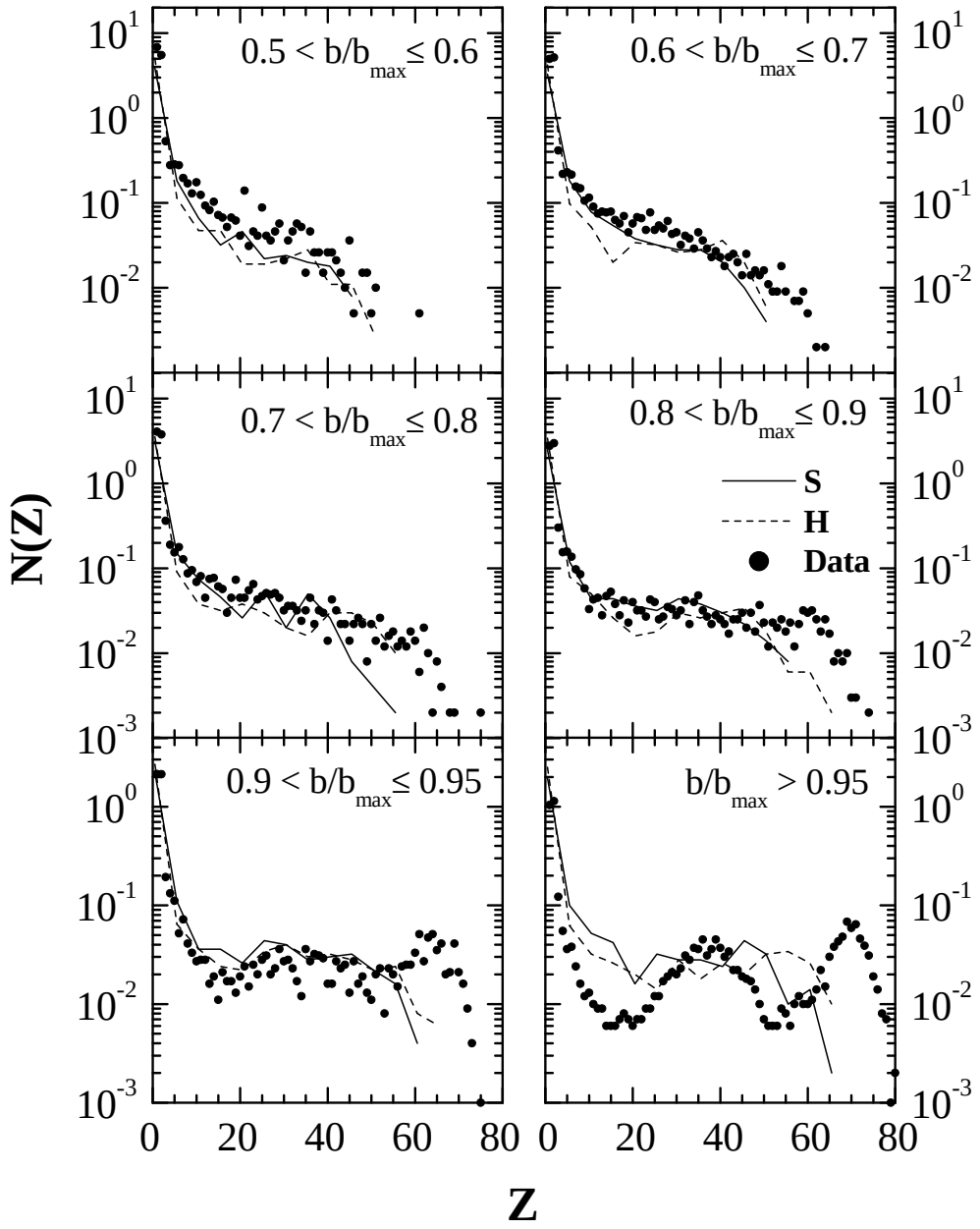

Figure 7.8: The charge distribution N(Z) obtained for Au (35 AMeV)+Au reactions at different impact parameter intervals using a 'soft' (solid line) and a 'hard' (dashed line) EoS. Filled circles depict experimental data points [42].

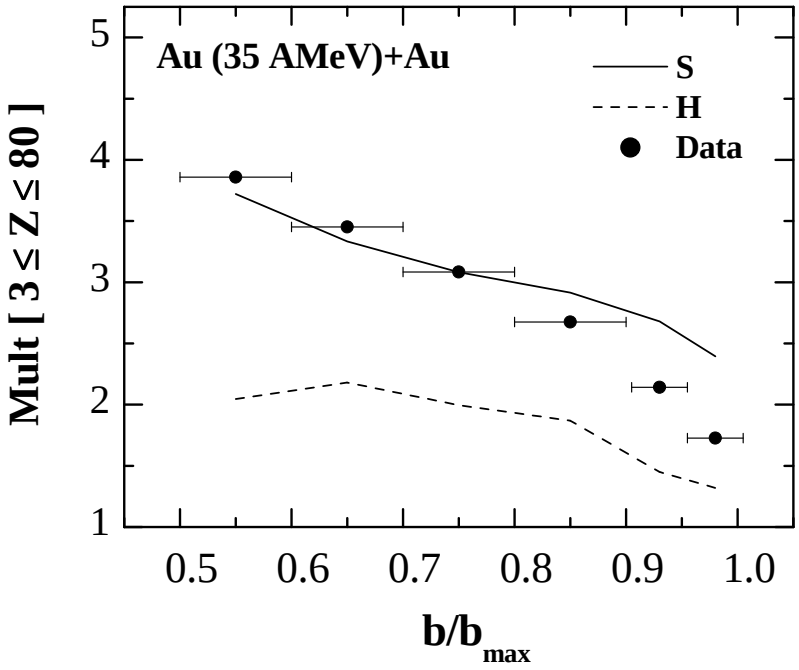

Figure 7.9: The impact parameter dependence of multiplicity of fragments with charge $3 \leq Z \leq 80$ obtained using a 'soft' (solid line) and a 'hard' (dashed line) equations of state in Au(35 AMeV)+Au collisions. Filled circles depict the experimental data points [42].

of charged particles with $3 \leq Z \leq 80$ (*i.e.* $\int_3^{80} N(Z)dZ$) at 100 fm/c as a function of 'reduced' impact parameter b/b_{max}. Calculated multiplicities along with the experimental data points [42] are displayed in Fig. 7.9.

It is worth mentioning that multiplicities were calculated keeping in mind the angular range covered by the combined Multics-Miniball array. A soft incompressibility modulus is observed to explain the impact parameter dependence of charged particle multiplicity obtained from the spectator matter decay much nicely. Due to more explosive nature of hard EoS, spectator matter mainly de-excites via emission of free nucleons and therefore, decline in multiplicity of heavier clusters occurs. An increasing trend of fragment multiplicity with centrality can be understood in terms of more excitation energy deposited in spectator matter. In semi-peripheral events, a larger chunk of excitation energy gets transferred to spectator matter, thereby, leading to rise in multiplicity of fragments with charge $3 \leq Z \leq 80$. A slight discrepancy between fragment charge multiplicity (using a soft EoS) and experimental data at extremely peripheral geometries may be due to lower detection

efficiency of combined Multics-Miniball array when *quasi-projectile* mainly flies off at laboratory angles smaller than minimum detection angle [42, 60]. Nuclear mean-field seems to be important factor governing the outcome of spectator decay, while nucleon-nucleon collisions dominate the participant matter physics. This analysis clearly illustrates the relatively *softer* nature of nuclear matter in accord with previous findings [3, 11].

7.6 Summary

In conclusion, dynamical calculations within the framework of QMD approach are performed to probe the nuclear incompressibility in low energy domain. First of all, we have analyzed the inter-play of different *n-n* cross sections using the soft and hard equations of state in ^{197}Au +^{197}Au collisions at 35 AMeV. The choice of different cross sections has marginal role to play in the reaction dynamics at such low excitation energies. These findings allow us to constrain the nuclear EoS parameter '$\mathcal{K}$' to a very precise level. The stopping of fragments and charge yields obtained from the spectator decay are observed to be highly sensitive towards nuclear incompressibility of the nuclear matter. The hard EoS results in enhanced emission of free nucleons and fewer heavier fragments. Model calculations using soft EoS for charge yields from the decay of *quasi-projectile* are in accord with experimental trends. These findings favor *softer* nature of nuclear matter.

Bibliography

[1] H. Stöcker and W. Greiner, Phys. Rep. **137**, 277 (1986).

[2] C. F. von Weizsäcker, Z. Phys. **96**, 431 (1935); H. A. Bethe and R. F. Bacher, Rev. Mod. Phys. **8**, 82 (1936).

[3] D. H. Youngblood, H. L. Clark and Y. W. Lui, Phys. Rev. Lett **82**, 691 (1999); M. Itoh *et al.*, Nucl. Phys. A **687**, 52 (2001); J. Piekarewicz, Phys. Rev. C **69**, 041301(R) (2004), and references therein.

[4] B. G. Todd-Rutel and J. Piekarewicz, Phys. Rev. Lett. **95**, 122501 (2005).

[5] J. Cibor, J. Łukasik and Z. Majka, Z. Phys. A **348**, 233 (1994); F. Haddad *et al.*, Phys. Rev. C **53**, 1437 (1996).

[6] D. T. Khoa *et al.*, Nucl. Phys. A **619**, 102 (1992); D. T. Khoa, N. Ohtsuka, M. A. Matin, A. Faessler, S. W. Huang, E. Lehmann and R. K. Puri, Nucl. Phys. A **548**, 102 (1992); S. W. Huang *et al.*, Prog. Part. Nucl. Phys. **30**, 105 (1993); G. Batko *et al.*, J. Phys. G: Nucl. Part. Phys. **20**, 461 (1994)

[7] G. Peilert, H. Stöcker, W. Greiner, A. Rosenhauer, A. Bohnet and J. Aichelin, Phys. Rev. C **39**, 1402 (1989).

[8] M. Berenguer *et al.*, J. Phys. G: Nucl. Part. Phys. **18**, 655 (1992).

[9] R. K. Puri *et al.*, Nucl. Phys. A **575**, 733 (1994).

[10] M. D. Partlan *et al.*, Phys. Rev. Lett. **75**, 2100 (1995).

[11] D. J. Magestro, W. Bauer and G. D. Westfall, Phys. Rev. C **62**, 041603(R) (2000).

[12] A. D. Sood and R. K. Puri, Phys. Rev. C **73**, 067602 (2006).

[13] S. Kumar, S. Kumar and R. K. Puri, Phys. Rev. C **78**, 064602 (2008); Y. K. Vermani and R. K. Puri, J. Phys. G: Nucl. Part. Phys. **36**, 105103 (2009).

[14] Y. K. Vermani and R. K. Puri, DAE Symposium on Nuclear Physics **53**, 577 (2008).

[15] B. D. Serot and J. D. Walecka, Adv. Nucl. Phys. **16**, 1 (1986).

[16] B. D. Serot and J. D. Walecka, Int. J. Mod. Phys. E **6**, 515 (1997).

[17] H. Kruse, B. V. Jacak and H. Stöcker, Phys. Rev. Lett. **54**, 289 (1985); H. Kruse, B. V. Jacak, J. J. Molitoris, G. D. Westfall and H. Stöcker, Phys. Rev. C **31**, 1770 (1985).

[18] S. Koonin and J. Randrup, Nucl. Phys. A **474**, 173 (1987).

[19] G. F. Bertsch and S. Das Gupta, Phys. Rep. **160**, 189 (1988); W. Cassing, V. Metag, U. Mosel and K. Niita, Phys. Rep. **188**, 363 (1990).

[20] J. Aichelin, A. Rosenhauer, G. Peilert, H. Stöcker and W. Greiner, Phys. Rev. Lett. **58**, 1926 (1987); C. Gale, G. F. Bertsch and S. Das Gupta, Phys. Rev. C **35**, 1666 (1987); C. Gale, G. M. Welke, M. Prakash, S. J. Lee and S. Das Gupta, Phys. Rev. C **41**, 1545 (1990).

[21] T. H. R. Skyrme, Nucl. Phys. **9**, 615 (1959).

[22] W. Zuo, A. Lejeune, U. Lombardo and J.-F. Mathiot, Nucl. Phys. A **706**, 418 (2002).

[23] E. van Dalen, C. Fuchs and A. Faessler, Nucl. Phys. A **744**, 227 (2004).

[24] G. A. Lalazissis, J. Konig and P. Ring, Phys. Rev. C **55**, 540 (1997).

[25] M. Baldo and C. Maieron, J. Phys. G: Nucl. Part. Phys. **34**, R243 (2007).

[26] B.-A Li, L. W. Chen and C. M. Ko, Phys. Rep. **464**, 113 (2008).

[27] L. W. Chen, C. M. Ko, B.-A Li and G. C. Yong, Front. Phys. China **2**, 327 (2007); Y. Yano, Nucl. Instr. and Meth. B **261**, 1009 (2007).

[28] G. C. Yong, B.-A Li, L. W. Chen and X. C. Zhang, Phys. Rev. C **80**, 044608 (2009).

[29] J. N. De and S. K. Samaddar, Phys. Rev. C **78**, 065204 (2008).

[30] G. Chaudhuri and S. Das Gupta, Phys. Rev. C **80**, 044609 (2009).

[31] B.-A Li, C. M. Ko and W. Bauer, Int. J. Mod. Phys. E **7**, 147 (1998).

[32] K. G. R. Doss *et al.*, Mod. Phys. Lett. A **3**, 849 (1988).

[33] Ch. Hartnack, R. K. Puri, J. Aichelin, J. Konopka, S. A. Bass, H. Stöcker and W. Greiner, Eur. Phys. J A **1**, 151 (1998).

[34] Q. Pan and P. Danielewicz, Phys. Rev. Lett. **70**, 2062 (1993).

[35] A. B. Larionov, W. Cassing, C. Greiner and U. Mosel, Phys. Rev. C **62**, 064611 (2000).

[36] P. Danielewicz, R. Lacey and W.G. Lynch, Science **298**, 1592 (2002).

[37] A. Andronic *et al.*, Phys. Lett. B **612**, 173 (2005).

[38] C. Bhattacharya, S. Bhattacharya and K. Krishan, Phys. Rev. C **49**, 3147 (1994); C. Bhattacharya, S. Bhattacharya and K. Krishan, Phys. Rev. C **54**, 3099 (1996).

[39] Aparajita Dey, C. Bhattacharya, S. Bhattacharya, T. K. Rana, S. Kundu, K. Banerjee, S. Mukhopadhyay, S. R. Banerjee, D. Gupta and R. Saha, Phys. Rev. C **75**, 064606 (2007).

[40] S. Kundu, A. Dey, K. Banerjee, T. K. Rana, S. Muhkopadhayay, D. Gupta, R. Saha, S. Bhattacharya and C. Bhattacharya, Phys. Rev. C **78**, 044601 (2008).

[41] C. Beck *et al.*, Phys. Rev. C **80**, 034604 (2009).

[42] M. D'Agostino *et al.*, Nucl. Phys. A **650**, 329 (1999).

[43] J. Cugnon, T. Mizutani and J. Vandermeulen, Nucl. Phys. A **352**, 505 (1981).

[44] A. D. Sood and R. K. Puri, Phys. Rev. C **70**, 034611 (2004); A. D. Sood and R. K. Puri, Phys. Lett. B **594**, 260 (2004).

[45] G. Q. Li and R. Machleidt, Phys. Rev. C **49**, 566 (1994).

[46] M. D. Cozma and M. Petrovici, Prog. Part. Nucl. Phys. **62**, 419 (2009).

[47] Q. Li, C. Shen and M. Di Toro, Mod. Phys. Lett. A **25**, 669 (2010).

[48] Y. Yuan, Q. Li, Z. Li and F. H. Liu, Phys.Rev.C **81**, 034913 (2010).

[49] A. Bohnet, N. Ohtsuka, J. Aichelin, R. Linden and A. Faessler, Nucl. Phys. A **494**, 349 (1989); N. Ohtsuka, R. Linden, A. Faessler and F. B. Malik, Nucl. Phys. A **465**, 550 (1987); J. Janicke *et al.*, Nucl. Phys. A **536**, 201 (1992).

[50] R. V. Reid, Ann. Phys. **50**, 411 (1968).

[51] M. I. Haftel and F. Tabakin, Nucl. Phys. A **158**, 1 (1970).

[52] A. Fassler, Nucl. Phys. A **495**, 201 (1989).

[53] S. Kumar, R. K. Puri and J. Aichelin, Phys. Rev. C **58**, 1618 (1998); S. Kumar, M. K. Sharma, R. K. Puri, K. P. Singh and I. M. Govil, Phys. Rev. C **58**, 3494 (1998).

[54] J. Singh, S. Kumar and R. K. Puri, Phys. Rev. C **62**, 044617 (2000); A. D. Sood and R. K. Puri, Eur. Phys. J. A **30**, 571 (2006); Int. J. Mod. Phys. E **15**, 899 (2006); R. Chugh and R. K. Puri, Int. J. Mod. Phys. E (2010)-in press.

[55] K. Tanaka *et al.*, Phys. Rev. Lett. **104**, 062701 (2010).

[56] R. K. Puri and J. Aichelin, J. Comput. Phys. **162**, 245 (2000); Y. K. Vermani and R. K. Puri, Europhys. Lett. **85**, 62001 (2009).

[57] Y. K. Vermani, J. K. Dhawan, S. Goyal, R. K. Puri and J. Aichelin, J. Phys. G: Nucl. Part. Phys. **37**, 015105 (2010).

[58] D. Durad *et al.*, Phys. Lett. B **345**, 397 (1995).

[59] R. T. DeSouza *et al.*, Nucl. Instr. Meth. A **295**, 109 (1990).

[60] M. Belkacem *et al.*, Phys. Rev. C **54**, 2435 (1996).

Chapter 8

Stability of Nuclei Propagating with Momentum Dependent Interactions and Multifragmentation

8.1 Introduction

The parametrization of Skyrme interaction described in chapter 3 is an oversimplified prescription. It neglects the exchange effects of nucleon-nucleon (n-n) interaction that gives rise to momentum dependence of nuclear mean field. The idea of momentum dependence of mean field comes from the optical model potential fitted to n-n scattering data. In fact, momentum dependent interactions (MDI) explain the repulsive nature of mean field as demanded by the optical model potential fits. In theory, nuclear potentials based on the Brueckner approach produce an effective mass of a nucleon in the range $m^*/m = 0.6 - 0.7$ due to momentum dependence in low incident energy regime, and $m^* = m$ at higher energies [1]. In the present chapter, we plan to study the role of momentum dependent interactions in fragmentation and finite size effects observed in heavy-ion collisions. However, one is always concerned about the stability of nuclei propagating within momentum dependent interactions. Even a use of cooling procedure via Pauli potential is also reported in the literature [2]. Before one applies the momentum dependent potential to study fragment formation, one should also study the behavior of single computational nuclei propagating with momentum dependent interactions. We shall shed light on this aspect as well and then extend this study to the case of heavy-ion reactions where target and projectile initialized within QMD approach undergo fragment formation. Our calculations are done at final stage of the reaction when nuclear matter

is dilute and cold.

8.2 Importance of momentum dependent potentials

Important aspect related with the study of momentum dependent mean fields is the constrain on nuclear matter compressibility '$\mathcal{K}$' [3, 4]. This interaction along with soft equation of state (EoS) is observed to mimic the *stiff* equation of state. The momentum dependent interactions are reported to lower the value of $\mathcal{K}$ predicting rather a *soft* EoS [3, 5]. Earlier HI experiments indicated that flow angle and transverse momentum distribution of nucleons could be explained assuming a 'stiff' EoS with an incompressibility $\mathcal{K} \sim 400$ MeV [6]. This data is easily explained when momentum dependent interactions (MDI) are properly taken into account in BUU equation along with a '*soft*' EoS [7]. Aichelin and Collaborators have also made extensive study for the influence of momentum dependent interactions on observables in heavy-ion collisions [8–12]. It was shown that the momentum dependence of n-n interaction suppresses the π, κ, λ yields, and results in larger transfer of momentum in transverse direction compared to static soft case [5, 13].

In a similar manner, momentum dependence of G-matrix potential was calculated in Brueckner theory from Reid soft-core potential. Such momentum dependent potential has been used earlier in QMD approach to study reactions of $^{93}Nb + ^{93}Nb$ at 400 AMeV [11]. The G-matrix potential results in increase in transverse momenta quite earlier during the reaction [11]. As a result, smaller central density is reached in nuclear system and lesser stopping of nuclear matter occurs. This many-body approach based on the non-relativistic Brueckner theory [14] is however, not able to reproduce the saturation properties (*i.e.* saturation density and energy) of nuclear matter correctly, when two-body forces are applied [15]. It has been observed that the use of non-relativistic G-matrix theory may not give reliable results regarding the fragment formation as it is only summing the ladder diagrams and not calculating the effective interactions in the nuclear medium [16]. The Skyrme-type effective interactions, however, show reasonable agreement when momentum dependence is taken into account.

At low incident energies, Pauli principle comes into play due to fermionic nature of nuclear matter. In general, Pauli potential which is also a repulsive momentum-dependent potential is employed to mimic the fermionic nature of nuclear matter in ground state. The use of Pauli potential becomes relevant at low incident energies around the Coulomb

barrier where fusion-fission events dominate the scenario [17, 18]. One of the earlier efforts to describe the fermionic nature of nuclei in ground state was made by Wilets and Collaborators [19]. They introduced a momentum dependent repulsive potential consisting of 2-body terms as:

$$V^{Pauli} = V_\circ \left(\frac{\hbar}{q_\circ p_\circ}\right)^3 \sum_{i,j\neq i} exp\left[-\frac{r_{ij}^2}{2q_\circ^2} - \frac{p_{ij}^2}{2p_\circ^2}\right] \delta_{\tau_i,\tau_j}\delta_{\sigma_i,\sigma_j}, \tag{8.1}$$

where $V_\circ > 0$ and r_{ij} and p_{ij} are the distances between points (r_i, p_i) and (r_j, p_j) of the two particles in $\mathcal{R}_3$ and $\mathcal{P}_3$ spaces, respectively. The parameters $q_\circ$ and $p_\circ$ are related to excluded phase space volume that is used to mimic fermionic nature of nuclear system. This form of Pauli potential is though able to reproduce the kinetic energy of free Fermi gas [20], it could not explain the multifragmentation data within the QMD model [2]. Donangelo *et al* have attributed this discrepancy to the overestimated heat capacity due to inclusion of such a repulsive potential [21]. Exact explanation to this failure has not been found yet. Recent calculations by Taruna *et al* [22] also highlighted basic flaws in the use of above form of Pauli potential in the simulation of HI collisions. Their calculations have shown that it fails to reproduce other characteristics of free Fermi gas such as momentum distribution and 2-body correlation function. The simulation of interior neutron star as a cold Fermi gas was performed by García *et al* [23] employing Pauli potential using 500 fermions at density $\rho_\circ$=0.16 fm^{-3} and temperature T=0.1 MeV. Their calculations showed that system has tendency to crystallize, spoiling the uniformity of cold Fermi gas.

At higher incident energies, not only density dependence, but also mean field potential in whole ρ, p-plane *i.e.* $U(\rho, \mathbf{p})$ becomes equally important in the description of reaction mechanism at intermediate energies. Khoa *et al* [10] obtained the sensitivity of temperature and density of the nuclear medium formed in heavy-ion collisions towards momentum dependent potential. The MDI results into smaller central density reached in the nuclear system. Temperature of the nuclear medium is obtained through effective mass m^* which was higher than obtained with static soft case by $50 - 400$ %. These investigations reveal the importance of momentum dependent interactions in the studying the observables related to the heavy-ion collisions. It has been argued recently that momentum dependent potentials are important to account for the non-equilibrium effects and softening of EOS [4, 24]. The role of MDI becomes crucial at peripheral collisions. It is found to enhance the energy of disappearance of flow in central collisions [25], whereas it reduces the energy of disappearance of flow in peripheral collisions [26, 27]. Another study by KaoS Collabora-

tion [4] on anisotropy of in-plane to out-plane proton emission in Bi+Bi collisions showed that momentum dependent mean field characterized by the effective mass of m*/m=0.70 nicely explains the experimental data.

8.3 Momentum dependent interactions (MDI) in QMD model

The mean field potential U^{Sk} used in QMD model is motivated by a local Skyrme interaction [28] which was later on used in Hartree-Fock calculations [29]. In its simplified form, the mean field potential is given by:

$$U^{Sk}(\rho) = \frac{3}{4}t_\circ\rho + \frac{3}{16}t_3\rho^2 + \frac{3}{80}(3t_1 + 5t_2)k_F^2\rho \tag{8.2}$$

Neglecting the momentum dependence, Skyrme interaction gets reduced to a density dependent potential in the limit of infinite nuclear matter limit:

$$U^{Sk} = \alpha\left(\frac{\rho}{\rho_o}\right) + \beta\left(\frac{\rho}{\rho_o}\right)^\gamma. \tag{8.3}$$

In order to parameterize the mean field (8.2) for the momentum dependence, we substitute the term containing k_F^2 with parameterized form of real part of optical proton-nucleus potential [9]:

$$U^{mdi}(\Delta\mathbf{p}) = \delta\ \ell n^2\left[1 + \epsilon\cdot(\Delta\mathbf{p})^2\right]\frac{\rho}{\rho_o}. \tag{8.4}$$

This parametrization could reproduce the energy dependence of experimental data upto 1 AGeV [9, 30, 31]. In Fig. 8.1 is displayed experimental data for optical potential along with phenomenological parametrization of Eq.(8.4) used in QMD approach along with microscopic G-matrix potential. We see that both Skyrme parametrization and G-matrix potential agree with that extracted from experiment. We have used this Skyrme parametrization to simulate the nuclear collisions and study multifragmentation phenomenon. In an infinite nuclear matter limit, generalized n-n potential (Eq.(8.3)) leads to following density and momentum dependent potential (without Coulomb and Yukawa terms):

$$U(\rho,\mathbf{p}) = \alpha\left(\frac{\rho}{\rho_\circ}\right) + \beta\left(\frac{\rho}{\rho_\circ}\right)^\gamma + \delta\ \ell n^2[1 + \epsilon\cdot(\mathbf{\Delta p})^2]\left(\frac{\rho}{\rho_\circ}\right). \tag{8.5}$$

Parameters α, β and γ in Eq.(8.5) have to be re-adjusted in the presence of momentum dependent interactions so as to reproduce the ground state properties of nuclear matter

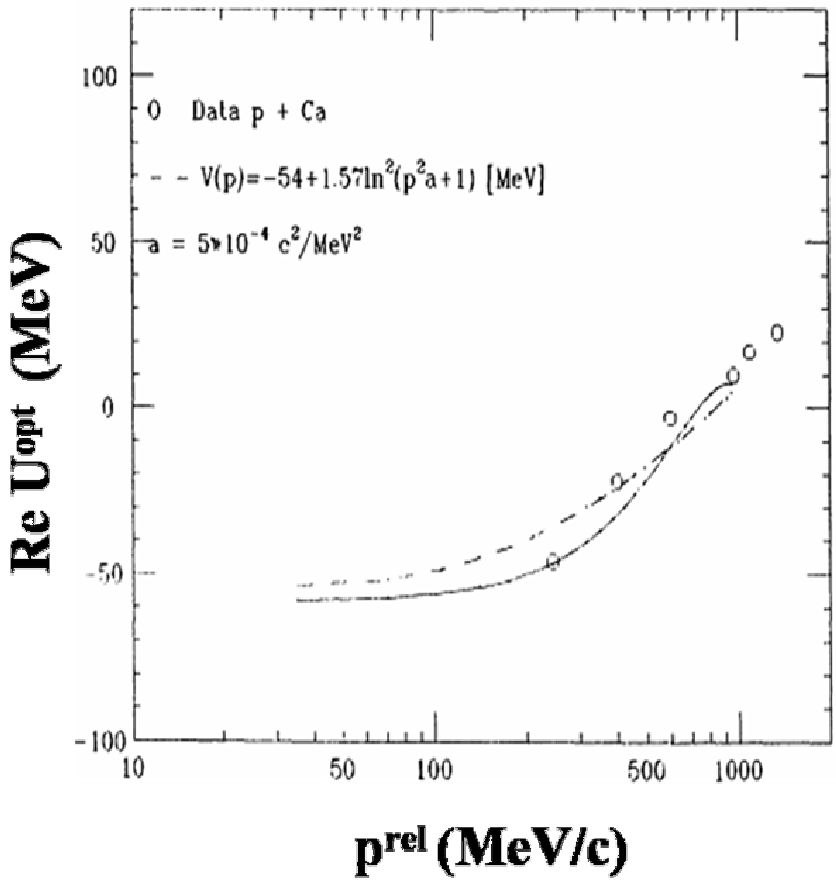

Figure 8.1: The optical potential as a function of the relative momentum between scattered particles. Results obtained for parametrization used in QMD approach (dashed line) and microscopic G-matrix potential (solid line) are compared with experimental data (dots). Figure is taken from the Ref. [11].

Table 8.1: The parameters of momentum dependent potential (Eq. (8.5)) employed in QMD model and the incompressibility values.

EoS	$\mathcal{K}$	α (MeV)	β (MeV)	γ	δ (MeV)	ϵ (c^2/GeV^2)
SM	200	-390.0	320.0	1.14	1.57	500
HM	380	-130.0	59.0	2.09	1.57	500

and same incompressibilities as with their static counterparts. The parameters of momentum dependent potential for soft (SM) and hard (HM) equations of state resulting from the interaction $U^{Sk} + U^{mdi}$ are given in Table 8.1.

Another parametrized form was also suggested by Hartnack and Aichelin [32] which

was based upon extensive experimental analysis of Hama *et al* [31]. Here the bare interaction $V(\triangle \mathbf{p})$ was folded with gaussian wave function. The results were fitted in the QMD model using the formula:

$$U_{12}(\mathbf{p_1} - \mathbf{p_2}) = 0.0667 - \frac{0.0589}{(\mathbf{p}_1 - \mathbf{p}_2)^2 + 0.4837} \tag{8.6}$$

This optical potential is found to be much more repulsive at energies above 400 AMeV. Calculations based on the QMD model simulation showed that kaon yield gets suppressed when using (8.6), however no influence was reported on the pion production and results agree with the older parametrization within statistical errors.

8.4 On the stability of cold QMD nuclei propagating with momentum dependent interactions

To address the question of stability of computational nucleus in the presence of momentum dependent interactions (MDI), we initialize a single cold projectile using soft (S) and soft momentum dependent (SM) equations of state. Earlier theoretical attempts ranging from the giant monopole resonances [33] to the nucleo-synthesis of heavy elements in mergers of neutron stars [34] could be explained if EoS is relatively *softer* than when it is *stiff*. Another study concerning the linear momentum transfer occurring in central HI collisions also showed that a soft compressibility modulus is needed to explain the experimental data [35]. These theoretical and experimental observations motivated us for the choice of comparatively softer EoS. We follow the cluster emission pattern and rms radii of few computational nuclei. Figure 8.2 shows the time evolution of cold QMD nuclei of ^{58}Ni, ^{93}Nb and ^{197}Au initialized with static soft (S) and soft momentum dependent (SM) interactions. The cluster emission is followed for the time span of 200 fm/c. Here, A^{max} denotes the size of residual nucleus. This should be close to that of parent nucleus if there is no destabilization of the nucleus.

The sizes of all the three parent nuclei of ^{58}Ni, ^{93}Nb and ^{197}Au reduce with the inclusion of MDI compared to nuclei propagating with static soft interactions alone. This happens due to an enhanced emission of free nucleons and light charged particles LCPs $[2 \leq A \leq 4]$ with SM interactions. However, medium mass fragments MMFs $[5 \leq A \leq 9]$ and IMFs $\{[5 \leq A \leq A_P/3];\ A_P$ being the mass of projectile$\}$ are almost insensitive towards momentum dependent interactions. Superscript marked as asterisk '*' in the

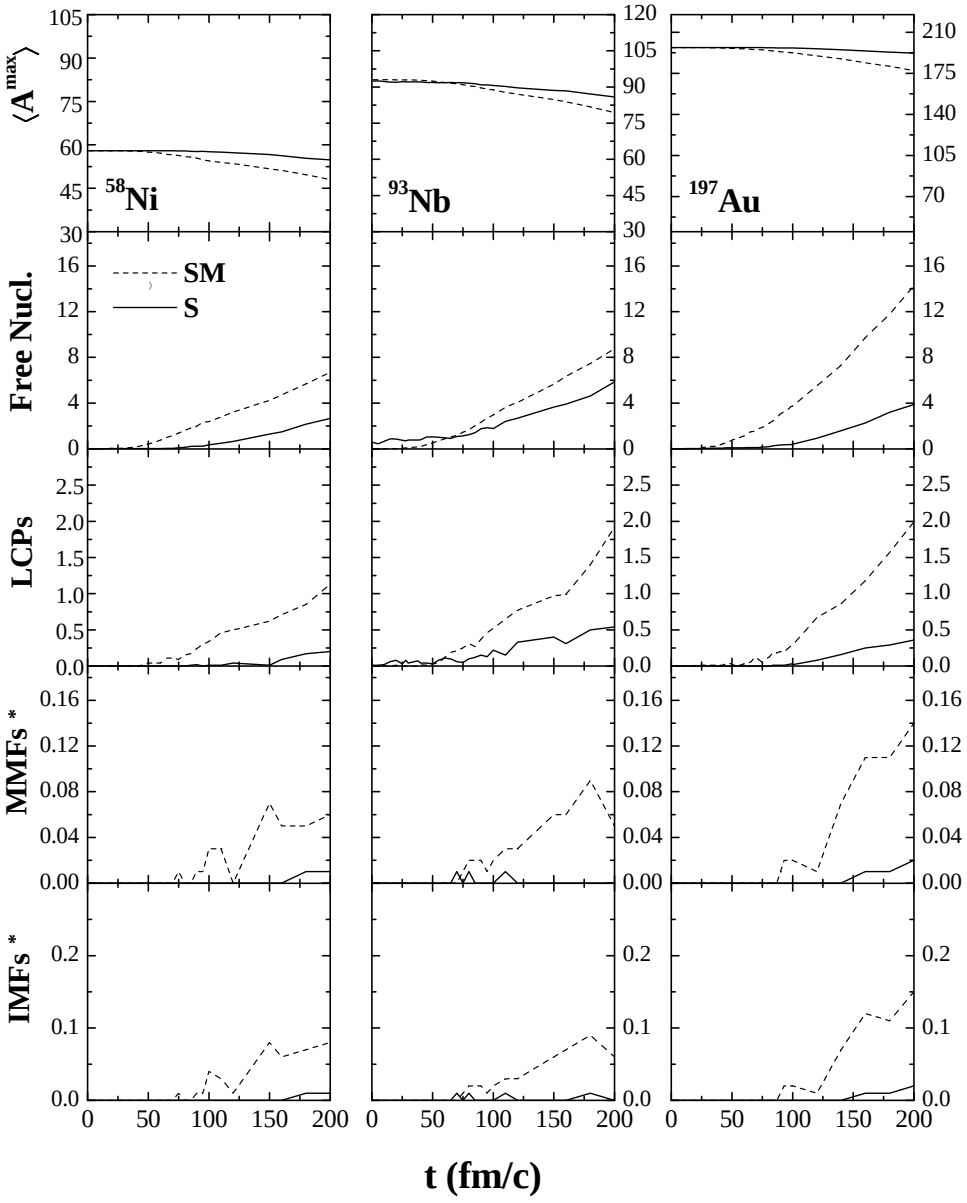

Figure 8.2: The time evolution of heaviest fragment $\langle A^{max} \rangle$, free nucleons, LCPs [$2 \leq A \leq 4$], $MMFs^*$ [$5 \leq A \leq 9$] and $IMFs^*$ [$5 \leq A \leq A_P/3$] (A_P being the mass of projectile nucleus) emitted from a single cold nucleus of ^{58}Ni (left), ^{93}Nb (middle) and ^{197}Au (right). Results obtained with soft (S) equation of state (solid curve) are compared with soft momentum dependent (SM) interactions (dashed curve). The superscript '*' indicates that heaviest fragment has been excluded.

figure indicates that A^{max} has been excluded from the multiplicities of MMFs and IMFs. Only a small fraction is emitted as intermediate mass fragments. It seems that nucleons close in the space are emitted in bulk, therefore, leading to an enhanced emission of light clusters. On the contrary, very few nucleons, LCPs and heavier clusters are emitted when propagating with soft EoS. The enhanced evaporation with MDI is also due to the repulsive nature of these interactions. Does this enhanced emission prohibits one to use MDI for fragmentation ? If one sees carefully, majority of mass that leaves the gold nucleus (for example, with MDI about 19 units are emitted and $\langle A^{max} \rangle$ is close to 177) is in the form of free nucleons. In the above gold nucleus, out of 19 units about 15 are in terms of free nucleons. In other words, we see that nucleons from the surface are emitted and there is no contribution towards emission of intermediate mass fragments. One sees that even with MDI, only 0.15 IMFs are emitted on the average. Realizing that as many as 10-12 IMFs can be seen emitted in Au+Au reactions [36, 37], this number with MDI is negligible.

A survey of time evolution of rms radii of single QMD nuclei also depicts the same picture. Figure 8.3 displays the time evolution of rms radii of ^{58}Ni, ^{93}Nb and ^{197}Au nuclei followed till 200 fm/c, which is also the characteristic time of heavy-ion reactions. The rms radius of nucleus with SM interactions increases gradually compared to that initialized with static soft interactions. This behavior reflects that MDI create additional repulsions among nucleons which leads to enhanced emission of free nucleons. The rms radii of these QMD nuclei in soft case shows negligible deviation for the characteristic time of HI collision. As discussed above, this enhanced radius is due to the emission of free nucleons and not due to the IMFs. Therefore, one can study the fragmentation with MDI since the structure of IMFs is not altered by the inclusion of MDI.

8.5 System size effects and role of momentum dependent interactions in heavy-ion collisions

After conforming the behavior of cold nuclei initialized with momentum dependent interactions, let us study the effect of momentum dependent forces in heavy-ion reactions. In this section, we shall present systematic study of fragment observables *viz.* the time evolution of density and collision rate, rapidity distribution of fragments, multiplicities of various fragments obtained in central and peripheral collisions. We shall also discuss the

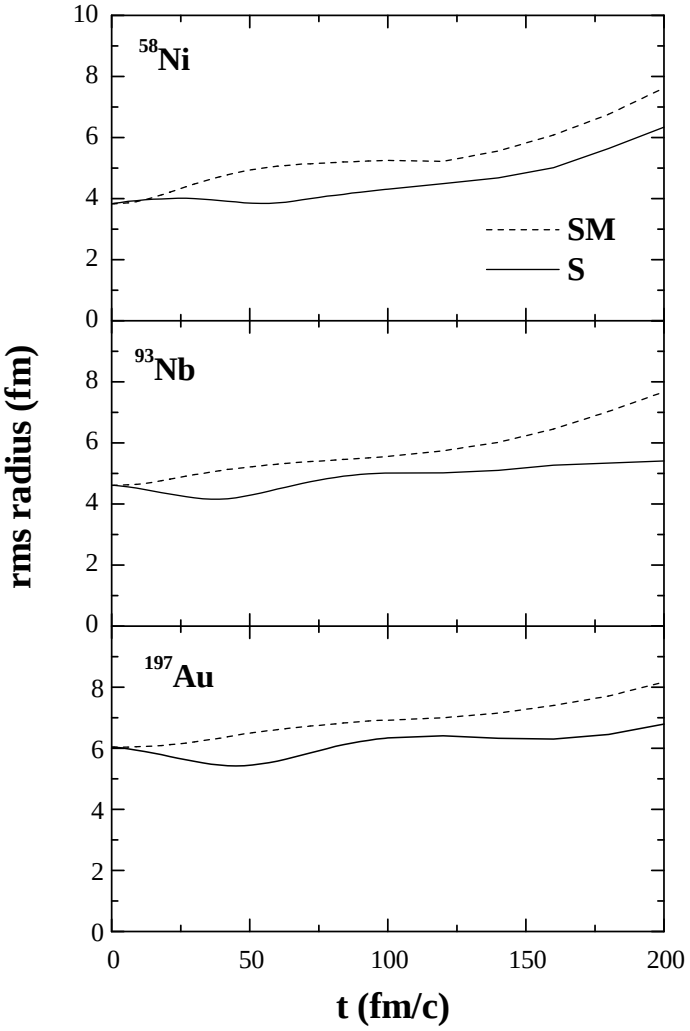

Figure 8.3: The time variation of rms radii of single cold nuclei of ^{58}Ni (top panel), ^{93}Nb (middle panel) and ^{197}Au (bottom panel) using soft (S) equation of state (solid curve) and soft momentum dependent (SM) interactions (dashed curve).

system size effects in the presence of momentum dependent interactions.

8.5.1 The nucleon density and collision rate

One of the observables linked with the compression and expansion of nuclear matter is the density of fragmenting system. The total nuclear matter density is obtained as :

$$\rho^{avg} = \langle \frac{1}{A_T + A_P} \sum_{i=1, j\neq i}^{A_T+A_P} \frac{1}{(2\pi L)^{3/2}} e^{-(\mathbf{r}-\mathbf{r}_i(t))^2/2L} \rangle. \tag{8.7}$$

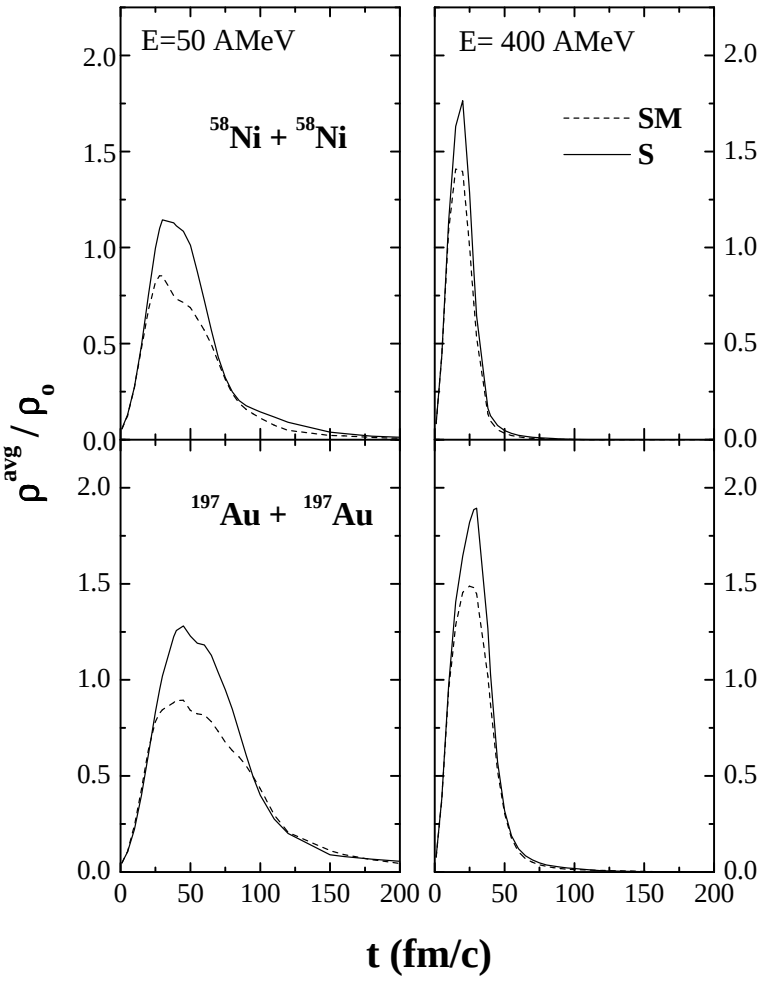

Figure 8.4: The mean central density ρ^{avg}/ρ_o versus reaction time for the central collisions of $^{58}Ni + ^{58}Ni$ (top panel) and $^{197}Au + ^{197}Au$ (bottom panel). The results obtained with soft (S) and soft momentum dependent (SM) interactions are compared at 50 AMeV (left) and 400 AMeV (right).

Here A_T and A_P stand for the target and projectile masses, respectively. In our approach, average nuclear matter density ρ^{avg}/ρ_o is calculated in a sphere of 2 fm radius.

In Fig. 8.4, we display the time evolution of average nucleon density $\rho^{avg}/\rho_\circ$ reached in the central region for the head-on collisions of $^{58}Ni + ^{58}Ni$ and $^{197}Au + ^{197}Au$ at incident energies of 50 and 400 AMeV. The maximal average density tends to reduce with inclusion of momentum dependent interactions. This happens due to additional n-n repulsions created in the system that prohibits compression of nuclear matter to a significant level. This difference in the behavior of ρ^{avg}/ρ_o calculated using S and SM

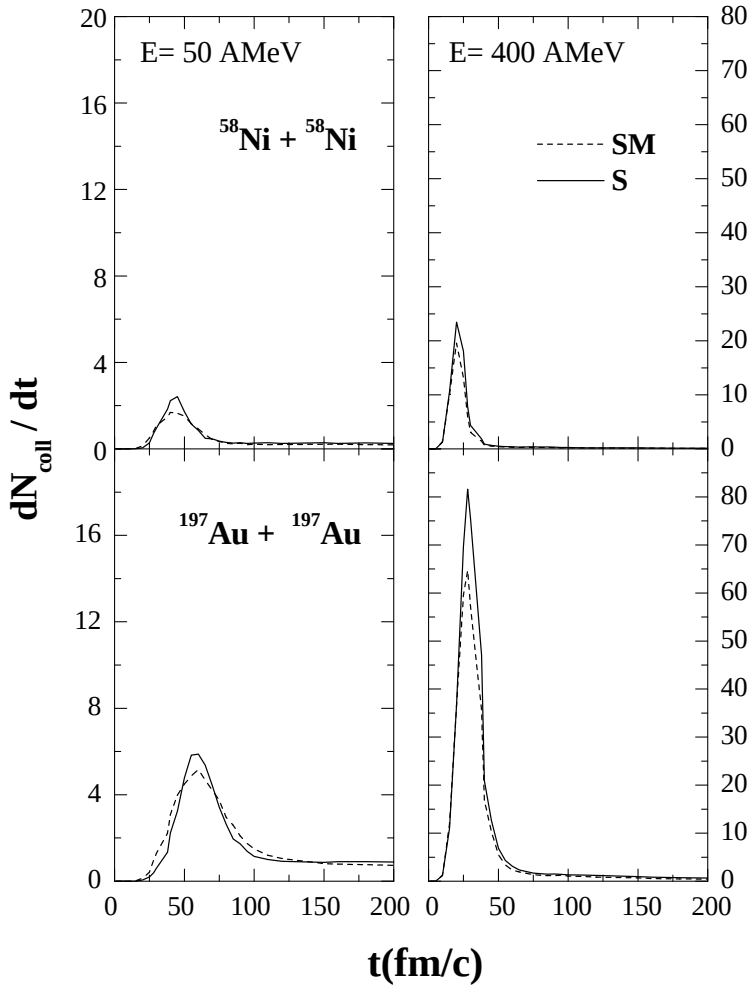

Figure 8.5: The nucleon-nucleon collision rate dN_{coll}/dt versus reaction time for the central collisions of $^{58}Ni +^{58} Ni$ (top panel) and $^{197}Au +^{197} Au$ (bottom panel). The results obtained with soft (S) and soft momentum dependent (SM) interactions are compared at 50 AMeV (left) and 400 AMeV (right).

interactions diminishes at higher incident energies (400 AMeV). This is due to the fact that in central collisions at 400 AMeV, most of the initial *n-n* correlations are already destroyed and matter is already scattered, and therefore, repulsion generated due to MDI does not play any significant role. As a result, we do not see much difference in average central density reached at higher incident energy. Another important quantity related with the initial compression of nuclear matter is the rate of binary collisions.

Figure 8.5 shows similar behavior observed for the *n-n* collision rate dN_{coll}/dt also. Due to additional repulsion created in the nuclear medium by momentum dependent

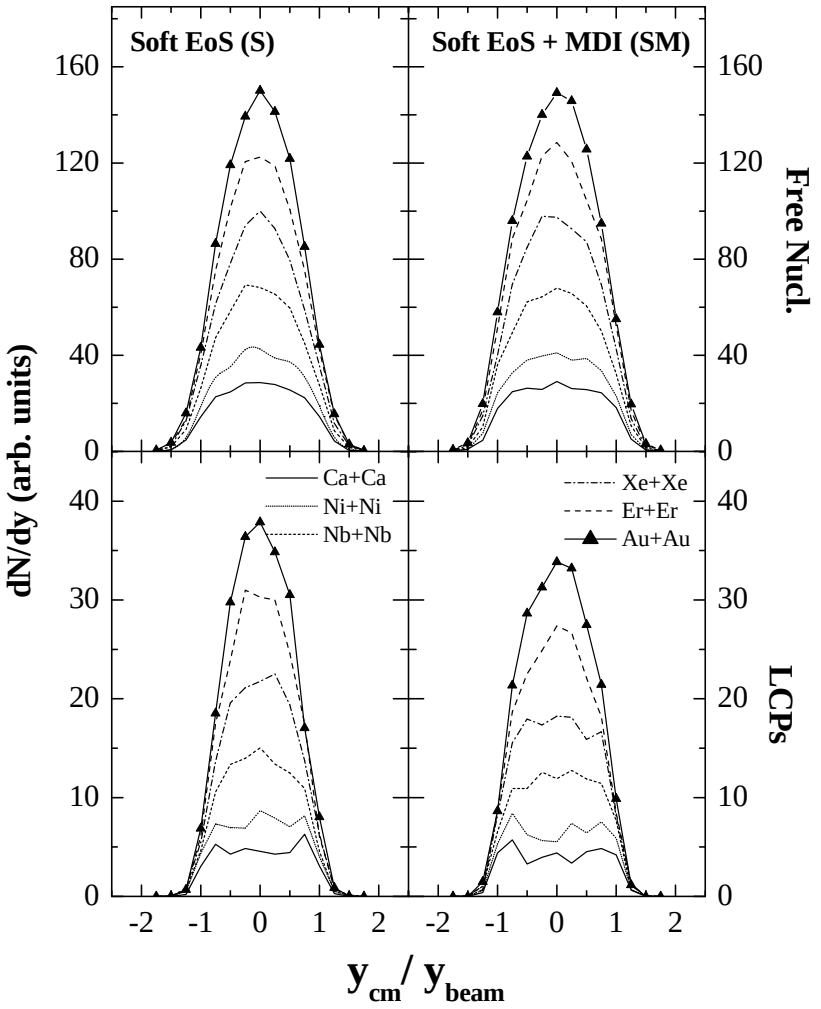

Figure 8.6: The rapidity distribution dN/dy of free nucleons and LCPs [$2 \leq A \leq 4$] as a function of scaled rapidity y_{cm}/y_{beam}; y_{beam} being rapidity of the projectile beam for the head-on collisions at incident energy of 400 AMeV.

forces, the nucleon-nucleon collisions are suppressed. This is clearly indicated by smaller peak collision rate with SM interactions.

8.5.2 Rapidity distribution and transparency effect

The rapidity distribution of fragments is another useful tool to characterize the stopping and thermalization of the nuclear matter. To infer the role of momentum dependent interactions and system size effects, we simulated the central collisions of six symmetric systems $^{40}Ca +^{40} Ca$, $^{58}Ni +^{58} Ni$, $^{93}Nb +^{93} Nb$, $^{131}Xe +^{131} Xe$, $^{168}Er +^{168} Er$ and $^{197}Au +^{197} Au$ at incident energies of 50 and 400 AMeV. We display in Fig. 8.6, the

rapidity distribution dN/dy of free nucleons and LCPs for these symmetric reactions at 400 AMeV. The results shown here are using soft EoS (left panel) and soft EoS including MDI (right panel). The rapidity distribution is more 'isotropic' and nearly full stopping is achieved in heavier systems like Au+Au and Er+Er. In lighter systems, on other hand, a larger fraction of particles is concentrated near target and projectile rapidities resulting into broad gaussian shape. This feature can be seen in both S and SM cases. The lighter systems, therefore, exhibit larger *transparency* effect *i.e.* less stopping. Such features are also observed in the experimental data of FOPI-group [38]. Based on the experimental observations and theoretical trends, one can say that smaller the system, lesser is the stopping. With MDI, a slight increase in the *transparency* effect is seen due to lesser stopping of particles in longitudinal direction. This happens due to the reduction in n-n collisions which deflect the fragments in transverse direction. As a results, one obtains less particles being stopped in longitudinal direction.

8.5.3 Final state fragment multiplicities and system size effects

To infer the role of MDI on fragment emission characteristics and system size effects, we calculate the average size of heaviest fragment A^{max} and multiplicities of various fragments for six reaction systems mentioned above. These reactions were simulated at impact parameters b=0 and b=0.6 b_{max} using S and SM interactions. Figure 8.7 shows the mean size of heaviest fragment A^{max} obtained as a function to total mass of the system A_{tot} at incident energies of 50 and 400 AMeV. It is clear that momentum dependent interactions lead to overall reduction in the size of the heaviest fragment at central and peripheral geometries. Eventually, nuclear matter is emitted as free nucleons or broken down into light charged particles (LCPs) and heavier clusters. To look for the system size effects in the presence of MDI, we display in Figs. 8.8 and 8.9, the 'reduced' multiplicities (*i.e.* multiplicity per nucleon) obtained at central (b=0) and peripheral (b=0.6 b_{max}) geometries. Here we parameterized the multiplicities as a function of total mass of the composite system using a power law of the form: cA_{tot}^{τ}; A_{tot} being the total mass of the system. It is clear from Fig. 8.8 that system size effects are more visible in soft equation of state compared to soft momentum dependent case. A negative slope obtained for the multiplicities of free nucleons, fragments with mass A=2, and LCPs at 50 AMeV indicates their origin from the surface of interacting nuclei. As we move to momentum dependent version, additional break up of n-n correlations leads to

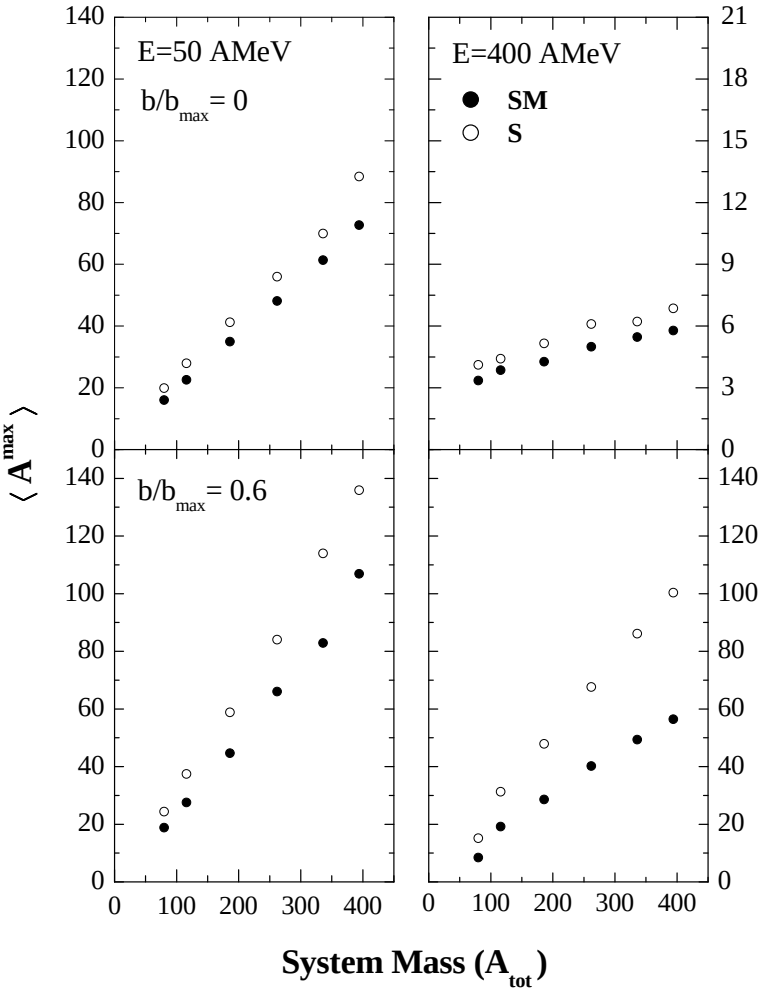

Figure 8.7: The mean size of heaviest fragment $\langle A^{max} \rangle$ vs total mass of the system A_{tot}. Results are shown here for S (open circles) and SM (filled circles) interactions obtained at central (b=0; top panel) and peripheral (b=0.6b_{max}; bottom panel) respectively.

enhanced emission of free nucleons and light charged particles. This reflects the explosive character of momentum dependent interactions. Due to this, multiplicity of $MMFs^*$ $[5 \leq A \leq 9]$ and $IMFs^*$ $[5 \leq A \leq min\{A_P/3, 65\}]$ (excluding largest fragment A^{max}) gets reduced at 400 AMeV, indicating the vanishing of system size effect with MDI. In higher energy regime, cluster production via emission of $MMFs^*$ and $IMFs^*$ is strongly suppressed in the presence of MDI. It is worth mentioning that earlier studies, for example see Ref. [40], also reported the momentum dependent potential to be more repulsive for high momentum nucleons. This leads to enhanced emission of free nucleons and LCPs. A similar enhancement of the nucleons emission and light cluster production was predicted on inclusion of momentum dependent effective interactions in the isoscalar

nuclear potential and symmetry potential [39, 40]. Contrary to this, with static soft equation of state, the production probability of MMFs and IMFs scale with the system size as power law: cA_{tot}^{τ} with exponent τ close to 3/2. In peripheral collisions also similar trends are visible, however, explosive character of MDI gets reduced. As far as heavier fragments (MMFs and IMFs) are concerned, the role of MDI has just become opposite. Now the spectator matter decay dominates resulting into enhanced production of MMFs and IMFs in the presence of MDI as compared to static soft case. Free nucleons and light charged particles follow the well known trends of emission from the surface region as indicated by negative slopes. However due to peripheral geometry, the impact of collisions is not so large. As a result, a larger chunk of nuclear matter goes as medium mass and intermediate mass fragments only. The vanishing of system size effects is visible even in this case also. Multiplicities of MMFs and IMFs tend to saturate irrespective of the total mass of the system A_{tot}.

8.6 Confrontation with experimental data on IMF multiplicity

Let us now try to confront our calculations with experimental data of ALADiN group [37]. This comparison also bears relevance in view of earlier failure of QMD approach to explain the multifragmentation data [36]. The experimental data is very fascinating because there has been observed a *rise and fall* in the multiplicity of intermediate mass fragments with impact parameter [37]. However universality is observed with respect to target mass and bombarding energies exceeding 400 AMeV. In Fig. 8.10, we display the multiplicity of intermediate mass fragments as a function of impact parameter using soft (S) and soft momentum dependent (SM) equations of state. We see that entire spectrum with projectile beam energy ranging from 400 AMeV (top) to 1000 AMeV (bottom) is very well reproduced within the soft momentum dependent interactions. Our model calculations using MDI are in exceptional agreement with experimental IMF multiplicity particularly at peripheral geometries. One should also keep in the mind that for central impact parameters, different experimental groups like FOPI [41], ALADiN [36, 37] and Miniball [36] differ significantly in the multiplicities of IMFs. Overall, we see a clear need of momentum dependent interactions in heavy-ion collisions.

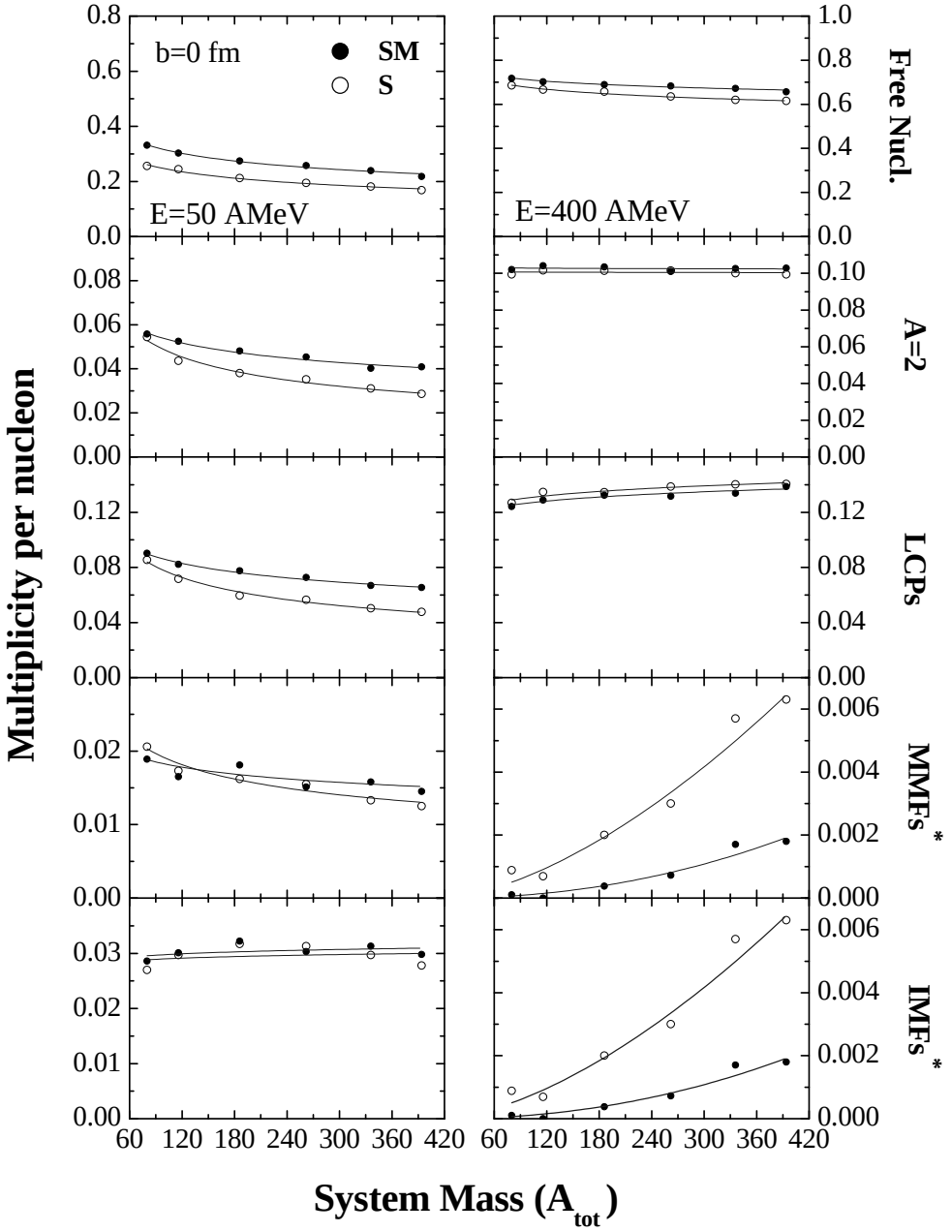

Figure 8.8: The final state scaled multiplicity (calculated at 200 fm/c) of free nucleons, fragments with mass A=2, LCPs [$2 \leq A \leq 4$], $MMFs^*$ [$5 \leq A \leq 9$] and $IMFs^*$ [$5 \leq A \leq min\{A_P/3, 65\}$] as a function of total mass of the system A_{tot}. Results shown here are at incident energies of 50 AMeV (l.h.s) and 400 AMeV (r.h.s). Open circles depict the calculations with soft (S) interaction while solid circles are for soft momentum dependent (SM) interactions. The superscript '*' means that heaviest fragment has been excluded.

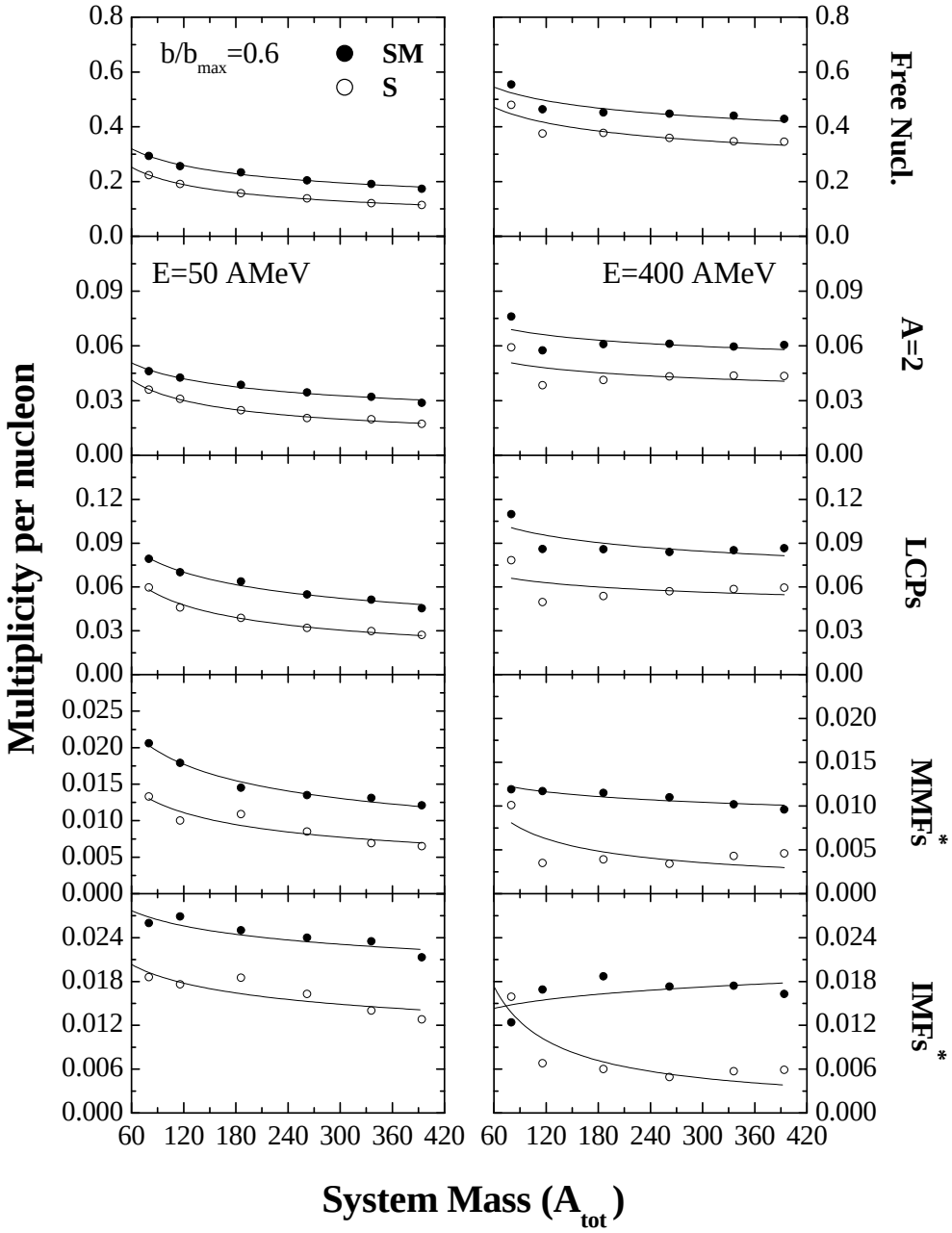

Figure 8.9: Same as Fig. 8.8, but at b/b_{max} =0.6.

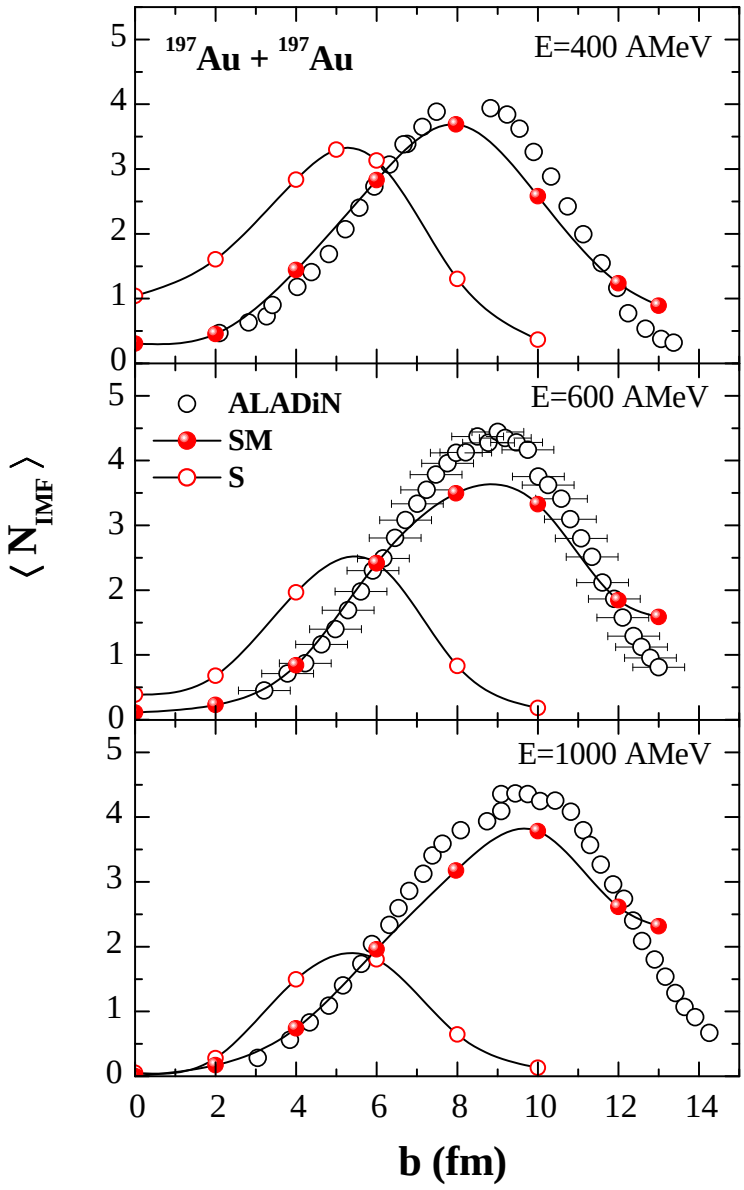

Figure 8.10: The mean IMF multiplicity $\langle N_{IMF} \rangle$ vs the impact parameter b for the $^{197}Au + ^{197}Au$ reactions. The QMD calculations for the final state IMF multiplicity obtained using soft EoS (S) and soft momentum dependent (SM) EoS are shown. Also shown is the ALADiN experimental data (black, open circles) [37] at incident energies of 400, 600 and 1000 AMeV, respectively for comparison.

8.7 Summary

In this chapter, we have presented systematic study of fragmentation and related observables over wide range of system masses using soft (S) and soft momentum dependent (SM) equations of state. We started with the case of stability of single cold QMD nuclei. Initialization with SM case acts as *destabilizing* factor that leads to enhanced emission of free nucleons, thereby, reducing size of largest fragment A^{max} (*i.e.* parent nucleus). However, nuclei initialized with MDI don't reflect any artificial emission of clusters and remains stable for the characteristic reaction times. In the presence of MDI, lesser stopping is there and '*transparency*' effect dominates the scenario. This feature becomes more pronounced in case of lighter system masses. Momentum dependent forces tend to weaken system size dependence in the fragmentation. In peripheral collisions, explosive nature of momentum dependent potential leads to enhanced emission of IMFs out of spectator zone. This observation is quite encouraging in view of earlier discrepancy where QMD model using static soft equation of state underpredicted the IMF yield measured in ALADiN experiments [36, 37]. This analysis clearly brings out the importance of momentum dependent nuclear equation of state to study the reaction dynamics at intermediate energies.

Bibliography

[1] B. Friedman and V. R. Pandharipande, Phys. Lett. B **100**, 205 (1981).

[2] G. Peilert, H. Stöcker and W. Greiner, Rep. Prog. Phys. **57**, 533 (1994).

[3] T. L. Ainsworth, E. Baron, G. E. Brown, J. Cooperstein and M. Prakash, Nucl. Phys. A **464**, 740 (1987); L. P. Csernai, G. Fai, C. Gale and E. Osnes, Phys. Rev. C **46**, 736 (1992).

[4] T. Gaitanos, C. Fuchs, H. H. Wolter and A. Faessler, Eur. Phys. J. A **12**, 421 (2001); L. Shi, P. Danielewicz and R. Lacey, Phys. Rev. C **64**, 034601 (2001).

[5] J. Aichelin, A. Rosenhauer, G. Peilert, H. Stöcker and W. Greiner, Phys. Rev. Lett. **58**, 1926 (1987).

[6] P. Danielewicz and G. Odyniec, Phys. Lett. B **157**, 146 (1985).

[7] C. Gale, G. F. Bertsch and S. Das Gupta, Phys. Rev. C **35**, 1666 (1987).

[8] J. Aichelin and H. Stöcker, Phys. Lett. B **176**, 14 (1986); A. Rosenhauer, J. Aichelin, H. Stöcker and W. Greiner, J. Phys. (Paris), Colloq. **47**, C4-395 (1986); G. Peilert, H. Stöcker, W. Greiner, A. Rosenhauer, A. Bohnet and J. Aichelin, Phys. Rev. C **39**, 1402 (1989).

[9] J. Aichelin, Phys. Rep. **202**, 233 (1991).

[10] D. T. Khoa, N. Ohtsuka, M. A. Matin, A. Faessler, S. W. Huang, E. Lehmann and R. K. Puri, Nucl. Phys. A **548**, 102 (1992).

[11] J. Jaenicke, J. Aichelin, N. Ohtsuka, R. Linden and A. Faessler, Nucl. Phys. A **536**, 201 (1992).

[12] J. Singh and R. K. Puri, Phys. Lett. B **519**, 46 (2001); J. Singh and R. K. Puri, Phys. Rev. C **65**, 024602 (2002); A. D. Sood and R. K. Puri, Eur. Phys. J. A **30**, 571 (2006).

[13] Ch. Hartnack, R. K. Puri, J. Aichelin, J. Konopka, S. A. Bass, H. Stöcker and W. Greiner, Eur. Phys. J. A **1**, 151 (1998).

[14] K. A. Brueckner, C. A. Levinson and H. M. Mahmoud, Phys. Rev. **95**, 217 (1954); H. A. Bethe, Phys. Rev. **103**, 1352 (1956); J. Goldstone, Proc. R. Soc. London A **239**, 267 (1957).

[15] R. Machleidt, Adv. Nucl. Phys. **19**, 189 (1989).

[16] W. H. Dickhoff, A. Faessler, H. Müther and S. Wu, Nucl. Phys. A **405**, 534 (1983).

[17] N. Wang, Z. Li, X. Wu, J. Tian, Y. X. Zhang and M. Liu, Phys. Rev. C **69**, 034608 (2004).

[18] Y. Jiang, N. Wang, Z. Li and W. Scheid, Phys. Rev. C **81**, 044602 (2010).

[19] L. Wilets, E. M. Henley, M. Kraft and A. D. Mackellar, Nucl. Phys. A **282**, 341 (1977).

[20] G. Peilert *et al.*, Phys. Rev. C **46**, 1457 (1992).

[21] R. Donangleo, H. Schulz, K. Sneppen and S. R. Souza, Phys. Rev. C **50**, R563 (1994).

[22] J. Taruna *et al.*, J. Phys. A: Math. Theor. **41**, 035308 (2008).

[23] M. A. P. García, J. Phys.: Conf. Ser. **66**, 012041 (2007).

[24] C. Fuchs and T. Gaitanos, Nucl. Phys. A **714**, 643 (2003); T. Gaitanos, C. Fuchs and H. H. Wolter, Nucl. Phys. A **741**, 287 (2004).

[25] A. D. Sood and R. K. Puri, Phys. Rev. C **69**, 054612 (2004); Eur. Phys. J A **50**, 571 (2006).

[26] S. Soff, S. A. Bass, Ch. Hartnack, H. Stöcker and W. Greiner, Phys. Rev. C **51**, 3320 (1995).

[27] A. D. Sood and R. K. Puri, Phys. Rev. C **73**, 067602 (2006); R. Chugh and R. K. Puri, Phys. Rev. C (2010)-in press.

[28] T. H. R. Skyrme, Nucl. Phys. **9**, 615 (1959).

[29] D. Vautherin and D. M. Brink, Phys. Rev. C **5**, 626 (1972).

[30] E. D. Cooper, B. C. Clark, R. Kozack, S. Shim, S. Hama, J. I. Johansson, H. S. Sherif, R. L. Mercer and B. D. Serot, Phys. Rev. C **36**, 2170 (1987).

[31] S. Hama, B. C. Clark, E. D. Cooper, H. S. Sherif and R. L. Mercer, Phys. Rev. C **41**, 2737 (1990).

[32] Ch. Hartnack and J. Aichelin, Phys. Rev. C **49**, 2801 (1994).

[33] M. Itoh *et al.*, Nucl. Phys. A **687**, 52 (2001).

[34] S. Rosswog *et al.*, Astron. Astrophys. **341**, 499 (1999).

[35] J. Cibor, J. Łukasik and Z. Majka, Z. Phys. A **348**, 233 (1994); F. Haddad, J. B. Natowitz, B. Jouault, V. de la Mota, G. Royer and F. Sébille, Phys. Rev. C **53**, 1437 (1996).

[36] M. B. Tsang *et al.*, Phys. Rev. Lett. **71**, 1502 (1993); G. F. Peaslee *et al.*, Phys. Rev. C **49**, R2271 (1994); M. Begemann-Blaich *et al.*, Phys. Rev. C **48**, 610 (1993).

[37] A. Schüttauf *et al.*, Nucl. Phys. A **607**, 457 (1996).

[38] G. S. Wang, in *Proceedings of International Research Workshop, Poiana Brasov, Romania, October, 1996*, edited by M. Petrovici, A. Sandulescu, D. Pelte, H. Stöcker and J. Randrup, (World Scientific, Singapore, 1997), p. 182.

[39] V. Greco, A. Guarnera, M. Colonna and M. Di Toro, Phys. Rev. C **59**, 810 (1999).

[40] L. W. Chen, C. M. Ko and B.-A. Li, Phys. Rev. C **69**, 054606 (2004).

[41] W. Reisdorf *et al.*, Nucl. Phys. A **612**, 493 (1997).

Chapter 9

Entropy, Light Cluster Production and Thermalization in Heavy-Ion Collisions

9.1 Introduction

Various experimental and theoretical studies in the recent past have indicated a clear demarcation of colliding matter into participant and spectator zones especially at relativistic bombarding energies [1–4]. This is characterized by the formation of hot & dense fireball and relatively cold spectator zones. In earlier chapters, we have discussed, in detail, the characteristics of spectator matter fragmentation and universality behavior observed in the emission of intermediate mass fragments. Highly dense fireball is, however, formed for a very short duration ($< 10^{-22}s$) where temperature reached can be as high as 70-80 AMeV depending upon colliding geometry and bombarding energy. The bulk condition of thermal equilibrium may not be fully attained except for central collisions. This is partly because of rapid evolution of reaction from hot and dense excited zone to expansion and cooling thereafter. In addition, participant volume is also linked with the emission of composite particles and ultimately with the mechanism of the production of entropy [5–10]. Entropy produced in HI reactions is one of the thermodynamic observables that preserves the signature of violent phase of the reactions. Based upon hydrodynamics, it has been argued that at certain freeze-out time, the phase space density stays constant and entropy determines the abundance of clusters produced. The extraction of entropy from cluster abundances is, therefore, helpful in understanding the EoS of hot and dense nuclear matter. Entropy is observed to decline with increase in the strength of repulsive

forces between baryons, which in turn depend upon maximum compression achieved in the reaction [5, 11].

As a matter of fact, pion production also contributes significantly [12–15] towards the entropy generation at SPS [16, 17] and higher incident energies. At SPS energies (∼160 AGeV fixed target), the pion number increases with beam energy to about ten times the number of the nucleons [17]. There, an increase in the entropy production was observed with beam energy as one moves from AGS energies towards SPS and higher energies [15]. This enhancement may also be conjectured as manifestation of change in the collision dynamics at such high energy [18]. For the incident energy range considered (400-1050 AMeV) in the present work, the inclusion of the pion production is not going to affect the entropy production appreciably [13, 14, 19]. For instance, at SIS energies (upto 2 AGeV), the total number of pions is only 10 % of the nucleons [20].

In the present chapter, we shall address the thermal properties of participant zone via evolution of mean density and temperature reached in central region, the degree of equilibration and modeling composite particle formation. We would also compare cluster distribution in coordinate space and cluster-to-proton yield ratios obtained using soft (S) and soft momentum dependent (SM) equations of state. In the following section, we shall describe the method used to extract the baryonic entropy S_N from the yields of composite particles (*i.e.* $p,\ n,\ d,\ t,\ ^3$He, and α-particles).

9.2 Tracking the entropy

It has been conjectured that entropy information may be obtained from a classical charge symmetric *gas* of nucleons and deuterons in thermal and chemical equilibrium using the relation suggested by Siemens and Kapusta [5, 6]:

$$S_N = 3.945 - \ell n(d/p), \tag{9.1}$$

with d/p as deuteron-to-proton yield ratio established during early stages of fireball formation. One source of error arises due to neglect of other light composite particles *viz.* t, ^{3}He and α-particles. Bertsch and Cugnon [21] proposed to take into account these light clusters as well generalizing Eq.(9.1) as:

$$S_N \ = \ 3.945 - \ell n \tilde{R}_{dp} \tag{9.2}$$

with

$$\begin{aligned} \tilde{R}_{dp} &= d_{like}/p_{like} \\ &= \frac{d + \frac{3}{2}t + \frac{3}{2}\ ^3He + 3\alpha}{p + d + t + 2\ ^3He + 2\alpha}. \end{aligned} \tag{9.3}$$

In the above equation (9.3), denominator term depicts the participant proton multiplicity N_p that solely depends upon the size of the reaction volume. This neglects the contribution coming from low-excitation chunks of spectator matter. As can be seen from Eq.(9.3), $\tilde{R}_{dp}$ is the yield ratio of deuteron-like to proton-like fragments that takes into account these light clusters as well. It has been further established in experiments that highest proton multiplicity accounts for most of the charges in HI system, thus leaving no room for heavier clusters. Since in QMD model, there is no scope of isospin identification of nucleons, we can't distinguish between different isobars such as t and ^3He. For this reason and to compare our model predictions with experimental data, we define the yield ratio of deuteronlike (d_{like}) to protonlike (p_{like}) clusters in the following way [11]:

$$\tilde{R}_{dp} = \frac{Y(N_f = 2) + \frac{3}{2}Y(N_f = 3) + 3Y(N_f = 4)}{N_p}, \tag{9.4}$$

where Y(N_f) stands for the number of fragments with mass 'N_f' in one event. Analogous to experimental results, we calculate the total participant multiplicity N_p as:

$$N_p = \frac{Z_P + Z_T}{A_P + A_T}[Y(N_f = 1) + 2Y(N_f = 2) + 3Y(N_f = 3) + 4Y(N_f = 4)], \tag{9.5}$$

where Z_P+Z_T and A_P+A_T define the total charge and mass of the colliding system, respectively. This procedure allows us to estimate the baryonic entropy produced in a reaction. The phase space of nucleons is clusterized employing *minimum spanning tree* (MST) procedure [22] as discussed in chapter 4.

9.3 Results and discussion

9.3.1 Time evolution of $Nb + Nb$ reactions and thermalization

First of all we analyze the evolution of thermal properties such as average central density ρ^{avg}, local temperature 'T' reached in central zone, and degree of equilibrium for central $^{93}Nb +^{93} Nb$ collisions at bombarding energies of 400 and 650 AMeV. Figure 9.1 (a)-(b) compares the average density and temperature reached in the central region at these

bombarding energies. Temperature 'T' is calculated in the central zone of 2 fm radius using the hot Thomas Fermi formalism for two overlapping Fermi spheres [23]. To find the evolution of temperature at each point $(\mathbf{r}, t)$ in a HI reaction, in addition to nuclear matter densities of target and projectile;

$$\rho_T(\mathbf{r}, t) = \sum_{i=1}^{A_T} \rho_i(\mathbf{r}, t); \qquad \rho_P(\mathbf{r}, t) = \sum_{i=1}^{A_P} \rho_i(\mathbf{r}, t), \tag{9.6}$$

one needs to evaluate kinetic energy densities at this point as:

$$\Gamma_T(\mathbf{r}, t) = \sum_{i=1}^{A_T} \frac{\mathbf{p}_i^2(t)}{2m} \rho_i(\mathbf{r}, t); \qquad \Gamma_P(\mathbf{r}, t) = \sum_{i=1}^{A_P} \frac{\mathbf{p}_i^2(t)}{2m} \rho_i(\mathbf{r}, t). \tag{9.7}$$

These quantities are calculated in QMD simulations in the nucleus-nucleus c.m. frame. These are used then, in a generalized local density approximation to extract the temperature. Further details of this procedure can be found in Ref. [24]. The shaded area in Fig.9.1 corresponds to the time zone for highly excited nuclear matter which is followed by the decompression and cooling phase. With increase in incident energy, more compression and thus higher temperature is attained in the participant zone. Beyond this region, the nucleon density saturates and hard n-n collisions cease almost. In third row, we show the momentum anisotropy ratio $\langle R_{iso} \rangle$ which measures the degree of thermalization achieved by the heavy-ion system. The anisotropy ratio is defined as follows [25]:

$$\langle R_{iso} \rangle = \frac{\sqrt{\langle p_x^2 \rangle} + \sqrt{\langle p_y^2 \rangle}}{2\sqrt{\langle p_z^2 \rangle}}. \tag{9.8}$$

From Fig. 9.1(c), one can see that participant zone is already equilibrated around 40-45 fm/c just after the violent phase is over. One can, therefore, measure yields of composite particles and baryonic entropy at this time. It may be mentioned that full equilibrium with $\langle R_{iso} \rangle \approx 1$ is not possible in HI reactions even for the central geometry. This is due to surface effects that are more pronounced in lighter reaction systems. In the last two panels, we display the evolution of d_{like} and p_{like} cluster abundances. The slight enhancement in these yields at later times is due to de-excitation of and secondary emission from heavier clusters.

9.3.2 Coordinate space distribution of light clusters

Since it is well established that the production of light charged particles and clusters, and ultimately the entropy is related to the fireball, it is of interest to see their distribution

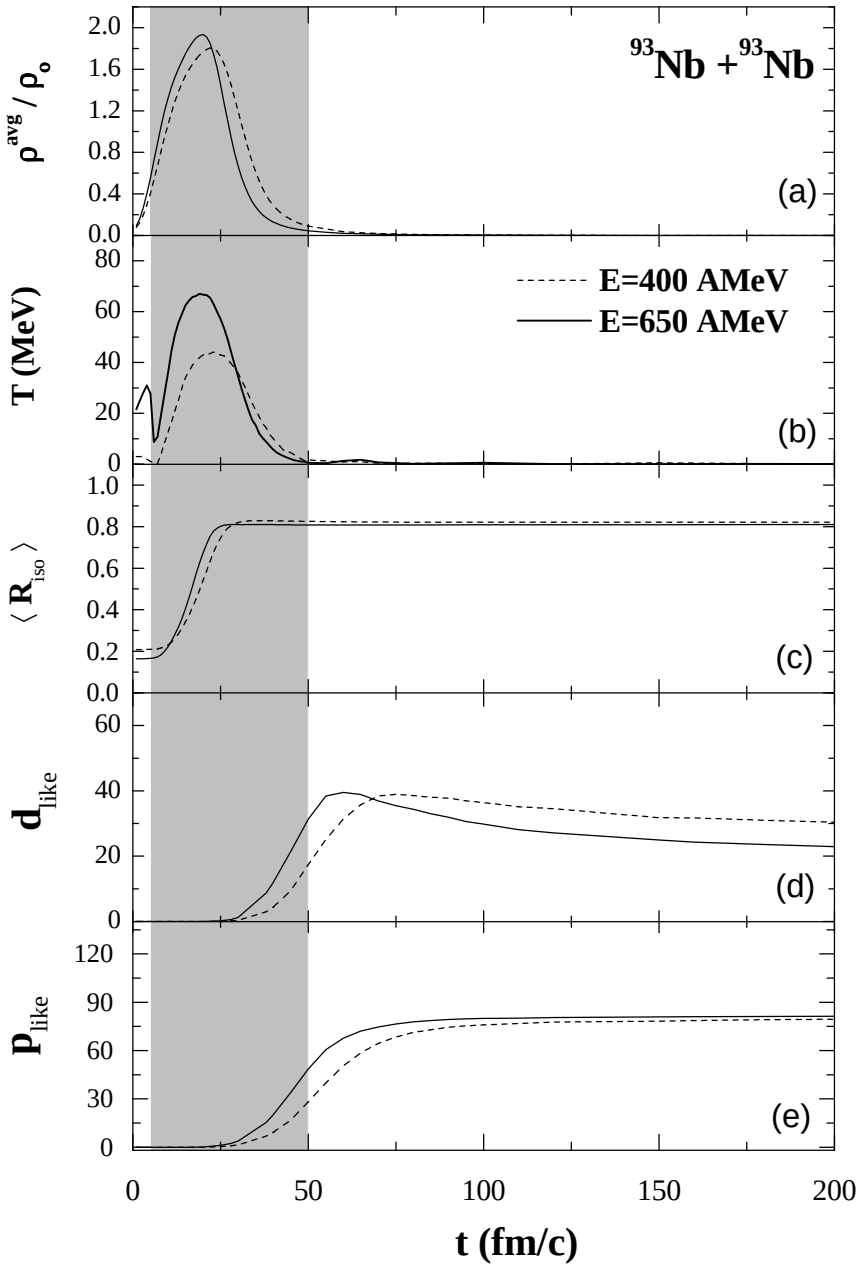

Figure 9.1: The time evolution of central collisions of $^{93}Nb + ^{93}Nb$ at incident energies of 400 and 650 AMeV. Results are shown here for: (a) average central nucleon density ρ^{avg}; (b) temperature T (in MeV); (c) anisotropy ratio $\langle R_{iso} \rangle$; (d)-(e) the yields of d_{like} and p_{like} clusters, respectively.

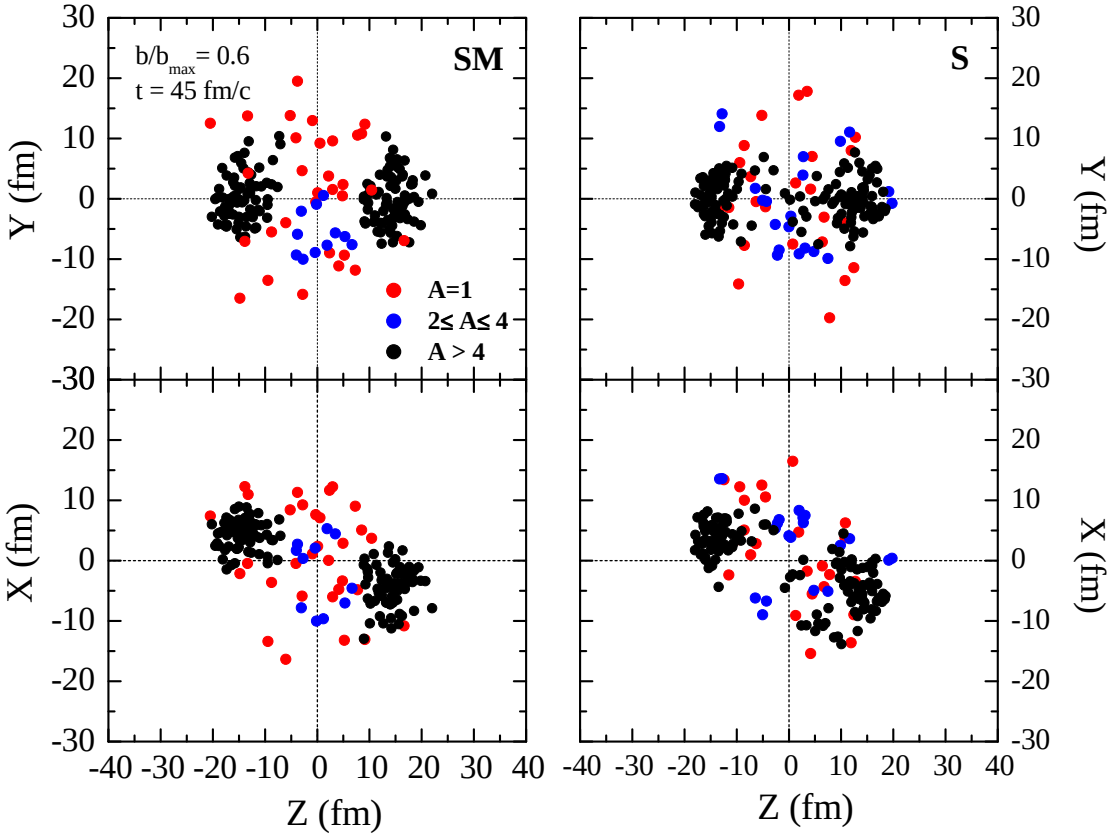

Figure 9.2: The 2-D snapshots of the distribution of nucleons in Z-X and Z-Y planes for a single event of Nb(650 AMeV)+Nb collisions at a 'reduced' impact parameter b/b_{max}= 0.6. Time taken here corresponds to the case when n-n collisions cease almost just after the violent phase of the reaction. Different colors depict the free particles, nucleons bound in light charged particles as well as in heavier fragments.

in coordinate ($\mathcal{R}_3$) space. In Fig. 9.2, we display the 2-D snapshots of ^{93}Nb +^{93} Nb collision at 650 AMeV and at a 'reduced' impact parameter b/b_{max}=0.6. Left and right panels depict the results for soft momentum dependent (SM) and static soft (S) equations of state, respectively. First of all, consistent with earlier attempts, we see that heavier fragments belong to the residue of either projectile or target, whereas lighter entities such as free nucleons and light charged particles LCPs [$2 \leq A \leq 4$] are produced due to the coalescence and emerge from the mid-rapidity region. As shown in Ref. [25], these light charged particles carry vital information about the stopping as well as thermalization of the nuclear matter, therefore, are also good candidates for estimating production of entropy in HI reactions. A very little influence can be seen of momentum dependent interactions.

9.3.3 Participant proton multiplicity dependence of composite particle yield ratios

Next we study the final state composite particle yield ratios X/p for the soft (S) and soft momentum dependent (SM) interactions. This is shown in Fig. 9.3 for the collisions of $^{93}Nb+^{93}Nb$ at incident energy of 650 AMeV as a function of impact parameter. Here 'X' stands for A=2, 3 and 4 clusters. From these curves, one can observe several interesting points:

1. The X/p ratio decreases with impact parameter (alternately, increases with N_P) indicating more production in central collisions compared to peripheral collisions. As shown by many authors [9–11], N_P remains same for nearly central collisions and decrease sharply for semi-central collisions and peripheral collisions.

2. For central impact parameters (or, higher N_P values), X/p ratios reach an asymptotic value indicating that for central events, small variation in impact parameter does not give different results.

3. Role of momentum dependent interactions is nearly marginal justifying the earlier attempts [26] and use of soft equation of state.

Since entropy production is mostly measured for central collisions, the use of momentum dependent interactions will not give different results compared to static soft (S) equation of state. These different yield ratios X/p also implied that one obtains different behavior of density reached, collision rate and multiplicity of various light mass fragments for S and SM interactions.

In Fig. 9.4, we extend the above study by including the ratio of deuteronlike (d_{like}) to protonlike (p_{like}) clusters. The calculations for d_{like}/p_{like} are done using a soft equation of state for the collisions of $^{40}Ca+^{40}Ca$ (at 400 and 1050 AMeV) and $^{93}Nb+^{93}Nb$ (at 400 and 650 AMeV) as a function of participant proton multiplicity. The results from Plastic Ball data [9] are also displayed for comparison. The Plastic ball data takes into account the overlap region for the yield of deuteronlike and protonlike clusters, while our ratios are calculated for the unfiltered events using MST procedure. The yield ratios

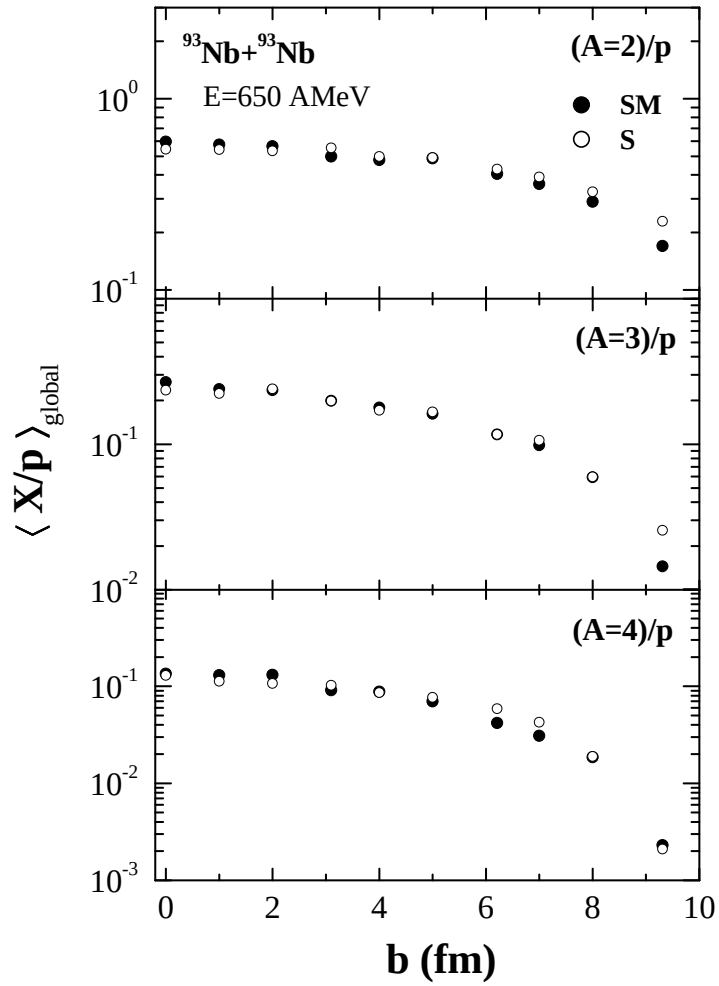

Figure 9.3: The yield ratio of light clusters to protons (X/p) as a function of impact parameter b using *minimum spanning tree* procedure. The term 'global' for the ratios X/p signifies that particle yield is calculated taking full ensemble into account and not the limited region only.

are calculated typically after 40 fm/c, when average nucleonic density saturates and n-n collisions practically cease. At this time, yield of composite particles is well established and may be compared with experimental data. One can clearly see that our model describes well the functional form of experimental d_{like}/p_{like} ratio which is found to increase with N_P (or centrality of the collision) and saturates at higher multiplicity end. At low N_P, there is a large drop in the yield ratios for the model calculations as also observed for individual cluster-to-proton (X/p) ratios (See Fig. 9.3). These trends are closely related with nuclear matter stopping and flow effects in the formation of hot & dense fireball. Recently, Dhawan *et al* [25] studied impact parameter dependence of light charged particles (LCPs)

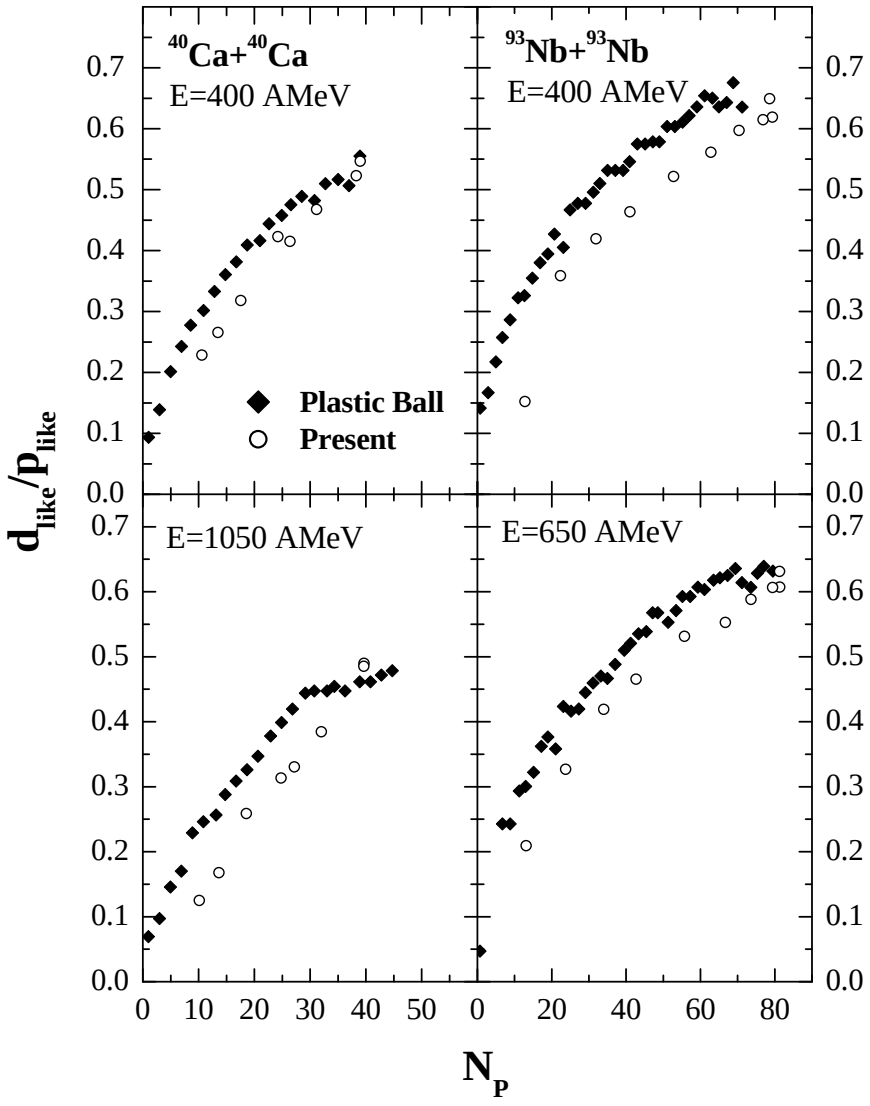

Figure 9.4: The d_{like}/p_{like} ratio as a function of baryon charge multiplicity N_p. The model calculations (open symbols) at the time of freeze out are compared with experimental data (solid symbols). The results are shown here for the reactions of $^{40}Ca +^{40} Ca$ (l.h.s.) and $^{93}Nb +^{93} Nb$ (r.h.s.)

yield and anisotropy ratio. It was found that LCPs production was maximum at central collisions where maximum stopping of nuclear matter is also achieved. Thus, production of light clusters can act an indicator of global stopping achieved in the nuclear matter. Interestingly, d_{like}/p_{like} ratios calculated using dynamical approach are in good agreement with experimental data. This shows that one can reliably explore the applicability of dynamical approach such as the QMD model to further investigate the formation of fireball at intermediate energies.

9.3.4 Participant proton multiplicity dependence of baryonic entropy

We have estimated the entropy produced in the fireball using Eq.(9.2). Figure 9.5 shows the baryonic entropy S_N calculated as a function of participant proton multiplicity N_P for the reactions of $^{40}Ca +^{40} Ca$, $^{93}Nb +^{93} Nb$, and $^{197}Au +^{197} Au$ at incident energies of 400 and 650 AMeV. Note that mass dependence has also been used to understand physics behind a particular phenomenon [27]. In central collisions (*i.e.* high N_P), entropy produced in highly dense matter is expected to be smaller. This happens due to the inhibition of *translational* expansion of hot nuclear matter. Contrary to this, lower density is reached in peripheral collisions leading to larger entropy production. It clearly brings out the participant-spectator picture of HI collisions at relativistic beam energies. One can clearly see that at given beam energy, it is the volume of participant nucleons (that is, N_P) which governs the entropy production rather than the total number of nucleons in the phase space. It means that participant volume solely determines entropy production, independent of the system size. These results are in agreement with the experimental data and theoretical approaches. In the next section, we try to understand beam energy dependence of baryonic entropy.

9.3.5 Beam energy dependence of baryonic entropy

Using the calculated yield ratios d_{like}/p_{like}, we tried to understand the beam energy dependence of S_N for the collisions of $^{40}Ca+^{40}Ca$ (at 400 and 1050 AMeV) and $^{93}Nb+^{93}Nb$ (at 400 and 650 AMeV). One of the earlier experiments on entropy measurement were done by Nagamiya *et al* [28]. Entropy was observed in the range $\sim 5-6$ and almost constant as a function of bombarding energy [29]. However, experimentalists have also used the QSM approach [8] to estimate entropy produced in the heavy-ion reactions. For Ca+Ca and Nb+Nb systems, it was found to be around $S_N \sim 4$ based upon Kapusta's prescription [5]. This points towards quite unusual mechanism for entropy formation.

In Fig. 9.6, we display our model predictions for baryonic entropy S_N along with experimental data taken with Plastic Ball detector [9]. The calculated S_N values in the range $\sim 4-5$ depict weak dependence on beam energy as is expected of an infinite nuclear matter source. Further, these trends are quite close to experimental values [9, 28]. Nearly no effect of beam energy on the baryonic entropy is visible in calculations as well as in

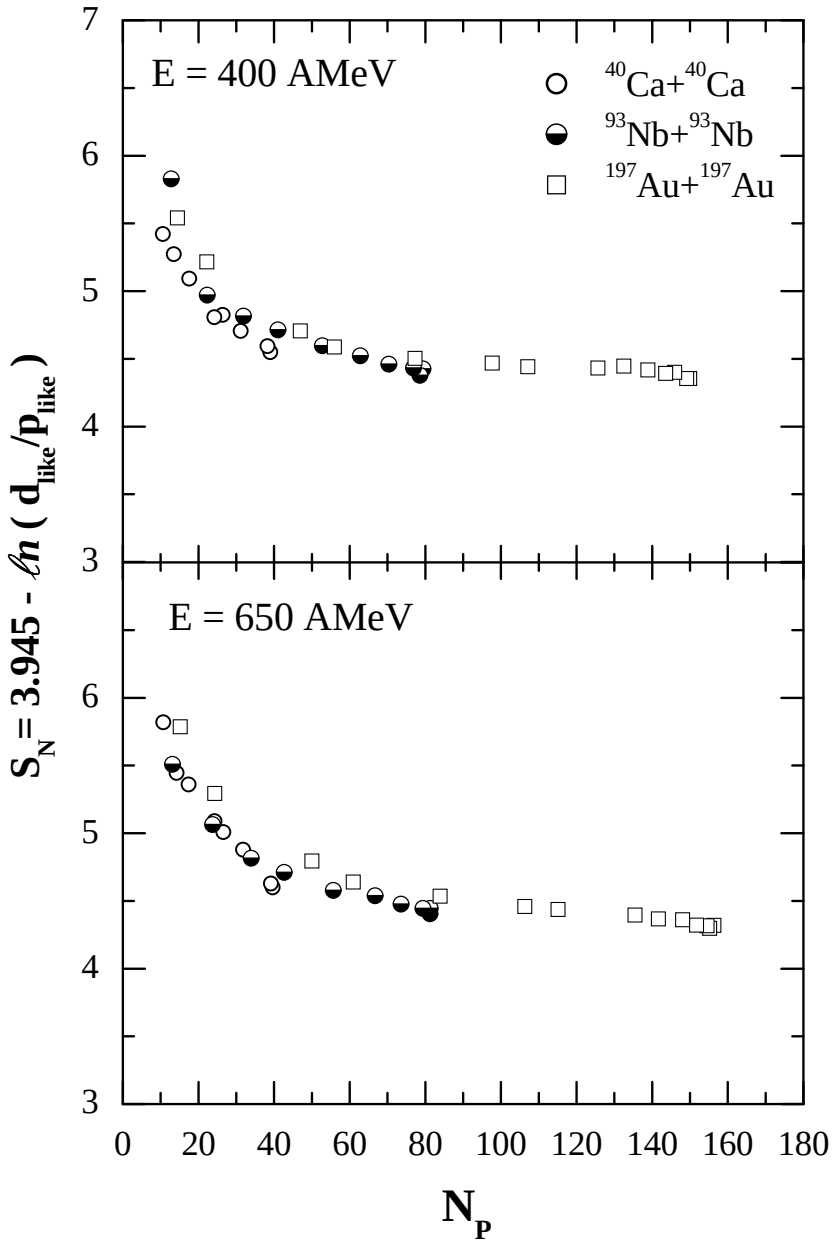

Figure 9.5: Entropy per nucleon S_N, as a function of baryon charge multiplicity N_p for the reactions of $^{40}Ca+^{40}Ca$ (open circles), $^{93}Nb+^{93}Nb$ (half filled circles), and $^{197}Au+^{197}Au$ (open squares). Calculations shown here are at incident energies of 400 (top) and 650 (bottom) AMeV.

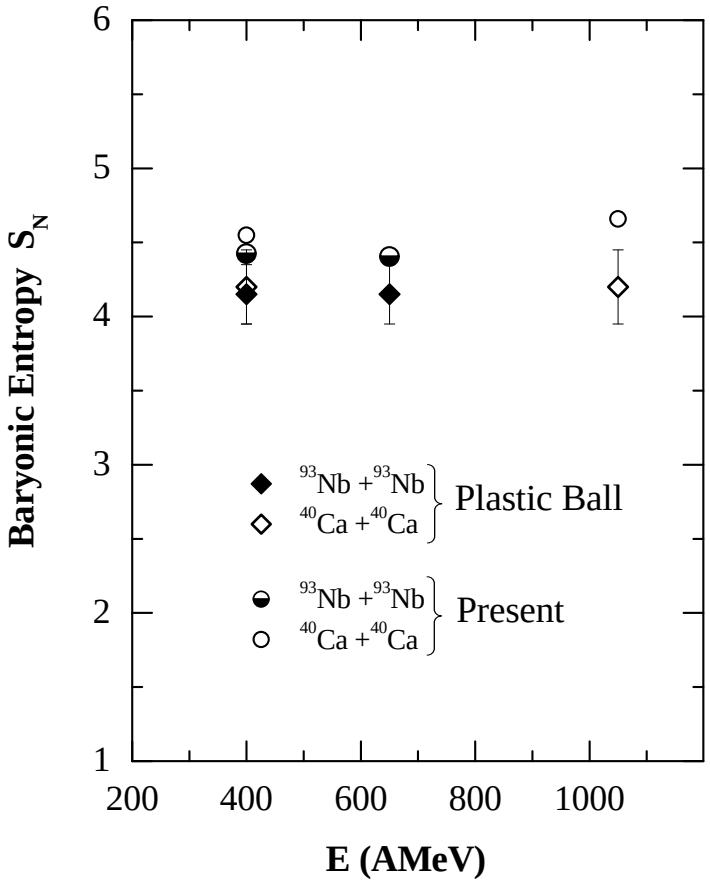

Figure 9.6: The relationship between baryonic entropy S_N and beam energy 'E' in lab. frame for the central collisions of $^{40}Ca + ^{40}Ca$ and $^{93}Nb + ^{93}Nb$. Also shown are entropy values extracted by the Plastic Ball group [9].

experimental results.

9.4 Summary

In this chapter, we have discussed, in detail, the thermal properties of hot and dense nuclear matter produced at different bombarding energies and colliding geometries. Our calculations indicate that compression and temperature achieved in the participant zone are directly linked with bombarding energy chosen. The degree of thermalization achieved, however, shows little sensitivity towards the bombarding energy chosen. Momentum dependent interactions are found to have negligible influence on the cluster distribution in coordinate space and cluster-to-proton (X/p) ratios. The d_{like}/p_{like} yield ratios calculated

as a function of participant proton multiplicity for unfiltered events accurately reproduce the experimental trends. The baryonic entropy calculated as a function of participant proton multiplicity is found to show system mass independence and depends solely on the volume of participants. Further, entropy calculated for central $Ca + Ca$ and $Nb + Nb$ collisions is largely independent of beam energy in accordance with experimental data based upon Siemens and Kapusta's formalism.

Bibliography

[1] G. J. Kunde *et al.*, Phys. Rev. Lett. **74**, 38 (1995).

[2] A. Schüttauf *et al.*, Nucl. Phys. A **607**, 457 (1996).

[3] B. de Schauenburg, F. Rami and P. Wagner, GSI Scientific Reports **98**-1, 56 (1997).

[4] T. Gaitanos, H. H. Wolter and C. Fuchs, Phys. Lett. B **478**, 79 (2000).

[5] P. J. Siemens and J. I. Kapusta, Phys. Rev. Lett. **43**, 1486 (1979).

[6] L. P. Csernai and H. W. Barz, Z. Phys. A **296**, 173 (1980); L. P. Csernai, B. Lukacs and J. Zimanyi, Nuovo Cimento Lett. **27**, 111 (1980).

[7] I. M. Mishustin, F. Myhrer and P. J. Siemens, Phys. Lett. B **95**, 361 (1980).

[8] H. Stöcker, Nucl. Phys. A **400**, 63c (1983).

[9] K. G. R. Doss *et al.*, Phys. Rev. C **32**, 116 (1985).

[10] J. Aichelin and E. A. Remler, Phys. Rev. C **35**, 1291 (1987).

[11] G. Peilert, H. Stöcker, W. Greiner, A. Rosenhauer, A. Bohnet and J. Aichelin, Phys. Rev. C **39**, 1402 (1989).

[12] P. Braun-Munzinger, J. Stachel, J. P. Wessels and N. Xu, Phys. Lett. B **344**, 43 (1998).

[13] L. Ahle *et al.*, Phys. Rev. C **57**, R466 (1998).

[14] J. Barrette *et al.*, Phys. Rev. C **62**, 024901 (2000).

[15] A. Andronic, P. Braun-Munzinger and J. Stachel, Nucl. Phys. A **772**, 167 (2006).

[16] P. Braun-Munzinger, I. Heppe and J. Stachel, Phys. Lett. B **465**, 15 (1999).

[17] S. V. Afanasiev *et al.*, Phys. Rev. C **66**, 054902 (2002).

[18] M. Gaździcki and D. Röhrich, Z. Phys. C **65**, 215 (1995); M. Gaździcki, Z. Phys. C **66**, 659 (1995).

[19] J. L. Klay *et al.*, Phys. Rev. C **68**, 054905 (2003).

[20] B. Hong *et al.*, Phys. Lett. B **407**, 115 (1997).

[21] G. Bertsch and J. Cugnon, Phys. Rev. C **24**, 2514 (1981); G. Bertsch, Nucl. Phys. A **400**, 221 (1983).

[22] S. Kumar, R. K. Puri and J. Aichelin, Phys. Rev. C **58**, 1618 (1998); J. Singh and R. K. Puri, J. Phys. G: Nucl. Part. Phys. **27**, 2091 (2001).

[23] M. Rashdan, A. Faessler, M. Ismail and N. Othsuka, Nucl. Phys. A **468**, 168 (1987); D.T. Khoa *et al.*, Nucl. Phys. A **529**, 363 (1991); G. Q. Li, D. T. Khoa, T. Maruyama, S. W. Huang, N. Ohtsuka, A. Faessler and J. Aichelin, Z. Phys. A **340**, 271 (1991).

[24] D. T. Khoa *et al.*, Nucl. Phys. A **542**, 671 (1992).

[25] J. K. Dhawan, N. K. Dhiman, A. D. Sood and R. K. Puri, Phys. Rev. C **74**, 057901 (2006).

[26] J. Aichelin, A. Rosenhauer, G. Peilert, H. Stöcker and W. Greiner, Phys. Rev. Lett. **58**, 1926 (1987).

[27] R. K. Puri *et al.*, Europhys. Lett. **9**, 767 (1989); R. K. Puri and R. K. Gupta, Phys. Rev. C **45**, 1837 (1992); J. K. Dhawan and R. K. Puri, Phys. Rev. C **75**, 057901 (2007).

[28] S. Nagamiya, M.-C. Lemaire, E. Moeller, S. Schnetzer, G. Shapiro, H. Steiner and I. Tanihata, Phys. Rev. C **24**, 971 (1981).

[29] H. Stöcker, J. Phys. G **10**, L111 (1984) and references therein.

Chapter 10

Concluding Remarks and Outlook

"*It is better to believe than to disbelieve; in so doing you bring everything to the realm of possibility.*" . . . . . Albert Einstein (1879-1955).

This thesis encompasses theoretical study of multifragmentation and related phenomena in intermediate energy heavy-ion collisions. The calculations are performed within the framework of dynamical approach namely *quantum molecular dynamics* (QMD) model. The phase space of nucleons is then analyzed by making use of various clusterization techniques which may be as simple as *minimum spanning tree* (MST) procedure, or more sophisticated one based on the *simulated annealing* technique used to minimize the binding energy of fragments.

First part of the thesis is concerned with beam energy dependence of fragment production and system size effects at the point of onset of multifragmentation. Our calculations for symmetric reactions over wide range of system masses indicate that peak center-of-mass energy (at which maximal IMF production occurs) exhibits a linear mass dependence. These results are in agreement with experimental mass dependence reported by MSU 4π-Array group. Interestingly, multiplicities of IMFs and other fragment species calculated as a function of composite mass of the system obey a power law of the form: cA_{tot}^{τ}; A_{tot} being total mass of the system. Interestingly, exponent τ is close to unity in all cases, indicating vanishing of surface-Coulomb effects. These calculations warrant detailed experimental verification of the same.

At relativistic bombarding energies, IMFs yields as a function of colliding geometry

is characterized by *rise and fall* behavior as observed in the ALADiN experiments. This trend was associated with the universality behavior, that is, it remains independent of the target-projectile combination and incident energy. We aimed to explain this universality and *rise and fall* behavior in the production of intermediate mass fragments using sophisticated clustering technique known as *simulated annealing clusterization algorithm* (SACA). For the first time, we are able to explain experimental data in the incident energy range 400-1000 AMeV using dynamical approach (QMD model, in our case). It also resolved earlier discrepancy, where QMD+MST approach couldn't explain unexpectedly larger yield of fragments from spectator zone. The clusterization algorithm, however, remains key tenet to describe the spectator fragmentation. This shows the importance of secondary clusterization models in describing the reaction dynamics in HI collisions. We further prescribed an improvement over original SACA method by optimizing the constant binding energy check of -4 MeV/nucleon with realistic binding energy of fragments. We have used modified Bethe-Weizsäcker (BWM) mass formula to calculate binding energy of fragments. This improvised version labeled as *SACA (2.1)* was used to study the ALADiN multifragmentation data at relativistic energies. Our calculations showed that fragment yields obtained using *SACA (2.1)* are still close to original SACA version and reproduce the ALADiN data quite accurately.

To further explore the applicability of SACA method, we extend this study to fragmentation of *quasi-projectiles* in ^{197}Au+^{197}Au reactions at incident energy as low as 35 AMeV. Our calculations are then compared with standard *minimum spanning tree* (MST) method for the charge distribution and charge of heaviest fragment obtained at different peripheral geometries. As noted MST method fails to predict experimental charge yields and size of the heaviest fragment even at 300 fm/c. SACA approach, on other hand, is on reliable footing that can recognize the stable fragment structure at an earlier time. This study indicates that SACA method is well suited to address the spectator matter physics over wide range of incident energies.

One can see that binding energy correlations among fragments play a decisive role to decide the final fragment structure. It would be of further interest to look into such energy based algorithms that can lead to still faster identification of fragment configuration and could provide improvisation over the present *simulated annealing* calculations.

The importance of *quasi-projectile* fragmentation was also highlighted to probe the incompressibility modulus via simulation of peripheral ^{197}Au+^{197}Au collisions at 35 AMeV. Theoretical simulations have shown that characteristics of spectator matter fragmentation during the collision process are directly linked with nuclear matter incompressibility of the participant matter. The nucleon-nucleon collisions at such low beam energy being Pauli blocked, reaction dynamics is insensitive to the choice of nucleon-nucleon cross section. This feature allowed us to predict the nuclear incompressibility to a very precise level. The prediction of *soft* compressibility modulus is in accord with earlier theoretical and experimental attempts.

Next, we tried to understand the role of momentum dependent interactions on the evolution of single cold QMD nuclei and fragment emission in HI collisions. The nucleus remains stable against the artificial emission of intermediate mass fragments, even with the inclusion of momentum dependent interactions. Our calculations using soft and soft momentum dependent equations of state depict the weakening of system size effects in the presence of momentum dependent interactions. The role of momentum dependent potential seems too explosive in nature in central collisions, which gets reduced in peripheral collisions. Also reaction systems, especially lighter ones exhibit larger *transparency i.e.* lesser stopping of nuclear matter in the presence of momentum dependent interactions. Confrontation with ALADiN experimental data clearly favors the need of momentum dependent interactions to explain the spectator matter fragmentation at relativistic energies. It would be of further interest to look into different strengths of this repulsive force and study space-time characteristics of fragments formed in detail.

As the last aspect, we aimed to study thermal properties of hot and & dense nuclear matter produced in the fireball. Our calculations showed that mean density and temperature reached in central zone is strongly influenced by bombarding energy chosen. The momentum anisotropy ratio, however, remains insensitive to the range of bombarding energy considered here. The full equilibrium could not be guaranteed in HI reactions even for the central geometry. This may be due to surface affects which are stronger in light systems and make the situation highly non-equilibrium. The yield ratios of deuteronlike-to-protonlike clusters exhibit universality phenomenon *i.e.* these remain independent of

system mass chosen and depend solely on volume of participants. Also baryonic entropy extracted from the yield ratios of deuteronlike-to-protonlike clusters is in nice agreement with data taken with Plastic Ball/Wall detector. These results showed that QMD model contains essential ingredients to describe the thermal features of fireball produced in intermediate energy HI collisions. It would be of further interest to extend this study in higher incident energy regime where pions also contribute significantly towards entropy production.

In summary, we have attempted to understand the clusterization mechanism and its role in faster recognition of fragments in heavy-ion collisions occurring at relativistic as well as in Fermi-energy domain. We also studied the role of model ingredients on the mass dependence of fragment production. As a last part of the thesis, we have modeled composite particles formation and extracted baryonic entropy for the heavy-ion collisions at intermediate energies.